Modeling and Analysis of Electric Vehicle Charging Interface

T. P. EZHIL REENA JOY

Modeling and Analysis of Electric Vehicle Charging Interface

A

Thesis Submitted

in Partial Fulfilment of the Requirements

for the Degree of

DOCTOR OF PHILOSOPHY

By

T. P. EZHIL REENA JOY

Department of Electronics and Electrical Engineering

Indian Institute of Technology Guwahati

Guwahati - 781 039, INDIA.

March, 2015

Certificate

This is to certify that the thesis entitled "**Modeling and Analysis of Electric Vehicle Charging Interface**", submitted by **T. P. Ezhil Reena Joy** (09610209), a research scholar in the *Department of Electronics & Electrical Engineering, Indian Institute of Technology Guwahati*, for the award of the degree of **Doctor of Philosophy**, has been carried out by her under my supervision and guidance. The thesis has fulfilled all requirements as per the regulations of the Institute and in my opinion has reached the standard needed for submission. The results embodied in this thesis have not been submitted to any other University or Institute for the award of any degree or diploma.

Dated:

Guwahati.

Dr. Praveen Kumar
Dept. of Electronics & Electrical Engg.
Indian Institute of Technology Guwahati
Guwahati - 781039, Assam, India.

To my mother

with love and gratitude ...

Acknowledgements

First and foremost, I thank my Lord and Savior Jesus Christ for granting me grace, time, health and essential wisdom to complete my research work. If words can express my thoughts and love then, with all my heart and with all my love I express my thanks to my loving mother L. Puspha Joy for her kindness, love, encouragement and prayers throughout my research. I am highly thankful to Prof. Somnath Majhi and his committee members for selecting me in interview and have given a chance to pursue doctoral research in this Institute. It is my bounden duty to thank Government of India, for establishing IIT Guwahati and for providing all facilities, web resources and scholarship to do the research. Then I knot my arms and express my sincere gratitude to my thesis supervisor Dr. Praveen Kumar, for the support and guidance given for me throughout my research work. I found my supervisor has some uniqueness in his guidance. I thank my supervisor, for guiding me to choose all my courses in my first year. I am grateful that he has helped me to complete all my academic requirements on time throughout my research period. I acknowledge that he has spent enough time in discussing my research problems, teaching me related basics and used to work my simulations during my initial days in Phd. In my second and third year, he taught me the importance to 'think' of a particular problem. He has also trained me how to structure the ideas in form of article. I acknowledge him gratefully that all chapters in this thesis are his ideas and that was worked out and elaborated in each pages. He has also spent his time to coordinate each work and get it done with a team by monitoring it continuously. I believe over the past years, I have absorbed some of his tactics in doing research. Under his guidance, I got acquainted with many software tools and learned many technical issues especially about electric vehicles, charging system, contactless system, energy storage systems and about other distributed energy resource. Along with my supervisor, I would like to thank Prof. Sanjay Kumar Bose, Prof. Pradeep Gururaj Yammiyavar and Prof. Somanath Majhi for serving in my doctoral exam committee. My doctoral committee members are always on time and spend their precious time to evaluate the progress of my work. Their suggestions are valuable and they have asked questions, which helped me to widen my knowledge and research work.

I am also indebted to my post graduate mentors especially Professor Anug Jaiprakash Kellogg and Dr. F.T. Josh at Karunya University, who have taught most of my courses in Power Electronics and made me to reach this stage. I must thank my Master program thesis supervisor Dr. T. Aruldoss

Albert Victorie, he is my first inspiration and one of the reasoner that i pursue my doctoral research. I also thank all my undergraduate mentors including Dr. N. Carolin Mabel and Mr. N.M. Spencer Prathap Singh for teaching me various courses in Engineering. Further, I am grateful to my school teachers who by delivering liberal yet rigorous education and prepared me to reach this level. My special thanks to Sister Lucia, Felix miss and Fathima miss, they are unforgettable and played a good role in my education. My teachers not only taught science and maths but also they have been a role model for humanity, kindness and dedication in work. In addition, I must thank my former colleague Ramesh and Aneesa, they are the prime reason for me to join in this Institute. I thank my colleagues here, Mukesh Singh, Kannan, Ankit, Brijesh and Guatam for their research collaboration. I could always discuss with them and it gave a concrete support in my research. My special thanks to Kannan and Ankit, they have always helped me whenever I approached them. I must thank Ambika mam and Josephine mams' family for helping me to grow spiritually. It has helped me to overcome my depression and my short temper. They are so kind enough and always greeted everyone and served delicious food. My special thanks to Ambika mam for taking care during my sick days. I thank my friends specially Sonali, Resmi, Sheeba, Malathi and Usha, I really had a good time with them. My special thanks to Usha and her help during my last days of my Phd. She kept an eye on me and insisted me to finish all my works quickly. I am grateful to all my other friends in IITG, my juniors and beyond, who have kept me happy and made me cheerful. I also acknowledge all the support and encouragements provided to me by other Professors and department non-teaching staffs and friends throughout my work. I also thank all the Professors who spend time to review my article. I pray to God to help all those who helped me. May God shower their lives with blessings according to Ezekiel 34:26.

Last but not the least, I thank all the readers who read my thesis. The chapters of this thesis are carefully done and I hope all the readers would surely gain knowledge on electric vehicle charging system and contactless system. Many relevant references are cited at the last pages of the thesis, which will also help you to understand and learn more about the recent technologies in EV charging systems. I thank one and all. Thank you

Thank you

(Reena Prathaf)

Abstract

As the energy demand and environmental issues are becoming increasingly prominent, the future of transportation is believed to be based on electric vehicles (EV). Apparently, the research on EV charging systems are very important for the development and popularization of EVs. This thesis describes the design, control and analysis of both contact based and contactless power transfer system suitable for EV charging system applications. The first chapter describes the classification of EV charging systems and has given the overview of contactless charging system including the principle of bidirectional charging system. The chapter has summarized the major challenges and goals identified in this research. The second chapter of this thesis has investigated the deployment of EVs aggregation through contact based charging system for the provision of voltage regulation at the distribution node. This chapter has modeled a contact based charging station and its control to coordinate multiple EVs arrived in the charging station. For this purpose, a charging station is modeled with multiple charging systems using ac-dc converter and a series connected dc-dc converter with suitable controllers to facilitate EVs of different ratings to charge and discharge. The developed charging system has been operated bidirectional to transfer power on both forward and reverse direction. This bidirectional power flow functionality of the charging system has been referred as grid-to-vehicle and vehicle-to-grid technology. The validation of the study is carried out for a 300kW charging station having 35 charging systems connected with EVs of different battery ratings. This charging system has been modeled to handle high power (up to a hundred kW) and high energy capacity (up to tens of kWh) batteries. However, charging and discharging such high capacity batteries using contact based charging systems in real time may cause the dangerous possibility of high voltage contact. If EVs are charged using contact-less technique, there are clear advantages to be gained in terms of safety, reliability and endurance. The third chapter of this thesis has focused on modeling, design and control aspects of parallel connected multiple contactless charging system connected to a common ac bus network.

Two types of charging station architectures are discussed. An electric equivalent circuit model has been used to describe the steady state electrical characteristics of contactless coil. The model has been validated with 500kVA charging station connected with ten 50kW charging systems. While, the contactless coil in the charging systems are designed using a fixed coupling factor assuming a perfect alignment between the coils. However, the usage of contactless system in EV battery charging applications are usually misaligned due to uneven road surface, tyre pressure, passenger weight etc. Therefore, the design of complete charging system becomes more complex due to this variations in the magnetic coupling between the coils. The variations in magnetic coupling affects the mutual inductance (MI) value and thereby causes fluctuations in the output voltage and affects the stability of the system. Therefore, an analytical approach is presented in the fourth chapter of the thesis to compute MI value with all its lateral and angular misalignments. The primary coil geometry is modelled as a straight line conductors and the MI value is calculated using flux linked to the secondary coil due to the primary coil. The method works by approximating the area of secondary coil and the flux distribution is calculated using Biot-Savart law. The results of computed MI value by analytical method are validated by finite element analysis and an experimental set-up. The values computed by three methods in all cases are in good agreement. Further, it has been observed, due to large leakage inductance and reduced magnetizing inductance, the value of MI gradually decreases when the distance increases. Therefore, compensation capacitors are required at the primary and secondary side of the contactless coil to reduce VA rating of the power supply and to increase the power transfer capability. The fifth chapter of this thesis presents an experimental study of four compensation topologies. Electric equivalent circuit model along with compensation topologies are developed to explain the mechanism of power transfer. The study investigates the behavior of contactless system and its characteristics plots are generated for wide range of frequency, load and distance such that the real time situations of contactless systems can be analyzed. The final analysis compares the efficiency of four compensation topology and its results are reported. The sixth chapter of the thesis has summarized the conclusion of the complete research work with some future direction of work.

Contents

List of Figures **xix**

List of Tables **xxv**

List of Acronyms **xxvii**

List of Symbols **xxxi**

List of Publications **xxxv**

1 Introduction **1**

1.1 Overview . . . 3

1.2 Electric vehicles and charging systems . . . 4

1.2.1 Classification based on the location . . . 4

1.2.2 Classification based on the charging level . . . 6

1.2.3 Classification based on the charging scheme . . . 6

1.2.4 Classification based on the charging method . . . 8

1.3 Contactless system . . . 8

1.3.1 Theory of CPT system . . . 9

1.3.1.1 Mutual flux and mutual inductance . . . 9

1.3.1.2 Leakage flux . . . 11

1.3.1.3 Contactless coils . . . 12

1.4 Contactless charging and electric vehicles . . . 15

1.4.1 Bidirectional charging systems . . . 16

1.4.2 Vehicle-to-grid (V2G) and Grid-to-vehicle (G2V) technology . . . 17

1.5 Major challenges and identified goals . . . 18

1.6 Contributions of this thesis . . . 20

1.7 Thesis organization . . . 22

2 Modeling of Contact based Charging Station for Voltage Regulation 23

2.1 Introduction . . . 25

2.2 Voltage regulation at distribution node . . . 28

2.2.1 Regulatory requirements . . . 28

2.2.2 Distribution node voltage control . . . 28

2.3 Frame work of simulation model . . . 29

2.3.1 Distribution system . . . 29

2.3.2 Layout of charging station (CS) . . . 30

2.3.3 Battery system . . . 31

2.4 Problem definition . . . 32

2.4.1 Fuzzy logic control (FLC) . . . 33

2.4.2 Aggregator . . . 35

2.4.3 Charging system . . . 36

2.4.3.1 CC-CV control . . . 36

2.4.3.2 Enhanced PLL based PWM control . . . 37

2.4.4 Control methodology . . . 40

2.5 Result analysis . . . 42

2.6 Conclusions . . . 48

3 Theoretical Modeling of Contactless Charging Station 51

3.1 Introduction . . . 53

3.2 Modeling of contactless charging station . . . 56

3.2.1 Types of charging station . . . 56

3.2.2 AC bus distributed EV charging station . . . 56

3.3 Bidirectional contactless charging system . . . 59

3.3.1 BCPT system configuration . . . 59

3.3.2 Contactless system modeling . . . 59

3.4 Problem description . . . 62

3.4.1 Charging station control strategy . . . 63

3.4.2 Scheduling algorithm . . . 63

3.4.3 Charging (BCPT) system . . . 65

3.4.3.1 G2V operation . . . 65
3.4.3.2 V2G operation . . . 68
3.4.4 Design of critical parameters . . . 69
3.4.4.1 Filter circuit . . . 69
3.4.4.2 Dc link capacitor . . . 70
3.5 Simulation results . . . 70
3.6 Conclusions . . . 74
4 Computation of Mutual Inductance for Contactless System 77
4.1 Introduction . . . 79
4.2 Possible variations of square coils . . . 81
4.3 Analytical modeling of square coil . . . 83
4.3.1 Modeling of mutual inductance . . . 83
4.3.2 Numerical evaluation . . . 85
4.4 Finite element modeling of square coil . . . 86
4.5 Experimental verification . . . 88
4.5.1 Description of power circuit and control circuit . . . 89
4.5.2 Experimental details . . . 90
4.6 Numerical results and discussion . . . 92
4.6.1 Perfect alignment - vertical and planar variation . . . 93
4.6.2 Lateral misalignment - horizontal and planar variation . . . 95
4.6.3 Angular misalignment . . . 96
4.6.4 Both lateral and angular misalignment . . . 97
4.7 Conclusions . . . 99
5 Compensation Topologies for Contactless System 101
5.1 Introduction . . . 103
5.2 Steady state electric circuit analysis . . . 106
5.2.1 Compensation topologies . . . 106
5.2.2 Mutual inductance coupling model . . . 107
5.2.3 Series-series (SS) compensation topology . . . 108
5.2.4 Series-parallel (SP) compensation topology . . . 111

5.2.5 Parallel-series (PS) compensation topology . . . 113
5.2.6 Parallel-parallel (PP) compensation topology . . . 115
5.3 Description of experimental set-up . . . 117
5.3.1 Design stages . . . 117
5.3.2 Block diagram . . . 118
5.3.3 Power circuit and coil description . . . 119
5.3.4 Control circuit description . . . 121
5.4 Results and discussion . . . 124
5.5 Conclusions . . . 137
6 Conclusions and Future Work 139
6.1 Concluding remarks . . . 141
6.1.1 Introduction chapter . . . 141
6.1.2 Modeling of Contact based Charging Station for Voltage Regulation . . . 141
6.1.3 Theoretical Modeling of Contactless Charging Station . . . 142
6.1.4 Computation of Mutual Inductance for Contactless System . . . 142
6.1.5 Compensation Topologies for Contactless System . . . 143
6.2 Suggestions for future work . . . 144
6.2.1 Future research on reducing the bulk semiconverters on either side of contactless system . . . 144
6.2.2 Future research on wide air gap distance and misalignments in the coils . . . 145
6.2.3 Future research on contactless coil arranged in a platform surface . . . 145
6.2.4 Future research on bidirectional charging system . . . 146
6.2.5 Future research on stability studies . . . 146
6.2.6 Future research to calculate power losses in contact based and contactless charging system . . . 146
6.2.7 Future research on active and reactive power exchange between the grid and the charging system . . . 146
6.2.8 Overall future research . . . 146
A Supplementary Materials 147
A.1 Additional figures from Chapter 2 . . . 149

A.2 Fuzzification & defuzzification for master control of Chapter 2 150
A.3 Membership function and rule base of CC-FLC, M-FLC and PA-FLC of Chapter 2 . . 152
A.4 Fuzzification and defuzzification process for power angle control of Chapter 3 154
A.5 Sample calculation for mutual inductance of Chapter 4 157
A.6 Remaining results of Chapter 5 157

Bibliography **163**

List of Figures

1.1 Classification of EV chargers [1–9]. 5

1.2 Two magnetically coupled coil. 10

1.3 Representation of contactless coil as series RLC circuit. 13

1.4 Vector diagram of series resonant circuit (a) Phasor diagram (b) Impedance diagram. 13

1.5 Block diagram of charging system 15

1.6 Block diagram of contactless charging system 16

1.7 Bidirectional contactless charging system 17

2.1 Illustration of CS connected at the DN. 28

2.2 Layout of charging station. 30

2.3 Circuit topology of charging system. 31

2.4 Battery equivalent circuit. 31

2.5 Membership functions for FLC (a) node voltage (V_1) (b) total energy availabilities of EVs (E_t) and (c) output power (S'). 34

2.6 Constant-current and constant-voltage charging strategy. 37

2.7 Enhanced PLL based PWM control. 38

2.8 Power angle control (PA-FLC). 39

2.9 Magnitude control (M-FLC). 39

2.10 Control process involved in EVs batteries. 40

2.11 Control operation of single unit of charging system. 41

2.12 Comparison of node voltage using P, Q and PQ control (G2V). 43

2.13 Comparison of node voltage using P, Q and PQ control (V2G). 44

2.14 Comparison of node voltage using P, Q and PQ control (both G2V and V2G). 44

2.15 DC link voltage (across C_{dc1}). 45

2.16 Power factor of the charging system. 45
2.17 State of charge of EVs batteries. 46
2.18 Battery power. 46
2.19 Estimated grid components using enhanced PLL method. 48
2.20 Apparent power injected/drawn by the CS. 48

3.1 Types of charging station 57
3.2 EV charging station architecture (a) AC bus distributed EV charging station (b) DC bus distributed EV charging station. 57
3.3 Single line diagram of EV charging station. 58
3.4 AC bus distributed charging station. 58
3.5 Configuration of bidirectional charging system. 60
3.6 Simplified equivalent circuit of contactless system (a) for G2V (b) for V2G. 60
3.7 Control operation of charging station. 64
3.8 Power angle control. 66
3.9 Membership function of phase angle-fuzzy control (PA-FLC) (a) Input: error and error rate (E_r/ ΔE_r) (b) Output: Power angle (δ'). 68
3.10 Equivalent circuit of grid connected inverter. 69
3.11 Power supplied from the EVs batteries. 72
3.12 SOC levels of EVs. 72
3.13 Charging and discharging current of EVs. 73
3.14 Power at the charging point. 73
3.15 Node voltage and node current. 74
3.16 Power at the distribution node. 74

4.1 Block diagram of contactless system. 80
4.2 Possible variations of contactless coils. 81
4.3 Schematics of square coils for analyzed variations (a) PA - vertical variation (b) PA - planar variation (c) LM - horizontal variation (d) LM - planar variation (e) angular misalignment (f) both lateral and angular misalignment. 81
4.4 Equivalent circuit model of an inductive coil. 83

4.5 Square current carrying coil (a) single turn (b) single turn segmented (c) multiple turn. 85
4.6 Flowchart describing the numerical evaluation. 87
4.7 FEA models of square coils for different variations (a) vertical (b) angular (c) planar. 88
4.8 Magnetic field lines for cut section of coils (a) vertical (b) angular 89
4.9 Schematic representation of power circuit. 90
4.10 Controller blocks. 90
4.11 Experimental setup for mutual inductance computation. 91
4.12 Experimental setup showing variations of coils. 92
4.13 Perfect alignment - vertical variation. 93
4.14 Perfect alignment - planar variation. 94
4.15 Lateral misalignment - horizontal variation. 95
4.16 Lateral misalignment - planar variation. 96
4.17 Angular misalignment - angular variation. 97
4.18 Both lateral and angular misalignment (angle = 10°, 20°, 30°). 98

5.1 Block diagram of contactless system with compensation. 104
5.2 Coil topology. 105
5.3 Equivalent circuit model of contactless coils (a) SS topology (b) SP topology (c) PS topology (d) PP topology. 107
5.4 Simplified equivalent circuit (a) with reflected impedance (b) with total impedance. . 109
5.5 Parallel compensated primary. 113
5.6 Block diagram of design procedure. 118
5.7 Basic building blocks of CPT system. 119
5.8 Power circuit. 120
5.9 Controller blocks. 122
5.10 Power circuit connected with controller. 123
5.11 Experiential set-up. 123
5.12 Voltage and current waveform at input and output side for SS compensation. 124
5.13 Voltage and current waveform at input and output side for SP compensation. 125
5.14 Voltage and current waveform at input and output side for PS compensation. 126
5.15 Voltage and current waveform at input and output side for PP compensation. 126

5.16 Voltage and current waveforms of capacitor and inductor at the primary side. 127
5.17 Voltage and current waveforms of capacitor and inductor at the secondary side. 127
5.18 Output power as function of operating frequency for varying distance (SS). 128
5.19 Output power as function of operating frequency for varying loads (SS). 128
5.20 Efficiency versus operating frequency for varying distance (SS). 129
5.21 Coupling versus distance for varying loads (SS). 129
5.22 Efficiency versus frequency at d=2cm, $R_L = 1.2\Omega$. 130
5.23 Efficiency versus frequency over variable load resistance (SS). 131
5.24 Comparison of input and output voltage (SS). 131
5.25 Comparison of input and output current (SS). 132
5.26 Output power versus distance for variable loads (SS). 132
5.27 Efficiency versus distance for variable loads (SS). 133
5.28 Efficiency versus distance at f=15.432kHz 133
5.29 Efficiency versus distance over variable frequency range. 134
5.30 Efficiency versus distance at f=15.432kHz, $R_L = 1.2\Omega$. 134
5.31 Efficiency as a function of load (SS) for variable distance. 135
5.32 Efficiency as function of load (SS) for variable frequencies. 135
5.33 Efficiency versus load resistance over variable distance (SS). 136
5.34 Efficiency versus load resistance at d=2cm, f=15.432kHz. 136

A.1 Simplified distribution system under study. 149
A.2 Load profile of subfeeder 4.3 during one day. 149
A.3 Input and output membership functions. 150
A.4 Output membership function. 151
A.5 Defuzzification process. 152
A.6 Membership function of constant current constant voltage fuzzy control (CC-CV FLC) and magnitude fuzzy control (M-FLC) (a) input: error (e) (b) input: error rate (e') (c) output: reference signals (u and v). 153
A.7 Membership function of power angle fuzzy control (PA-FLC) (a) input: error (e) (b) input: error rate (e') (c) output: power angle (δ'). 153
A.8 Input membership function: E_r and ΔE_r. 154

A.9 Output membership function. 156
A.10 Defuzzification process. 156
f-11 Input and output voltage and current waveforms at $f = f_o$. 158
f-12 Input and output voltage and current waveforms at $f > f_o$. 159
f-13 Input and output voltage and current waveforms at $f < f_o$. 159
f-14 Efficiency versus frequency at d=4cm, $R_L = 1.2\Omega$. 160
f-15 Efficiency versus distance at f=20kHz, $R_L = 1.2\Omega$. 160
f-16 Efficiency versus load resistance at d=4cm, f=15.432kHz. 161

List of Tables

1.1 Classifications of chargers [1, 2, 10–12] 5

1.2 Comparison of chargers' merits and demerits [1–9] 7

2.1 Rule base 35

2.2 Specifications of EVs' batteries. 42

2.3 Summary of injected and drawn power from/to the CS during several hours in a day. . 47

3.1 Rule base of power angle control (PA-FLC) 68

3.2 Simulation parameters of charging system. 71

3.3 Parameter of EV battery. 71

4.1 Coil parameters 82

4.2 Specifications of the components 89

4.3 Perfect alignment - vertical and planar variation 94

4.4 Lateral misalignment - horizontal and planar variation 95

4.5 Angular misalignment 97

4.6 Both lateral and angular misalignment (angle = 10° and 20° 98

4.7 Both lateral and angular misalignment (angle = 30°) 99

5.1 Specifications. 124

5.2 Summary of comparison of four compensation. 137

A.1 Rule base of CC-CV FLC and M-FLC 153

A.2 Rule base of power angle FLC (PA-FLC) 154

A.3 Results for sample calculation. 157

Nomenclature

CPT	Contactless power transfer
EV	Electric vehicle
MI	Mutual inductance
WPT	Wireless power transfer
IPT	Inductive power transfer
CET	Contactless energy transfer
ICPT	Inductively coupled power transfer
LCIPT	Loosely coupled inductive power transfer
CS	Charging station
SAE	Society of automotive engineers
DC	Direct current
SOC	State of charge
BES	Battery energy storage system
G2V	Grid to vehicle
V2G	Vehicle to grid
PCC	Point of common coupling
CB	Circuit breaker
BCPT	Bidirectional contactless power transfer system
AC	Alternating current
CP	Charging point
SPWM	Sinusoidal pulse width modulation
NB	Negative big
NVH	Negative very high
NH	Negative high

NM	Negative medium
NL	Negative low
NVL	Negative very low
PVL	Positive very low
PL	Positive low
PM	Positive medium
PH	Positive high
PVH	Positive very high
NS	negative small
Z	zero
PS	Positive small
PB	Positive big
VL	Very low
L	Low
M	Medium
H	High
VH	Very high
RF	Ripple factor
LCL	LCL filter
MI	Mutual inductance
FEA	Finite element analysis
EC	Excitation coil
OC	Observation coil
PA	Perfect alignment
VM	Vertical misalignment
LM	Lateral misalignment
AM	Angular misalignment
SS	Series-series
SP	Series-parallel
PS	Parallel-series

PP	Parallel-parallel
PWM	Pulse width modulation
MOSFET	Metal oxide semiconductor field effect transistor
AWG	American wire gauge
HO, LO	High and low side output
HIN, LIN	High and low side input
CC-CV	Constant current constant voltage fuzzy control
DN	Distribution node
PLL	Phase locked loop
FLC	Fuzzy logic control
M-FLC, PA-FLC	Magnitude and power angle fuzzy control
ICE	Internal combustion engine

Mathematical Notations

B	magnetic flux density
Φ/λ_1, Φ_{11}, Φ_{22}	magnetic flux, magnetic flux of the coil 1 and 2
L, L_1, L_2	inductance, self inductance of coil 1 and coil 2
φ_n	flux linked in the n^{th} coil
φ_m	flux linked in a single turn
${L_1}^m$, L_1'	main inductance, leakage inductance
$\Phi_{12}/\Phi_{21}/\lambda_{12}$	mutual flux
M, M_{12}/M_{21}	mutual inductance, mutual inductance between coil 1 and 2
k	coupling factor
ψ_{11}^m, ψ_{11}'	main flux linkage, leakage flux
ψ_{22}/ψ_1, ψ_{11}/ψ_2	self flux linkage of coil 1 and 2
ψ_{12}, ψ_{21}	mutual flux linkage of coil 1 and 2
V_1, V_2	voltage across primary and secondary coil
I_1, I_2	current in the primary and secondary coil
V_R, V_L, V_C	voltage across resistor, inductor and capacitor
Z_{coil}	total impedance of the coil
I_{coil}	current through single coil
L, C	inductance and capacitance
ω	angular frequency
f_o, ω_o	resonance frequency
ϕ	phase difference between voltage and current
t_a, t_d	arrival time, departure time
S_1 - S_6, D_1 - D_6	three phase grid bidirectional converter switches and diodes (charger circuit)
S_7 - S_{10}, D_7 - D_{10}	bidirectional inverter switches and diodes (charger circuit)

S_{11} - S_{14}, D_{11} - D_{14}	bidirectional inverter switches and diodes (EV battery system)
R_c, L_c, C_c	resistance, inductance, capacitance of contactless coil (charger circuit)
L_v, C_c, C_v	resistance, inductance, capacitance of contactless coil (vehicle circuit)
R_{L_c}, R_{L_v}	additional power electronic circuit and load of charger and vehicle
V_{dc}	Input dc voltage
f_{sw}	switching frequency
ΔI	ripple current
V_{conv}, I_{conv}	charging system voltage and current
V_c, I_c, V_v, I_v	voltage and current across contactless coil across charger circuit and vehicle
V_m	maximum peak voltage
f	frequency of operation
Z_{r_c}, Z_{r_v}	reflected impedance seen during G2V and V2G operation
Z_t	total impedance
Z_c, Z_v	impedance in the charger circuit and vehicle circuit
R, X_C, X_L	resistance, inductive reactance and capacitive reactance
L_{tf}, L_g	inductance of the transformer and grid network
$\overrightarrow{B_c}$	magnetic field at the center
A_n	n^{th} area of the small region
$\widehat{A}_n$	normal vector of the n^{th} area
Δx_n, Δy_n	length and width of the small divided region
$\overrightarrow{B}$	magnetic field due to one current carrying loop
$\overrightarrow{B_1}..\overrightarrow{B_4}$	magnetic field of the sides of the square coil
$\widehat{R}$	unit vector in the direction of position vector
$\overrightarrow{ds}$	differential element of current carrying conductor
$A_1...A_n$	multiple small area
$V_{carrier}$	carrier signal
V_{ref}	reference signal
V_{OC}, V_{EC}	voltage across EC and OC
L_p, L_s	inductance of excitation and observation coil
C_f	filter capacitor

L, W	length and width of the coil
N_p, N_s	number of turns in excitation and observation coil
I_1, I_{L1}, I_{C1}	supply, inductor and capacitor current in the charging circuit of contactless coil
I_{L2}, I_{C2}, I_L	inductor, capacitor and load current in the vehicle circuit of contactless coil
C_1, C_2	compensation capacitors in the primary and secondary side
Z_r, Z_s, Z_t	reflected, secondary side and total impedance of CPT system
P_i, P_o	input and output power of contactless coils
η_{SS}, η_{SP}	efficiency of SS and SP compensation
Q_1, Q_2	primary and secondary quality factor
VAR_1, VAR_2	volta-ampere rating in primary and secondary side
d	deviated horizontally from the center of the coil
h	deviated vertically from the center of the coil
θ	angle of observation coil with respect to excitation coil
g_7 - g_{10}	gate pulse of high frequency inverter
R_t, C_t, R_d	timing resistor, timing capacitor, potentiometer
C_r	Charge or discharge rate
P_2, P_L, P_1	active power of the node, load and CS
Q_2, Q_L, Q_1	reactive power of the node, load and CS
pf	power factor
C_{b1}, C_{b2}	boost strap capacitors
V_{o_i}	terminal voltage of i^{th} EV battery
Q_i	ampere hour rating of i^{th} EV battery
SOC_{lt}	user-defined SOC limits
$C_r{}'$	charge/discharge rate limits
V_1	distribution node voltage
E_t	total energy availabilities of EVs
S'	power output of FLC
E_1, $E_2...E_n$	individual energy availabilities of EVs
S_1, $S_2...S_n$	power distributed among EVs batteries
C_r	charge/discharge rate of the battery

$C_r^{'}$	user defined charge/discharge rate of the battery
$C_r{}^*$	current charge/discharge rate of the battery
SOC', SOC''	minimum and maximum SOC of EVs batteries
D	duty cycle
$i_o^{'}$, i_o	reference and measured battery current command
$v_o^{'}$, v_o	measured and reference battery voltage
$u_i^{'}$, u_i, $u_v^{'}$, u_v	per unit values of current and voltage
e_i, e_v	voltage and current error
e, e', u	input and output variable of the CC-CV FLC
C_{dc1}	stable dc link voltage
SOC_{lt}	user-defined SOC limits
$E_i{}^c$	required energy to charge the EVs
$E_i{}^d$	available energy to discharge the EVs
μ_v	aggregated membership function
L_b	inductor of bidirectional dc-dc converter
C_{dc1}, C_{dc2}	dc link capacitor
δ	power angle
p', q'	reference active and reactive power
p, q	measured active and reactive power
S	aggregated output
P_{bat}	battery power
v	magnitude
α	phase difference between voltage and current

List of Publications

Journal Publications

1. Joy E. R, Dalal. A and Kumar P., "The Accurate Computation of Mutual Inductance of Two Air Core Square Coils with Lateral and Angular Misalignments in a Flat Planar Surface", *IEEE Transactions on Magnetics*, vol. 50, no. 1, pp. 1-9, 2014.

2. Thirugnanam K, Joy E. R and Kumar P., "Modeling and Control of Contactless Based Smart Charging Station in V2G Scenario", *IEEE Transactions on Smart Grid*, vol. 5, no. 1, pp. 337-1348, Jan.2014.

3. Thirugnanam K, Joy E. R and Kumar P., "Mathematical Modeling of Li-Ion Battery Using Genetic Algorithm Approach for V2G Applications", *IEEE Transactions on Energy Conversion*, vol. 29, no. 2, pp. 332-343, Jun.2014.

Conference Publications

1. Joy E. R, Kushwaha B.K, Rituraj G. and Kumar P., "Impact of Circuit Parameters in Contactless Power Transfer System ", *IEEE International Conference on Power Electronics, Drives and Energy Systems Conference*, 2014.

2. Rituraj G, Joy E. R, Kushwaha B.K, and Kumar P., "Analysis and Comparison of Series-Series and Series-Parallel Topology of Contactless Power Transfer Systems ", *IEEE TENCON Conference*, 2014.

3. Joy, E.R., Thirugnanam K. and Kumar, P.,"A Multi-point Bidirectional Contactless Charging System in a Charging Station Suitable for EVs and PHEVs Applications", *Annual IEEE India Conference (INDICON)*, pp.1-6, Dec.2013.

4. Joy E. R, Thirugnanam K, and Kumar P.,"A Novel Reduced Switch Count Bidirectional Contactless Charging System for EVs and PHEVs Applications", *IEEE Students Conference on Engineering and Systems (SCES)* , pp.1-6, 2013.

5. Thirugnanam K, Joy E. R and Kumar P., "A Fuzzy Based Detunning Control Technology for Contactless Charging System of Electric Vehicles", *IEEE International Conference on Advanced Research in Engineering and Technology, (ICARET)*, DOI: 03.AETS.2013.2.79, vol.2, pp.374-379, 8th-9th Feb. 2013.

6. Thirugnanam K, Joy E. R and Kumar P.,"A Novel Fuzzy based Phase Angle Estimation Scheme for Grid Connected Bidirectional Contactless Power Transfer and PHEVs System suitable for Evs and PHEVs", *IEEE International Conference on Advanced Research in Engineering and Technology, (ICARET)*, DOI: 03.AETS.2013.2.81, vol.2, pp. 386 - 391, 8th-9th Feb.2013.

7. Joy E. R, Thirugnanam K, and Kumar P.,"Bidirectional Contactless Charging System using Li-ion Battery Model", *7th IEEE International Conference on Industrial and Information Systems (ICIIS)*, pp.1-6, 2012.

8. Joy E. R, Thirugnanam K, and Kumar P.,"A New Concept for Bidirectional Inductively Coupled Battery Charging System based on ac-dc-ac Converter for PHEV's and EV's using Fuzzy Logic Approach ", *IEEE Transportation Electrification Conference and Expo (ITEC)*, pp.1-6, 2012.

9. Ansari M. N, Thirugnanam K, Joy E. R and Kumar P.,"Powertrain Selection for Electric City Bus based on the Multicriteria Decision Making ", *14th International Power Electronics and Motion Control Conference (EPE/PEMC)*, pp.T6-140-T6-148, 2010.

Journal submitted

1. Joy E. R, Thirugnanam K and Kumar P., "Coordination of Electric Vehicles with Charging Systems in Distribution Network for Voltage Regulation ", *IEEE Transactions on Vehicular Technology.*

2. Joy E. R, Thirugnanam K and Kumar P., "Bidirectional Contactless Charging Station for Electric Vehicle Charging Facility ", *Journal of Emerging and Selected Topic in Power Electronics.*

Conference submitted

1. Joy E. R, Kushwaha B.K, Rituraj G. and Kumar P., "Analysis and Comparison of Four Compensation Topologies of Contactless Power Transfer System ", *IEEE India Conference (INDICON)*.

2. Kushwaha B.K, Rituraj G, Joy E. R and Kumar P., "Modeling and Analysis of Inductively Coupled Power Transfer System ", *IEEE India Conference (INDICON)*.

1

Introduction

Contents

1.1	Overview	3
1.2	Electric vehicles and charging systems	4
1.3	Contactless system	8
1.4	Contactless charging and electric vehicles	15
1.5	Major challenges and identified goals	18
1.6	Contributions of this thesis	20
1.7	Thesis organization	22

भारतीय प्रौद्योगिकी संस्थान गुवाहाटी
Indian Institute of Technology Guwahati

1.1 Overview

An electric vehicle (EV) charging system serves as a platform to interconnect EVs batteries to the utility grid. Therefore, the research on charging systems are very important for the development and commercialization of EVs. An EV battery can be charged using contact based and contactless charging system. Due to inherent advantages of contactless power transfer (CPT) system , contactless charging of EVs has presently become an economically feasible solution. CPT systems are designed to deliver power efficiently from a stationary primary source to one or more secondary loads over large air gap. Recent developments in CPT systems have largely attracted the interest of automobile industry to develop contactless charging system for EVs. However, the success story behind the adaptation of CPT systems for EVs has been shadowed by many technical problems; as the coupling between the coils depends on the dimension and positioning of the air gap distance of EVs. The magnetic coupling between the primary and secondary side of an EV lowers the mutual inductance (MI) of the coil. Moreover, the characteristics of CPT system changes due to misalignments and has large leakage inductance and reduced magnetizing inductance. Hence, the value of mutual inductance (MI) is one of the crucial factor in the design of CPT system and plays an important role in the determination of efficiency, power transfer and other components. This fact motivates to develop a method for MI computation, which should also consider the misalignments in the coil. Moreover, to compensate large leakage inductance problem effectively, compensation circuits can be added by connecting series or parallel capacitors at the primary and secondary winding of the coil. This makes the CPT system to operate at resonance and achieves maximum output power with minimum VA rating of the power supply.

This thesis has addressed the above mentioned problems in different chapters. This chapter introduces the reader the background of the research work. It summarizes the main problems, challenges, objectives of the work and the contributions of the thesis. Literatures most relevant to the work are mainly referred inside the chapters; only a brief description of the outward status of the works are mentioned here in this chapter. Throughout the chapters, various components of EV charging interface has been explained including its modeling, design and control concepts. The other chapters in this thesis are formed with introduction as the start along with its theoretical descriptions, which is then followed by simulation studies or experimental evaluations.

1.2 Electric vehicles and charging systems

Electric vehicles (EV) are the most viable way to achieve clean and efficient transportation that is important for the sustainable development of the whole world. In the near future, EVs will dominate the clean vehicle market and it is expected that more than half of new vehicle sales will likely be EVs by 2020 [13]. In the early years of 1900s, EVs are almost double that of gasoline power cars. However by 1920, EVs almost disappeared and gave the whole market to internal combustion engine (ICE) cars; due to the limitations of heavy battery weight, short trip range and poor durability of batteries at that time [10–12]. This battery weight problem and short trip range could be significantly reduced, if these batteries are charged at the bus stops or along the route [14]. Therefore, the crucial issue involved in the development of EVs is the efficient design of charging system. In addition, the success of EVs will be highly dependent on whether chargers can be built for easy access. This is also important for the potential grid support that EVs can provide. EVs' battery chargers are quite different from those used in consumer electronic devices such as laptops and cell phones. They are required to handle high power (up to a hundred kW) and high energy capacity (up to tens of kWh) within a limited space and weight and at an affordable price. Extensive research efforts and investments have been given to the charging methods and chargers that are suitable for EVs all over the world [2, 13, 15–18]. There have been various standards regarding the energy transfer, connection interface and communication for EV charging [1,2,10–12]. The first place considered for charging is homes and workplaces. Other potential locations with high populations includes shopping complex, restaurants, entertaining places, highway rest areas, municipal facilities and schools. The basic classification of commonly available chargers for EVs batteries [3–9] are shown in Figure 1.1 and Table 1.1 and 1.2. In this section, the theoretical background of EV charging systems, existing charging methods and technologies are discussed.

1.2.1 Classification based on the location

Based on the location of chargers, EVs are classified into onboard chargers, offboard chargers and integrated chargers. **On board chargers** are located on the vehicle itself. The electronic components that comprise the charger are incorporated into and are part of the vehicle design. i.e., charging circuit required to charge the vehicle will be incorporated inside the vehicle design. In the earlier EVs of the year 1900s used this method of charging [19]. The charger, because it is a part of the vehicle, always goes where the vehicle goes and it increases the overall weight of the vehicle. Since this option requires

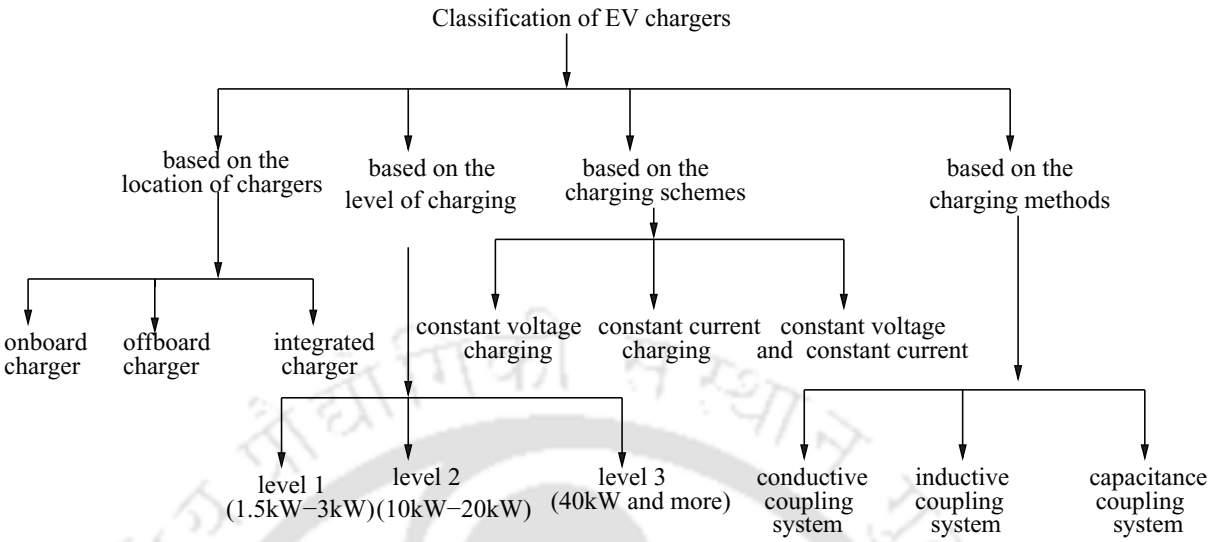

Figure 1.1: Classification of EV chargers [1–9].

Table 1.1: Classifications of chargers [1, 2, 10–12]

charger level	charger types	voltage level	power level	charger location	typical use
Level 1 (slow)	on-board (1-phase)	$120V_{ac}$ $230V_{ac}$	1.5kW to 3kW	vehicle itself	at home or office outlets
Level 2 (semi-fast)	on-board (1 or 3 phase)	$230V_{ac}$ $400V_{ac}$	10kW to 20kW	vehicle itself	at private outlets or office outlets
Level 2+ (slow)	integrated (1 phase)	$120V_{ac}$ $230V_{ac}$	1.5kW to 30kW	both vehicle and charging station	home /office public charging outlet
Level 3 (fast)	off-board (3 phase)	$240V_{ac}$ $600V_{ac}$ V_{dc}	50kW to 100kW and more	charging stations only	private /public charging stations or filling stations

an extra charging circuit, it increases the total cost of the vehicle due to the presence of charger in the vehicle. The power rating is limited due to space and weight restrictions on the vehicle; also it takes more time to fully charge a vehicle battery compared to off-board chargers, discussed later. With an on-board charger, a vehicle can be charged at any outlet that is available at home garages or workplaces with ground protection. **Off board chargers** is a separate piece of equipment and is not

the part of the vehicle i.e., this type of chargers remains outside the vehicle. It requires a dedicated charging station (CS) for charging the EVs battery and the vehicle needs to go where the charger is located in order to recharge the battery. The chargers can be placed at the bus stops along the road so that the EVs' batteries could be charged at the bus stops. Availability of such charging places will increase the acceptance of EVs technology. On the other hand, off-board chargers make use of fast charging and can charge a vehicle in a considerably shorter amount of time. It is possible to charge a battery in 10 minutes to increase its state of charge (SOC) by 50% with an off-board charger rated at 240 kW. **Integrated chargers**, can charge the battery at high power level that reduce the charging time. These types of chargers are classified as Level 2+ chargers, it takes about one hour to put 80% SOC to a battery rated at 30 kWh, which has been discussed later. The integrated chargers not only connect the vehicle's battery to most available standard 120V and 240V home garages outlets but also it couples the EV to an off-board charger, if faster charging is needed.

1.2.2 Classification based on the charging level

According to the Society of Automotive Engineers (SAE) standard J1772, there are three charging levels [4, 5, 8, 9]. Level I and Level II are the most suitable for home. If for example, one considers 2 kW as the average power demand of a typical home, then the charging load of **Level I** is about 70-100% of the average home power consumption. The charging power of **Level II** can be over 5 times higher than that of Level I. Therefore, it may be necessary to limit the charge rate to accommodate the rating of the on-board devices. **Level III** is for fast charging, which can give an EV 300 km range in one hour charging. This type of charger has to be off-board since the charging power can exceed 100 kW, which is significantly higher than Level I and Level II. It is obvious that Level III is not suitable for home use. It may be a better scheme for a company with a fleet of EVs. The total power and time that it takes to charge a group of EVs charged together at a low level can be the same as the fast charging of each vehicle in sequence. However, it is much more advantageous for an EV in the fleet can be charged quickly in less than 10 minutes.

1.2.3 Classification based on the charging scheme

The commonly used charging methods for EVs batteries [20] are constant voltage charging, constant current charging and combination of constant voltage and current charging. In **Constant voltage charging** method, EV battery is charged at a constant voltage. This method is suitable for

Table 1.2: Comparison of chargers' merits and demerits [1–9]

charger level	merits	demerits
Level 1 (slow)	Vehicle can be charged at any outlet available at home or office with ground protection	1. Power rating is limited. 2. Extra charging circuit increases the overall weight of the vehicle. 3. Takes more time to charge
Level 2 (semi-fast)	Vehicle can be charged at any private or public outlet	Extra charging circuit inside the vehicle increases the overall weight and cost of the vehicle
Level 2+ (slow)	It possess the advantage of level 1 and level 2 charger	Extra charging circuit increases the overall weight of the vehicle
Level 3 (fast)	1. Fast charging is possible 2. Charger can be placed at the bus stops	1. Charger requires dedicated charging station 2. Vehicle needs to go to the charger location to charge 3. Not suitable for home outlets

all kinds of batteries and probably the simplest charging scheme. The charging current of the battery varies along the charging process. The charging current can be large at the initial stage and gradually decreases to zero when the battery is fully charged. The drawback in this method is the requirement of very high power in the early stage of charge (SOC) level, which is not available for most residential and parking structures. In **Constant current charging** scheme, the charging voltage applied to the battery is controlled to maintain a constant current to the battery. The SOC will increase linearly versus time for a constant current method. In case of **Combined constant voltage and constant current charging**, during the charging process of a battery both the charging methods are used. At the initial stage, the battery can be pre-charged at a low, constant current if the cell is not pre-charged before. Then, it is switched to charge the battery with constant current at a higher value. When the battery voltage (or SOC) reaches a certain threshold point, the charging is changed to constant voltage charge. Constant voltage charge can be used to maintain the battery voltage afterward if the DC charging supply is still available.

1.2.4 Classification based on the charging method

The classification of charging methods are of three types: conductive charging system, induction coupling system and capacitance coupling systems. In **conductive charging systems**, metal-to-metal contact is used to transfer the electricity from the charger to the vehicle, similar to the traditional plug. Thus, in a conductive charging system, the connector is a plug [3–9, 19]. While for **induction coupling systems**, the power is transferred by induction principle, which is a magnetic coupling between the windings of separate coils rather than transferring power by a direct wire connection [21–23]. In **capacitance coupling systems**, power is transferred by electrostatic principle, which is a pair of conductors or plates separated by a dielectric between the two systems [24–28]. This types of charging scheme have not developed much and has been used only for low power levels.

In summary, as EVs have high power battery it comes under Level III charging, off-board chargers are most suitable in this applications. This thesis has mainly dealt with off board chargers employing an induction coupling system due to their inherent charging accessibility, ease of use and efficiency.

1.3 Contactless system

An EV battery can be charged using contactless charging system based on induction coupling principle. The term contactless system can be used to describe the power transfer between two objects that are physically unconnected. The word 'contactless' infers some sort of remote action, so that the power transfer could occur over a physical distance i.e., a non-galvanic contact is established between the source and the load that enables power transfer. CPT systems are becoming increasingly feasible as flexible and relatively safe mode of energy transfer. Two subclasses of contactless systems have recently evolved: wireless power transfer (WPT) systems and inductive power transfer (IPT) systems. The objective of a WPT system is to create maximum flexibility and thus to increase the WPT distance. High efficiency is the most important in an IPT system and thus the air gap is minimized as much as in the application of inductively coupled systems. This thesis has discussed the later and the nomenclature CPT system is used for IPT system throughout the chapters. Based on the known principle of electromagnetic induction and developing it further to meet modern industrial needs, CPT systems have achieved a technological breakthrough in the field of electrification. With the developments in power electronics, CPT system has found much success due to its simplicity, size and reliability [29]. A large number of terms have been used in literature that describes the same

phenomenon. Some of the terms are contactless energy transfer (CET), inductively coupled power transfer (ICPT), inductive power transfer (IPT), loosely coupled inductive power transfer (LCIPT), witricity etc. The term contactless power transfer (CPT) has been used and followed in this thesis. CPT is a method to transfer power magnetically rather than by direct physical contact i.e., from a primary winding to a galvanically isolated secondary winding [30–33]. This technology offers several advantages such as safety, durability, robustness, no sparking, no short circuits, no contact resistances, no wear and tear on the electrical contact and they are unaffected by dirt, dust and water and power compatibility [22, 30, 31, 34, 35]. Recent advancements in CPT systems have led to various medium to high power applications such as biomedical engineering, portable electronic equipments, machine tools, electric vehicle battery charging systems, personal rapid systems, aerospace, linear actuators, industrial robots etc [22, 30–33, 36–38].

1.3.1 Theory of CPT system

1.3.1.1 Mutual flux and mutual inductance

The principle of CPT system is mainly based on the theory described by Maxwell's equations. A current through a conductor produces a magnetic field also known as magnetic flux density B, which causes a flux ϕ. This flux is proportional to the current. The proportionality coefficient is the inductance L.

$$\Phi = LI \tag{1.1}$$

If there are two coils (designated as 1 and 2) in some arbitrary relative position to each other, the current i_1 that flows through coil 1 will cause a flux through coil 1 (as per the definition stated in (1.1)).

$$\Phi_{11} = I_1 L_1 \tag{1.2}$$

Some of the flux will also flow through coil 2 as designated by Φ_{21} and if the secondary coil is closed, then the current i_2 in the secondary coil will cause a mutual flux Φ_{12} as shown in Figure 1.2. This flux will oppose a mutual flux from the first coil. And the mutual inductance between coils 1 and 2 is given by definition:

$$M_{21} = \frac{\Phi_{21}}{i_1} \qquad M_{12} = \frac{\Phi_{12}}{i_2} \tag{1.3}$$

The concept of mutual flux and mutual inductance is very important in contactless transformer as they are the measure of system's ability to transfer power from one winding to the other. Mutual flux,

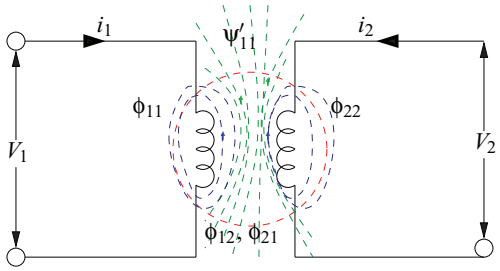

Figure 1.2: Two magnetically coupled coil.

as mentioned is the flux linking on both windings. Here, the magnetic flux Φ_{21} is less or equal to Φ_{11}, then a coupling coefficient ($k \leq 1$) can be defined.

$$\Phi_{21} = k\Phi_{11} \tag{1.4}$$

Now by principle of reciprocity, the same holds true for the current flowing through coil 2 and the flux through coil 1 can be calculated. The coupling coefficient stays the same.

$$\Phi_{12} = k\Phi_{22} \tag{1.5}$$

Now on substituting (1.4) and (1.5) and by multiplying both mutual inductances given in (1.3),

$$M_{21}M_{12} = \frac{k\Phi_{11}}{i_1}\frac{k\Phi_{22}}{i_2} = k^2\frac{\Phi_{11}}{i_1}\frac{\Phi_{22}}{i_2} \tag{1.6}$$

Then by definition of inductance (given in (1.1))

$$M^2 = k^2\left(L_1L_2\right) \tag{1.7}$$

$$M = k\sqrt{L_1L_2} \tag{1.8}$$

The inductance of a coil is determined by the geometrical shape and the physical arrangement of the conductor as well as the permeability of the medium. The mutual inductance between two coils is dependent on the distance and the relative position of the two coils. The ratio between the mutual inductance and the square root of the product of the self-inductances is the coupling coefficient, k.

$$k = \frac{M}{\sqrt{L_1L_2}} \tag{1.9}$$

where k lies between 0 to 1 ($0 \leq k \leq 1$). This coefficient measures the magnetic coupling between the coils and is independent of the number of turns in the coils. It only depends on the relative positions of the two coils and the physical properties of the media surrounding the coils. In an ideal CPT system, the mutual flux is equal to the total flux created by the primary and secondary windings (the combination of their fluxes). However, this is not the case in practical systems. The magnetic flux is not always links with the secondary coil. Some portion of the flux transverses outside the coil and takes outside the winding. This creates the so-called leakage flux which is explained in the following section.

1.3.1.2 Leakage flux

The self-flux linkage created by a magneto motive force will tend to follow through air with some reluctance. This means that the flux will resist flowing through the air that has a very small permeability. The self-flux linkages are composed of two parts. The main flux linkage (Ψ_{11}^m) that connects with other coils and the leakage flux linkage (Ψ'_{11}) that does not connect with any other coil. The name main flux linkage comes from the fact that in transformers the main flux linkage is the dominant part of the flux linkage. This is not the case with contactless transformer which has large leakage flux.

$$\Psi_{11} = \Psi_{11}^m + \Psi'_{11} \tag{1.10}$$

The main flux linkage is the mutual flux linkage linked with the coil that produced it.

$$\Psi_{11}^m = N_1 \Phi_{12} \tag{1.11}$$

The main flux linkage is scaled by a factor $\frac{N_1}{N_2}$,

$$N_1 \Phi_{12} = \frac{N_1}{N_2} N_2 \Phi_{12} \tag{1.12}$$

and is expressed as a scaling of the mutual inductance.

$$\psi_{11}^m = \frac{N_1}{N_2} M I_1 \tag{1.13}$$

Dividing by the current gives the main inductance (${L_1}^m$).

$$L_1^m = \frac{N_1}{N_2} M \tag{1.14}$$

$$L_1' = L_1 - {L_1}^m \tag{1.15}$$

It is easy to see that in the case of no secondary coil, the mutual inductance is zero and the self inductance (L_1) consists only of the leakage inductance ($L_1{}'$). If the coupling coefficient k goes to one then the leakage inductance goes to zero but in contactless system the coupling of the coil is always less than 1. According to Faraday's law, an alternating flux linkage will cause an induced electromotive force or voltage [39].

$${L_1}' = L_1 - {L_1}^m \tag{1.16}$$

The negative sign in (1.16) has been compensated by changing the direction of the winding of the secondary coil. From the current i_1 through the first coil, a voltage V_2 will be induced with the second coil. If a secondary coil is closed, a current will flow in the second coil. Using superposition, the total flux linkage of the second coil will be described as a combination of the self-flux linkage (ψ_{22}) and the mutual flux linkage (ψ_{12}).

$$\psi_2(t) = \psi_{12}(t) - \psi_{22}(t) \tag{1.17}$$

Some flux from the current in the second coil will link with the first coil and the total flux linkage of the first coil is defined in the same way.

$$\psi_1(t) = \psi_{11}(t) - \psi_{21}(t) \tag{1.18}$$

These equations are now described in terms of inductances.

$$\begin{aligned} \psi_1(t) &= L_1 i_1(t) - M i_2(t) \\ \psi_2(t) &= M i_1(t) - L_2 i_2(t) \end{aligned} \tag{1.19}$$

Using Faraday's law on the total flux linkages of each coil (assuming the inductances are time variant) leads to the relationship between input voltage, current and output voltage and current.

$$\begin{aligned} V_1(t) &= L_1 \tfrac{di_1(t)}{dt} - M \tfrac{di_2(t)}{dt} \\ V_2(t) &= M \tfrac{di_1(t)}{dt} - L_2 \tfrac{di_2(t)}{dt} \end{aligned} \tag{1.20}$$

1.3.1.3 Contactless coils

The contactless coils can be represented with a series capacitor, a resistor and an inductor as shown in Figure 1.3. As it is known, connecting capacitors with inductors can cause phase shifts. The phase shift is expressed by the equation of the impedance. Since one of the components cause a phase shift

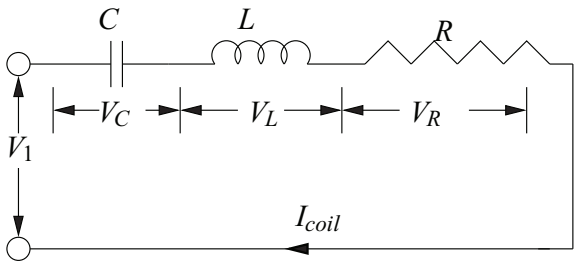

Figure 1.3: Representation of contactless coil as series RLC circuit.

of +90 degrees and the other can cause a phase shift of -90 degrees. Thus, they can be used to cancel each other out and the condition of resonance can be achieved in the circuit. The series coil shown in Figure 1.3, acts as a series resonance circuit with a total impedance given by (1.21)

$$Z_{coil} = -jX_C + R + jX_L = R + j(\omega L - \frac{1}{\omega C}) \tag{1.21}$$

The current flowing through L, C and R is the same. Using (1.21), a phasor diagram can be made as shown in Figure 1.4(a). I_{coil} is taken as a real vector, then dividing the voltage phasors by $|I_{coil}|$ to obtain the impedance diagram as shown in Figure 1.4(b). The phasors are rotating counterclockwise with angular speed ω. The absolute values of the rms voltage across the inductor and the capacitor

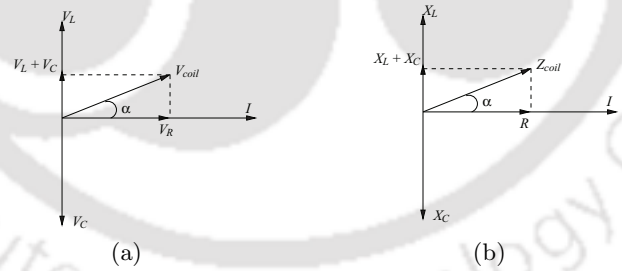

Figure 1.4: Vector diagram of series resonant circuit (a) Phasor diagram (b) Impedance diagram.

(i.e. $|V_L|$ and $|V_C|$ respectively) can be much higher than the absolute value of the supply voltage $|V_{coil}|$, if R is small compared to X_L and X_C. The circuit is said to be in resonance ω_o, if inductive reactance X_L equals capacitive reactance X_C, so if

$$\omega_o L = \frac{1}{\omega_o C} \quad ; \quad \omega_o = \frac{1}{\sqrt{LC}} \tag{1.22}$$

$$f_o = \frac{1}{2\pi\sqrt{LC}} \tag{1.23}$$

This is the resonance frequency. At this frequency, resonance occurs in the circuit and the current caused by the collapsing magnetic field in the inductor charges the capacitor, and then the discharging capacitor provides an electric current through the inductor that builds a magnetic field in the inductor. The energy in the system shifts between magnetic energy and the electric energy. This process is repeated continually. The magnitude of inductive reactance and the capacitive reactance gets canceled each other and the only component left in the circuit is resistance. Therefore, at resonance:

$$Z_{coil} = R \tag{1.24}$$

At resonance frequency, the phasor difference between the output voltage and the output current can be calculated as:

$$\alpha = \tan^{-1}\left(\frac{X_L - X_C}{R}\right) = \tan^{-1}\left(\frac{0}{R}\right) = 0 \tag{1.25}$$

In an ideal case, there are no losses at resonance and the system will continue to resonate. However, in reality there are resistance in the inductor and capacitor that will lead to losses and the ringing will die out. If the coil is not at resonance and if $\omega < \omega_o$, then using (1.21)

$$\omega L < \frac{1}{\omega C} \tag{1.26}$$

$$\omega L - \frac{1}{\omega C} < 0 \tag{1.27}$$

For this frequency range, the coil acts as a capacitive load and the applied voltage lags behind the current. In another case, for the coil not in resonance and if $\omega > \omega_o$, then using (1.21)

$$\omega L > \frac{1}{\omega C} \tag{1.28}$$

$$\omega L - \frac{1}{\omega C} > 0 \tag{1.29}$$

So for this frequency range, the coil acts as an inductive load with the applied voltage leading the current. In both situations, there will be a nonzero phase shift between the voltage and the current.

$$\alpha = \tan^{-1}\left(\frac{\omega L - \frac{1}{\omega C}}{R}\right) \tag{1.30}$$

$$\alpha = \tan^{-1}\left(\frac{\omega^2 LC - 1}{\omega RC}\right) \tag{1.31}$$

1.4 Contactless charging and electric vehicles

The term contactless system refers the system where the power transfer occurs between two or more physically unconnected electric circuits or devices by means of magnetic induction. Contactless system has been developed within a last few years. If EVs are charged using contact-less technique, there are clear advantages to be gained in terms of safety, reliability and endurance. Contactless charging is safe, efficient and easy to use for an EV [21–23, 31, 36]. EVs depend upon rechargeable batteries as a power sources and are recharged at the contact terminals [40]. EVs require a large amount of power (380V, 400Ah) to recharge its batteries [15]. Charging and discharging such high power batteries using on board chargers with traditional plug and socket method may cause the dangerous possibility of high voltage contact. Therefore, in such applications the implementations of contactless power transfer technique is very important [41]. Figure 1.5 explains the connection of electric grid to EV battery systems through the point of common coupling (PCC). PCC is the mode to transfer power between EVs. Here, charging circuit is found off the vehicle and EV battery system is present on the vehicle. This PCC can be replaced by induction coupling system which is explained later.

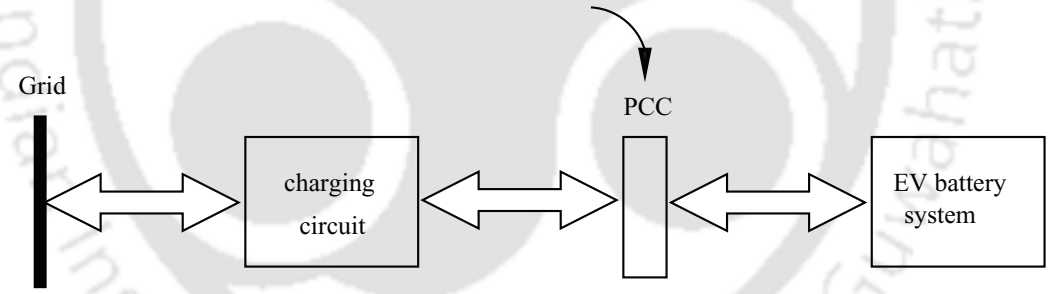

Figure 1.5: Block diagram of charging system

As discussed , contactless power transfer (CPT) system is a technique in which electrical energy is transferred between two or more EVs batteries through inductive coupling as opposed to energy transfer through conventional "plug-and socket" connectors [22]. Figure 1.6 shows the schematics of contactless coils placed between the electric grid and the power electronic converter. The primary and secondary of the transformer windings are electrically isolated from each other. The power electronic system lies outside the vehicle or off the vehicle, which is referred as charging circuit and the EV battery system lies on the vehicle. This charging system can be implemented for both moving applications and

in battery charger for idle vehicles. In the first case, the secondary coil moves along a primary coil and captures the horizontal flux component. In the second case, both primary and secondary windings are stationary and captures the vertical flux component [36,42]. Thus, CPT systems are used to transmit several kilowatts of power without any mechanical stress or aging. By this technology, trailing cables in the EVs can be removed and therefore cable breaks can be avoided. Other advantages are no metal oxidation of the electric plug, no wear and tear on the electrical contacts, no contact resistance, no sparking and no non-protected voltage-carrying contacts [41].

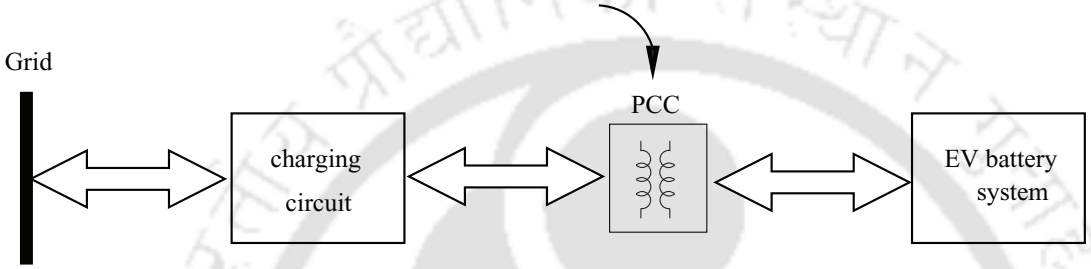

Figure 1.6: Block diagram of contactless charging system

A common feature of all applications for which CPT systems are used up to now is the relatively small air gap in a range of several millimeters between the primary and secondary system [31, 36, 41–50]. Therefore, such magnetic assemblies can be accurately described by means of commonly known magnetic equations. However, in applications such as automatic battery charging station require a large air gap of several centimeters [31, 36, 42]. In order to achieve efficient power transfer through this large air gap between the windings of the contactless transformer, principle of resonance is used. To increase the power transfer capability and to reduce the VA rating of the contactless system, capacitive compensation is used in both primary and secondary windings of the CPT systems [31,36]. The extension of contactless system to longer distance would open new application field for this technology.

1.4.1 Bidirectional charging systems

EVs are primarily considered as a method of clean transport but they can also be used as a potential source of energy by supplying power back to the grid. With bidirectional converters in the charging system, EVs' batteries will be able to transfer power between the grid and the EVs [51]. This process is coined as Vehicle-to-grid (V2G) and Grid-to-vehicle (G2V) technology, where G2V implies charging

the EVs batteries from the grid and V2G means delivering the stored energy back to the grid [52]. The V2G and G2V services are provided through bidirectional charging systems with bidirectional power flow functionality [51, 53, 54]. This re-electrification process can be achieved through bidirectional converters i.e., the power converters are made of bidirectional switches to facilitate power transfer on both the directions. This makes EVs an ideal candidate to assist the power system operation. Figure 1.7 shows the basic schematics of bidirectional charging system connected to an EV battery.

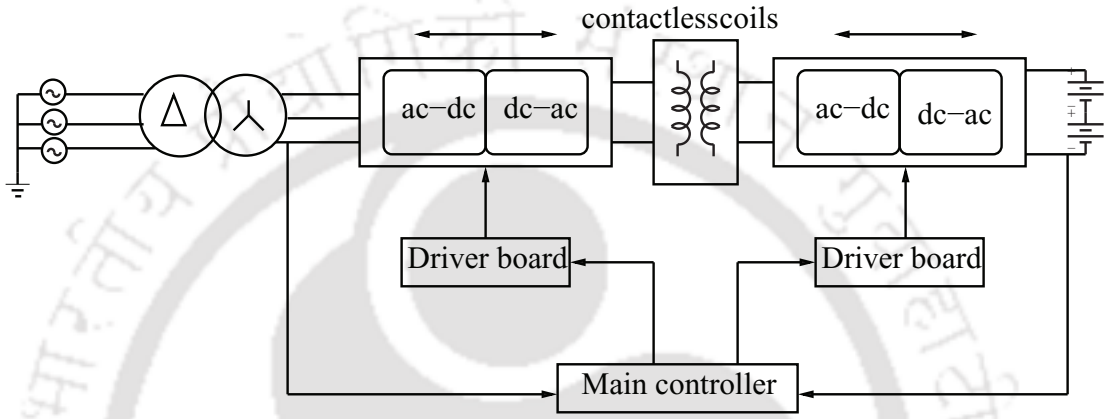

Figure 1.7: Bidirectional contactless charging system

1.4.2 Vehicle-to-grid (V2G) and Grid-to-vehicle (G2V) technology

As explained earlier, EVs provide economic and environmental benefits; they can also be used as a potential source of energy storage which is valuable to the electric power grid [52, 55, 56]. With the additional bidirectional arrangement of converters in the charging system; EVs can charge its battery from the grid and discharge the stored energy back to the grid. Thus, EVs can become an ideal candidate to assist the power system operation such as voltage regulation, frequency regulation, power quality improvement, peak load shaving and other grid ancillary services by increasing the security and reliability of the power system [52]. By incorporating bidirectional switches in the converters of the contactless system this process can be achieved. Hence, EV's batteries are able communicate the grid through coil coupling induction principle with high safety and low repair rate features [51,53,54]. The term G2V implies charging the EVs battery from the grid [52]. V2G describes a system in which EVs communicate with the power grid to sell demand response services by either delivering electricity into the grid or by throttling their charging rate [57,58]. Since most vehicles are typically driven only a few

hours per day and are parked the rest of the time (during the night or work) their batteries could be used to let electricity flow from the vehicle to the power lines and back. This ability to exchange energy with the grid gives the opportunity to furnish several services to the grid while optimizing the charging and discharging operations [57–60]. The service from G2V and V2G is done through EV charging system. However, charging or discharging of individual EV battery cannot provide any meaningful service to the grid, as it is usually in tens of kWh level. This is far below the base requirement for making transaction in electricity market, which is usually in MWh level. Therefore, the EVs should be synchronized with many vehicle. These problems could be addressed by introducing the concept of aggregator in the architecture of V2G system [55, 60, 61]. Rather than individual EVs batteries, effective impact on grid service provision can be obtained by grouping together a large number of vehicles through this aggregator. A sufficiently large number of aggregated parked EVs could provide several important services to the grid such as regulation, peak power, spinning reserves and other ancillary services [55, 60, 61].

While, two chapter of this thesis has dealt with the modeling and simulation details of power electronic converters and control requirements for bidirectional charging systems; the rest of the two chapters focus on mutual inductance computation and compensations requirements of contactless coils. Experimental set-ups are built in the laboratory to validate the MI computation and compensation circuits. While the hardware prototype for bidirectional charging systems have not been done.

1.5 Major challenges and identified goals

In comparison to conventional vehicles, EVs suffer from heavy battery weight, limited driving range and long charging time. Recent studies suggest that the existence of EV charging systems at the bus stops or along the route will address this issue to some extent [2, 62–64]. The present research is focussed on modeling and analysis of EV charging interface. This thesis have modeled a contact based EV CS with multiple charging systems, which facilitates bidirectional power flow between EVs and the power grid. However, such CS will have numerous challenges to overcome. The bulk charging and discharging of EVs can cause adverse impacts both on charging system and the distribution network [65, 66]. Therefore, the CS should be coordinated for the effective utilization of EVs in the distribution network. As a further benefit of this application, the CS with large fleet of EVs should be designed in such a way that the CS should be capable of handling the sudden arrival

and departure of EVs and will have significant impact on the DN voltage profile. Proper active and reactive power control would provide better coordination and control and regulates the voltage at the distribution node. A fuzzy controller and an aggregator is designed in this thesis to externally control the CS to handle the sudden arrival of multiple EVs in the CS. For this purpose, an idea of active and reactive power approach have been demonstrated to control and coordinate multiple EVs arrived in the CS for achieving voltage regulation in the distribution network. On the other hand, contactless charging system offers many advantages such as safety, power compatibility, connector robustness and durability to the users of EVs [23, 38, 67]. Additionally, the development of bidirectional contactless charging system would allow EVs batteries to both charge their batteries and to support power back to the grid [51, 53]. Although, the amount of literature in this area grows very fast; there are many technical issues which still hinders the fast development of contactless charging systems.

One important focus in contactless charging system is to interface multiple charging system in a CS connected to the utility grid. Several studies have been carried out in this area but most of the works are aimed to study the impact of charging systems in the power distribution network and many other studies in the literature have focussed on the design and analysis of contactless system. Nevertheless, no studies in the literature have reported the contactless based multiple charging system connected to a common ac bus network to demonstrate the charging and discharging operation of EVs. Therefore, in order to prepare for the large proliferation of EVs in the market, this thesis has modeled a multiple contactless based charging system to examine the charging/discharging operation of EVs, which is essential for the future implementation of EV charging systems.

Another important design challenge for contactless system is the theoretical estimation of MI [68]. The design of contactless coils are very complex as the coils are usually misaligned due to variations in the system and worsen the coupling between the coils [69, 70]. A simple theoretical computation of MI with all its lateral and angular misalignments must be fully addressed, which is the first step and an important step for studying the characteristics of such systems. Although, there are various methods available to estimate the mutual inductance of contactless coils, it has been observed these methods are well suited for fixed coil systems and they are not tolerant for misalignments in the coils. Therefore, this thesis has suggested an analytical approach for computing the mutual inductance of the coil with lateral and angular misalignments.

The principle of CPT system is similar to a conventional transformer, where the magnetic field is

confined to a particular core. In contrast to conventional transformer, contactless transformer has a large air-gap and are used without high permeability common magnetic core. Due to this air-gap, the characteristics of contactless system has large leakage inductance and reduced magnetizing inductance. To compensate large leakage inductance problem effectively, in addition to contactless coil, suitable compensation circuit can be added by connecting a series or parallel capacitor at the primary and secondary winding of the coil [31, 71]. This makes the contactless circuit to operate at resonance and achieves maximum output power with minimum input VA rating of the power supply. A large number of studies have been found in the literature, where CPT system has been analyzed using a particular compensation focussing a specific application. While, there are no studies found in the literature, where all compensations has been examined to analyze its variations for frequency, load and distance. In order to fill the research gap, this thesis has analyzed the four basic compensation topologies and studied its variations with respect to frequency, load and distance.

The thesis has addressed the above mentioned issues, there are still many open areas in contactless and bidirectional contactless system which is unaddressed in this thesis. Some future research work has been suggested at the end of the thesis. The problems dealt in this thesis have been detailed in the foregoing section, which can give a better understanding of the work done.

1.6 Contributions of this thesis

The main goal of this thesis is to design and analyze the long term work on bidirectional contactless charging system that would connect the grid and the EVs batteries. Such a system should facilitate charging the EV batteries from the grid (forward flow of power) and discharging its energy back to the grid during times of power shortage (reverse power flow). However, the thesis has narrowed its study to certain specific areas on the design and modeling of contact based and contactless charging system. Simulation studies have analyzed the bidirectional power flow functionality of EVs for both contact based and contactless charging systems. While, the hardware prototypes are made only for contactless system. In particular, the thesis has investigated the following areas:

I. Modeling of Contact based Charging Station for Voltage Regulation

A contact based multi-point charging station model is described to regulate the distribution node (DN) voltage. An idea of active and reactive power exchange through EV CS for voltage regulation at

the DN is presented based on the node voltage variations and energy availabilities of EVs batteries. A CS is modeled has multiple charging systems which enables EVs of different battery ratings to charge and discharge. The individual charging system is composed of grid connected bidirectional three phase ac-dc converter and a series connected dc-dc converter with suitable controllers. Voltage profile evaluation have been done with different power transfer approaches such as active power, reactive power and combined active and reactive power to foresee the CS behavior. Finally, validation of the study is carried out using a realistic distribution system of a typical city considering 35 EVs of different battery ratings connected at the DN via CS. The analysis shows that the combined active and reactive power transfer has a significant impact on flattening the DN voltage profile as compared to other approaches.

II. Theoretical Modeling of Contactless Charging Station

The demand for more Electric Vehicles (EVs) will increase the power distribution requirements of future EV CS. Similar to petrol stations, multiple charging systems will be co-located to form a CS. To increase safety and reduce the CS maintenance time, these charging systems have to be developed with contactless systems. The work presented in this chapter describes a parallel connected multiple bidirectional contactless charging system. An operating framework of CS is described to manage the interactions of EVs, between parallel connections of multiple charging systems that share a common ac bus network. The individual charging systems are controlled to control the charging and discharging process of each EVs and avoids distribution grid congestion, while satisfying the requirements of EV owners. To coordinate the complete CS, a control strategy is developed; which estimates the line voltage and frequency at the common coupling point of the distribution system and state of charge of EVs and manages the parallel ac lines by scheduling the charging and discharging operations of EVs. The complete CS having ten EVs is validated using detailed simulations. Theoretical analysis and the simulation results demonstrates the feasibility of the proposed CS as an ideal power interface for efficient contactless integration of multiple EVs into a typical distribution network.

III. Computation of Mutual Inductance for Contactless System

An analytical approach for computing the mutual inductance between two air core square coils of contactless system placed in a flat planar surface is described. The mutual inductance of the coils are calculated for all possible variations including lateral and angular misalignments in space. In contrast

to conventional approximated formulae, the straightforward approach based on Biot-Savart principle is used and their integrals are computed numerically. The results of computed mutual inductance by analytical method are validated by finite element analysis and an experimental setup. Finally, the analysis compares the three mutual inductance calculations: an analytical method, the finite-element model and an experimental results. The values computed by three methods in all cases are in good agreement.

IV. Compensation Topologies for Contactless System

Due to large leakage inductance, compensations are necessary in contactless system to achieve the required power transfer. Analysis of four compensation topologies suitable for use in CPT applications has been presented. Primary compensation is designed to make the primary phase angle equal to the secondary resonant frequency with minimum VA rating of the power supply. Secondary compensation is designed to increase the power transfer capability. The modeling of CPT system, design criteria and its controller details are discussed. The study investigates the behavior of CPT system under variable frequency, load and distance and its characteristics plots are generated. The analysis compares the efficiency of four compensation topologies, such that the real time performance of CPT systems can be examined. With the results obtained from the experiments, the theory of CPT systems can be well understood and it provides a foundation for future design and implementation of CPT systems.

1.7 Thesis organization

This thesis has organized into five chapters. Chapter I has given an overview of charging system, theory of contactless systems and the role of bidirectional charging systems. Chapter II describes the modeling and control of contact based CS with multiple charging systems to regulate the DN voltage. Chapter III describes the theoretical modeling, design, control and simulation of multiple parallel connected contactless charging system connected with EVs batteries. Chapter IV describes an analytical approach suitable for computing mutual inductance between two air core square coils for contactless system. Chapter V has presented four compensation topologies suitable for contactless system. Finally conclusion of this thesis is given in Chapter VI with some future directions of work.

2

Modeling of Contact based Charging Station for Voltage Regulation

Contents

2.1	Introduction	25
2.2	Voltage regulation at distribution node	28
2.3	Frame work of simulation model	29
2.4	Problem definition	32
2.5	Result analysis	42
2.6	Conclusions	48

Abstract

In this chapter, a contact based multi-point charging station model is described to regulate the distribution node (DN) voltage. The increased penetration of electric vehicles (EVs) in real time may result in voltage rise or drop at the DN. An idea of active and reactive power exchange through contact based EV charging station (CS) for voltage regulation at the DN is presented based on the node voltage variations and energy availabilities of EVs batteries. A CS is modeled has multiple charging systems which enables EVs of different battery ratings to charge and discharge. The individual charging system is composed of grid connected bidirectional three phase ac-dc converter and a series connected dc-dc converter with suitable controllers. An enhanced phase locked loop (PLL) technique with pulse width modulation (PWM) control is used for three phase ac-dc converter, which makes it possible to exchange the active and reactive power transfer between the DN and the CS. The designed dc-dc converter adopts constant-current and constant-voltage (CC-CV) charging strategy to charge or discharge the EVs batteries of different ratings. In order to handle multiple EVs arrived at the CS and to regulate the DN voltage, the complete CS is externally controlled by a fuzzy controller and an aggregator. Voltage profile evaluation have been done with different power transfer approaches such as active power, reactive power and combined active and reactive power to foresee the CS behavior. Finally, validation of the study is carried out using a realistic distribution system of a typical city considering 35 EVs of different battery ratings connected at the DN via CS. The analysis shows that the combined active and reactive power transfer has a significant impact on flattening the DN voltage profile as compared to other approaches.

The work presented in this chapter is submitted in a Journal, titled, "Coordination of Electric Vehicles with Charging Systems in Distribution Network for Voltage Regulation"

2.1 Introduction

With the worldwide interest in EV, the design and control of EV CS has gained much research interest. Charging station is the vital supporting infrastructure that plays an important role in the grid integration of EVs batteries and helps in realizing the vehicles batteries as a load and an efficient power source [1, 2, 72]. Thus, a cluster of EVs can be utilized as a load and a well-defined source of energy comparable in reliability to fossil-fuel based power plants [73–75]. To achieve this concept, the

CS should have multiple charging systems with bidirectional power flow functionality that facilitates EVs of different battery ratings to charge or discharge. This bidirectional power flow functionality of CS are referred as G2V and V2G technology [1, 40]. The G2V and V2G process can be achieved when the CS is situated near the DN in a parking lot with a charging bay [66]. The parking lot can be a residential complex or office complex or shopping complex, where EVs tends to stay for longer duration and thereby this concept can be easily achieved [74]. Thus it is possible to exchange active as well as reactive power between the grid and the EVs batteries using bidirectional converters in the charging systems [76]. Therefore, it is required to develop a CS which can handle multiple EVs of different ratings mainly in terms for voltage regulation at the distribution node (DN).

Many studies on EVs and battery models have been published in recent years [28, 77–79] and many other studies have focussed on battery charging systems [2, 62–64]. Concerning the power converters involved in charging systems, a two stage structure composed of three-phase rectifier followed with dc-dc converter is the simplest and most economical form of circuit [1,2]. Few traditional charging systems have used two-stage structure with an isolated transformer [62,64]. Non-isolation type battery charging systems are more preferable when considering the efficiency, volume and cost [1,2,63]. Very few studies have reported non-isolation type battery charging systems because of the difficulty in handling batteries of different ratings during its two way power transfer [1, 2]. Another set of studies have focussed on optimization models to represent EV charging systems [57,58,80–82]. Among those, few of which have paid more attention to prove the validity of EVs in terms of frequency regulation [80–83]. In [57, 58], a control algorithm is developed for scheduling the charging and discharging of EVs' batteries for autonomous distributed V2G systems. All of these studies have pointed the need to coordinate the charging or discharging in some way to accommodate a large number of EVs. However, a very few works have addressed on voltage regulation issue using EV charging system. In [73], authors have studied the V2G existence using load flow techniques for voltage regulation at the DN. They have considered the aggregated EVs' energy in a particular area and analyzed the impact on the distribution network. In [65,66], a real-time coordination of plug-in EVs charging have been explained to minimize the power losses and to improve the voltage profile. These system level control approaches aims at the effective utilization of EVs for grid support. However, it has been observed from the literature; so far these studies have dealt only with active power transfer to realize the CS for DN voltage regulation. Nevertheless, there has not been much technical analysis done in both active and reactive power

transfer with component level contact based EV charging system model to regulate the DN voltage. While, the benefits of active and reactive power transfer have been widely studied in wind, photovoltaic and other grid integrated converter applications [84–86]. In similar manner, if EVs' batteries exchange active as well as reactive power to the distribution network, a better coordination and control can be achieved. Moreover, the multiple charging systems of the CS also needs an additional control mechanism to coordinate the sudden arrival and departure of EVs, yet to be reported. Based on the above discussions, the following are the main objectives of the present chapter.

- Design and simulation of EV charging systems with its associated controllers to enable successful integration of EVs during its bidirectional power transfer.
- Design of grid connected three-phase ac-dc and dc-dc converter with enhanced PLL based PWM control and CC-CV charging strategy; to improve the quality of grid waveform and to increase the performance of the battery during charge/discharge operation.
- Design of master controller and an aggregator to control and coordinate multiple EVs arrived at the CS.
- Investigating the behavior of CS with different power transfer approaches such as active, reactive and combined active and reactive power.

The CS designed in this chapter has multiple charging systems which facilitates EVs of different ratings to charge or discharge their batteries. To control and coordinate the sudden arrival and departure of EVs and to regulate the specified voltage limit (1 ± 0.13), the CS is externally controlled using a fuzzy logic controller (FLC) and an aggregator. Here, the usage of other traditional control methods; often results in computational burdens due to large number of operations such as trigonometric functions, parametric identifications, filtering and so forth. An FLC indeed, does not require neither detailed knowledge of the system under control nor its precise description in terms of mathematical model. FLC here acts as a master control, which decides the total power to be injected or drawn from the DN. Aggregator distributes the power among multiple EVs arrived in the CS. EVs in the CS exchange active power or reactive power or both through charging systems from/to the DN. A CS has been modeled in simulation environment and has been tested with 35 EVs of different ratings connected to a realistic radial distribution system of Guwahati city (shown in Appendix A.1) [87].

This chapter is organized as follows: Section 2.2 explains the voltage regulation concept at the distribution node. Section 2.3 describes the framework of the simulation model. Problem definition is detailed in Section 2.4. Simulation results are discussed in Section 2.5 and the conclusions are given in Section 2.6.

2.2 Voltage regulation at distribution node

2.2.1 Regulatory requirements

Integrating EV charging systems with the DN will have direct impact on the utility grid which might cause voltage rise or drop at the DN. Since the voltage of the distribution network is based on radial power flow; this would affect various nodes of the distribution system. This can be regulated when the CS is operated in a controlled and coordinated manner based on the grid conditions. The distribution network operator is obliged to maintain the voltage profile within its limits (1±0.13). Therefore, before interconnecting the CS with the DN, the distribution network operators should ensure that the DN voltage will not be affected by the charging or discharging operations of EVs.

2.2.2 Distribution node voltage control

Figure 2.1 illustrates the single line diagram of the simplified distribution network connected to the CS together with the local load by an overhead line cable with an impedance (Z). Here, V_2 is the voltage at bus A, V_1 and I are the total injected or drawn voltage and current from/to the CS. R and X are the resistance and reactance of the line. The power exchange at the CS can cause large voltage

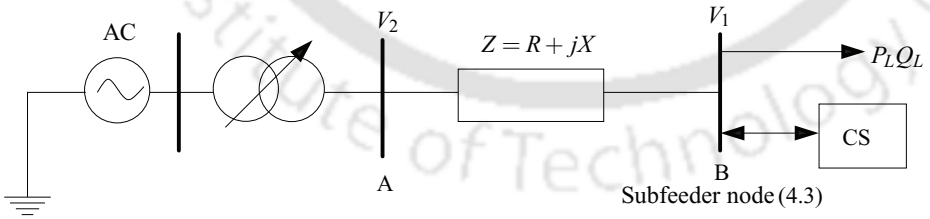

Figure 2.1: Illustration of CS connected at the DN.

rise or drop due to bulk charging or discharging of EVs, this can be estimated by (2.1).

$$\Delta V \approx V_2 - V_1 + R(P_2 - (P_L \pm P_1)) + X(Q_2 - (Q_L \pm Q_1) \tag{2.1}$$

where P_2, P_L and P_1 represents the active power of the DN, load and CS. Q_2, Q_L, Q_1 represents the reactive power of the DN, load and CS. It can be seen (2.1) is governed by DN voltage (V_1), impedance of the line ($R+jX$) and active and reactive power flow of the line. Theoretically, the voltage regulation can be achieved by adjusting either V_1, R, X, active power, reactive power and or both. Among these factors, adjusting the injected or drawn voltage at the substation may cause adverse impacts on any of its customer. This may also affect EVs with varying state-of-charge (SOC) and charge or discharge rate (C_r) conditions. While, upgrading the conductor size is an effective approach, but it is very expensive. At the same time, active power exchange alone seems very attractive because it requires only minor modifications in the inverter control logic. However, minimizing the amount of active power during voltage rise would result in increased output power losses. As an alternate solution, the DN voltage can be more effectively controlled, if the CS can exchange relatively large reactive power. This may result in higher currents and losses in the subfeeder. In this case, CS do not work anymore at unity power factor (pf). Managing the voltage profile in DN by reactive power exchange alone can be justified in some cases [88,89], nevertheless its application is limited because distribution network operator may stipulate the CS to operate at or close to unity pf. Generally for the distribution network, X/R ratio tends to be low (typically ≤ 1), so neither active nor reactive power is negligible. Therefore, both active and reactive power exchange would play a vital role to regulate the voltage at the DN. Hence, the charging system should ensure to draw or inject maximum active power at minimum reactive power. Both P and Q should be regulated and controlled by injecting or drawing the power, either by controlling V_2 and phase angle (δ) between V_1 and V_2 or current (I) and power factor angle (θ) between V_2 and I.

2.3 Frame work of simulation model

2.3.1 Distribution system

The system under study comprises of 33kV, 5MVA main feeder and 11kV/440V, 500kVA distributed subfeeder, typically operated in a radial fashion. There are 12 numbers of nodes (1.1 to 4.3) in the subfeeder. The CS considered for this study has been connected to the subfeeder 4 of the DN **4.3** to regulate the DN voltage in the system (Figure A.1 shown in Appendix A.1). The daily load profile of the **DN 4.3** of the Guwahati distribution network has been used for the study (load data is shown in Figure A.2 in Appendix A.1). The simulation is carried out in real time on the modeled

network of the Guwahati distribution system.

2.3.2 Layout of charging station (CS)

A real time simulation model of CS has been built to analyze the charging or discharging operation of EVs' batteries. The CS designed in this work has thirty five charging systems connected with EVs of 35 different ratings, which represents multiple EVs connected at the CS. The layout of CS is shown in Figure 2.2. The individual charging system is comprises of bidirectional ac-dc and dc-ac converter with suitable controllers as shown in Figure 2.3. The developed charging system has the ability to control the power flow of each EVs present in the CS. The control algorithm present in the EVs' battery considers terminal voltage (V_{o_i}), ampere hour rating (Q_i), user-defined SOC limits (SOC_{lt}) and charge/discharge rate limits ($C_r{}'$) based on user's preference. The complete CS is externally controlled using a fuzzy controller and an aggregator to coordinate multiple EVs arrived at the CS. The fuzzy controller decides the magnitude and direction of power to be flown from or to the CS.

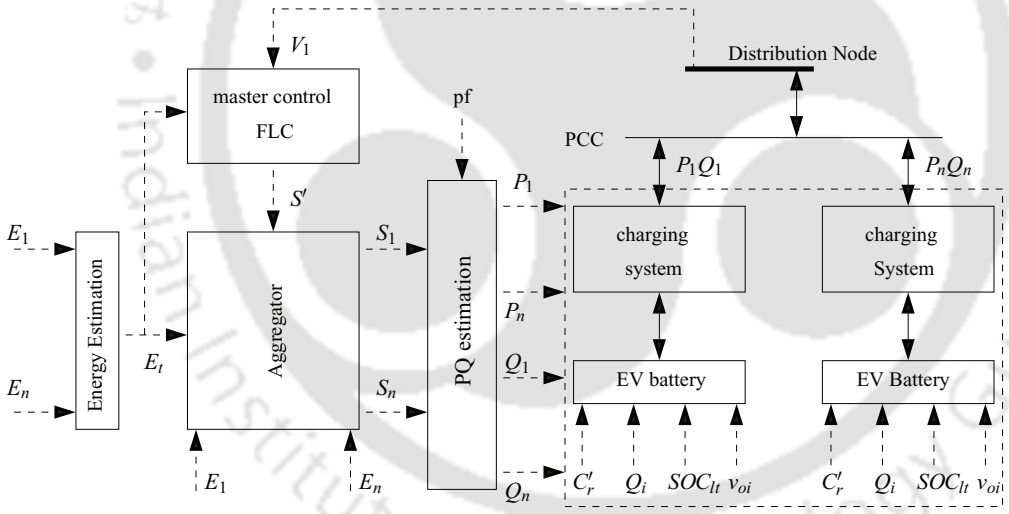

Figure 2.2: Layout of charging station.

The FLC receives DN voltage (V_1) as input from the DN and total energy availabilities of EVs (E_t) from the CS. The output of FLC is the power (S') which decides the total power to be supplied/drawn from or to the CS. The power decided by the FLC is divided by the aggregator. The aggregator takes S', E_t and energy available (E_1, E_2...E_n) from individual EVs' batteries and distributes the power (S_1, S_2...S_n) among EVs present at the CS. The power output S' can be positive or negative. Positive power represents that the charging system will perform charge (G2V) operation and the negative

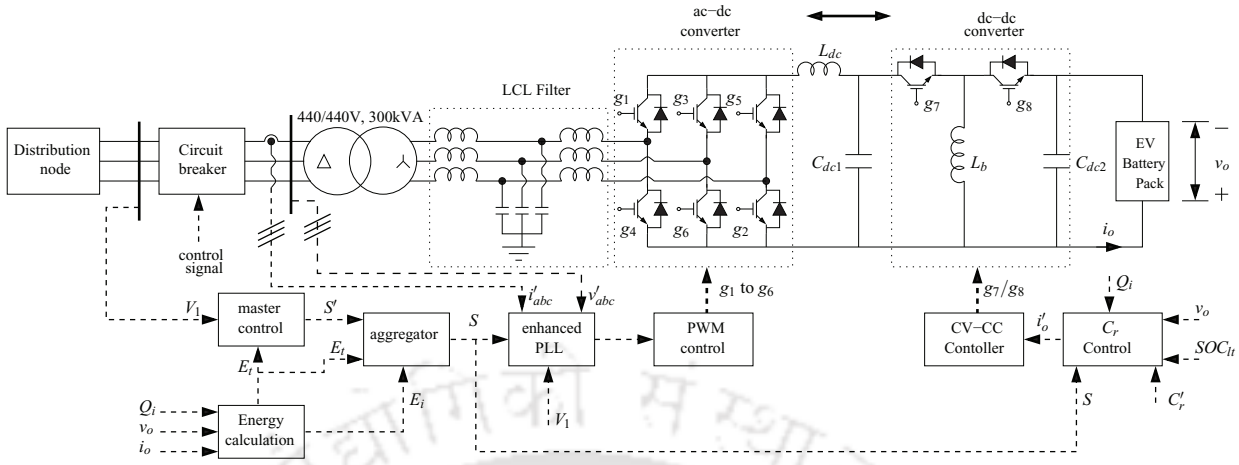

Figure 2.3: Circuit topology of charging system.

power implies that the corresponding charging system will perform discharge (V2G) operation. Based on the distributed power from the aggregator, the EVs' batteries present in the charging systems injects or draws P and Q to or from the DN.

2.3.3 Battery system

An electric circuit based battery model have been used to represent the aggregated model of EV battery packs. The electric equivalent circuit of EV battery model is shown in Figure 2.4.

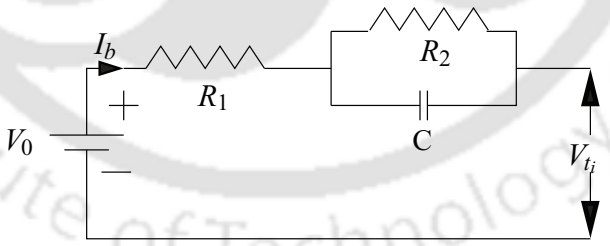

Figure 2.4: Battery equivalent circuit.

The model is based on a controlled voltage source, which can be positive or negative depending on the power flow. The parameters of the electric equivalent circuits are calculated by polynomial equations explained in [79]. Unlike other distributed energy storage systems, the usage of EV battery to support the grid has lot of constraints. The performance of the EV battery get affected due to

continuous charge/discharge operations. Therefore, to use the vehicles battery effectively, the SOC and C_r limits of the battery has been taken into account. A control algorithm is developed inside the battery system design to achieve better control and coordination of EVs' arrived in the CS. The power of the CS is controlled by controlling the C_r of EVs battery. The control algorithm present in the EVs battery considers V_{o_i}, Q_i, user defined SOC limits (SOC_{lt}) and C_r limits ($C_r^{'}$) based on user's preference. The current C_r of the battery ($C_r{}^*$) is calculated from (2.2).

$$C_r{}^* = \frac{S_i}{V_{oi} Q_i} \tag{2.2}$$

where S_i is the power decided by the aggregator either to charge or discharge i^{th} EV battery. The algorithm present inside an EVs' battery chooses the minimum of C_r^* and C_r' to charge/discharge the battery. The required energy to charge and the available energy to discharge the i^{th} EV battery for a specified time is calculated using (2.3) and (2.4). The total energy (E_t) of the CS can be calculated using (2.5).

$$E_i{}^c = V_{o_i} Q_i \left(SOC'' - SOC^*\right)/100) \tag{2.3}$$

$$E_i{}^d = V_{o_i} Q_i \left(SOC^* - SOC'\right)/100) \tag{2.4}$$

$$E_t = \sum_{i=1}^{n} E_i^c + E_i^d \tag{2.5}$$

where, Q_i and V_{o_i} are the ampere hour rating (Ahr) and terminal voltage of the i^{th} battery, SOC' and SOC'' represents the minimum and maximum SOC limit of an EV, SOC^* is the current SOC of the EV battery and i varies from 1 to n. Thus, depending on the SOC constraints of the user, the discharge or charge energy of the EVs' batteries are controlled such that SOC limits at the end of the time period remains between the range SOC' and SOC''.

2.4 Problem definition

Electric vehicles are emerging as one of the most promising alternatives; as it can be used as a potential source of energy and a sound transportation system. However, integrating multiple EVs to the distribution network may cause adverse impacts due to uncontrolled and random charging or discharging process. On the other hand, if EVs batteries are controlled via charging systems, it coordinates and controls the charge or discharge operation and thereby these adverse impacts can be avoided. Therefore, the study of controlled charging systems in a CS combined with distribution network is very essential to analyze the potential benefits and impacts for the public acceptance of EVs.

Various elements involved in the CS model and its control strategies are explained in the succeeding parts.

2.4.1 Fuzzy logic control (FLC)

Fuzzy logic controller has been used as a master control to externally control the power flow between the CS and the DN. FLC receives information such as V_1 and E_t and it decides the power S' which should flow between the DN and the CS. Fuzzy controller is particularly used in this work to handle uncertainty caused by the sudden arrival and departure of EVs; as it considers all inputs and outputs within a bound by using sufficient number of rules. The fuzzy model developed incorporates the experience or human knowledge based on offline information of the CS to express the uncertainties. In FLC, V_1, E_t and S' are mapped by a set of membership functions known as "fuzzy sets", which are represented by linguistic variables as shown in Figure 2.5. The maximum and minimum voltage inputs of DN is taken between 0.83p.u to 1.13p.u. This has been considered because the distribution network operator is obliged to maintain the voltage profile within its limits (1 ± 0.13). The energy and power limits of the CS is considered based on the capacity of the CS. The fuzzy controller output is intended to perform both charging or discharging operation. The input and output membership functions are related using rules which provides description of the membership functions. The control rules are defined as IF-THEN structure, which relates V_1 and E_t in the IF part to S' in the THEN part. The rules of FLC are formed based on the DN voltage variation and the energy status of the battery. The derivation of fuzzy control rules are heuristic in nature and the rules are derived using linguistic variables. The rules are formed considering the variations of V_1 and E_t based on the following four basic criteria:

- If V_1 and E_t lies in the range of $(0.83 \leq V_1 \leq 0.987)$ and $(0.55 \leq E_t \leq 0.999)$, then S' lies between -1 to -0.1, denotes V2G operation.
- If V_1 and E_t lies in the range of $(0.987 \leq V_1 \leq 1.13)$ and $(0 \leq E_t \leq 0.5)$, then S' lies between 0.1 to 1, denotes G2V operation.
- If V_1 and E_t lies in the range of $(0.83 \leq V_1 \leq 0.987)$ and $(0 \leq E_t \leq 0.5)$, then S' will be zero, indicates there cannot be any power transfer in the CS.'
- If V_1 and E_t lies in the range of $(0.987 \leq V_1 \leq 1.13)$ and $(0.55 \leq E_t \leq 0.999)$, then S' will be zero indicates, there cannot be any power transfer in the CS.

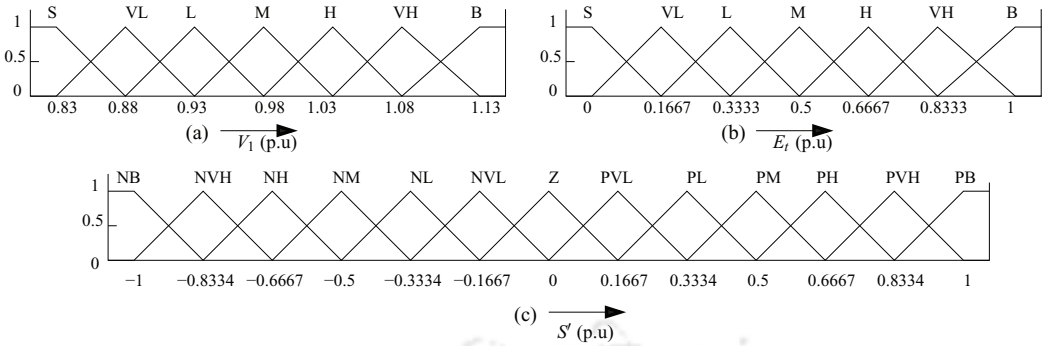

Figure 2.5: Membership functions for FLC (a) node voltage (V_1) (b) total energy availabilities of EVs (E_t) and (c) output power (S').

Seven fuzzy subset such as S (Small), VL (Very Low), L (Low), M (Medium), H (High), VH (Very High) and B (Big) have been chosen for the input variable V_1 and E_t. Thirteen membership function such as NB (Negative Big), NVH (Negative Very High), NH (Negative High), NM (Negative Medium), NL (Negative Low), NVL (Negative Very Low), Z (Zero), PVL (Positive Very Low), PL (Positive Low), PM (Positive Medium), PH (Positive High), PVH (Positive Very High) and PB (Positive Big) have been chosen for the output variable (S'). Triangular membership functions are used as it is more simple, realizable and easy to implement. A total of forty nine rules are defined to relate the input and output membership functions. Table 2.1 has the rules used for the FLC controller. An example of the control rule is given as, "If V_1 is VL and E_t is S then S' is Z".

Defuzzification is performed using the center of gravity method by finding the center of the area encompassed by all the rules and is mathematically described by (2.6).

$$S' = \frac{\sum_{i=1}^{n} u_i \mu_v(u_i)}{\sum_{i=1}^{n} \mu_v(u_i)} \tag{2.6}$$

Simplifying (2.6) gives the defuzzified overall control output, where u_i refers to the output variable and μ_v represents the aggregated membership function. The positive and negative power output values from FLC decides the power flow direction between the DN and the CS. The process of fuzzification and defuzzification for a practical example has been explained in Appendix A.2.

Table 2.1: Rule base

V_1	E_t	S'	V_1	E_t	S'	V_1	E_t	S'	V_1	E_t	S'	V_1	E_t	S'
S	S	Z	VL	L	NL	L	H	NH	M	B	Z	VH	VL	PVH
S	VL	NVL	VL	M	NM	L	VH	NVL	H	S	PB	VH	L	PH
S	L	NL	VL	H	NH	L	B	NL	H	VL	PVH	VH	M	PM
S	M	NM	VL	VH	NVH	M	S	NVL	H	L	PH	VH	H	PL
S	H	NH	VL	B	NB	M	VL	NVL	H	M	PM	VH	VH	PVL
S	VH	NVH	L	S	Z	M	L	NVL	H	H	PL	VH	B	Z
S	B	NB	L	VL	NVL	M	M	Z	H	VH	PVL	B	S	PB
VL	S	Z	L	L	NL	M	H	PVL	H	B	Z	B	VL	PVH
VL	VL	NVL	L	M	NM	M	VH	Z	VH	S	PB	B	L	PH
B	M	PM	B	H	PL	B	VH	PVL	B	B	Z	-	-	-

2.4.2 Aggregator

Since the individual capacity of an EVs' battery is too small (usually in kWh), an aggregator is used in the CS model to coordinate multiple EVs to meet the base power requirement of the grid. Aggregator plays an important role in charging or discharging more than hundreds or thousands of EVs. This is an intermediate system deals with multiple small-scale power of EVs and makes efficient use of distributed power of EVs in the CS to produce the desired grid-scale power. The aggregator designed in this work obtains input both from FLC and EVs' batteries. The individual energy of EVs $(E_1, E_2...E_i)$, total energy (E_t) of EVs and FLC output (S') are given as input to the aggregator. Based on the three inputs, it divides and distributes the reference power (S) among multiple EVs' present in the CS as given by (2.7).

$$S = \frac{E_i}{\sum_{i=1}^{n} E_i} S' \tag{2.7}$$

Thus, EVs pertaining to the aggregator would charge or discharge alternatively based on the command from the grid operator and EV owner to meet the requested demand of both the grid and EVs. The aggregator also controls the sequence, rate of charging or discharging and distributes power among multiple EVs present in the CS.

2.4.3 Charging system

To realize the CS operation discussed in Section IIIB and to integrate the EVs batteries into utility grid, thirty five component level charging system model is built with advanced real time simulation system. The detailed circuit topology of an individual charging system is shown in Figure 2.3. The main components of the charging systems are bidirectional three-phase ac-dc and dc-dc converter (g_1-g_8). The three phase ac-dc (g_1-g_6) converter realizes the line side sinusoidal voltage waveform using enhanced PLL with PWM control strategy. The elements L_{dc} and C_{dc1} provides a bypass for the current and voltage waveform and reduces the spikes in the output, when the switches are turned on or off. The dc-dc converter (g_7-g_8) is connected to an inductor (L_b) with capacitor (C_{dc1} and C_{dc2}) on both sides. It regulates the power to be flown between the grid and the EVs batteries. It performs three different operating modes: buck, boost and cascade operating mode. The buck-operating mode is operated when the EV battery rating is less than the peak input dc voltage. The duty cycle lies in the range $0.1 \leq D \leq 0.5$. The boost operation is performed when EV battery voltage rating is higher than the input voltage (D > 0.5). Cascade mode is operated when the input voltage is equal to the EVs voltage rating ($D = 0.5$). The dc-dc converter perform this operating modes using CC-CV charging strategy. Besides, an LCL filter is used at the terminals of the charging system at the grid side to suppress the transferring switching harmonics. The charging system is able to work in G2V and V2G operating modes. The operating modes follow the criterion explained in Section 2.4.1. When the node voltage is high and the EVs battery energy is low, the EVs will absorb the power from the grid; while when the battery energy is high it supports the grid. Once if the grids condition is unsuitable to support or draw the power, the circuit breaker will open and the charging system will get disconnected from the coupling point of the DN. In this manner, the power flow of the charging system is controlled based on the grids condition and the energy availabilities of EVs. The control circuits of the charging systems are composed of two groups: Constant current - constant voltage (CC-CV) charging strategy and enhanced PLL with PWM control, which has been explained below.

2.4.3.1 CC-CV control

Usually, the initial SOCs of each EVs arrived at the CS are considerably different. A vehicle with low SOC battery may need a large charging current but requires a fast charging and an EV with highest initial SOC can discharge fast but may require longest discharging time. In order to meet such

simultaneous requirements of multiple users, CC-CV charging strategy is used for dc-dc converters by considering C_r and SOC limits as its inputs from the user.

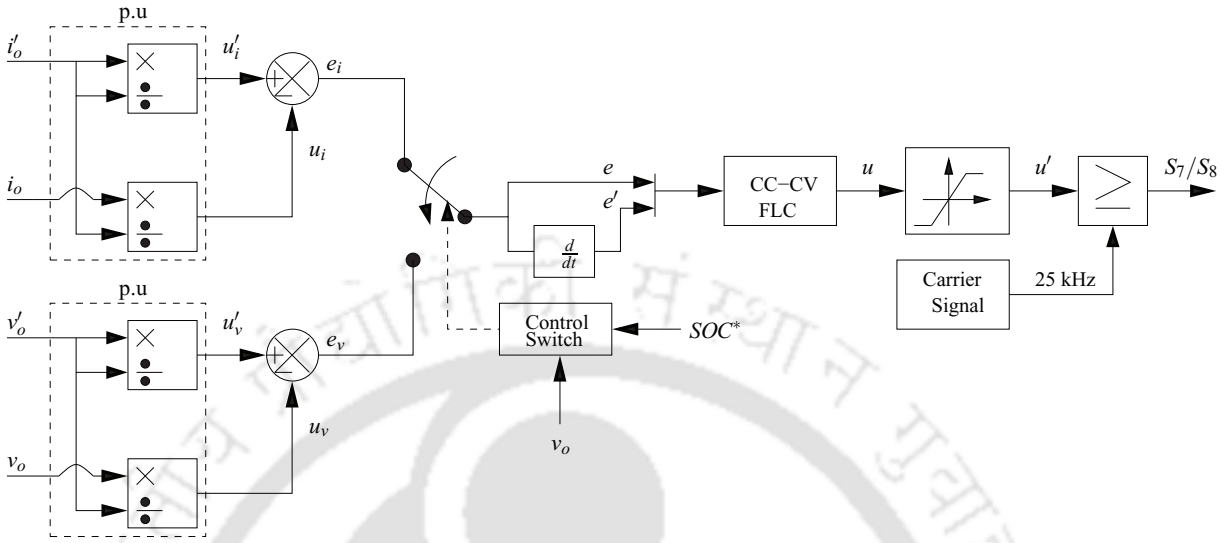

Figure 2.6: Constant-current and constant-voltage charging strategy.

The control scheme of CC-CV charging strategy is shown in Figure 2.6, where i'_o is the reference battery current command (obtained from C_r control shown in Figure 2.3), i_o is the measured battery current, v'_o is the reference battery voltage command, v_o is the measured battery voltage, u'_i, u_i, u'_v and u_v are the per unit values of current and voltage, e_i and e_v are the voltage and current error, e is the error and e' is the first derivative of the error. The controller has two input variable: e and e' and u as the output variable of the CC-CV fuzzy controller (CC-CV FLC), which is then given to the limiter. The limiter output u' is then compared with a carrier signal of 25kHz to generate a required pulse for dc-dc converter. To control the C_r of the battery, initially a constant current command i'_o is applied and i_o tracks i'_o until the battery terminal voltage has risen to a predetermined value. At that point, CC mode is switched to CV mode and the charging voltage v_o is held constant according to v'_o and the charging current is reduced. The current direction in the dc-dc converter is changed conveniently depending on the aggregator output based on which the power flow direction is reversed to charge or discharge the EVs batteries.

2.4.3.2 Enhanced PLL based PWM control

Enhanced PLL with PWM control is used to control six fully controlled bidirectional switches ($g_1 - g_6$) including LCL filter on the ac side and L_{dc} and C_{dc1} on the dc side. The block diagram of

the enhanced PLL is shown in Figure 2.7.

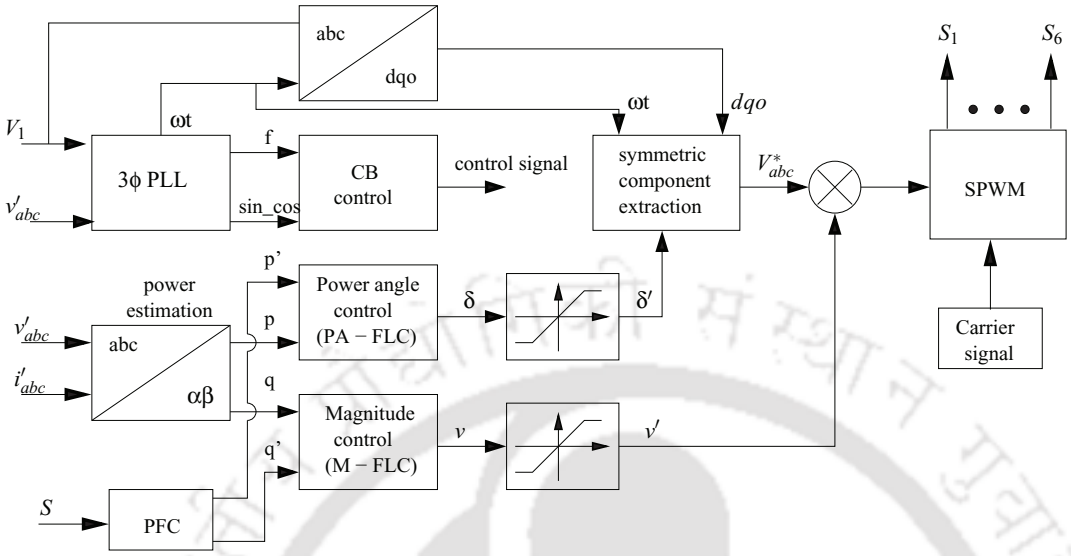

Figure 2.7: Enhanced PLL based PWM control.

During G2V operation, the converter switches are switched to draw a sinusoidal current with a defined power angle δ' to provide a stable dc link voltage across C_{dc1}, which in turn regulates the current using L_{dc}. For V2G operation, the switches are switched to return a current in a similar sinusoidal form with less power line disturbance on the utility grid. While for parallel connected charging systems, a very precise synchronization is required prior to each charging panel connection to the grid in order to avoid catastrophic transients. To estimate the power angle, open-loop and closed-loop methods can be used. The closed loop methods are commonly known as phase locked loop (PLL) methods, which has been used in this work. The controller contains three loops. The first loop takes grid signal (V_1) as its input to three-phase PLL and extracts the grid components (ωt, f, $sin - cos$). This provides the phase information for dqo-abc and abc-dqo coordinate transformation. The second loop takes signal from the terminals of the converter (v'_{abc}, i'_{abc}) and estimates the active and reactive power (p & q). The power estimation block process the instantaneous v'_{abc} and i'_{abc} using multipliers, coordinate transformations, rms converters and filters to process p and q. The third loop takes the signal from aggregator (S) and provides reference active and reactive power (p' and q') to be regulated. The power given by aggregator is in the form as given by (2.8), where S is the apparent power from which the reference power p' and q' are obtained by correcting its power factor (PFC).

$$S = p' + q' \ = \ v_o i_o \tag{2.8}$$

The power factor of the system is initially set to 0.91 to obtain a voltage of 1.01p.u. The pf is allowed to vary within its operating limits to control the power based on S. The phase angle control (PA-FLC) take p and p' as its input and gives power angle (δ) as the output. q and q' are the inputs for magnitude controller (M-FLC) and v is obtained as its output. The schematics of the PA-FLC and M-FLC is shown in Figure 2.8 and 2.9.

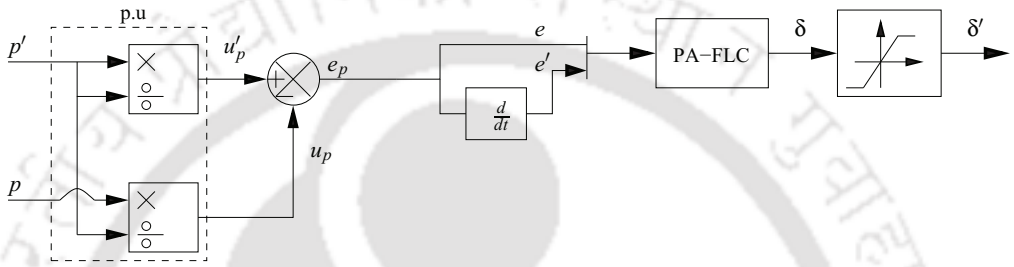

Figure 2.8: Power angle control (PA-FLC).

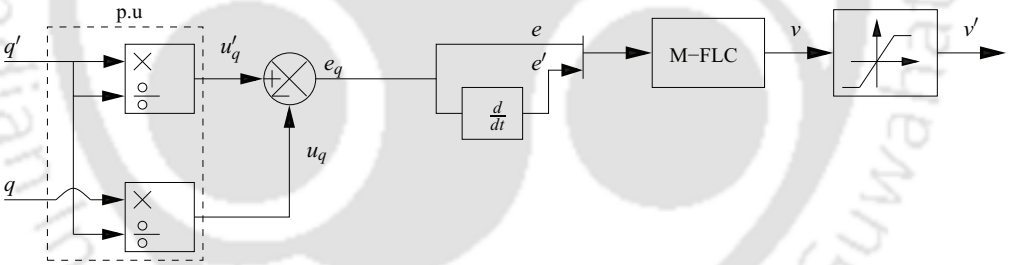

Figure 2.9: Magnitude control (M-FLC).

The outputs δ and v are then passed through a limiter, which then produces required phase shift and amplitude variation (δ', v') to control the power flow. Thus to control the power flow from or to the converters, the charging system must be able to vary its output in amplitude and phase with respect to grid variations. Hence, the obtained δ' provides the required delay information for $dqo-abc$ and $abc-dqo$ coordinate transformations and gives the reference voltage (v^*_{abc}). The obtained v^*_{abc} is then multiplied by a factor v' to obtain the required magnitude of reference voltage. This reference is then compared with the triangular carrier wave at a switching frequency of 4kHz to control the converter switches.

The input given to the controllers are converted to p.u value and then e and e' has been used as inputs for all three controllers, which lies in the range of -1 to 1. However, the range of output for CC-CV FLC and M-FLC is 0 to 1 and PA-FLC is 0° to 90°. Twenty five rules are used to describe the membership functions. The principle of rules and membership functions are not different from that explained in Section 2.4.1, which has been given Appendix A.3.

2.4.4 Control methodology

The control process involved in single EV battery is explained in [79] and shown in Figure 2.10. The EVs' batteries take the reference power S_i from the aggregator as its controller input. This input along with V_{o_i} and Q_i of the battery estimates the calculated charge/discharge rate (C_r*). The C_r* goes to the next stage operation to check with user-defined charge/discharge rate ($C_r{}'$).

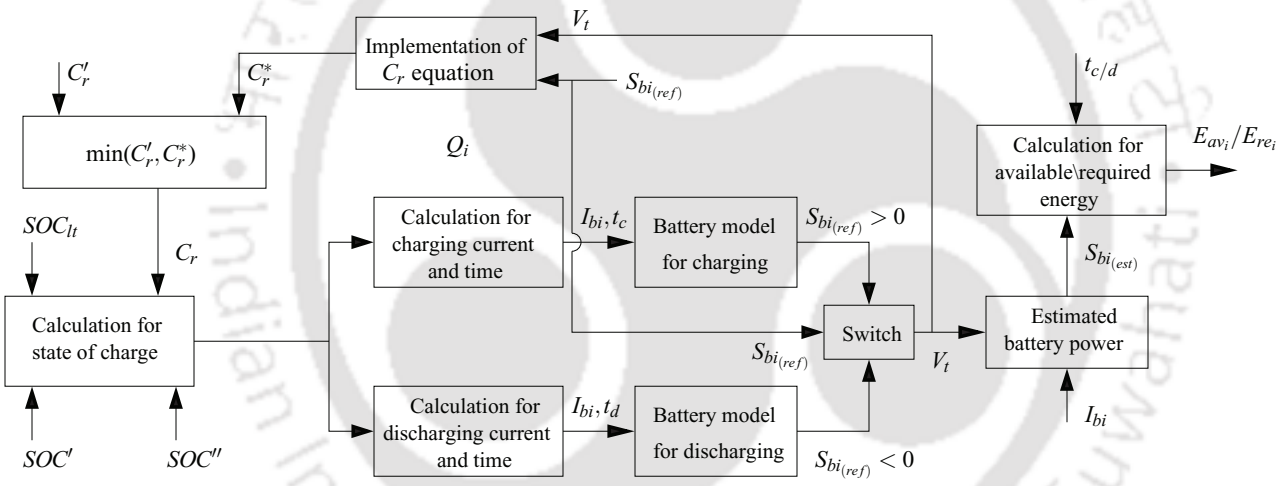

Figure 2.10: Control process involved in EVs batteries.

The minimum of charge/discharge rate value (C_r) is chosen for charging/discharging operation of an EV. The controller also accounts the SOC'' and SOC' to ensure that the battery would not cross its operational limits. This process has been carried out for each batteries in the CS. These signal helps in regulating the battery current in every individual EVs in the CS. Based on these control signals, the charge/discharge current (i_{0_i}) and time for charging/discharging operation (t_c/t_d) are decided and fed to the charge/discharge model i.e., battery model to calculate the $E_i{}^c/E_i{}^d$ to accomplish the charge/discharge operation.

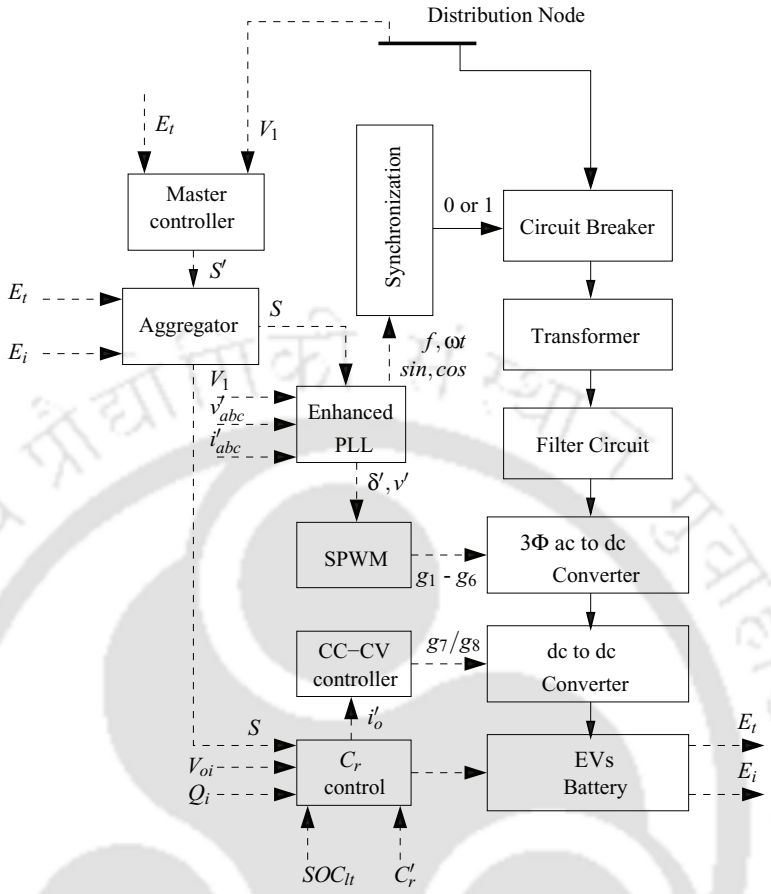

Figure 2.11: Control operation of single unit of charging system.

Figure 2.11 shows the flow chart describing the complete power flow between EV battery and the DN. The FLC decides the reference power S' to be flown from the CS to the DN based on voltage sensitivity (V_1) in the lines and energy availabilities of EVs' batteries (E_t). The decision of FLC is very important as it has a direct influence to control the aggregator and thereby the CS. Aggregator is used to divide and distribute the power among i^{th} EV battery. Enhanced PLL with PWM control is used to control the switches of ac-dc converter and CC-CV charging strategy is used for dc-dc converter. This controllers takes S and system outputs as its control input and produces required gate pulse (g_1 to g_8) to the converter during charge/discharge operations based on the input command. C_r control considers V_{o_i}, Q_i, SOC_{lt} and $C_r{}'$ limits of EVs to control the battery current to discharge within its SOC_{lt} that extends the life cycle of the battery. $C_r{}^*$ is calculated and the minimum of $C_r{}'$ and $C_r{}^*$ is chosen to prevent the battery charging/discharging at high current.

2.5 Result analysis

The CS described in the previous sections have been evaluated by simulation. The CS is considered to have 35 charging systems and thirty five EVs of different ratings are connected with charging systems for representing multiple EVs arrived at the CS. The total size of CS studied in this work is 300kW. For simplification of analysis, EVs' batteries are grouped into five types and are assumed to have same voltage ratings (250V) and different SOC^*. The specifications of EVs' batteries and SOC ratings are given in Table 2.2.

Table 2.2: Specifications of EVs' batteries.

		SOC_{lt}		SOC^*			
EVs	Energy (kWh)	SOC''	SOC'	G2V	V2G	both	$C_r{}'$
EV_1-EV_7	24	100	15	24	70	32	3.0
EV_8-EV_{14}	35	98	20	22	95	95	2.5
EV_{15}-EV_{21}	32	95	23	25	85	24	3.5
EV_{22}-EV_{28}	56	97	19	18	65	80	2.5
EV_{29}-EV_{35}	42	90	25	20	75	29	4.0

The CS connected with EVs batteries are examined with active power (P), reactive power (Q) and both active and reactive power (PQ) exchange to observe the variation of distribution network voltage profile. The real time situations of EVs are examined by the following three cases of EVs present at the CS.

- EVs' batteries with low SOC connected during off-peak hours for G2V operation (0000hrs to 1000hrs), the node voltage is usually high between 1.043p.u to 1.13 p.u.
- EVs' batteries with high SOC connected during peak hours for V2G operation (1500hrs to 2230hrs), the node voltage is generally below 0.91 p.u.
- EVs' batteries with both high and low SOC connected during normal hours for both G2V and V2G operation (between 1000hrs to 1500hrs and 2230hrs to 2400hrs).

These three cases of EVs are tested with P, Q and PQ exchange to study the node voltage rise or drop as shown in Fig. 2.12 - Fig. 2.14. Due to page limitation, other characteristic plots are shown only for combined G2V and V2G operation tested during normal hours with EVs of high and low SOC batteries. To avoid repetition of graphs only 5 EVs' batteries results are shown throughout the section.

Figure 2.12 shows the comparison of node voltage before and after performing G2V operation during off-peak hour period using P, Q and PQ power support from the grid. In this case, all the EVs in the CS are considered to have low value of SOCs and have arrived to charge their batteries for G2V operation. The node voltage is initially high above 1.043p.u before G2V operation. It has been observed from Figure 2.12; the node voltage is high around 1.1p.u before supporting the CS. When the CS has drawn the power from the grid, the voltage rise in the DN has been reduced and regulated to the nominal voltage level of the distribution network.

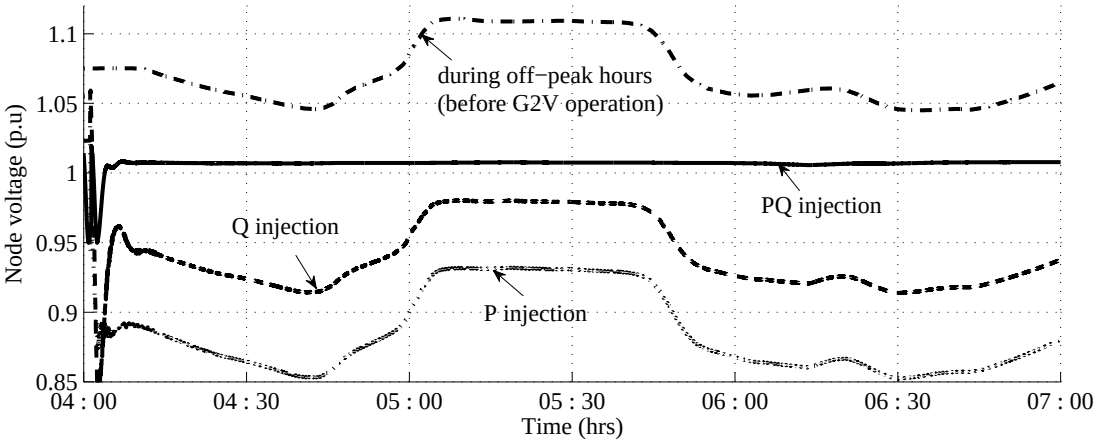

Figure 2.12: Comparison of node voltage using P, Q and PQ control (G2V).

It has also been observed P and Q support has almost similar performance with small difference in voltage drop. The combined PQ power support is found to have better voltage regulation than individual P and Q power transfer.

Figure 2.13 shows the comparison of node voltage before and after performing V2G operation using P, Q and combined PQ support during peak hour. In this case, all the EVs arrived at the CS is considered to have high value of SOCs. In Figure 2.13 during peak-hours, initially their is a drop in the node voltage of around 0.86p.u. After injecting power from EVs, the node voltage got raised to 0.99p.u. It has been observed among P, Q and PQ support, the voltage regulation achieved using combined PQ support is better than individual P and Q support. The voltage is regulated within the specified nominal voltage of the distribution network.

Figure 2.14 shows the comparison of node voltage before and after performing both G2V and V2G operation during normal hour period. In this case, the EVs arrived at the CS is considered to have high and low value of SOCs. In Figure 2.14 during normal hours, the node voltage is around 1.0045p.u

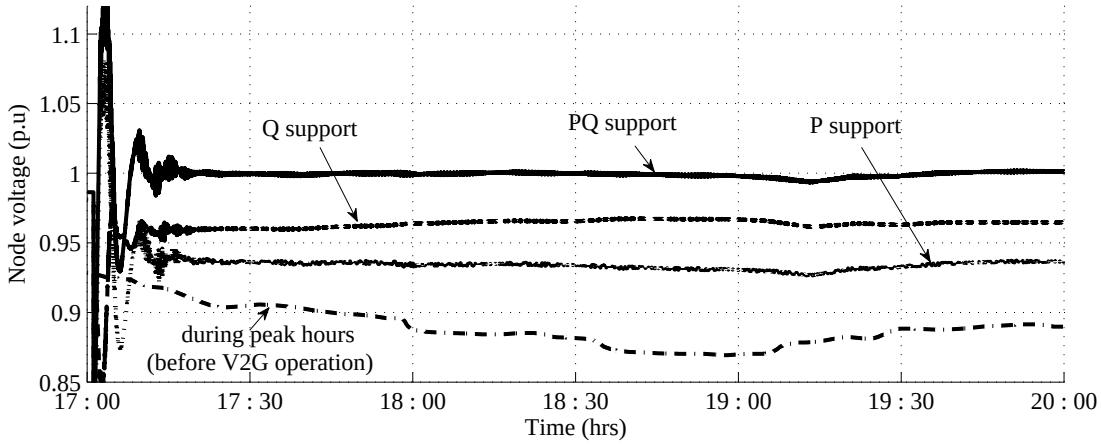

Figure 2.13: Comparison of node voltage using P, Q and PQ control (V2G).

during peak hour. After performing charge/discharge operation with the CS, the node voltage has reduced to 0.96p.u. While comparing to individual P and Q control the voltage regulation provided by combined PQ seems to be better.

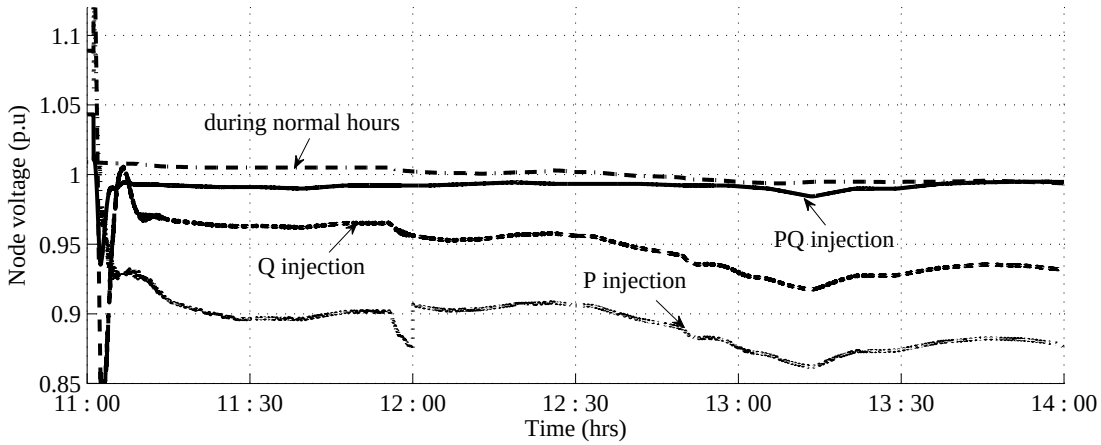

Figure 2.14: Comparison of node voltage using P, Q and PQ control (both G2V and V2G).

Figure 2.15 shows the dc link voltage across C_{dc1} at the terminals of the three-phase converter. The dc link capacitor helps to maintain the voltage level during its power transfer in both the direction. The dc link voltage is rectified from three-phase ac input and is about 1.35 times the ac input voltage for G2V operation. During V2G operation, the voltage across the coupling capacitor is regulated and maintained by the dc-dc converter. The transients in the dc link voltage is smoothed with this large

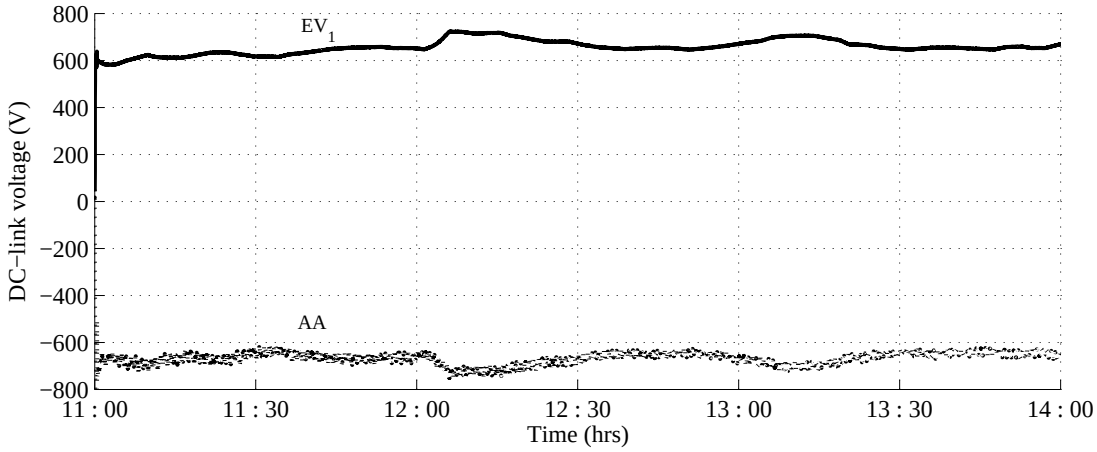

Figure 2.15: DC link voltage (across C_{dc1}).

capacitor.

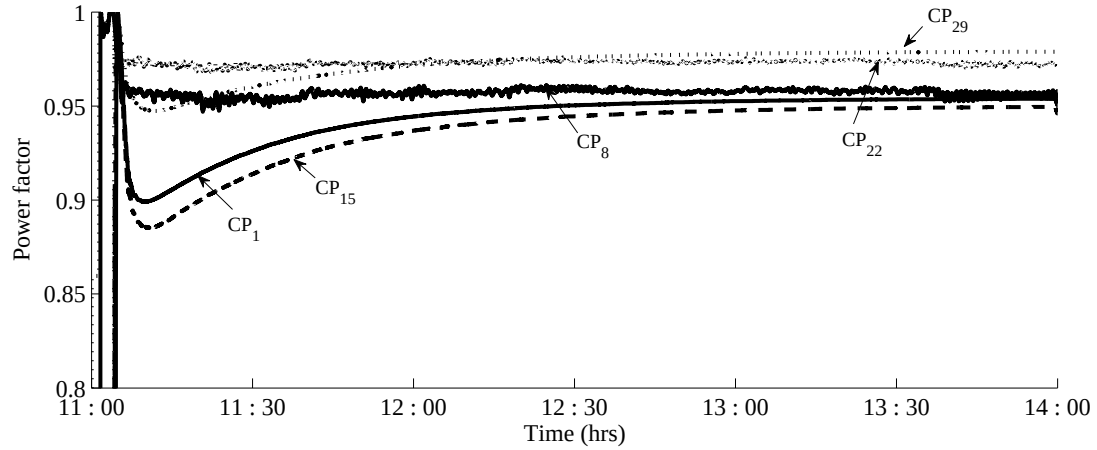

Figure 2.16: Power factor of the charging system.

Figure 2.16 shows the power factor of the charging system at five different charging points (CP) of the CS. It has been noticed the power factor of the charging system is maintained near to unity. This shows the most efficient loading of the charging systems at the distribution network. High power factor achieved in the system is the result of minimum phase difference between the voltage and the current. The controllers used in the charging systems has controlled the voltage and current to maintain the power factor of the system close to unity.

The state of charge (SOC) characteristics of the EV batteries are shown in Figure 2.17. For EV_1,

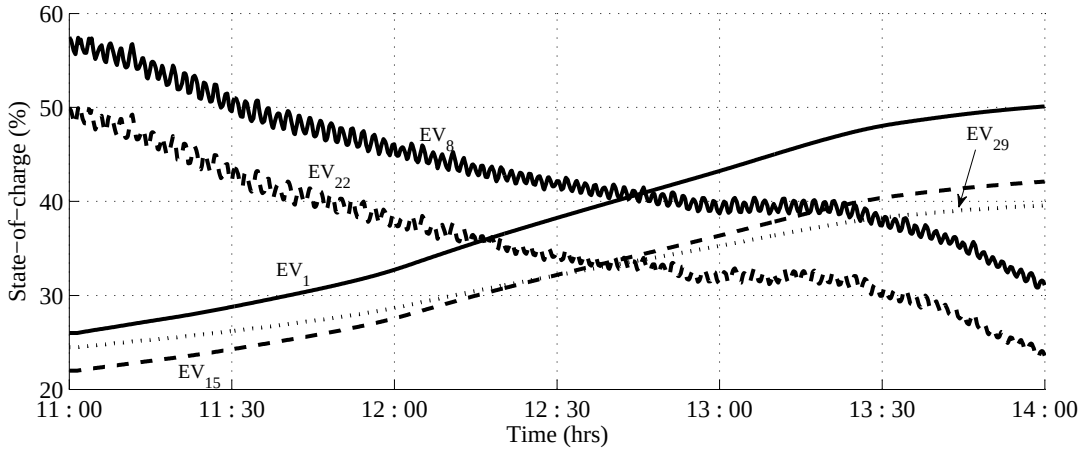

Figure 2.17: State of charge of EVs batteries.

EV_{15} and EV_{29}, the SOC of the battery has increasing characteristics during G2V operation. For EV_8 and EV_{22}, the SOC of the battery has decreased while supporting the grid.

In Figure 2.18, the total battery power drawn and the total power injected by 5 EVs at the charging points (CP) of the CS is shown to demonstrate the response of the regulation signal. As explained above, positive power indicates that the EVs in the CS have low SOC value and have come for charge operation. While other two group EVs have drawn power from the grid.

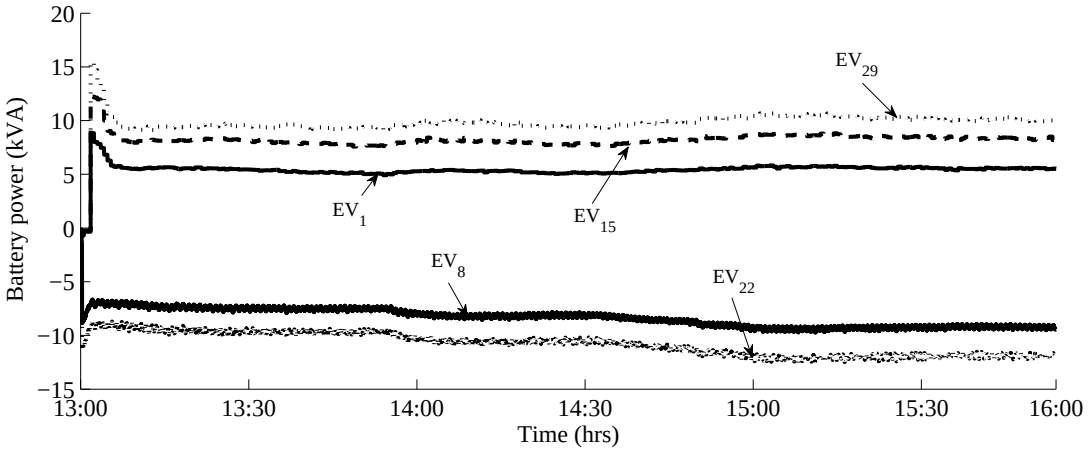

Figure 2.18: Battery power.

Figure 2.19 shows the estimated frequency, sine component, amplitude (v'), ωt, cosine component, power angle (δ') using enhanced PLL control. Fast and accurate extraction of the frequency (f) is

Table 2.3: Summary of injected and drawn power from/to the CS during several hours in a day.

Time (hrs)	Mode of operation	S' (kVA)	S (kVA)	E_t (kWh)	P_{bat} (kW)	Active power (kW)	Reactive power (kVar)	pf
			$S_1 = 4.901$		$P_{b_1} = 4.881$	$P_1 = 4.692$	$Q_1 = 1.385$	$pf_1 = 0.9589$
at	G2V		$S_2 = 6.576$	101.781	$P_{b_2} = 6.533$	$P_2 = 6.384$	$Q_2 = 1.434$	$pf_2 = 0.9756$
0530	off-	240.702	$S_3 = 5.119$	(required)	$P_{b_3} = 5.013$	$P_3 = 4.979$	$Q_3 = 1.095$	$pf_3 = 0.9758$
hrs	peak		$S_4 = 11.395$		$P_{b_4} = 11.201$	$p_4 = 10.971$	$Q_4 = 2.771$	$pf_4 = 0.9689$
	hours		$S_5 = 6.395$		$P_{b_5} = 6.305$	$P_5 = 6.311$	$Q_5 = 0.911$	$pf_5 = 0.9895$
		$\frac{240.702}{7}$	$\sum_{i=1}^{5} S_i \times 7$	101.781×7	$\sum_{i=1}^{5} P_{b_i}$	$\sum_{i=1}^{5} P_i \times 7$	$\sum_{i=1}^{5} Q_i$	Avg. pf
		$= 34.386$	$= 240.702$	$= 712.467$	$= 237.531$	$= 233.359$	$= 53.172$	$= 0.974$
			$S_1 = -4.476$		$P_{b_1} = -4.402$	$P_1 = -4.229$	$Q_1 = -1.248$	$pf_1 = 0.9789$
at	V2G		$S_2 = -8.778$	106.052	$P_{b_2} = -8.750$	$P_2 = -8.546$	$Q_2 = -1.921$	$pf_2 = 0.9761$
1730	peak	-250.593	$S_3 = -6.812$	(available)	$P_{b_3} = -6.613$	$P_3 = -6.556$	$Q_3 = -1.445$	$pf_3 = 0.9651$
hrs	hours		$S_4 = -8.611$		$P_{b_4} = -8.587$	$p_4 = -8.331$	$Q_4 = -2.125$	$pf_4 = 0.9874$
			$S_5 = -7.122$		$P_{b_5} = -7.102$	$P_5 = -7.019$	$Q_5 = -1.012$	$pf_5 = 0.9784$
		$\frac{-250.593}{7}$	$\sum_{i=1}^{5} S_i \times 7$	106.052×7	$\sum_{i=1}^{5} P_{b_i}$	$\sum_{i=1}^{5} P_i \times 7$	$\sum_{i=1}^{5} Q_i$	Avg. pf
		$= -35.799$	$= -250.593$	$= 742.364$	$= -248.178$	$= -242.767$	$= -54.257$	$= 0.977$
			$S_1 = 5.287$	70.461	$P_{b_1} = 5.176$	$P_1 = 5.006$	$Q_1 = 1.639$	$pf_1 = 0.9504$
at	both	162.141	$S_2 = -8.812$	(required)	$P_{b_1} = -8.894$	$P_2 = -8.379$	$Q_2 = -2.481$	$pf_2 = 0.9589$
0300	normal	-141.498	$S_3 = 7.982$	59.851	$P_{b_1} = 7.857$	$P_3 = 7.621$	$Q_3 = 2.089$	$pf_3 = 0.9644$
hrs	hours		$S_4 = -11.402$	(available)	$P_{b_1} = -11.589$	$P_4 = -10.923$	$Q_4 = -2.783$	$pf_4 = 0.9690$
			$S_5 = 9.894$		$P_{b_1} = 9.567$	$p_5 = 9.351$	$Q_5 = 2.652$	$pf_5 = 0.9621$
		$\frac{162.141}{7}$	$\sum_{i=1,3,5} S_i \times 7$	70.461×7	$\sum_{i=1,3,5} P_{bat_i} \times 7$	$\sum_{i=1,3,5} P_{cpi} \times 7$	$\sum_{i=1,3,5} Q_{cpi} \times 7$	Avg. pf
		$= 23.163$	$= 162.141$	$= 493.227$	$= 158.2$	$= 153.846$	$= 44.660$	$= 0.962$
		$\frac{x}{-141.498}$	$\sum_{i=2,4} S_i \times 7$	59.851×7	$\sum_{i=2,4} P_{bat_i} \times 7$	$\sum_{i=2,4} P_{cpi} \times 7$	$\sum_{i=2,4} Q_{cpi} \times 7$	Avg. pf
		$= -20.214$	$= -141.498$	$= 418.95$	$= -143.381$	$= -135.114$	$= -36.848$	$= 0.962$

obtained by three-phase PLL. The result of angular frequency (ωt) is given when the natural frequency is (314rad/sec). It is also shown that the sine and cosine component are tracked faithfully using the PLL. The modulation index (v) is calculated using M-FLC, which is then passed through a limiter to obtain v'. The value of MI ranges from 0 to 1. The PLL calculates the phase angle (δ') using PA-FLC control. The phase angle calculated PA-FLC is found to be unaffected by oscillations in the system. The detected phase angle (δ') shifted by 4° phase angle.

Figure 2.20 shows the apparent of 5 group of EVs in the CS which shows the power drawn or injected at the charging point by EVs arrived in the CS.

Table 2.3 shows the summary of power division at the FLC (S), aggregator (S'), total battery energy (E_t), battery power (P_{bat}), active and reactive power and power factor (pf) at certain hours in the CS during off-peak, peak and normal hours. Five group of EVs are shown in the Table 2.3, where

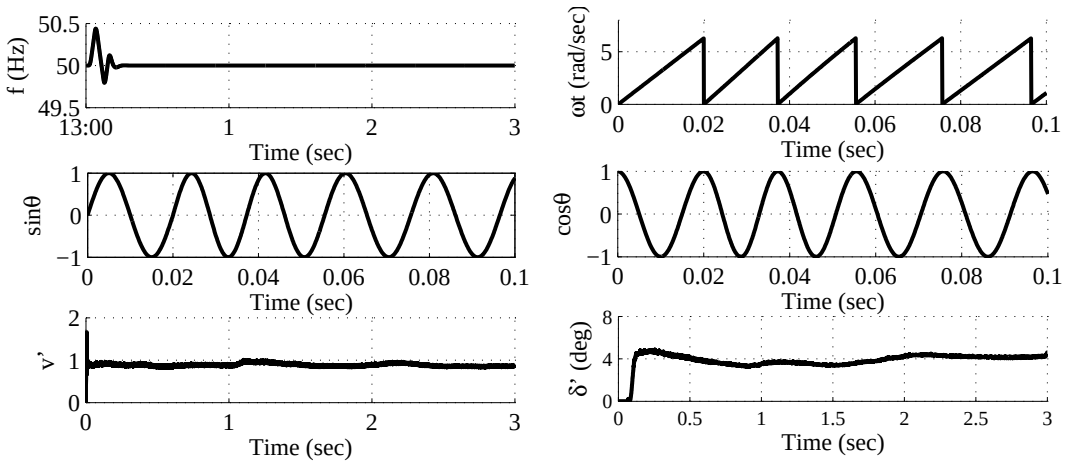

Figure 2.19: Estimated grid components using enhanced PLL method.

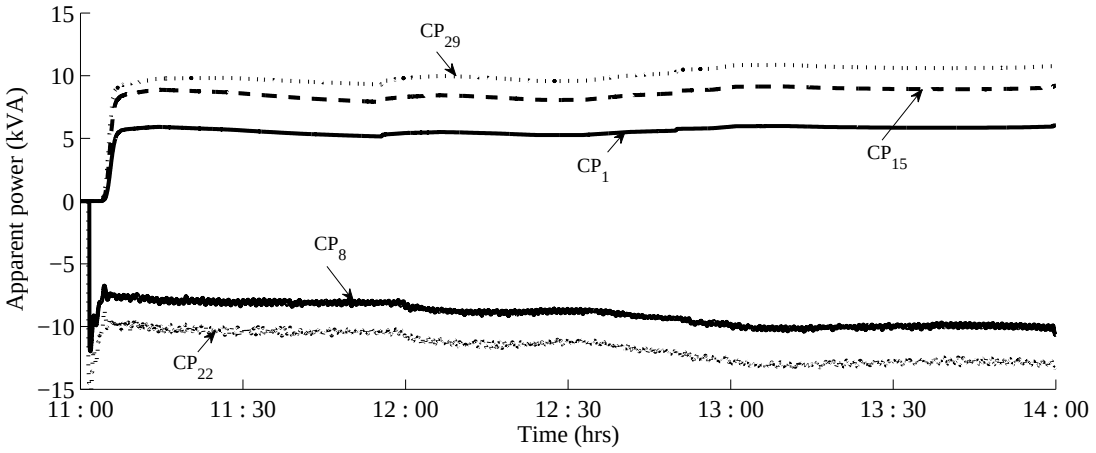

Figure 2.20: Apparent power injected/drawn by the CS.

each group denotes seven sets of EVs in the CS as mentioned in Table 2.2 (example: S_1 denotes 7 group of EVs).

2.6 Conclusions

A CS has been modeled with thirty five charging systems with its controller and an aggregator to maintain the voltage regulation at the DN. Enhanced PLL with PWM control and CC-CV charging strategy has been used in the converters of the CS to control the power flow between CS and the DN. Simulation study has been performed considering a practical distribution system of Guwahati city. The CS has been evaluated to check its power flow functionality for both G2V and V2G operations.

A comparative study has been done considering different power exchange such as active, reactive and combined active and reactive power to study the node voltage variations. The analysis shows that the combined active and reactive power exchange has significant impact on flattening the voltage profile. The results shows that the charging system and its controllers are found to be efficient in performance since it provides better voltage control, while managing the EV batteries in the CS.

Thus the chapter of this thesis had discussed a contact based CS for the provision of voltage regulation at the distribution network. However, charging/discharging high power EV batteries through contact based CS would cause the dangerous possibility of high voltage contact. Recent developments in modern power electronics have enabled contactless charging of EVs an economically feasible solution. The advantage of contactless systems are reliability and ease of maintenance. Therefore, the next chapter of this thesis has modeled a multiple parallel connected contactless CS for EV charging facility.

3

Theoretical Modeling of Contactless Charging Station

Contents

3.1	Introduction	53
3.2	Modeling of contactless charging station	56
3.3	Bidirectional contactless charging system	59
3.4	Problem description	62
3.5	Simulation results	70
3.6	Conclusions	74

भारतीय प्रौद्योगिकी संस्थान गुवाहाटी
Indian Institute of Technology Guwahati

Abstract

The demand for more Electric Vehicles (EVs) will increase the power distribution requirements of future EV charging stations (CS). Similar to petrol stations, multiple charging systems will be co-located to form a CS. To increase safety and reduce the CS maintenance time, these charging systems have to be developed with contactless systems. The work presented in this chapter describes a parallel connected multiple bidirectional contactless charging system. An operating framework of CS is described to manage the interactions of EVs, between parallel connections of multiple charging systems that share a common ac bus network. The individual charging systems are controlled to control the charging and discharging process of each EVs and avoids distribution grid congestion. To coordinate the complete CS, a control strategy is developed; which estimates the line voltage and frequency at the common coupling point of the distribution system and state of charge of EVs and manages the parallel ac lines by scheduling the charging and discharging operations of EVs. The complete CS having ten EVs is validated using detailed simulations. Theoretical analysis and the simulation results demonstrates the feasibility of the proposed CS as an ideal power interface for efficient contactless integration of multiple EVs into a typical distribution network.

The work presented in this chapter will be submitted in a Journal titled, "Bidirectional Contactless Charging Station for Electric Vehicle Charging Facility"

3.1 Introduction

The development of EVs are expected to increase significantly as a newly emerging traffic-tool, which is both energy conserving and environment protective [90, 91]. In addition, EVs' batteries are potentially proven to be capable of fulfilling the energy storage needs of the electric grid [92, 93]. In order to meet this needs, an EV battery requires a physical infrastructure so called charging system, which plays an important role in the grid integration of its batteries [16]. As like petrol stations, multiple charging systems will be co-located to form an EV charging station (CS) [67]. Besides, the recent advancements in contactless system enables contactless charging of EVs an economically feasible solution [23,38]. It is possible to obtain two-way power transfer between EVs batteries and the grid through bidirectional contactless power transfer (BCPT) systems [53]. Through BCPT systems, EVs batteries can simply be charged/discharged by parking the vehicles in a predefined position

either on a parking lot of a corporate or public CS or in an office complex or shopping mall [51, 94]. This bidirectional power flow functionality of BCPT systems are referred as Grid-to-vehicle (G2V) and Vehicle-to-grid (V2G) technology. The term G2V implies charging the EVs batteries from the grid and V2G describes a system, where EVs communicates with the power grid by delivering electricity into the grid [51, 94]. However, if charging/discharging operations of EVs batteries in a CS is unmanaged; it causes negative impacts both on EVs and the distribution grid and this in fact poses significant challenges to the power distribution requirements of future EV CSs [95, 96]. Charging an EV battery is an additional load that can lead to extra large and undesirable peaks in electricity consumption, while discharging might cause sudden rise in node voltage [87]. The overall load profile of electrical system changes due to random charging and discharging process. This issues can be further exacerbated due to sudden interactions of multiple EVs arrived in the parallel connected charging systems that share a common ac bus. Thus, vehicle electrification has a real challenge to deal with multiple EVs arrived at the charging system. Therefore, it is important to study the power architecture of contactless based EV charging system in a CS, which is considered to be one of the most important power electronic applications in the electrification of transportation.

Recently, many charging system architecture have been reported to charge or discharge the EV batteries in a wide range of input and output conditions [1, 2, 16, 62, 97–102]. The authors of [1, 2, 102], have provided the overview of battery charger topologies and bidirectional charging systems , while the authors of [16, 62, 97, 98, 100, 101] have validated the functioning of several new controller and converter topologies suitable for EV charging systems. However it has been observed; very few works in the literature have focussed on the applications of contactless coils for EV charging system [23, 36, 38, 53, 103–108]. Such studies have been conducted either to improve magnetic coupling structure or to select most appropriate compensation topologies and are limited to unidirectional power transfer i.e., charging EVs batteries [23, 36, 38, 103–105]. Only a few researches have reported bidirectional systems to demonstrate G2V and V2G operations between EVs and the power grid [53, 106–108]. These studies have explained the circuit topology and its operating modes of a single charging unit of BCPT system. Nevertheless, their is lack of research in modeling a complete parallel connected multiple BCPT model, as there are serious challenges in its adoption. In one of the prior research, a BCPT system with multiple secondary pick ups is described, which shows both the magnitude and direction of power flow between EVs can be controlled through either phase or magnitude modulation

of voltages [51]. However, if the charging/discharging operations of EVs are unmanaged, the electricity grid and the EV batteries can be affected negatively; it has to be scheduled in the CS.

On the other hand, there are many other studies exist in the literature; which has focussed on the impacts of EVs on the distribution network, optimal charging strategies of V2G system, economic benefits of V2G system, coordination of EVs etc [92, 93, 95, 96]. All of these studies have developed different optimization models to examine the system level real time impacts of EVs on the distribution network. While the literature review suggests that the analysis of EV charging system and its potential benefits is quite extensive, still there is room for research to analyze the complete multi-point BCPT system by managing the charging/discharging operation of EVs batteries based on grids congestion and customers choice.

This chapter describes an operating framework of parallel connected multi-point BCPT system in a CS, which has been fed from a common ac bus network. The individual charging systems are controlled to control the power flow during charging and or discharging operations of EVs. A control strategy has been used in the CS which schedules all EVs connected to the charging system to avoid distribution grid congestion; while satisfying the requirements of EV owners. The architecture of CS is modeled with ten charging systems and are connected with EVs . The theory of BCPT system and its control logics are explained and the key characteristic of the system is compared with analytical model. Furthermore, the theoretical analysis and the simulation results indicates that a well-managed parallel connected multiple BCPT system infrastructure could be certainly used for the future design and implementation of EV CS.

The experimental setup for this kind of complex and high cost system is not feasible, real-time simulations were carried out to prove the effectiveness of the developed model. A multi-point contactless charging system is designed and tested by simulation for a 500kVA system with ten EVs interfaced with a common ac bus network. In detail, Section 2.2 describes the contactless charging station architecture. Bidirectional contactless power transfer system and its modeling is detailed in Section 2.3. Section 2.4 explains the problem description and its functional details. Section 2.5 and 2.6 reports the simulation results and conclusion.

3.2 Modeling of contactless charging station

As discussed, bidirectional contactless charging station can be used to transfer power between grid and EVs. A bus arrangement is necessary to enable energy sharing between multiple EVs; based on the grids condition and energy availabilities of EVs. Two main CS architectures can be used: AC and DC bus distributed EV CS. The power level of this type of charging systems falls under Level 2 or Level 3 type charging [2], where the primary and secondary winding of contactless coils are stationary and stays parallel to capture vertical flux component. The features of the two types of CS is described in the following section.

3.2.1 Types of charging station

The two types of contactless based EV CS architecture is shown in Figure 3.1, which is detailed in Figure 3.2. The architecture based on DC bus distributed CS seems to be more convenient way to integrate multiple charging systems to a common DC bus bar. Unlike AC distributed CS, DC bus distributed CS utilizes one main ac to dc converter instead of multiple smaller ones in each parallel connected ac lines shown in Figure 3.2(b). It requires only a fewer stages of power conversion, which is beneficial interms of efficiency and cost and thus reduces losses and hardware cost. However, an occurrence of wear out or catastrophic failure in the main ac-dc converter, affects the complete functioning of parallel connected charging systems. Thus, the reliability of using single power converter for ac-dc power conversion in DC bus distributed CS becomes questionable. While for AC bus distributed CS, even in case of failure of one converter in a charging system, the other parallel connected charging systems can be used as shown in Figure 3.2(a). Failure of one converter doesn't affect the functioning of the complete CS, which is more convenient and reliable for the proper functioning of CS.

3.2.2 AC bus distributed EV charging station

The work has considered AC bus distributed CS for modeling the CS. In AC bus distributed CS, the charging systems are connected in parallel as shown in Figure 3.2(a) to the common ac bus bar with the coil distance of the interval around 2.5m - 3m distance. A reclosing control strategy has been used in the CS to schedule the complete charging systems based on distribution grids congestion and EV owner's choice. Figure 3.3 shows the single line diagram of parallel connected charging system studied in this work. Each charging systems has contactless coil with primary and secondary side. The primary winding of each contactless coils with its charging circuit are buried underneath the

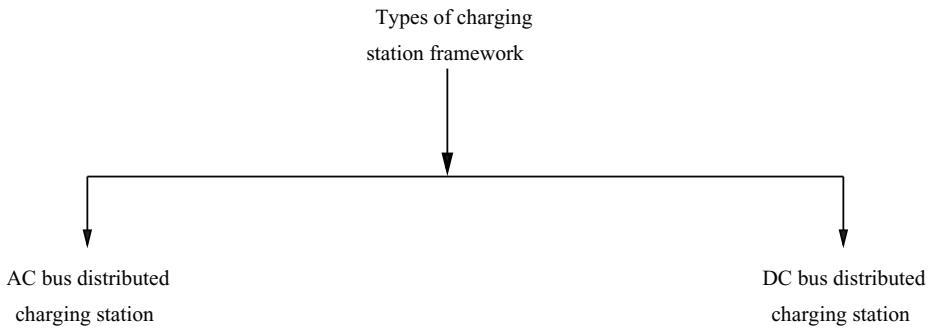

Figure 3.1: Types of charging station

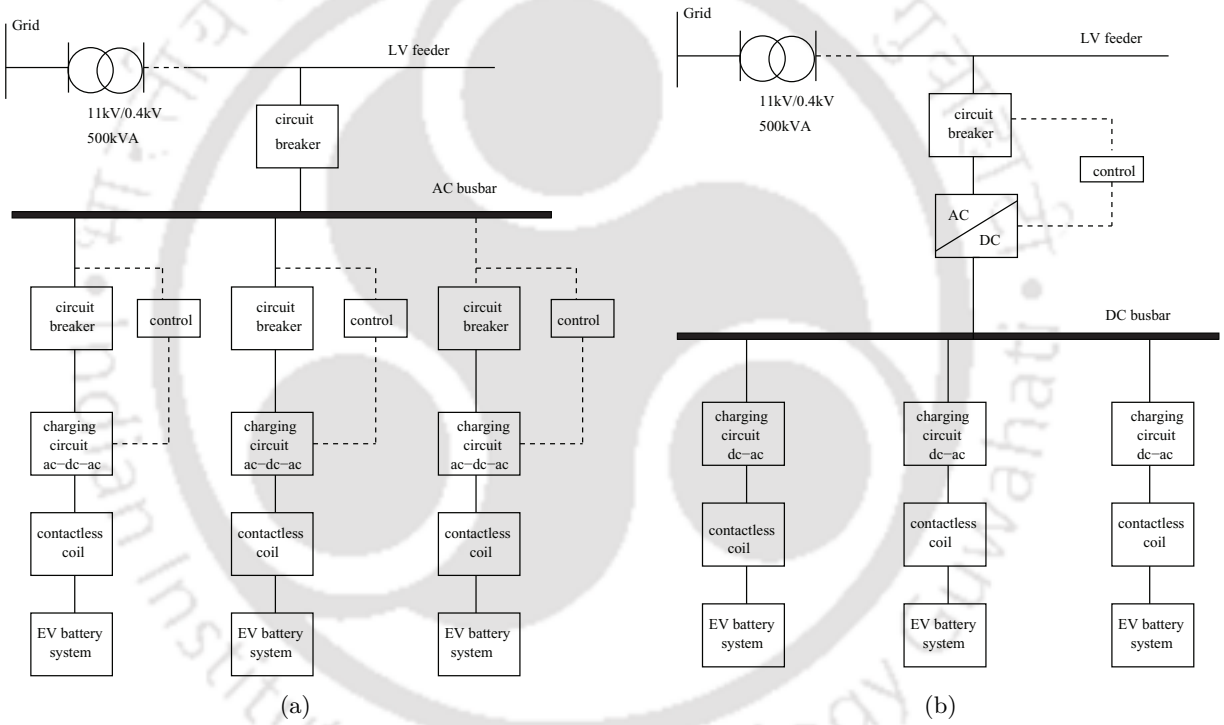

Figure 3.2: EV charging station architecture (a) AC bus distributed EV charging station (b) DC bus distributed EV charging station.

ground and are connected to the common ac bus network. The secondary winding of contactless coil with EV battery system stays parallel to the primary winding and transfers power between grid and EVs through mutual coupling. The reclosing control shown in Figure 3.3 manages the complete CS by scheduling the charging and discharging operation of multiple EVs arrived in the CS. Thus, the AC bus distributed CS architecture with its control strategy shares its energy demand based on grids congestion and energy availabilities of EVs. The detailed schematics of AC bus distributed CS is

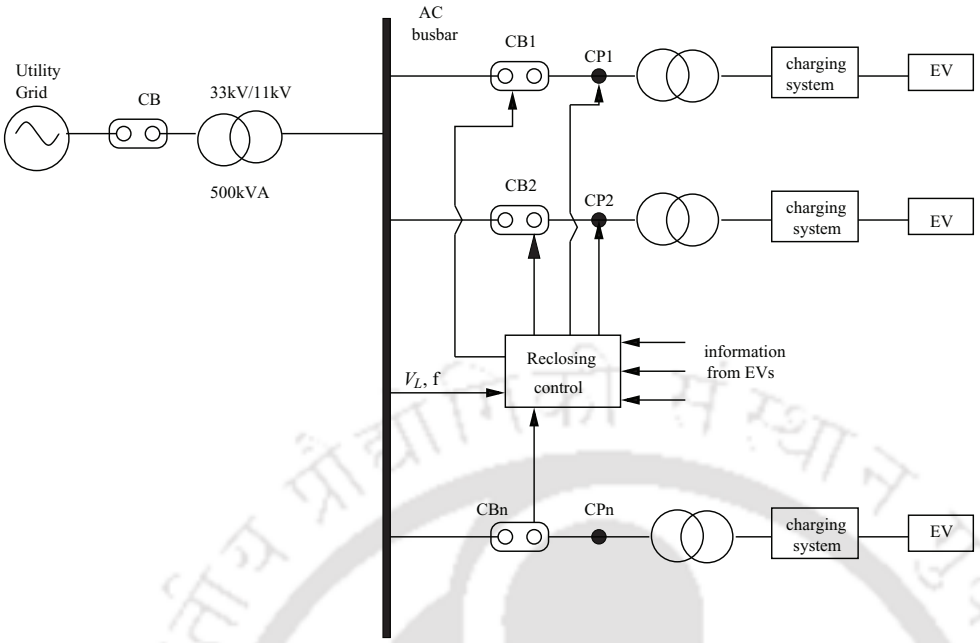

Figure 3.3: Single line diagram of EV charging station.

shown in Figure 3.4. In Figure 3.3 and 3.4, CB_1....CB_n refers circuit breakers and CP_1....CP_n refers charging points of 'n' parallel connected charging system.

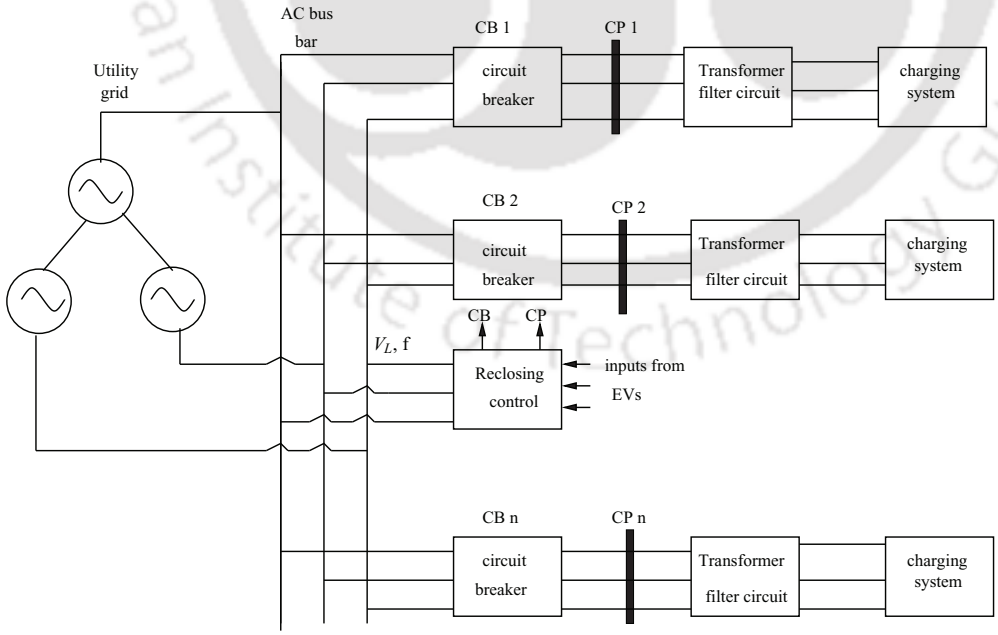

Figure 3.4: AC bus distributed charging station.

3.3 Bidirectional contactless charging system

The CS architecture described in the previous section facilitates the integration of multiple EVs through BCPT (charging) systems shown in Figure 3.4. The following section explains the system configuration and modeling of BCPT system.

3.3.1 BCPT system configuration

Figure 3.5 shows the schematic diagram of a single unit of BCPT (charging) system. Each BCPT system in a CS has two sides. The primary side is the charging circuit buried under the ground, which is connected to the three phase ac bus bar line and the secondary side of the coil is present under side of the vehicle connected to EVs' battery system. The primary and secondary side of the coil is magnetically coupled to each other. Power is transferred from the primary to the secondary through weak magnetic coupling. Compensation capacitors C_c and C_v are used on both sides of contactless coils. Primary compensation is used to minimize the VAR requirement and the secondary compensation increases the power transfer capability. The primary coil inductance L_c is magnetically coupled through M to the secondary coil L_v. The power electronic converters are employed on both sides of contactless coils with bidirectional switches to perform bidirectional power transfer between EVs and the grid. Single phase full-bridge bidirectional inverters are used as high frequency power supply on both sides of contactless coils, where the primary side is connected through three phase bidirectional rectifier to the ac line and the secondary side of the converter is connected to the load. The three phase bidirectional converter and high frequency inverter are controlled using power angle control and energy injection control to control the switches in the converter, which has been explained later. The output of the secondary circuit are connected to the EV battery, which are represented here as DC supply to either absorb or deliver the power to the grid. Electric equivalent circuit based battery model have been used for modeling the EV battery [79]. The contactless system modeling is described in the following section.

3.3.2 Contactless system modeling

Consider a CS with 'n' parallel connected charging systems. The steady state behavior of 1^{st} contactless transformer of a charging system have been analyzed using mutual inductance coupling model for G2V and V2G operation as shown in Figure (3.6(a)) and (3.6(b)). The coupling effect between the charging circuit and the EV battery system can be expressed using the concept of induced

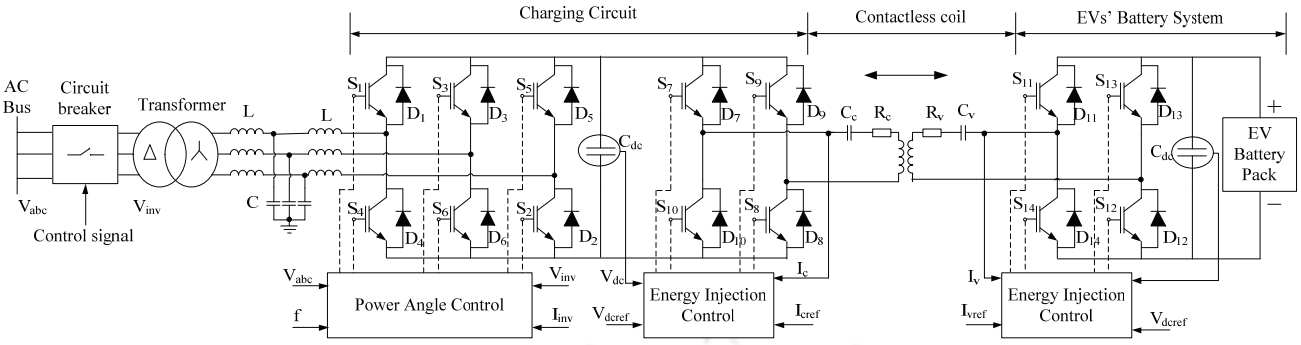

Figure 3.5: Configuration of bidirectional charging system.

and reflected voltage.

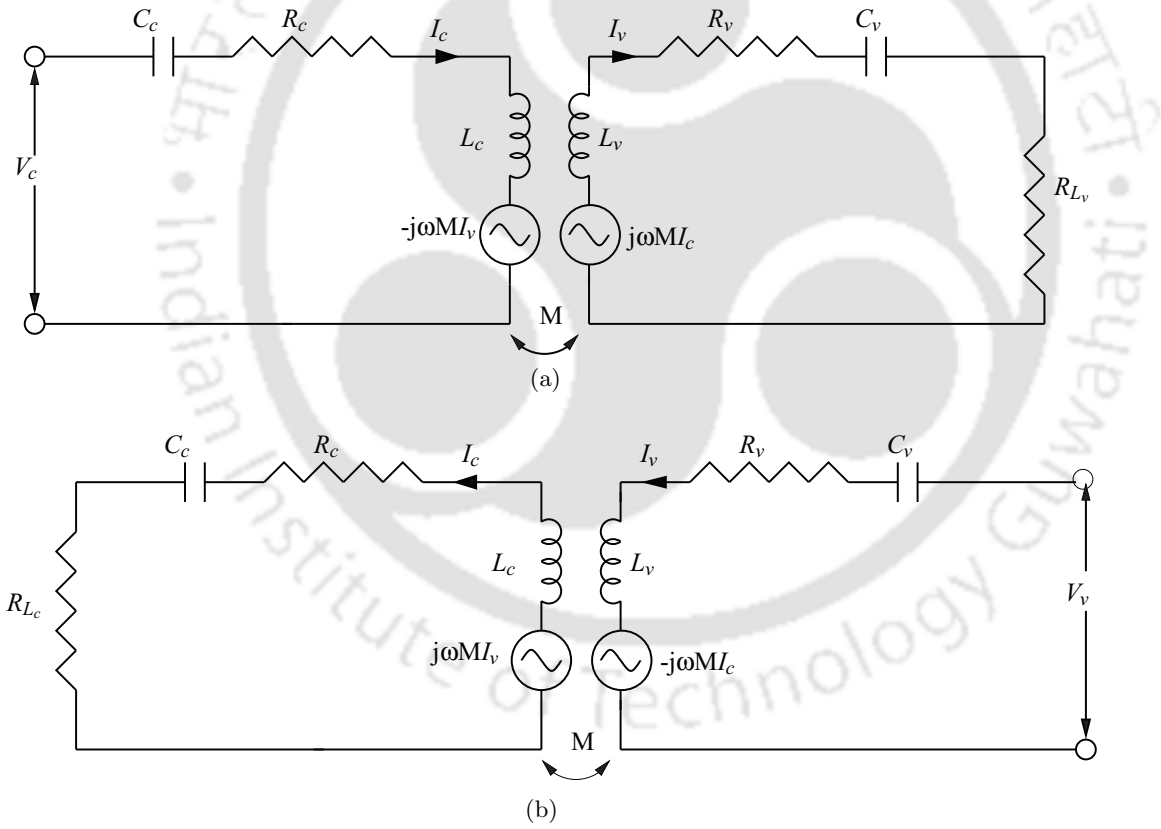

Figure 3.6: Simplified equivalent circuit of contactless system (a) for G2V (b) for V2G.

Assuming all currents and voltages sinusoidal, the steady state voltage equations at primary and secondary side voltage at an angular frequency ω shown in Figure 3.6(a) can be written in phasor

form as given by (3.1) and (3.2).

$$V_{c,1} = \frac{I_{c,1}}{j\omega C_{c,1}} + I_{c,1}R_{c,1} + j\omega L_{c,1}I_{c,1} - j\omega M_1 I_{v,1} \tag{3.1}$$

$$j\omega M_1 I_{c,1} = I_{v,1}R_{v,1} + j\omega L_{v,1}I_{v,1} + I_{v,1}R_{L_{v,1}} + \frac{I_{v,1}}{j\omega C_{v,1}} \tag{3.2}$$

In equation (3.1)- (3.2), $V_{c,1}$, $V_{v,1}$, $I_{c,1}$ and $I_{v,1}$ are the rms voltage and current of the 1^{st} charger circuit and the vehicle side circuit in the charging system. $C_{c,1}$ and $C_{v,1}$ are the series resonant capacitors in the charger and vehicle side circuit. Similarly, $R_{c,1}$, $L_{c,1}$, $R_{v,1}$ and $L_{v,1}$ are the coil resistance and self inductance of the charger and the vehicle side circuit respectively. M_1 is the mutual inductance of the contactless transformer in the charging system and is given by (3.3). $R_{L_{v,1}}$ denotes the EV battery and additional power electronics of vehicle during G2V operation and $R_{L_{c,1}}$ denotes the grid impedance and additional power electronics during V2G operation and K_1 is the inductive coupling factor between the primary and secondary coil. .

$$M_1 = k_1\sqrt{L_{c,1}L_{v,1}} \tag{3.3}$$

Simplifying the above equations, the current of the contactless coil at the vehicle side is given by (3.4), where $Z_{v,1}$ is the approximated secondary side coil impedance.

$$I_{v,1} = \frac{j\omega M_1 I_{c,1}}{Z_{v,1}} \tag{3.4}$$

$$Z_{v,1} = R_{v,1} + R_{L_{v,1}} + j\omega L_{v,1} + \frac{1}{j\omega C_{v,1}} \tag{3.5}$$

The EV battery is considered as a load during G2V operation and it consumes power from the charger circuit. The voltage reflected to the charger circuit is described by (3.6), where $Z_{r_{c,1}}$ is the transformed impedance or the reflected impedance as seen from the charger circuit.

$$V_{r,1} = Z_{r_{c,1}}I_{c,1} \tag{3.6}$$

$$Z_{r_{c,1}} = \frac{-\omega^2 {M_1}^2}{Z_{v,1}} \tag{3.7}$$

Therefore, the current in the charger circuit is given by (3.8), where $Z_{t,1}$ is the total impedance seen from the charger circuit.

$$I_{c,1} = \frac{V_{c,1}}{Z_{t,1}} \tag{3.8}$$

$$Z_{t,1} = R_{c,1} + j\omega L_{c,1} + \frac{1}{j\omega C_{c,1}} + \frac{\omega^2 {M_1}^2}{Z_{v,1}} \tag{3.9}$$

To achieve high efficiency at the output of the charging system, the charger circuit and the EV battery system should be operated at resonance frequency, therefore,

$$\omega_o = \frac{1}{\sqrt{L_{c,1}C_{c,1}}} = \frac{1}{\sqrt{L_{v,1}C_{v,1}}} \ldots\ldots\ldots \frac{1}{\sqrt{L_{c,1}C_{c,1}}} = \frac{1}{\sqrt{L_{v,n}C_{v,n}}} \tag{3.10}$$

The compensation capacitance at the charger circuit and the vehicle side is given by (3.11) and (3.12).

$$C_{c,n} = \frac{1}{{\omega_o}^2 L_{c,1}} = \frac{1}{{\omega_o}^2 L_{c,2}} \ldots\ldots \frac{1}{{\omega_o}^2 L_{c,n}} \tag{3.11}$$

$$C_{v,n} = \frac{1}{{\omega_o}^2 L_{v,1}} = \frac{1}{{\omega_o}^2 L_{v,2}} \ldots\ldots\ldots \frac{1}{{\omega_o}^2 L_{v,n}} \tag{3.12}$$

The compensation capacitance ($C_{c,1}$) in the charger circuit is chosen such that the impedance seen from the high frequency inverter (supply side) is purely resistive in nature. That is, it has to cancel the reactive element and should have minimum VA rating i.e., the input voltage and current are in phase with each other. The secondary compensation ($C_{v,1}$) is to increase the power transfer capability. The choice of resonance capacitor in the charging circuit ensures, the impedance of the secondary circuit ($Z_{v,1}$), the reflected impedance ($Z_{r_{c,1}}$) seen from the charger circuit and the net impedance seen by the power supply ($Z_{t,1}$) are purely resistive in nature at resonance frequency $\omega = \omega_o$. Similar procedure described from (3.1) and (3.12) can be used to analyze the steady state behavior during V2G operation.

3.4 Problem description

The modeling of multiple charging system in a CS and its coordination with grid is a challenging task. This is because the EVs arrived in the CS may perform charging as well as discharging operation. Moreover, the grids condition will not always suitable to exchange the power with the CS. Hence, the study on managing multiple EV in a CS is a major issue, which has to be addressed. Therefore, the main objectives of the work are:

- To develop component level multi-point charging (BCPT) system.
- To develop the suitable control strategy required to schedule the CS and to control the power flow between the charging system and the grid.

3.4.1 Charging station control strategy

A reclosing control have been used in the CS to schedule the charging and discharging operation of EVs. It connects the charging system lines through parallel connected ac bus to share energy among EVs in the CS. Reclosing control obtains arrival time (t_a), SOC status and departure time (t_d) as its input parameter and assign the charging systems for EVs arrived in the CS. The reclosing control has used a scheduling algorithm for charging system assignment. The control process involved in reclosing control is described in Figure 3.7. This explains the scheduling process to manage multiple EVs arrived in the CS. An EV owner can specify his planned departure time or leave it undefined, if he doesn't have a departure deadline. Thus, EV owner can request a specific charging/discharging depending on the actual parking time or departure time. If the grid is identified to be unsuitable to exchange power between the charging system lines, it disconnects the charging system line by opening the circuit breaker (CB).

3.4.2 Scheduling algorithm

A scheduling algorithm has been developed in the reclosing control to manage the EVs arrived in the parallel connected charging systems. It identifies the SOC status of each EVs in the CS and makes the charging system assignment depending upon the vehicle check-in and thus guarantee a certain amount of energy that one EV will be provided from the other one. An EV arrived to support the grid and an EV arrived to charge will be allocated depending on the time of arrival. The reclosing control keeps every update about the EV arrived in the CS and assigns the charging systems. If several request are received , the controller gives preference to the earliest request and suitable vehicle will be allocated fast. Thus, SOC levels and charging/discharging time are specified to each charging systems and the controller. In a particular case, if all EVs arrived in the CS is found to either charge or discharge its EVs, then the CS checks the grids condition and allows the EVs to charge or discharge from the grid. A request from EV owner will be rejected under two cases: if all EVs arrived in the CS is to charge and the grids condition is already in peak-hour period or if all EVs arrived in the CS is to discharge and the grids condition is off-peak hour and cannot accept any power support from the CS. Then the EV owners are unable to share its energy and will have to leave the CS. Figure 3.7 shows the flow chart of scheduling process in reclosing control to schedule EVs in the CS.

Assuming, four EVs (EV_1, EV_2, EV_3 and EV_4) have arrived at the CS with SOC levels 90%, 10%,

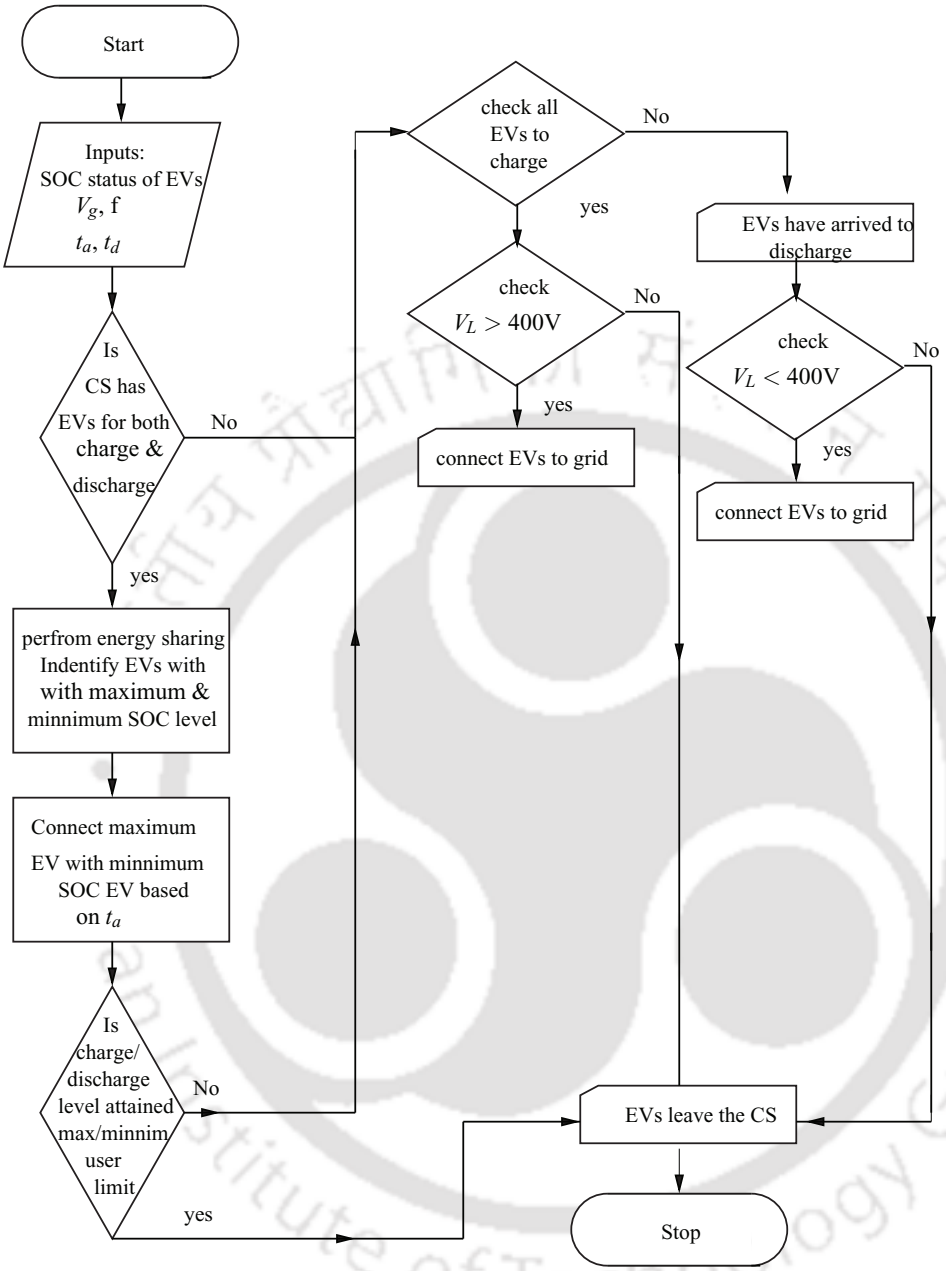

Figure 3.7: Control operation of charging station.

85% and 15% at time t_1, t_2, t_3 and t_4 to both charge and discharge its EVs. The time interval has been considered as $t_4 < t_3 < t_2 < t_1$. The reclosing control finds the EV arrived at the earliest and its SOC status. It also checks the next arrived EV. Here, in this case it assigns EV_1 to discharge its energy to support EV_2. It interconnects the charging points CP_1 and CP_2 to share the energy demand between

EV_1 and EV_2. Likewise, it interconnects EV_3 to EV_4 depending on the time of arrival and SOC status. The maximum and minimum SOC levels the EVs should charge and discharge is defined by the EV owner's depending on which the controller assigns the charging systems. An EV owner also defines the SOC limit to which an EV have to perform the charge/discharge operation. For convenience sake, the reclosing developed in this work has considered the maximum SOC to be greater than or equal to 70% and and minimum SOC to be less than or equal to 20% and the charging systems are assigned based on the time of arrival. The energy sharing takes place between the selected EVs in the CS through ac bus network. If suppose the initially allocated EV cannot fulfill the energy demand of other EV, the controller reassign or reallocate another possible EV to fulfill the minimum charging/discharging requirement as per the CS standard. In a situation, if the controller cannot assign suitable EVs to share its energy or to exchange power with grid, the EV owners will have to wait till the arrival of next EV or will have to leave the CS.

3.4.3 Charging (BCPT) system

To analyze multiple EVs arrived in the charging system and to examine its power flow capability, ten component level charging systems are modeled in the simulation environment. The circuit topology for single charging system is shown in Figure 3.5. The charging systems are able to operate in two modes: G2V operating mode and V2G operating mode. This section has detailed the circuit arrangement and its bidirectional power transfer during G2V and V2G operation.

3.4.3.1 G2V operation

EVs are scheduled to charge their batteries through any parallel connected charging system connected with high SOC batteries or it can be charged from the utility grid during off-peak hours. EVs are connected to the power supply through three phase converters (S_1 - S_6) present in the charging system. Therefore, the two systems should be properly synchronized and controlled to transfer the power from one system (sender) to the other (receiver) system. For this reason, the charging system is controlled using power angle control shown in Figure 3.8. It takes sender systems' voltage as its reference and controls the three phase converter switches (S_1 - S_6) to transfer power from sender to the receiver system. The power angle control has three phase PLL block and a fuzzy logic controller (PA-FLC) as shown in Figure 3.8. It takes the reference voltage, frequency and current from sender and receiver system. Initially, both the system is synchronized based on the sensed information and

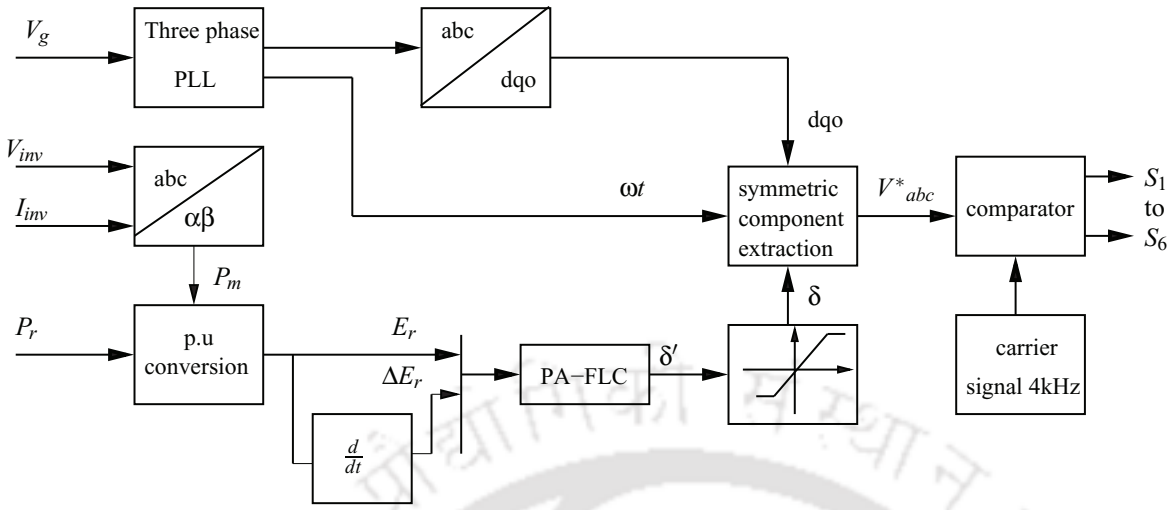

Figure 3.8: Power angle control.

the system is interconnected. Power angle control senses the grid voltage directly and tracks the phase and frequency variations of the utility grid. In this system, the three phase utility voltage can be represented by (3.13).

$$V_g = V_{abcn} = \left[\sin(\theta) \quad \sin\left(\theta - \frac{2\pi}{3}\right) \quad \sin\left(\theta + \frac{2\pi}{3}\right)\right]^T \tag{3.13}$$

where,

$$V_{abcn} = [V_{an} \;\; V_{bn} \;\; V_{cn}]^T \tag{3.14}$$

The voltage equation (3.13) can be transformed to the d-q axis frame as given by (3.15).

$$V_{qdo} = T_s V_{abcn} \tag{3.15}$$

where, T_s is the transformation matrix and is given by (3.16).

$$T_s = \frac{2}{3}\begin{bmatrix} \sin\omega t & \sin(\omega t - \frac{2\pi}{3}) & \sin(\omega t + \frac{2\pi}{3}) \\ \cos\omega t & \cos(\omega t - \frac{2\pi}{3}) & \cos(\omega t + \frac{2\pi}{3}) \\ \frac{1}{2} & \frac{1}{2} & \frac{1}{2} \end{bmatrix} \tag{3.16}$$

The V_{qdo} given in (3.16) is obtained from three phase grid voltage. The frequency of each phase is extracted from the grid voltage and this will be same for all the three phases. The power (P_m) has been calculated from the output of the three phase bidirectional converter by sensing its voltage and

current. Measured (P_m) and reference power (P_r) are given as input to PA-FLC. Error (E_r) and error rate (ΔE_r) is estimated based on the measured (P_m) and the reference power (P_r). The PA-FLC calculates the required power angle (δ). Using the power angle, the new symmetrical components are extracted and the required three phase reference voltage is obtained using equation (3.17).

$$v_{abc}{}' = T_m V_{qdo} \tag{3.17}$$

where, T_m denotes the new transformation matrix and is given by (3.18).

$$T_m = \frac{2}{3}\begin{bmatrix} \sin(\omega t + \frac{\pi}{6} - \delta) & \cos(\omega t + \frac{\pi}{6} - \delta) & 1 \\ \sin(\omega t - \frac{\pi}{2} - \delta) & \cos(\omega t - \frac{\pi}{2} - \delta) & 1 \\ \sin(\omega t + \frac{5\pi}{6} - \delta) & \cos(\omega t + \frac{5\pi}{6} - \delta) & 1 \end{bmatrix} \tag{3.18}$$

The three phase reference voltages are generated and pulses are produced using sinusoidal pulse width modulation (SPWM) technique. Thus, during G2V operation the bidirectional three phase converter acts as a rectifier and converts three phase ac voltage to dc. This converter is cascaded with the next converter (S_7 - S_{10}), which converts dc to high frequency ac current in the primary winding. Because of the mutual coupling between the primary and secondary coil, the required power transfer on the secondary side can be regulated by controlling the high frequency ac current in the primary coil through switches (S_7 - S_{10}). The circuit operation is based on the principle of resonance [109]. When the switches (S_7 - S_8) is controlled to be on, the source voltage is injected into the primary coil in positive direction. When the current falls to zero, the switches (S_9 - S_{10}) is on in the reverse direction. The controller present in the primary side converter maintains a high frequency ac current in the secondary side. As the coils are magnetically coupled through M, the secondary side converter switches (S_{11} - S_{14}) converts high frequency ac current to dc and regulates the amount of power extracted from the primary coil to meet the vehicle demand. In many cases, a bidirectional dc-dc converter is also employed at the secondary side to regulate the output voltage to regulate the vehicles of different voltage and current ratings. The pattern of membership function of PA-FLC is shown in Figure 3.9 and its rule base is given in Table 3.1.

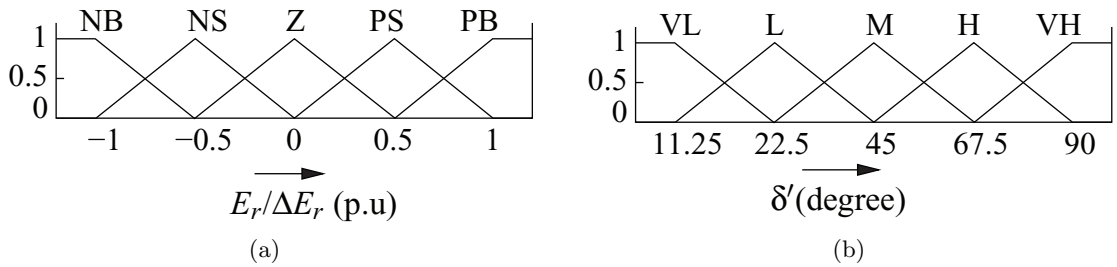

Figure 3.9: Membership function of phase angle-fuzzy control (PA-FLC) (a) Input: error and error rate (E_r/ ΔE_r) (b) Output: Power angle (δ').

Table 3.1: Rule base of power angle control (PA-FLC)

$E_r/\Delta E_r$	NB	NS	Z	PS	PB
NB	VL	L	M	H	VH
NS	VL	L	M	H	VH
Z	VL	L	M	H	VH
PS	VL	L	M	H	VH
PB	VL	L	M	H	VH

Five fuzzy subsets such as Negative Big (NB), Negative Small (NS), Zero (Z), Positive Small (PS) and Positive Big (PB) are chosen as input membership function and for the output Very Low (VL), Low (L), Medium (M), High (H) and Very High (VH) are chosen in order to obtain required control action. Triangular membership functions are used as it is simpler and easier to implement.

3.4.3.2 V2G operation

During V2G operation, the secondary side converter switches (S_{11} - S_{14}) converts EVs battery voltage to high frequency ac current to feed the contactless coils. This works on the principle of resonance as described above. The required power flow in the charging circuit side is regulated using the controller present in the vehicle side converter. As the vehicle side coil inductance (L_v) is magnetically coupled to the charging circuit side coil inductance (L_c), the high frequency ac current will get induced in the charging circuit. Further, the primary side converter acts as an inverter (S_1 - S_6) to convert dc to three phase ac. Thus, the power is transferred in the reverse direction using bidirectional switches in the converter. The amount of power supplied from the vehicle (sender) is decided by the power angle control explained above. The maximum power that can be transferred is at an angle $\delta = 90°$

3.4.4 Design of critical parameters

3.4.4.1 Filter circuit

Figure 3.10 shows the equivalent circuit of three-phase bidirectional converter connected to the grid through an isolation transformer. The switching frequency effects in the converters of the charging station can inject harmonics to the grid. These harmonics requires the connection of low pass filter between the inverter and the grid. The filter attenuates most low order harmonics in the output.

The inductor (L) determines the ripple in the current and reduces the low frequency harmonic components. The voltage across the filter component (V_{dc}) with respect to the switching frequency (f_{sw}) and ripple current (ΔI) is given by (3.19).

$$\mathrm{V_{dc}= L\Delta I_{conv} f_{sw}} \tag{3.19}$$

According to the harmonic standards, 15-20% of the rated ripple current is allowable; 20% is assumed

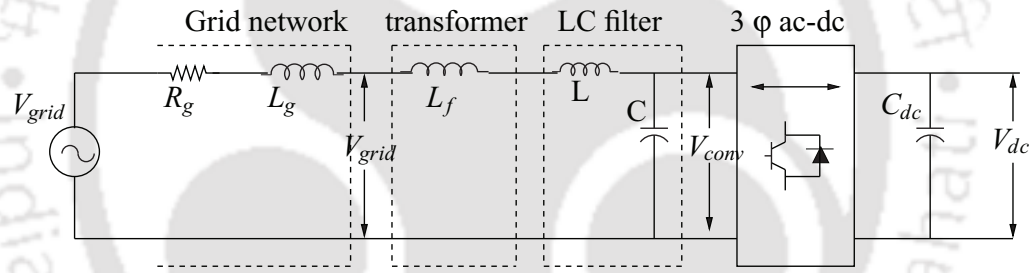

Figure 3.10: Equivalent circuit of grid connected inverter.

in this study. The maximum ripple depends on the inductance, dc voltage (V_{dc}) and f_{sw}. The dc link voltage and switching frequency is constant and the inductance can be calculated using (3.20).

$$L = \frac{1}{8}\frac{V_{dc}}{\Delta I_L f_{sw}} \tag{3.20}$$

The high frequency components have to be eliminated from the inductor current when connected to the grid. This must be performed by the shunt impedance which is low at high frequencies. Assuming, V_{conv} is the charging system voltage, I_{conv} is the charging system current and C, L_{tf}, L_g and L are the capacitor, inductance of the transformer and grid network and filter inductor respectively, then the ratio of I_{conv} to V_{conv} is given by (3.21).

$$\frac{I_{conv}}{V_{conv}} = \frac{1}{s^3LC(L_g + L_{tf}) + s^2LR_gC + s(L + L_{tf} + L_g) + R_g} \tag{3.21}$$

$$C = \frac{\frac{V_{conv}}{I_{conv}} - s\left(L + L_{tf} + L_g\right) - R_g}{s^3L\left(L_g + L_{tf}\right) + s^2LR_g} \tag{3.22}$$

3.4.4.2 Dc link capacitor

The three phase ac-dc converter in the charging system is made of bidirectional switches, which converts three phase phase ac-dc conversion in the forward direction and dc-ac conversion during reverse power flow. During charging operation, the peak-to-peak dc output voltage of the rectifier contains harmonics in the output voltage and that can be written as given by (3.23) [110]. While in case of reverse operation, this capacitor acts as a dc link capacitor.

$$V_{dc}(pp) = \frac{V_m}{2fZ_LC_{dc}} \tag{3.23}$$

where V_m is the maximum peak value, f is the input side frequency, Z_L is the load impedance and C_{dc} is the filter capacitance. The ripple factor (RF) can be determined from the RMS and average output voltage, which can be expressed as given by (3.24).

$$RF = \frac{1}{\sqrt{2}(4fZ_LC_{dc} - 1)} \tag{3.24}$$

From the above equation C_{dc} can be solved as given by (3.25).

$$C_{dc} = \frac{1}{4fZ_L\left(1 + \frac{1}{\sqrt{2}RF}\right)} \tag{3.25}$$

3.5 Simulation results

The CS described in the previous section has been tested in simulation environment. In order to verify its functioning, a 500kVA capacity CS has been modeled with ten parallel connected charging system fed from $440V_{rms}$, 50Hz ac bus network. The circuit topology used for charging system is shown in Fig. 3.5. The contactless coils are fed by high frequency inverter. The secondary side of the coil is connected to 300V EV battery. The circuit parameters of the charging systems are given in Table 3.2. The primary and secondary side of the coils are magnetically coupled at a coupling factor of 0.2537. For ease of analysis, EVs batteries are divided into five groups based on the terminal voltage (V), energy (kWh) and SOC levels. To avoid repetition the results are shown only for five sets of EVs

batteries.

Table 3.2: Simulation parameters of charging system.

Parameter	Description	Values	Parameter	Description	Values
C_c, C_v	compensation capacitance	1.17μF, 1.17μF	L_c, L_v	Coil inductance	34.8μH, 34.8μH
M	mutual inductance	8.83 μH	R_c, R_v	coil resistance	433 $\mu\Omega$
k	coupling factor	0.2537	C_{dc_c}	dc link capacitor (charger)	100mF -
LCL	LCL filter	600μF, 80μF, 800μF	C_{dc_v}	dc link capacitor (vehicle)	180μF

For convenience of analysis, the following assumptions are made in this work:

- Each charging systems are designed for a maximum power handling capacity of 50kW.
- The EVs batteries are not allowed to discharge below 20% SOC level and the charging level is limited to 85% SOC.

The parameters of EV battery are given in Table 3.3.

Table 3.3: Parameter of EV battery.

EVs	Voltage (V)	Energy (kWh)	SOC (%)	E_r (kWh)	E_a (kWh)
EV_1 to EV_2	300	40.2	15	11.9	-
EV_3 to EV_4	300	42.6	94	-	13.22
EV_5 to EV_6	300	47.4	81	-	11.36
EV_7 to EV_8	300	54.6	19	19.14	-
EV_9 to EV_{10}	300	64.2	98	-	28.28

In Table 3.3, there are 3 sets of EVs to discharge its energy and two sets of EVs arrived to charge. The charging systems with high SOC batteries are allowed to discharge its energy to support the charging system with low SOC EVs. However, EV_9 cannot be scheduled in the charging system, as the charging systems are already interconnected. This can be connected to grid and therefore EV_9 is allowed to discharge its energy to support the grid. Figure 3.11 shows the battery power of five EVs arrived in the charging system for two hour period. Among this, EV_3 and EV_5 discharges its energy to support EV_1 and EV_7. EV_9 discharges its energy to support the grid.

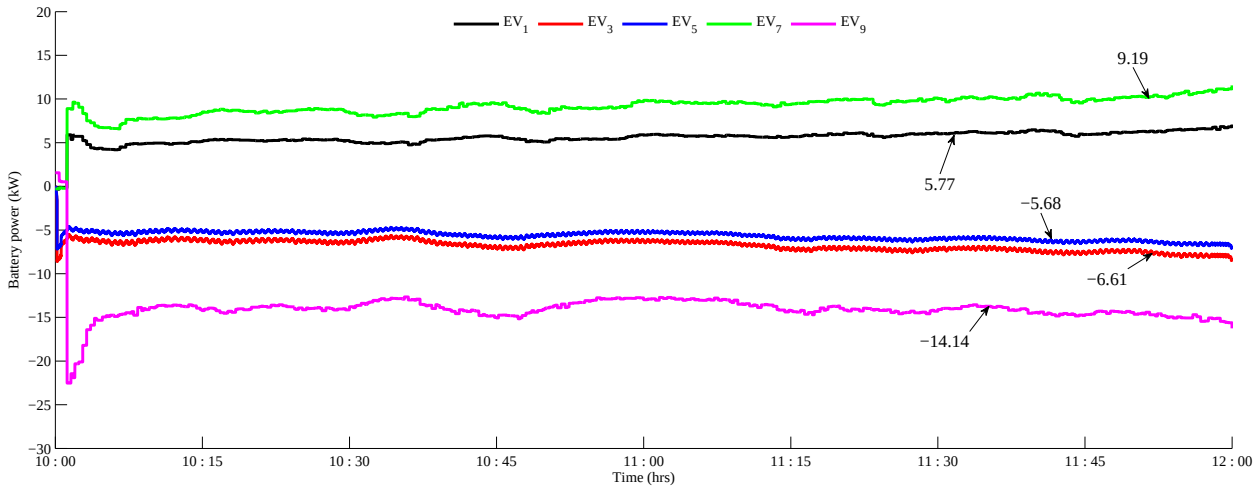

Figure 3.11: Power supplied from the EVs batteries.

Figure 3.12 shows the SOC levels of five EVs, after charging/discharging operations in the CS for two hours. EV_3, EV_5 and EV_9 has arrived in the charging system with high SOC batteries and has discharged its energy. EV_1 and EV_7 has arrived in the charging system with low SOC batteries to charge its batteries.

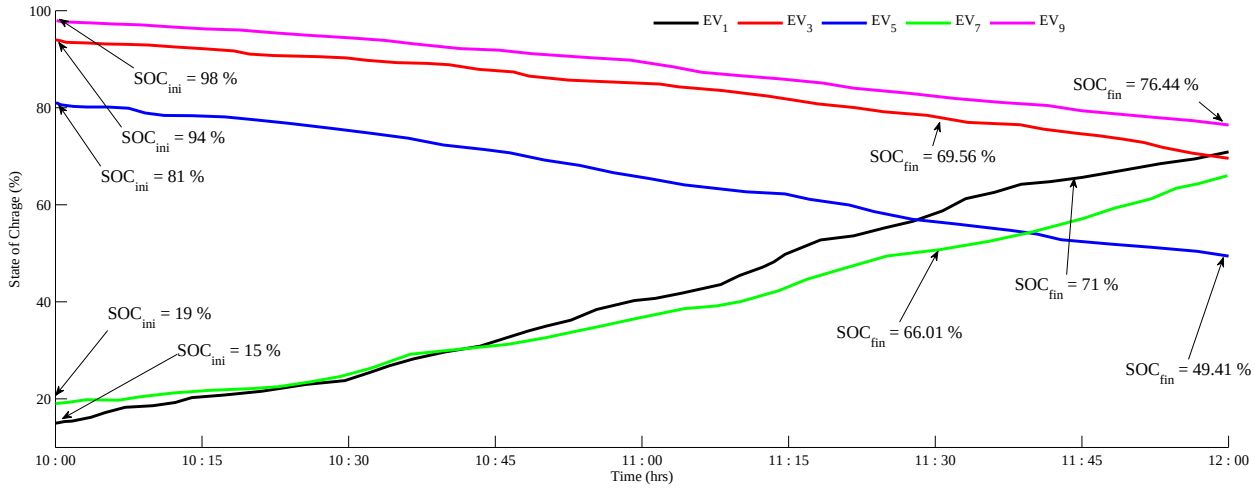

Figure 3.12: SOC levels of EVs.

The charging and discharging current of five sets of EVs shown in Figure 3.13. The positive current curves denotes EVs arrived in the charging system is performing charging operation and

negative current denotes EVs are discharging its energy to support other EVs or to support the grid.

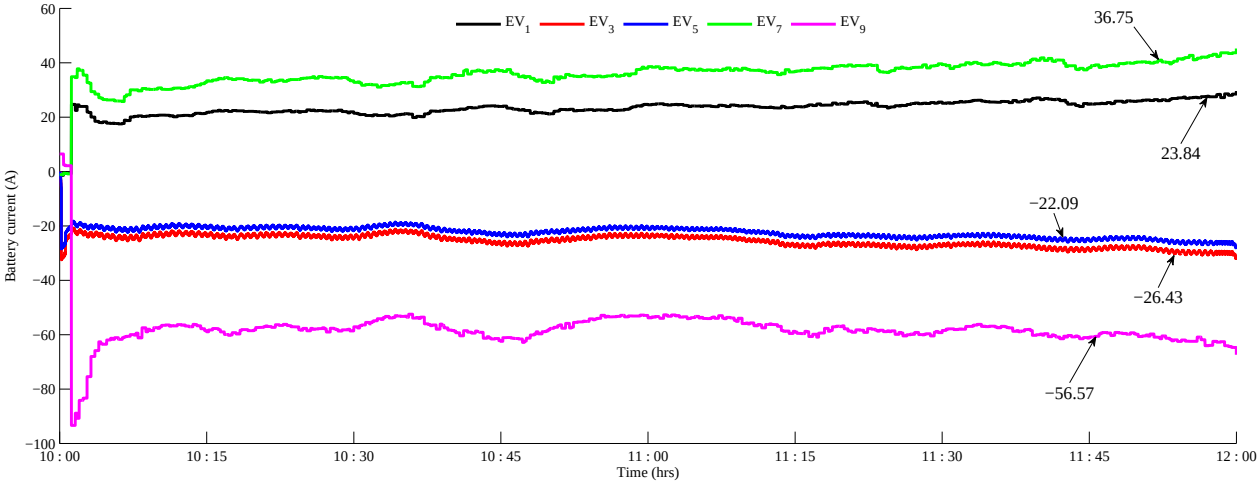

Figure 3.13: Charging and discharging current of EVs.

Figure 3.14 show the charging system voltage at the terminals of the bus bar. The positive and negative power represents the power flow in two directions. The amount power flow is decided by the user and controlled by the charging system.

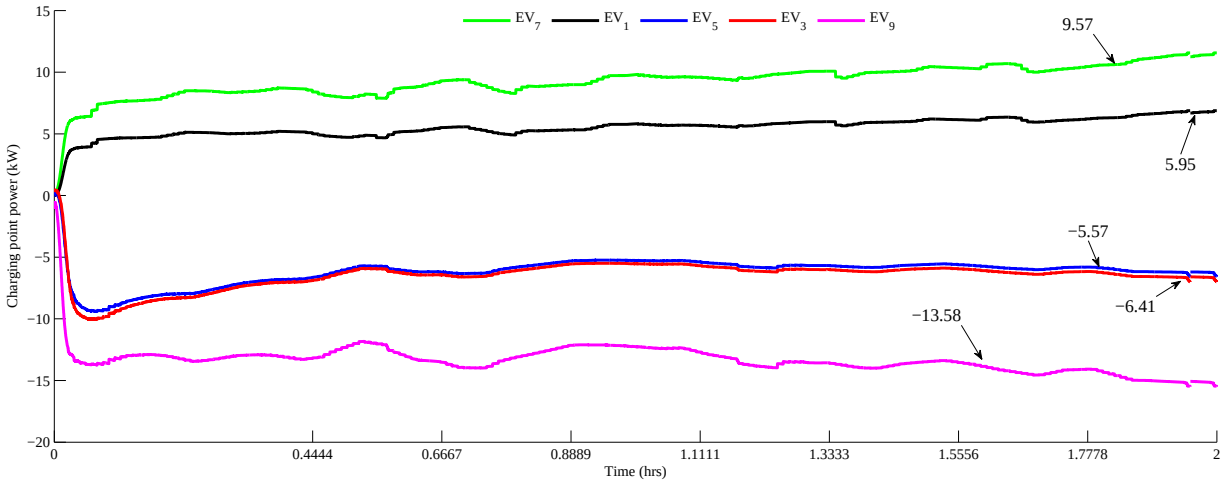

Figure 3.14: Power at the charging point.

Figure 3.15 show the node voltage and node current at the terminals of the CS. Figure 3.16 shows the distribution node power.

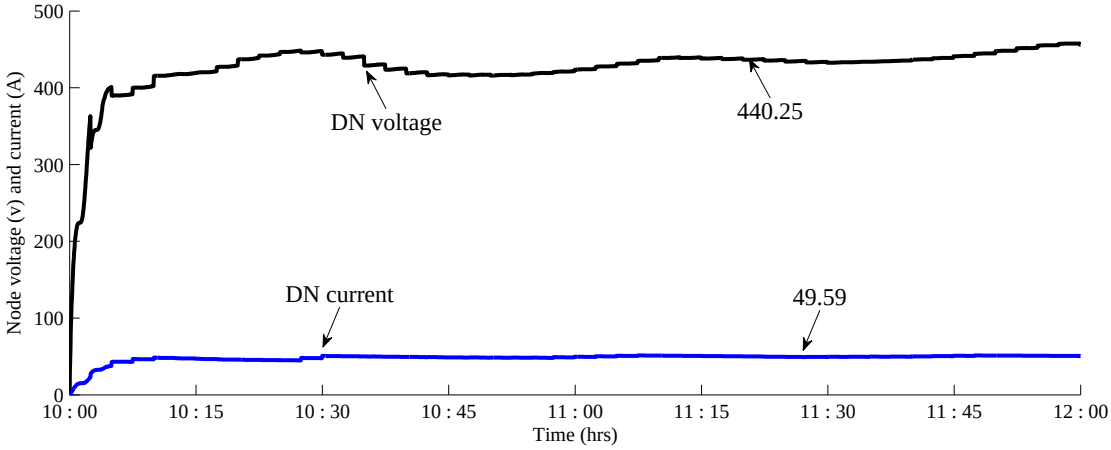

Figure 3.15: Node voltage and node current.

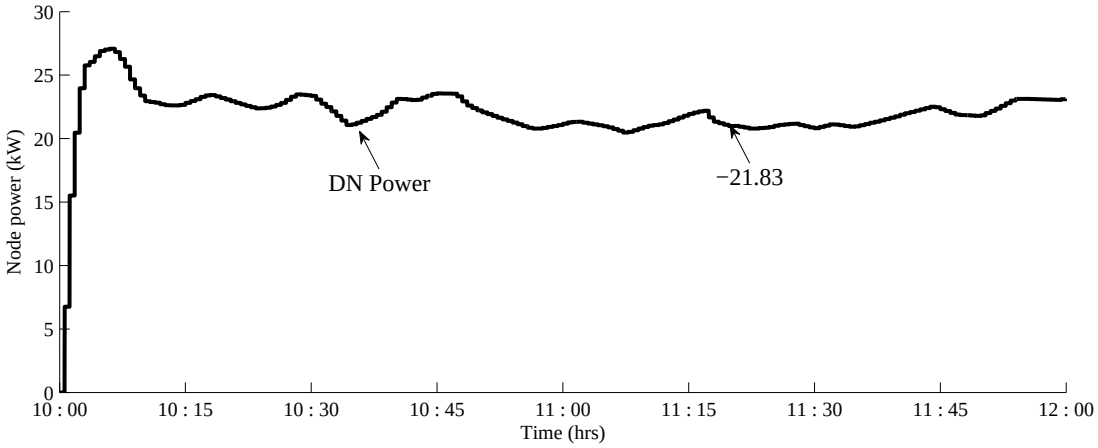

Figure 3.16: Power at the distribution node.

3.6 Conclusions

In this chapter, a CS has been modeled using multiple parallel connected charging (BCPT) systems. The theoretical operation of the parallel connected BCPT systems has been analyzed for G2V and V2G operation. The individual charging system are controlled to control the power flow in both the direction. A control strategy has been used to schedule the charging/discharging operation of multiple EVs in the CS. A 500 kVA multiple BCPT system is modeled in the simulation environment and the validation of the study has been carried out using five EVs batteries of different ratings.

The contactless charging system modeled in this chapter has considered a fixed coupling coefficient;

but in realtime the coils can be misaligned and its coupling coefficient may change because of uneven surface impacts, due to heavy battery weights and roads. This necessitates the need to compute MI between two coils with its misalignments. The next chapter discusses an analytical approach to compute MI between two coils including lateral and angular misalignments.

4

Computation of Mutual Inductance for Contactless System

Contents

4.1	Introduction	79
4.2	Possible variations of square coils	81
4.3	Analytical modeling of square coil	83
4.4	Finite element modeling of square coil	86
4.5	Experimental verification	88
4.6	Numerical results and discussion	92
4.7	Conclusions	99

Abstract

This chapter presents an analytical approach for computing the mutual inductance between two air core square coils placed in a flat planar surface. The mutual inductance of the coils is calculated for all possible variations including lateral and angular misalignments in space. In contrast to conventional approximated formulae, the straightforward approach based on Biot-Savart principle is used and their integrals are computed numerically. The results of computed mutual inductance by analytical method are validated by finite element analysis and an experimental setup. Finally, the analysis compares the three mutual inductance calculations: an analytical method, the finite-element model and an experimental results. The values computed by three methods in all cases are in good agreement.

The work presented in this chapter is published in [30].

4.1 Introduction

The computation of mutual inductance (MI) between two coils is a classical problem in electrical engineering and that remains important to this day for a wide variety of physical disciplines [111]. Some important applications such as transcutaneous transformers, coil guns, linear motors, contactless based electric vehicle charging systems etc., are modeled with inductively coupled circuits such as transformers and contactless power transfer (CPT) systems [36, 48, 112–114]. Recent developments in CPT systems have prompted more the requirement to investigate the MI of the coil [22, 23, 70]. The design of contactless coils in BCPT systems are very complex as the coils are usually misaligned due to variations in the system and worsen the coupling between the coils [69, 70]. These misalignments could cause fluctuations in the output voltage and affects the stability of the system [113]. Therefore, the computation of MI with all its lateral and angular misalignments must be fully addressed, which is the first step for studying the characteristics of such systems.

A survey of past literature shows that, Grover's tabular data remains the most standard for calculating the MI for a wide variety of coils and wire forms [115–119]. However, its use has mostly been restricted to zeroth and first-order calculations and it is proved to be inaccurate for loosely coupled and short coils [116–119]. Several contributions for MI computation are found in the literatures [115, 117–126]. In some work, MI is calculated by means of approximated formulae [116, 120, 121], Heuman's lambda function [111, 122–124], Bessel and Struve functions [125, 126] and in other works using Biot-Savart law [127, 128]. However, much of the earlier works are devoted for circular and

coaxial coils [111, 116–126]. These coil geometries are well suited for fixed coil systems and they are not tolerant for misalignments in the coils. Square and rectangular coil geometries are found to be well suited for mid-distance CPT systems; as they show better tolerance for misalignments [36, 129]. Although, there are numerous works carried out in this area, only very few work have studied these coil geometries with its misalignment effects [22, 23, 36, 69, 70, 114, 129–132]. In [69, 70], an analysis is presented based on rectangular coil geometry. However, these works mainly focused on the design of charger based on resonant magnetic coupling to transfer power wirelessly over a long distance. It has been observed from the literature, the effects of misalignments of the coils have not been investigated in detail from both geometrical stand point and circuit design stand point.

This chapter describes an analytical approach to compute the MI between two coils. A detailed investigation of all possible lateral and angular misalignments with horizontal and vertical variations are presented. Square coil geometry has been chosen here to analyze the misalignments of the coils. The proposed analytical approach is capable of calculating MI for all positions of the coil, thus reducing complex mathematical equations. The results of the analytical model are compared with 3-D finite element analysis (FEA) and an experimental setup. Figure 4.1 shows the main building blocks used for MI computation. The coil which is excited is referred as excitation coil (EC) and the coil where the output variations are observed is referred as observation coil (OC). The finite element results and experimental evaluation justifies the accuracy of the analytical model in all cases.

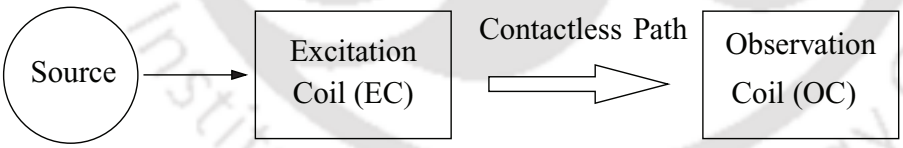

Figure 4.1: Block diagram of contactless system.

For clear interpretation, the possible variations of square coils is presented in Section 4.1. The analytical modeling of square coil is given in Section 4.2. Finite element modeling is addressed in Section 4.3. Experimental verification is done in Section 4.4. Results are described in Section 4.5, this section is followed by conclusions in Section 4.6.

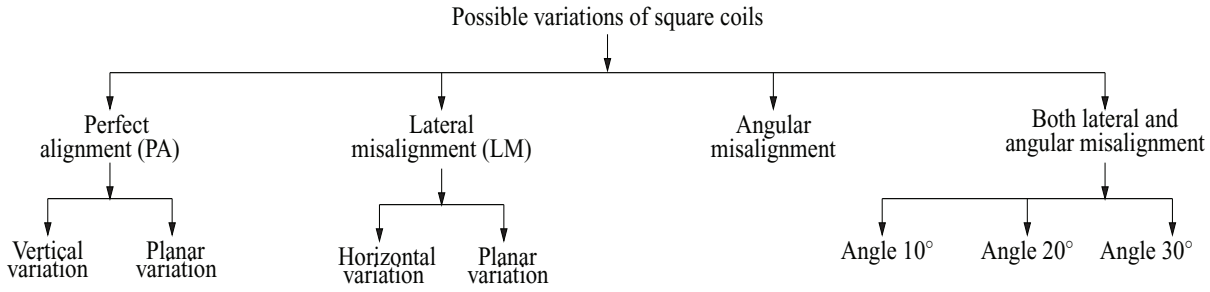

Figure 4.2: Possible variations of contactless coils.

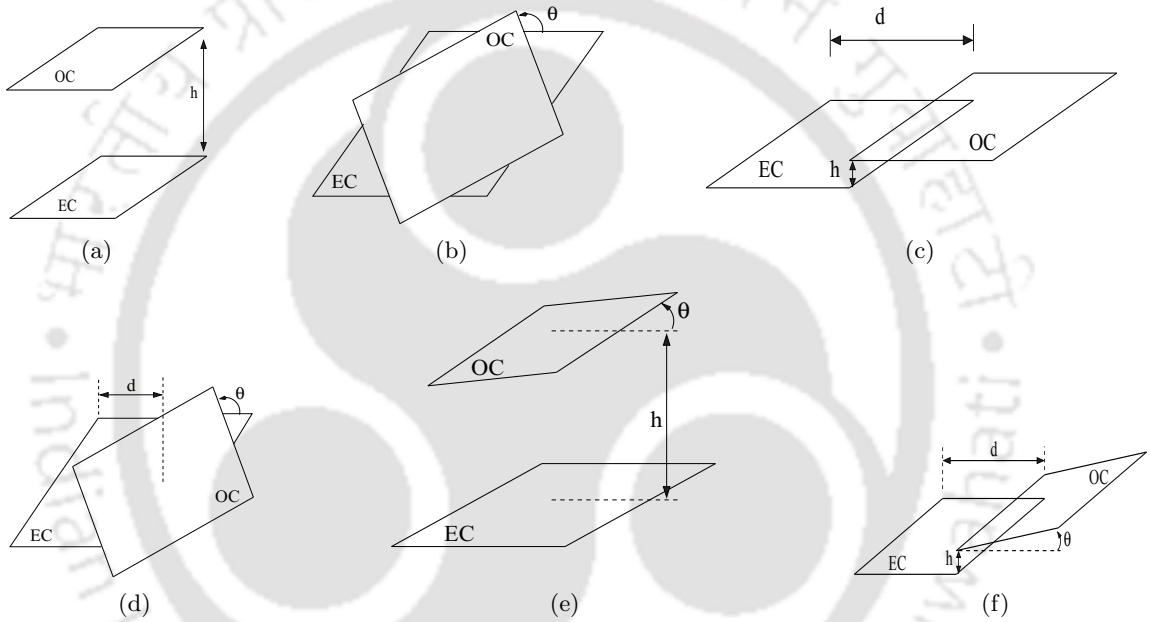

Figure 4.3: Schematics of square coils for analyzed variations (a) PA - vertical variation (b) PA - planar variation (c) LM - horizontal variation (d) LM - planar variation (e) angular misalignment (f) both lateral and angular misalignment.

4.2 Possible variations of square coils

The analysis presented in this chapter computes MI between two air core square coils, placed in a flat planar surface coinciding in space. As the MI of the coil varies with the change in position of the coils, different variations of the coils i.e., misalignments are analyzed throughout this chapter. Different cases of variations of OC with respect to EC are taken into account, which are shown in Figure 4.2 and its corresponding schematics are shown in Figure 4.3. The coil parameters used in this work are described in Table 4.1.

Table 4.1: Coil parameters

EC, OC	Excitation coil, observation coil
h	deviated vertically from the center of the coil
d	deviated horizontally from the center of the coil
θ	Angle of OC with respect to EC

If the EC and OC are placed in a flat planar surface with coinciding axes, such arrangement of coils is referred as *perfect alignment (PA)*. Two types of variations like vertical and planar variation are analyzed in this case as shown in Figure 4.3(a) and Figure 4.3(b). The flux linkage will be maximum when OC and EC are perfectly aligned and the coils are close to each other. When OC is moved vertically away from EC, the coupling between the coil changes and MI decreases. In planar variation, EC and OC are placed near to each other and OC is rotated along its axis at various angle as shown in Figure 4.3(b). As the distance between the coils is kept constant, the coil overlapping area doesn't vary much and due to this the variation of flux linkage in this case would be nominal.

There can be another misaligned case in real time systems, where the coils are situated in parallel plane and displaced horizontally, such arrangement of coils is referred as *lateral misalignment (LM)*. This type of misalignment is observed for different horizontal distances between the axes of the coils. For LM, horizontal and lateral variations are studied which are shown in Figure 4.3(c) and Figure 4.3(d). The flux linkage and MI of the coils depends on the distance of OC from EC and it would drop when it moves away from the EC. Apart from this, there can be a situation where OC can be titled up or down with certain angle (0° to 90°) due to unequal surface impacts; such arrangement of coils is referred as *angular misalignment* which is shown in Figure 4.3(e). In similar way, there can be a general case where OC can be both tilted and varied horizontally, such arrangement of coils is referred as *both lateral and angular misalignments*, as shown in Figure 4.3(f). In this misaligned case, MI depends on both the tilted angle and horizontal distance. The misalignments described above are calculated using an analytical approach and are validated by both FEA models and an experimental setup. The details of evaluation methods, its results and comparison are explained in later sections.

4.3 Analytical modeling of square coil

4.3.1 Modeling of mutual inductance

The circuit topology of the two coupled coils EC and OC resembles an inductively coupled transformer, which is represented by an equivalent circuit as shown in Figure 4.4.

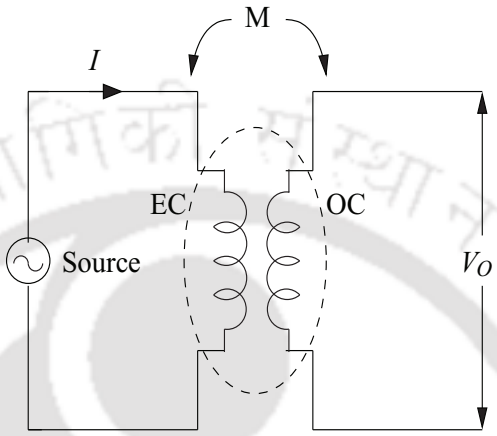

Figure 4.4: Equivalent circuit model of an inductive coil.

Consider EC and OC placed near to each other as shown in figure. When EC is connected to the power supply, current (I) flows in it, which produces a magnetic flux (λ_1) and a part of the flux (λ_{12}) links with the secondary side coil OC. Then, the MI of the coil is represented as M and is given by (4.1).

$$M = \frac{\lambda_{12}}{I} \tag{4.1}$$

The flux linked with the OC due to current in the EC can be calculated analytically by considering the flux distribution of each individual coil turns of the OC. The method works by approximating the area of OC with small regions, encompassing the entire square and thereby considering the complete spiral square coil. The flux through each small region of the OC is taken into account to calculate the flux linked to OC due to EC. To carry out this process, a sequence of program routine have been used. The total flux linked in the OC is obtained by the sum of the flux linked in each small grid for all the turns of the OC. Assuming φ_n is the flux linked with the n^{th} region of the area enclosed by single turn of the OC, then λ_{12} can be estimated by (4.2). The limit of the summation depends on

the number of small regions formed in a single turn of OC.

$$\lambda_{12} = \sum \varphi_n \tag{4.2}$$

The flux linked to each of these small regions of OC due to EC is calculated with the following assumptions.

- The insulated coil conductors are placed such that there is no space between conductors of any two loops and they are touching each other.
- The magnetic field in the small region of OC caused due to EC (Figure 4.5(b)) is assumed to be constant and its value is calculated at the center of that small region.

Having made the above assumptions, φ_n for each small region is calculated using (4.3) and (4.4), which depends on the magnetic field at the center ($\overrightarrow{B_c}$) of the small region, n^{th} area (A_n) and normal vector of the n^{th} area ($\widehat{A_n}$).

$$\varphi_n = \overrightarrow{B_c} \cdot (A_n \cdot \widehat{A}_n) \tag{4.3}$$

$$A_n = \Delta x_n \cdot \Delta y_n \tag{4.4}$$

Here, Δx_n and Δy_n are the length and width of the small divided region as shown in Figure 4.5(b). The magnetic field $\overrightarrow{B_c}$ at the center of the small region is caused due to EC. $\overrightarrow{B_c}$ is calculated for P turns of EC and is given by (4.5). The individual coil turns of EC is modeled by four straight current carrying conductors. Let $\overrightarrow{B}$ is the magnetic field due to one current carrying loop of EC as shown in Figure 4.5(a) and is given by (4.6).

$$\overrightarrow{B_c} = \sum_{m=1}^{P} \overrightarrow{B} \tag{4.5}$$

$$\overrightarrow{B} = \sum_{n=1}^{4} \overrightarrow{B_n} \tag{4.6}$$

In the above equation, n represents the four sides of the single current carrying loop and $\overrightarrow{B_1}$, $\overrightarrow{B_2}$, $\overrightarrow{B_3}$ and $\overrightarrow{B_4}$ are the magnetic fields of the sides of the square coil AB, BC, CD and DA. $\overrightarrow{B_n}$ can be calculated from the Bio-Savart law for magnetic field. The basic magnetic field equation ($\overrightarrow{B_n}$) at any point in space due to a straight current carrying conductor is given by (4.7).

$$\overrightarrow{B_n} = \int \frac{\mu_0 I \overrightarrow{ds} \times \widehat{R}}{4\pi R^2} \tag{4.7}$$

The vector $\widehat{R}$, in the above equation is the unit vector in the direction of position vector of the observation point, originating from the differential element of current carrying conductor ($\overrightarrow{ds}$). The direction of $\overrightarrow{ds}$ is in the direction of current in the conductor. The integration in (4.7) is performed over the length of the conductor. Similarly, the magnetic field at a point in space and flux linkage calculations can be done for spiral square coils with multiple turns as shown in Figure 4.5(c), where L and W are the length and width of the coil.

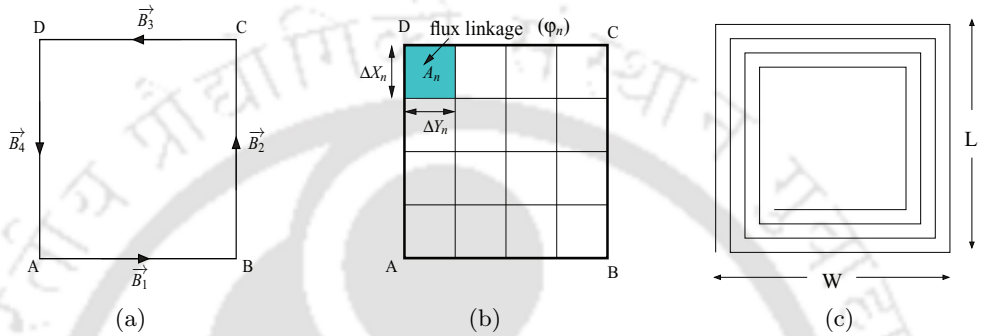

Figure 4.5: Square current carrying coil (a) single turn (b) single turn segmented (c) multiple turn.

4.3.2 Numerical evaluation

The MI for the mutually coupled coils is calculated numerically using the equations discussed in the previous section. The procedure for numerical calculation is explained in the following steps.

- The total number of turns for EC (P) and OC (Q) are determined.
- 3D co-ordinates of a single turn of EC and OC are determined.
- Diameter of conductor and distance between EC and OC (depending on the type of variation) is determined.
- The selected turn of the coil is divided into multiple small areas from $A_1.....A_n$ as shown in Figure 4.5(b).
- Calculate the total flux linked to each small region of OC using (4.8) by calculating the magnetic field at the center .

$$\varphi_1 = \sum_{n=1}^{4} \frac{\mu_0}{4\pi} \int \frac{I\overrightarrow{ds} \times \widehat{R}_1}{R_1^2} \cdot \left(A_1 \cdot \widehat{A}_1\right) \tag{4.8}$$

- The flux linked in a single turn (φ_m) of OC is obtained by summing all the fluxes using (4.9).

$$\varphi_m = \sum_{k=1}^{P} \sum (\varphi_1 + \varphi_2 ..... + \varphi_n) \tag{4.9}$$

- This procedure is repeated for all turns of EC and OC and λ_{12} is calculated using (4.10).

$$\lambda_{12} = \sum_{m=1}^{Q} \varphi_m \tag{4.10}$$

- Therefore from these equations MI is calculated using (4.1).

The detailed description of this evaluation is given in the flowchart shown in Figure 4.6. This procedure has been used for all variations of EC and OC with their corresponding new coordinates and vertices. Thus, the method adapted in this work has used only Biot-Savart law for a straight current carrying conductor; which is the basic equation for calculating the magnetic field. It does not require any double or triple integration functions for its computation. This gives an interesting compactness for the calculation of MI by avoiding complicated mathematical equations. An example for particular case of variations is given in Appendix (see Appendix A.5).

4.4 Finite element modeling of square coil

The commercial 3-D finite element tool ANSYS Maxwell 14.0.0 has been used for validating the analytical model. The EC and OC considered in this work have 11 and 9 turns respectively. The EC is excited with a current of 10A. The EC and OC are modeled for different variations and are analyzed by changing their co-ordinates in simulation environment. To simplify the analytical calculations and to reduce the computation time, following assumptions are made in this investigation for flux linkage calculations.

- As the 3-D FEA model for spiral square coil takes very long time and sophisticated computation environment, the models are analyzed with all the dimensions reduced to one fifth of the original. This adjustment is justified as the variation of the flux linkage is linear with the dimension of the whole system, which can be proved analytically.

- To reduce the computational time, OC is put as a surface whose area is equal to that of EC and flux linked to the surface has been calculated.

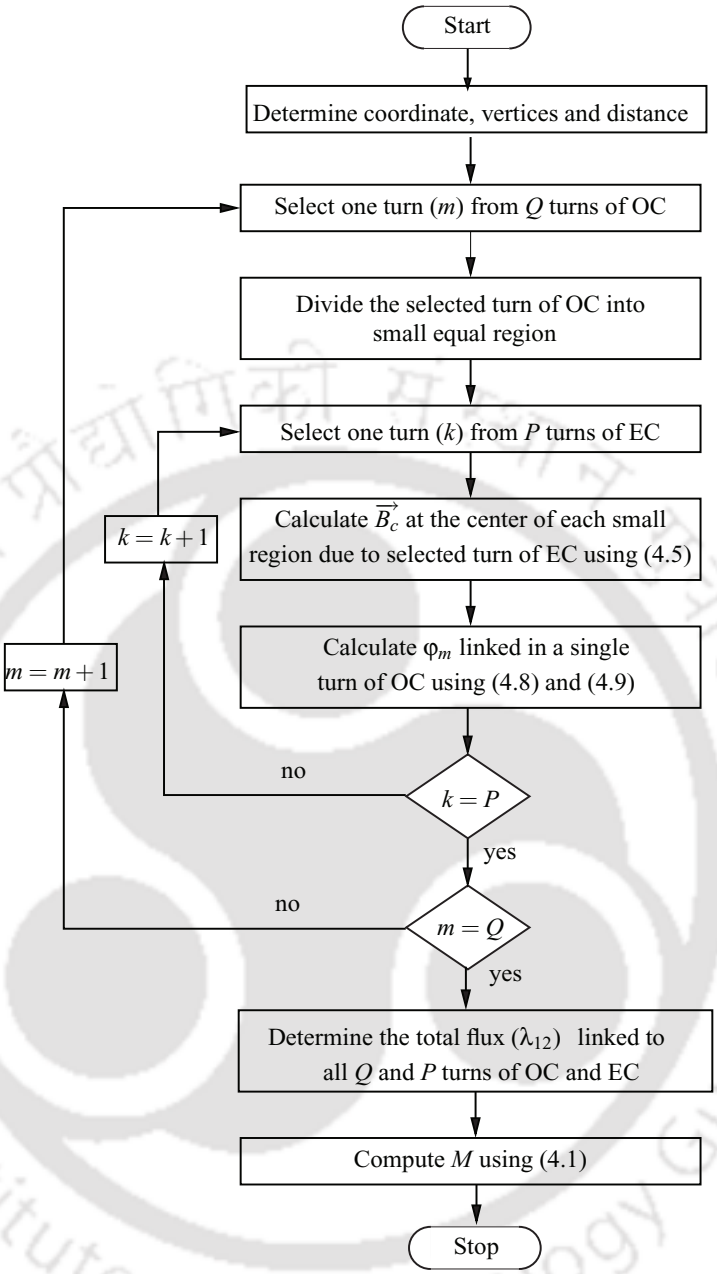

Figure 4.6: Flowchart describing the numerical evaluation.

- The multiple turns of EC and OC are assumed to be placed near with no space between the turns of the coils.

The models are created using the co-ordinates taken from the experimental setup. The FEA models are formed for all the configurations of the coils and various positions of OC by changing its coordinates. Figure 4.7 shows the FEA models of the coils for different variations such as vertical,

angular and planar.

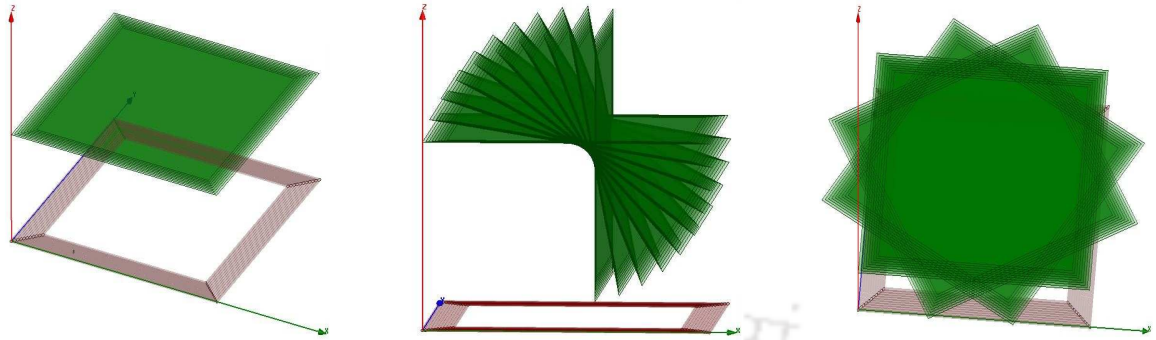

(a) (b) (c)

Figure 4.7: FEA models of square coils for different variations (a) vertical (b) angular (c) planar.

The flux linked in the OC due to EC is found by integrating the magnetic field over the area of OC using Maxwells field calculator. To ease the calculations script files are recorded and used for all the models. This type of coil arrangement and usage of script files is more convenient and simple to evaluate the flux linked in the OC. This avoids creating the model every time for various angles or distance. Figure 4.7(a) shows the side view of the vertical variation of the square coil at a particular distance. The fan shaped arrangement shown in Figure 4.7(b) is the side view of the angular variation of the coil. Here the OC is placed for a range of angles from 0° to 90° at an interval of 10° at certain vertical height. Figure 4.7(c) depicts the top view of OC placement of planar variation rotated along its axis at various angles. The angle between two adjacent positions of OC is 15°. Figure 4.8 shows the 2D plot of magnetic field lines of EC and OC having four conductors each. Figure 4.8(a) shows two positions of vertical variation of OC at small and large distances. Figure 4.8(b) shows two positions of angular variation of OC at 0° and 45° angles. As it can be seen from the plots, the magnetic field lines crossing the OC are less when the coils are away as compared to the coils placed near to EC.

4.5 Experimental verification

In order to verify the analytical and FEA results an experimental setup is built in the laboratory. The circuit topology and its control blocks are shown in Figure 4.9 and Figure 4.10. Table 4.2 shows the specifications of the components used for evaluation.

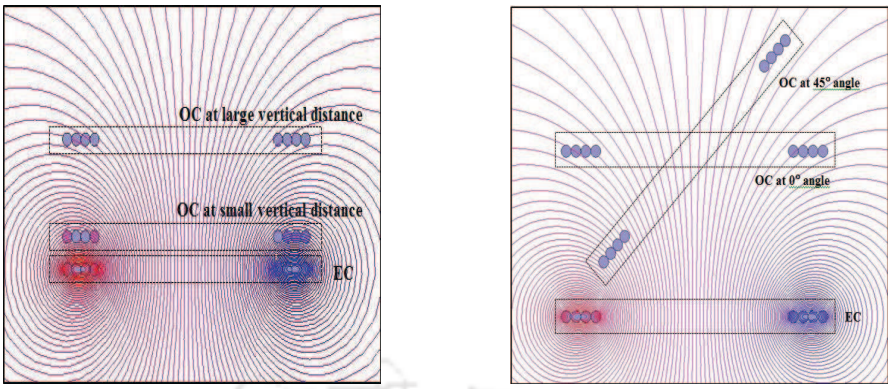

(a) (b)

Figure 4.8: Magnetic field lines for cut section of coils (a) vertical (b) angular

Table 4.2: Specifications of the components

symbol	Description	Values
V_{dc}	DC supply	0-30V
L_p	Inductance of EC	54μH
L_s	Inductance of OC	37μH
f	Frequency	18kHz
C_f	Filter capacitor	1.44μF
W	Width of the coil	18cm
L	Length of the coil	18cm
N_p	Number of turns in EC	11
N_s	Number of turns in OC	9

4.5.1 Description of power circuit and control circuit

The coils are accommodated in the flat planar surface without overlapping each other. The excitation circuit is made of a simple MOSFET based converter to convert dc voltage to high frequency ac voltage. The LC tank circuit shapes the voltage waveform and obtains an alternating voltage of resonant frequency across the coil to produce a variable magnetic field. The harmonics in the circuit are filtered by parallel LC resonance circuit. The filter capacitor has been calculated using the formula given by (4.11).

$$C_f = \frac{1}{\omega^2 L_p} \tag{4.11}$$

A PWM based gate control circuit is used for controlling the power circuit. For achieving the fast turn on and off, a carrier signal of 18 kHz frequency is used, as the coil requires high frequency source to energize it. The control blocks used for triggering the power circuit is shown in Figure 4.10.

The control circuit is fed with 15V supply, the carrier signal ($V_{carrier}$) of 18kHz is compared with the reference voltage (V_{ref}) and pulses are generated to trigger the MOSFET.

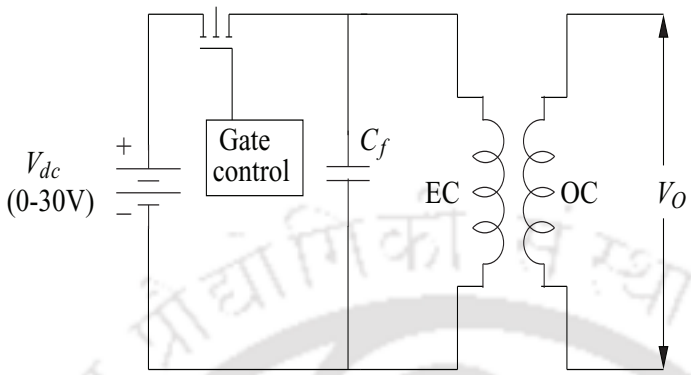

Figure 4.9: Schematic representation of power circuit.

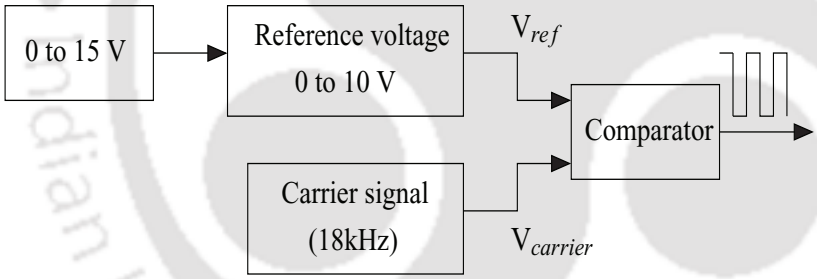

Figure 4.10: Controller blocks.

4.5.2 Experimental details

For the complete experiment, EC is fixed on the flat planar surface. The various positions of OC are observed with the help of wooden staffs. The details of experimental setup for different variations are briefly explained below:

- For vertical variation, the arrangement in wooden staff is made to vary the distance between OC and EC.

- For planar variation, the whole supporting system of wooden staff is rotated in a circle around

EC.

- For lateral variation, the wooden staff arrangement is made such that OC can be moved over the wooden staffs horizontally.
- For angular misalignment, OC is fixed in a supporting rod above EC at a vertical height and tilted.

In similar way, the other variations are observed. Figure 4.11 shows the complete hardware arrangement made for the experimental evaluation of MI. The geometry developed in the laboratory has taken multiple turns of EC and OC into account. Both the coils are wounded in a same manner and there is an insulation layer to separate the two conductors. Both the coils are made of copper conductors with a diameter of 1.83mm.

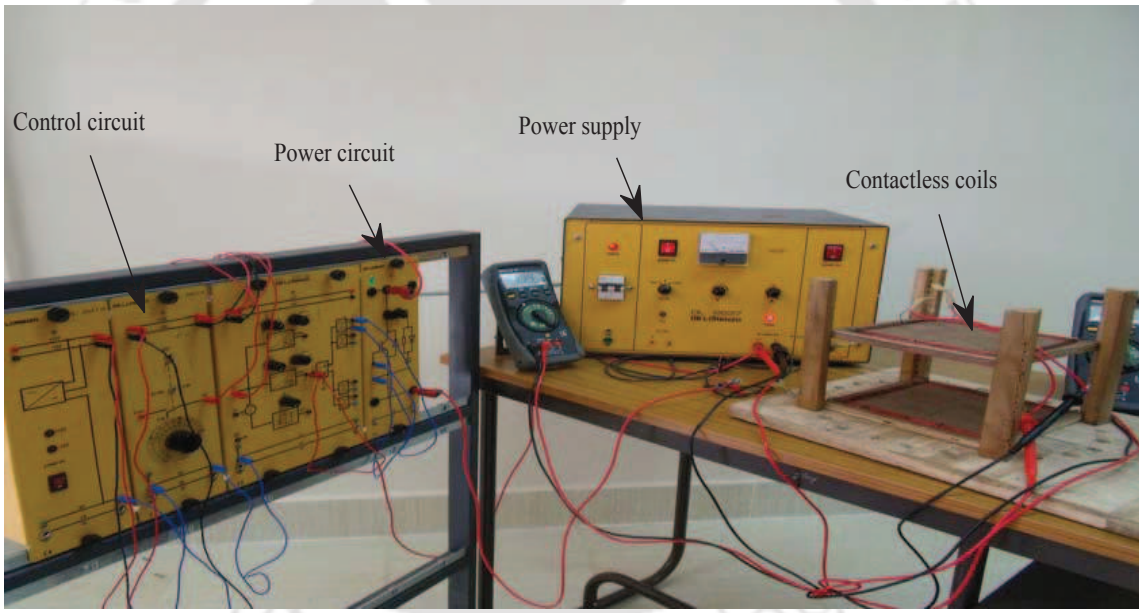

Figure 4.11: Experimental setup for mutual inductance computation.

The conductors of the coils are placed such that there is no space between the conductors of any two loop and they are not touching each other. The conductors are spread in a distance of 1.98cm and 1.65cm for EC and OC. The inner area which is not occupied by the conductor is 197.12cm^2 and 216.27cm^2 for EC and OC respectively. The experimental setup built is made to analyze all possible position of the coil including lateral and angular misalignments. The schematics of different variations are shown in Figure 4.12. The details of numerical results obtained for various positions of OC and the

comparison of results are described in Section 4.6. The formula used for experimental computation of MI is given by (4.12).

$$MI = \frac{V_{OC}}{V_{EC}} L_p \tag{4.12}$$

Where, V_{EC} and V_{OC} are the voltages obtained across EC and OC.

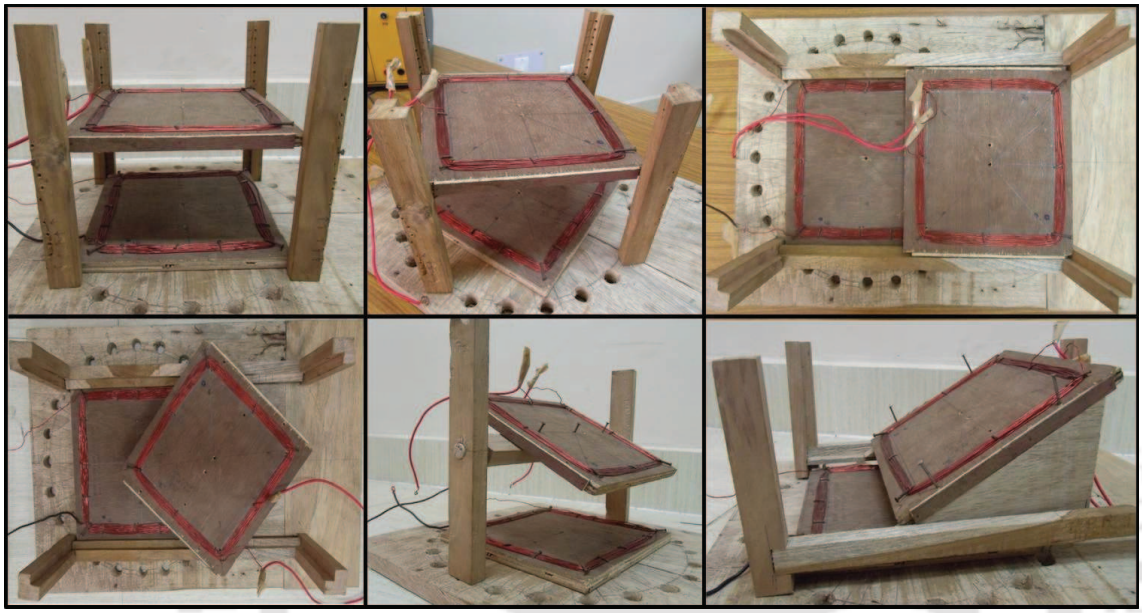

Figure 4.12: Experimental setup showing variations of coils.

4.6 Numerical results and discussion

The numerical results obtained from three analysis such as analytical method, finite element model and an experimental setup has been analyzed and compared throughout the sections. The numerical results of the three analyzes are given in Table 4.3 - 4.7 and the graphical representation are given in Figure 4.13 - 4.18. In order to compare the results, this study has considered the following general points:

- Maximum and minimum variations in vertical distance between EC and OC have been taken as 10cm and 2 cm.
- Maximum and minimum variation in horizontal direction have been taken as 11.4cm and 0cm.
- The maximum rotational variation considered is 90°. This is because the MI value would be repetitive for square geometry for angle beyond 90°.

- The vertical and horizontal distances are increased by 1cm for subsequent observations.
- The planar variation is recorded for a sequence of angles at an interval of 10° while, due to practical constraints the experimental readings are recorded for a step of 15° change.

4.6.1 Perfect alignment - vertical and planar variation

In this part, the numerical results for perfectly aligned vertical and planar variation for all three analysis are summarized and compared. Table 4.3 shows the numerical results of both vertical and planar variations. Figure 4.13 and Figure 4.14 shows the corresponding graphical plots.

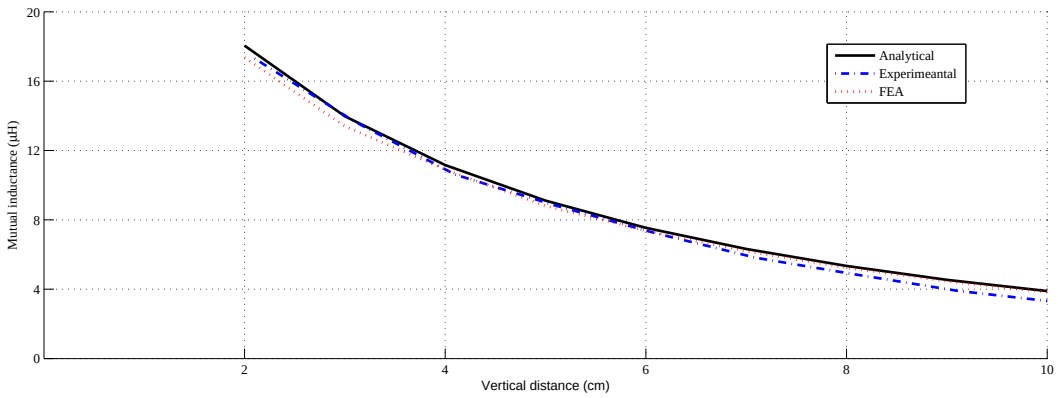

Figure 4.13: Perfect alignment - vertical variation.

In case of PA - vertical variation, numerical results are obtained for every 1cm distance between OC and EC vertically. The MI values are high for initial distance and rapidly decreases with increase in vertical distance between the coils.

Table 4.3: Perfect alignment - vertical and planar variation

vertical variation				planar variation				
distance (cm)	FEA (μH)	analytical (μH)	practical (μH)	angle (θ)	FEA (μH)	analytical (μH)	practical degree	(μH)
2	17.36	18.05	17.31	0	17.4	17.56	0	17.69
3	13.40	13.97	13.66	10	16.9	17.05	15	16.87
4	10.90	11.16	10.61	20	15.9	16.11	30	15.66
5	8.80	9.11	8.83	30	15.3	15.36	45	15.32
6	7.37	7.54	7.23	40	14.9	14.96	60	15.88
7	6.19	6.32	5.81	50	14.9	14.96	75	17.09
8	5.24	5.34	4.84	60	15.3	15.36	90	18.38
9	4.46	4.54	3.91	70	15.9	16.11		
10	3.83	3.89	3.26	80	16.9	17.05		
				90	17.4	17.56		

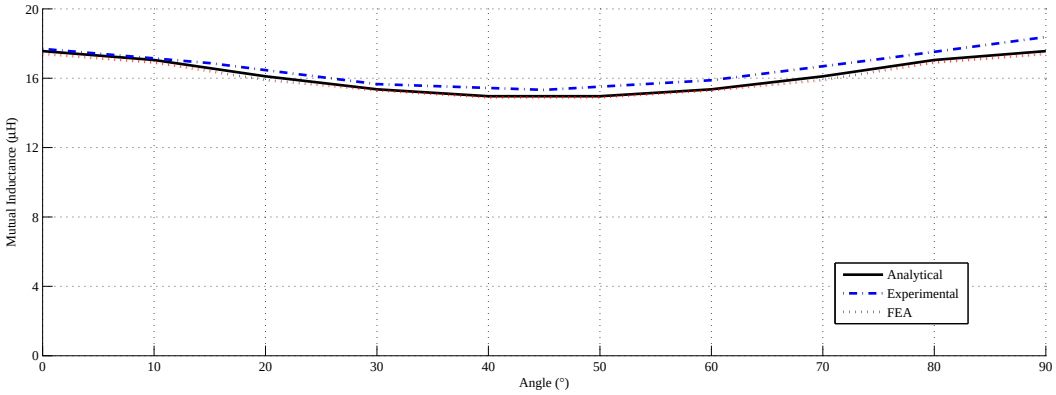

Figure 4.14: Perfect alignment - planar variation.

In case of PA - planar variation, the OC is placed at a height of 2.1cm and the observations are done by rotating OC along its axis. For FEA and analytical calculations, the observations are recorded for a sequence of angles at an interval of 10° variation, while due to practical limitation a step of 15° is chosen for experimental analysis. It has been observed from both numerical results and graphical plots, there is only marginal variation of MI with rotation of OC. This is because the overlapping area of the coil does not vary much with rotation of OC and the distance between the coils is kept constant.

4.6.2 Lateral misalignment - horizontal and planar variation

In this part, the numerical results for laterally misaligned case of horizontal and planar variation for all three analysis are summarized and compared. Table 4.4 shows the numerical results of both horizontal and planar variations. Figure 4.15 and Figure 4.16 shows the corresponding graphical plots.

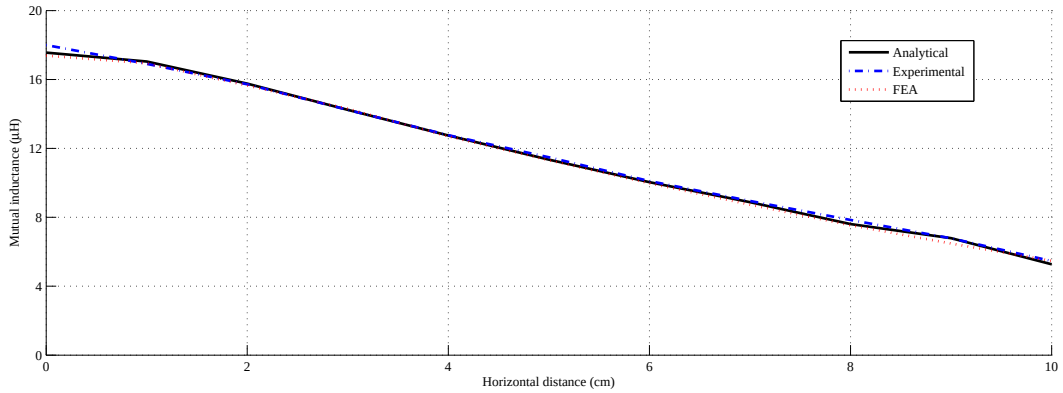

Figure 4.15: Lateral misalignment - horizontal variation.

In case of LM - horizontal variation, numerical results are obtained for every 1cm distance between OC and EC horizontally. The MI values are high for initial distance and rapidly decreases when OC is moved away horizontally from EC.

Table 4.4: Lateral misalignment - horizontal and planar variation

horizontal variation				planar variation				
distance (cm)	FEA (μH)	analytical (μH)	practical (μH)	angle (θ)	FEA (μH)	analytical (μH)	practical degree	(μH)
0	17.39	17.56	18.00	0	11.34	11.35	0	11.43
1	16.94	17.04	16.91	10	11.27	11.29	15	11.57
2	15.65	15.76	15.72	20	11.12	11.14	30	11.22
3	14.30	14.24	14.24	30	11.02	11.02	45	11.09
4	12.70	12.75	12.76	40	10.95	10.96	60	11.19
5	11.31	11.35	11.49	50	10.95	10.96	75	11.53
6	9.98	10.04	10.10	60	11.02	11.02	90	11.50
7	8.74	8.88	8.95	70	11.12	11.14		
8	7.54	7.61	7.85	80	11.27	11.29		
9	6.48	6.79	6.78	90	11.34	11.35		
10	5.47	5.27	5.46					

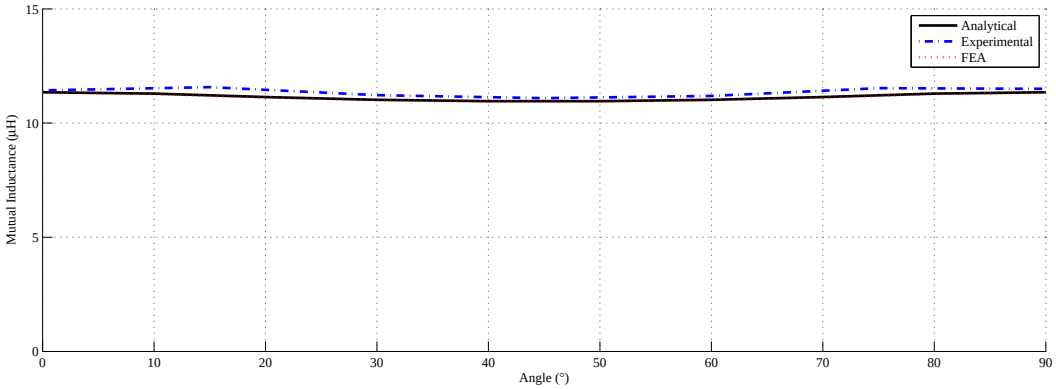

Figure 4.16: Lateral misalignment - planar variation.

In case of LM - planar variation, the OC is placed at a height of 2.1cm and fixed at a horizontal distance of 5cm. The observations are done from the displaced point by rotating OC along its axis. It has been observed from the results, there is only marginal variation of MI with rotation of OC. However, the magnitude of MI values got decreased from the PA - planar case. This is because the overlapping area in the former case is more than the later. Additionally, it can also be inferred from the results for larger horizontal distance, MI values would have further decreased.

4.6.3 Angular misalignment

In this part, the numerical results for angular misalignment for all three analysis are summarized and compared. Table 4.5 shows the numerical result of angular misalignment. Figure 4.17 shows the corresponding graphical plot.

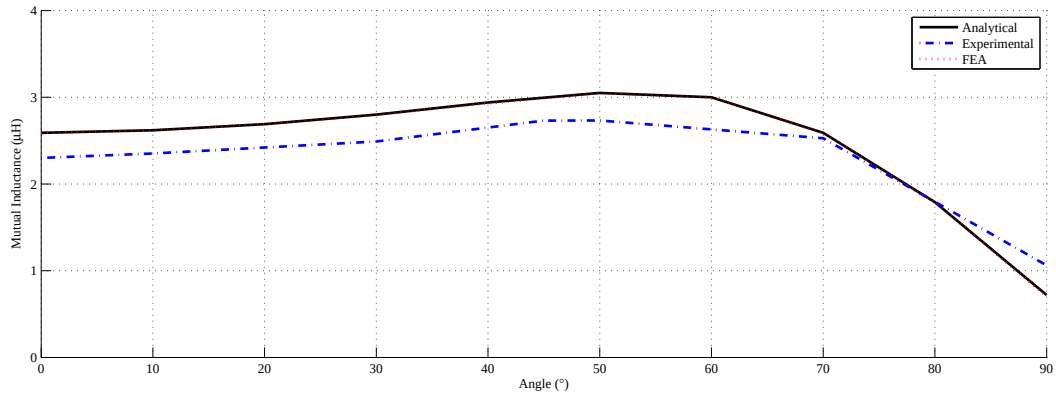

Figure 4.17: Angular misalignment - angular variation.

In case of angular misalignment, OC is placed in a rod of 0.60cm diameter and 12.8cm vertical height. Numerical values are noted by varying OC along with the rod for angles between 0° to 90°. The variation in MI is found to be marginal due to less change in overlapping area from 0° to 60°. As OC goes beyond 60°, it comes almost perpendicular to EC and due to this overlapping area decreases and MI value falls down drastically.

Table 4.5: Angular misalignment

distance (cm)	FEA	analytical	practical	
(θ)	(μH)	(μH)	degree	(μH)
0	2.59	2.59	0	2.30
10	2.62	2.62	10	2.35
20	2.69	2.69	30	2.49
30	2.80	2.80	45	2.73
40	2.93	2.94	50	2.73
50	3.05	3.05	70	2.53
60	3.00	3.00	90	1.06
70	2.59	2.59		
80	1.79	1.79		
90	0.70	0.72		

4.6.4 Both lateral and angular misalignment

In this part, the numerical results for a general case of both lateral and angular misalignment for all three analysis are summarized and compared. The variation in this case is observed by keeping

constant angle and moved horizontally. Thus, three different angles (10°, 20° and 30°) are chosen and its variations are observed. Table 4.6 and Table 4.7 shows the numerical results of both lateral and angular misalignment. Figure 4.18 shows the corresponding graphical plots.

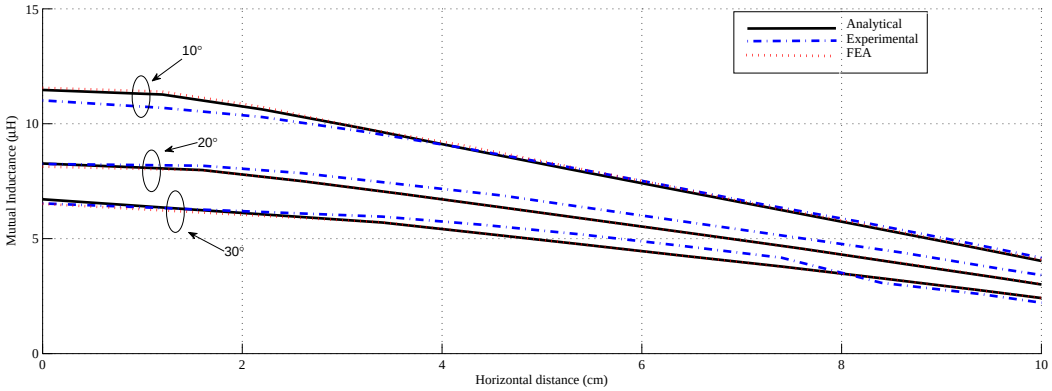

Figure 4.18: Both lateral and angular misalignment (angle = 10°, 20°, 30°).

The magnitude of MI value is more for 10° angle and with increase in angle, MI value decreases. However, MI value falls sharply when OC is horizontally moved away from EC.

Table 4.6: Both lateral and angular misalignment (angle = 10° and 20°

	angle 10°				angle 20°		
distance (cm)	FEA (μH)	analytical (μH)	practical (μH)	distance (cm)	FEA (μH)	analytical (μH)	practical (μH)
0	11.56	11.47	11.02	0	8.13	8.27	8.25
1.2	11.40	11.27	10.69	1.6	7.98	7.98	8.17
2.2	10.73	10.62	10.29	2.6	7.51	7.50	7.85
3.2	9.81	9.81	9.66	3.6	6.94	6.94	7.36
4.2	9.07	8.94	8.96	4.6	6.35	6.36	6.87
5.2	8.20	8.09	8.17	5.6	5.76	5.76	6.25
6.2	7.34	7.24	7.35	6.6	5.17	5.17	5.63
7.2	6.44	6.41	6.50	7.6	4.56	4.56	5.01
8.2	5.63	5.57	5.72	8.6	3.94	3.92	4.40
9.2	4.75	4.72	4.87	9.6	3.29	3.28	3.68
10.2	3.91	3.85	3.99	10.6	2.62	2.60	3.01

Table 4.7: Both lateral and angular misalignment (angle = 30°)

distance (cm)	FEA (μH)	analytical (μH)	practical (μH)
0	6.51	6.71	6.53
3.4	5.71	5.70	5.96
4.4	5.23	5.23	5.60
5.4	4.75	4.75	5.18
6.4	4.26	4.26	4.69
7.4	3.78	3.79	4.17
8.4	3.28	3.28	3.08
9.4	2.75	2.75	2.58
10.4	2.19	2.19	1.96
11.4	1.59	1.59	1.37

It has been noticed from the Figure 4.13 - Figure 4.18, the value computed in all the three cases are in good agreement. However, in some cases there is a slight difference in values between experimental and calculated (analytical and FEA) results. This is due to the error in measuring the geometrical parameters such as vertical height, horizontal distance and rotational angle. As an example of a case of both lateral and angular variation, where the coil has 10° angle shift at 1.2cm distance, MI value obtained is 12.18μH and at 11° angle it has a value of 11.26μH. Thus, there is 7.5% error occurred due to error of 1° in angle measurement.

4.7 Conclusions

In this chapter, an analytical method based on Biot-Savart law has been presented for estimating the MI between two air core square coils. A spiral square coil is modeled and MI is calculated. Different misalignment cases of contactless and its variations are analyzed. The analysis compares the analytical, FEA and experimental results in all misalignment cases. The analytical and FEA results show a very good agreement and experimental results has an error less than 10%. The following conclusions are drawn from the work:

- When the coils are placed close to each other with coinciding axes, MI values are maximum; which indicates high coupling between the coils and expected to have maximum power transfer in CPT systems.

- At large coil distances, relatively large horizontal and vertical misalignments; MI have no sig-

nificant effects. This indicates relatively low coupling in CPT system and it would not transfer any power.

- In case of planar variation MI value would vary marginally. Such type of variation would not affect the power transfer in CPT systems.
- An interesting behavior of MI is observed in angular misalignment, tilting OC at certain angle brings half of the coil closer to the perimeter of EC and due to this MI value increases and for other angles, MI values would suddenly decrease. Such type of variations in practical systems would cause instability.

From the results it has been noticed; larger the distance between EC and OC, lowers the coupling coefficient and MI value. This is due to large leakage inductance and reduced magnetizing inductance. Hence, compensation elements can be used on both sides of contactless coils to improve the MI value and to increase the power transfer capability. The next chapter has analyzed the use of four such compensation topologies in contactless system.

5

Compensation Topologies for Contactless System

Contents

5.1	Introduction	103
5.2	Steady state electric circuit analysis	106
5.3	Description of experimental set-up	117
5.4	Results and discussion	124
5.5	Conclusions	137

Abstract

Due to large leakage inductance, compensations circuits are necessary in contactless system to achieve the required power transfer. This chapter presents an experimental study of four compensation topologies connected on both sides of coils suitable for use in contactless charging system applications. Primary compensation is designed to make the primary phase angle equal to the secondary resonant frequency with minimum VA rating of the power supply. Secondary compensation is designed to increase the power transfer capability. Equivalent circuit models are used to explain the theory of contactless system with analytical expressions for voltage, current and impedance as well as the power transfer efficiency, by combining the primary and secondary network is detailed. The study investigates the behavior of compensation circuits in contactless system under variable frequency, load and distance and its characteristics plots are generated. The analysis compares the efficiency of four compensation topologies such that the real time performance of CPT systems can be analyzed. With these results obtained from the experiments, the theory of CPT systems can be well understood and it provides a foundation for future design and implementation of CPT systems.

The work presented in this chapter is accepted for publication in [133, 134] and submitted in [135, 136].

5.1 Introduction

The energy supply in electrical system is commonly realized by conventional plug and socket connectors and the power transfer equipment is one of the important subsystems. The traditional conductive wired systems cannot keep up with the present demands of customers in safety and simplicity [137]. With the developments in power electronics, CPT system has found much success due to its simplicity, size and reliability [29], which has been explained in chapter I. The principle of CPT system is similar to a conventional transformer, where the magnetic field is confined to a particular core. In contrast to conventional transformer, contactless transformer has a large air-gap and are used without high permeability common magnetic core [31]. This technology utilizes magnetic filed around a current carrying wire to magnetically couple power across large air-gap through weak magnetic coupling. Due to this large air-gap, the characteristics of contactless system has large leakage inductance and reduced magnetizing inductance and low efficiency as compared to conductive wired systems. To

compensate large leakage inductance problem effectively, suitable compensation circuit can be added by connecting a series or parallel capacitor at the primary and secondary winding of the coil as shown in Figure 5.1 [71]. This makes the contactless circuit to operate at resonance and achieves maximum output power with minimum input VA rating of the power supply.

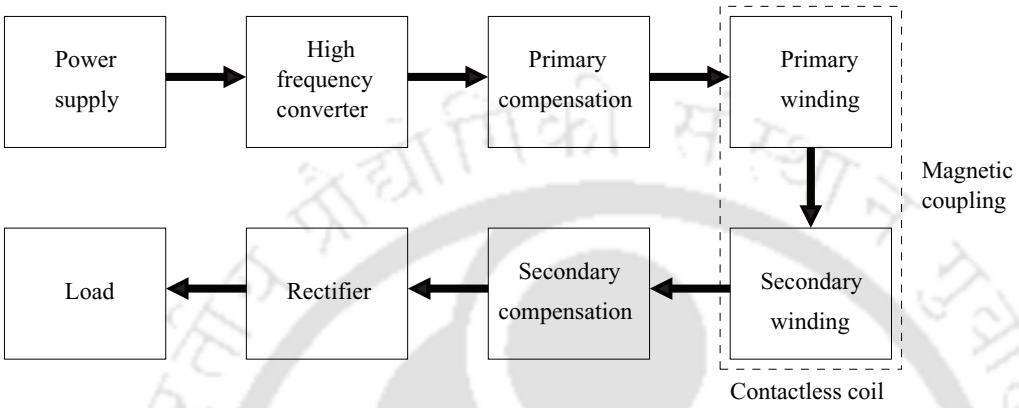

Figure 5.1: Block diagram of contactless system with compensation.

In addition, there could be an application where the system is connected to the variable load and the secondary side of the coil must be moved with the primary coil [32, 36, 37]. In such cases, the leakage inductance of the coils are larger than the magnetizing inductance leading to inefficient power transmission. CPT systems basically has a high frequency power converter to feed the coil at the input side and a rectifier in the secondary side connected to the load. The specifications of converter, controllers and its parameters differs for each applications. The frequency of the power supply should be controlled to attain a zero phase angle between the voltage and current at the input side of the coil [35]. Therefore, the role of compensations circuits in CPT systems and its impact for variations in parameters must be studied which is the first step in the design of such systems.

There are many applications of CPT systems exists in the literature. Power conversion methods and controllers of CPT system are reported in [29,107,109,138–140], while other researches have worked on the design of magnetic coupling structures [137,141]. Many other works have paid attention on the design of contactless coil [23, 45]. A very few works have studied compensation circuits in contactless system. Optimized design procedures are given to select the suitable compensation topology for efficient power transfer [23, 31, 36, 45]. In [34, 35, 142, 143], CPT model is analyzed to investigate

the sensitivity of the system for variation in operational frequency and load. In [22] and [143], an occurrence of bifurcation due to multiple operating modes in CPT system have been studied using higher order mathematical models. Few other works have studied the power transfer capability of contactless systems using compensation circuits [144, 145]. However, a very few works have studied the impact of system parameters in CPT systems. Among those, the most critical parameters are frequency, load, low magnetizing inductance and high leakage inductance. It has been found, there are no experimental investigation done so far to analyze the power transfer capability and controllability of the system. In this chapter, an experimental investigation have been done with four compensation

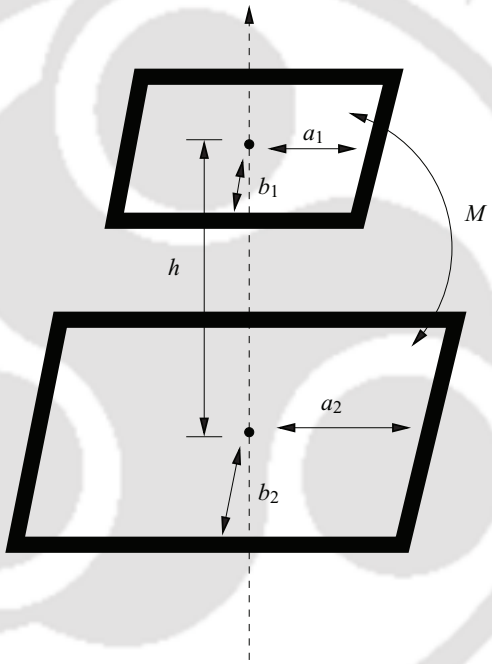

Figure 5.2: Coil topology.

topologies using rectangular primary (18cm × 14.5cm) and secondary coil (19cm × 11cm) shown in Figure 5.2. The primary side and secondary side of the coil is examined with both series and parallel compensation circuits. Series compensated primary is chosen to reduce the primary voltage level, while a parallel compensated secondary is able to supply a stable current. A series compensated secondary can supply a stable voltage, while a parallel compensated secondary is able to supply a stable current. Of particular interest, this work has studied the impact of compensation circuits for variation in frequency, distance and load; so that the practical behavior of CPT system can be visualized. The

analysis have been carried out by fixing the number of turns in primary and secondary side. Other prefixed parameters in this study are coil shape, dimensions of the coil and circuit topology. The variable parameters are air gap distance, operating frequency and load. Skin effect is not considered because both coils are wound using multi-strand copper wire. Electric equivalent circuit models of different compensation topologies are developed to explain the mechanism of power transfer. The performance of four compensation topologies are validated and its results are analyzed. The analysis compares the efficiency of four basic topologies of CPT system with variation in frequency, distance and load.

The rest of the chapter is organized as follows: Section 5.2 describes the steady state electric circuit analysis. Section 5.3 presents the description of experimental set-up. Finally, experimental results are presented in Section 5.4 and its conclusions are given in Section 5.5.

5.2 Steady state electric circuit analysis

For the purpose of mathematical analysis, the steady state behavior of air core transformer with a large air gap can be described by an equivalent circuit. An electric equivalent circuit makes the process of network analysis easier. CPT system combines two coupled primary and secondary windings, similar to a conventional transformer. Unlike transformer windings, contactless systems are usually loosely coupled without any common magnetic core. Hence, contactless system has large leakage inductance and therefore, compensations are required on both sides of the coils.

5.2.1 Compensation topologies

The purpose of compensation capacitors in contactless system is to increase its efficiency. Compensation capacitors are connected on both sides of primary and secondary windings of contactless coils. The purpose of primary compensation is to decrease the VA rating of the power supply and thereby ensuring power transfer at unity power factor and the purpose of secondary compensation is to enhance the power transfer capability. The primary compensation is chosen such that the impedance as seen from the source side is purely resistive in nature so as to ensure that the high frequency inverter which acts as the primary power source has minimum possible VA rating of the power supply. Four such compensation topologies are described in this chapter. Four compensation topologies are represented as SS, SP, PS and PP topology as shown in Figure 5.3, where 'S' stands for series connected topology and 'P' stands for parallel connected topology. Hence, series-series is named as SS topology,

series-parallel as SP topology, parallel-series as PS topology and parallel-parallel as PP topology. In Figure 5.3, I_1, I_{L1}, I_{C1} denotes supply current, inductor current and capacitor current of the primary side and I_{L2}, I_{C2} and I_L represents inductor current, capacitor current and load current of secondary side respectively. Similarly, L_1, C_1 and V_1 denotes inductor, capacitor and supply voltage in the primary side and L_2, C_2 and R_L denotes inductor, capacitor and load resistance in the secondary side respectively. The main criteria to increase the power transfer capability in all compensation is that

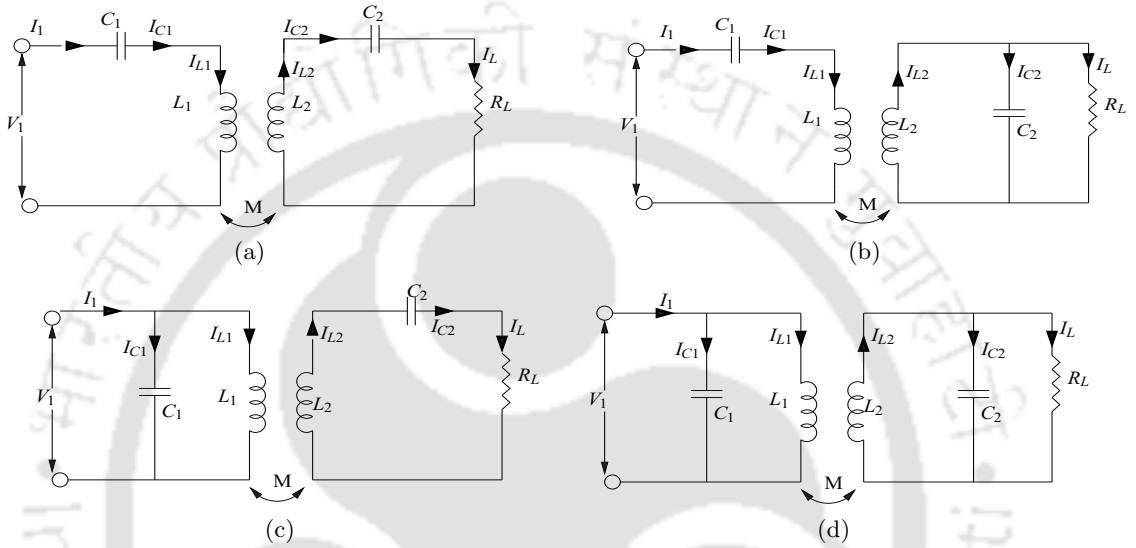

Figure 5.3: Equivalent circuit model of contactless coils (a) SS topology (b) SP topology (c) PS topology (d) PP topology.

the primary side of the system should operate at secondary side resonance frequency. When operating at secondary resonance frequency, the self inductance of the secondary winding is fully compensated by the primary compensation capacitance. Therefore, the impedance of the secondary as seen by the primary is purely resistive in nature. Thus, these capacitors essentially store and supply reactive power to and from the secondary and primary windings, reducing the amount of reactive power drawn from the supply.

5.2.2 Mutual inductance coupling model

The coupling between the primary and secondary coil and its operation can be analyzed using several modeling methods. Among various modeling methodologies, transformer model and mutual inductance coupling model are the most commonly used methods. The transformer model uses the concept of transformed voltage and reflected current to describe the coupling effects. The transformed voltage and reflected currents are simply defined by the turns ratio. Here, the coupling and leakage

inductance must be separated by circuit analysis. This coupling model is well suited for closely coupled CPT systems because the leakage inductance is usually negligible. In contrast, mutual inductance coupling model uses the concept of induced and reflected voltages to describe the coupling effect between the primary and secondary networks. Both the induced and reflected voltages are expressed in terms of the mutual inductance. This model does not require the coupling and leakage inductance to be separated for circuit analysis. Hence this model is well-suited for loosely coupled CPT systems, where the leakage inductance is too large to be ignored. In this chapter, mutual inductance model is used to analyze the coupling between the primary and secondary coils of CPT systems. The effect of the secondary must be considered together with the primary winding in the analysis of the primary network. Therefore, the effect of secondary can be represented by the equivalent reflected impedance. Compensation elements are required to compensate leakage inductance of the coil. The compensation elements can be connected in series or parallel on primary and secondary sides of the coil. For simplification purpose, neglecting coil resistances, the analysis of four compensation topologies using mutual inductance coupling models are presented in the following section.

5.2.3 Series-series (SS) compensation topology

Assuming all currents are sinusoidal, the steady state equations for primary and secondary series compensation can be written on phasor form as given by (5.1) and (5.2)

$$V_1 = I_1\left(\frac{1}{j\omega C_1}\right) + j\omega L_1 I_1 - j\omega M I_2 \tag{5.1}$$

$$j\omega M I_1 = j\omega L_2 I_2 + I_2\left(\frac{1}{j\omega C_2}\right) + I_2 R_L \tag{5.2}$$

where mutual inductance of the coil (M) is given by (5.3). From (5.1)-(5.2) it is observed, both the induced voltage and reflected voltage are represented in terms of mutual inductance (M) between the coils to describe the coupling effect between the primary and secondary network. The mutual inductance can be related with the magnetic coupling (k) as given by (5.3).

$$k = \frac{M}{\sqrt{L_1 L_2}} \tag{5.3}$$

The magnetic coupling of contactless coil is usually poor. In (5.3), the coupling between the primary and secondary of the coil depends on the leakage inductance (L_1, L_2) and magnetizing inductance (M). The leakage inductance in contactless coil is much larger than the magnetizing inductance. On

simplifying (5.2), current I_2 in series secondary coil can be written as (5.4).

$$I_2 = \frac{j\omega M I_1}{\left[j\omega L_2 + \left(\frac{1}{j\omega C_2}\right) + R_L\right]} \tag{5.4}$$

On substituting secondary side current I_2, given in (5.4) into (5.1), we get:

$$V_1 = I_1\left(\frac{1}{j\omega C_1}\right) + j\omega L_1 I_1 + \left(\frac{\omega^2 M^2}{j\omega L_2 + \left(\frac{1}{j\omega C_2}\right) + R_L}\right) I_1 \tag{5.5}$$

It can be observed from (5.5), from the point of view of the first coil, the secondary coil is seen as a transformed impedance or reflected impedance (Z_r) of the secondary network as seen from the primary side. Hence, for series compensated secondary:

$$Z_{r\_SS} = \frac{\omega^2 M^2}{\left[j\omega L_2 + \left(\frac{1}{j\omega C_2}\right) + R_L\right]} = \frac{\omega^2 M^2}{{Z_2}^S} \tag{5.6}$$

where, ${Z_s}^S$ is the secondary side impedance. The total impedance (Z_t) for series and parallel compensated system seen by the power supply is obtained from (5.5) is given by (5.7).

$$Z_{t\_SS} = \left(\frac{1}{j\omega C_1}\right) + j\omega L_1 + \frac{\omega^2 M^2}{j\omega L_2 + \left(\frac{1}{j\omega C_2}\right) + R_L} \tag{5.7}$$

Now the simplified version of contactless system is shown in Figure 5.4(a) and Figure 5.4(b) Therefore,

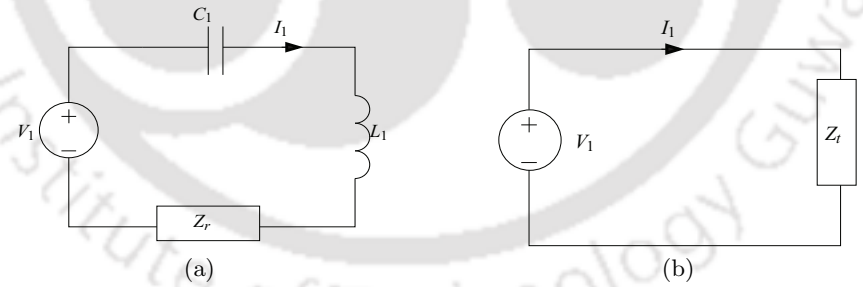

Figure 5.4: Simplified equivalent circuit (a) with reflected impedance (b) with total impedance.

the current observed from the source is given by (5.8).

$$I_1 = \frac{V_1}{Z_{t\_SS}} \tag{5.8}$$

In order to obtain high power transfer capability, the operating frequency of the system should be equal to the secondary resonant frequency (ω_o), which is given by (5.9)

$$\omega_o = \frac{1}{\sqrt{L_2 C_2}} \tag{5.9}$$

On substituting (5.9) into (5.6), we get the reflected impedance as given by (5.10).

$$Z_{r\_SS} = \frac{{\omega_o}^2 M^2}{R_L} = \frac{{\omega^2}_o M^2}{{Z_s}^S} \tag{5.10}$$

It can be observed from (5.10), if the secondary is series compensated Z_{r_SS} is purely resistive. Thus to obtain high efficiency, the primary side of the system should operate at resonance frequency of the secondary side of the system. Therefore for SS compensation, C_1 and C_2 can be given by (5.11).

$$C_1 = \frac{1}{{\omega_o}^2 L_1} \quad ; \qquad C_2 = \frac{1}{{\omega_o}^2 L_2} \tag{5.11}$$

Then, the total impedance of the system is given by (5.12).

$$Z_{t\_SS} = \frac{{\omega_o}^2 M^2}{R_L} \tag{5.12}$$

On substituting (5.11) into (5.2), the relation between I_2 and I_1 can be obtained, where I_2 leads I_1 at some angle.

$$\frac{I_2}{I_1} = \frac{j\omega_o M}{R_L} \tag{5.13}$$

$$I_2 = G_1 I_1 \, ; \quad G_1 = \frac{j\omega_o M}{R_L} \tag{5.14}$$

Using (5.1) - (5.14), the input power (P_i), output power (P_o) and total efficiency of the system are calculated.

$$P_i = {I_1}^2 Z_{t\_SS} \tag{5.15}$$

$$P_o = I_2^2 R_L = G_1^2 I_1^2 R_L \tag{5.16}$$

Using these equations, efficiency for SS compensation is given by (5.17).

$$\eta_{SS} = \frac{{G^2}_1 R_L}{Z_{t\_SS}} \tag{5.17}$$

5.2.4 Series-parallel (SP) compensation topology

The steady state equations for primary series and secondary parallel compensation can be written on phasor form as given by (5.18) and (5.19)

$$V_1 = I_1\left(\frac{1}{j\omega C_1}\right) + j\omega L_1 I_1 - j\omega M I_2 \tag{5.18}$$

$$j\omega M I_1 = j\omega L_2 I_2 + I_2\left(\frac{R_L\left(\frac{1}{j\omega C_2}\right)}{R_L + \left(\frac{1}{j\omega C_2}\right)}\right) \tag{5.19}$$

Similar to the procedure explained in Section 5.2.3, simplifying (5.19), current I_2 in parallel secondary coil can be written as (5.20).

$$I_2 = \frac{j\omega M I_1}{\left[j\omega L_2 + \left(\frac{R_L\left(\frac{1}{j\omega C_2}\right)}{R_L + \left(\frac{1}{j\omega C_2}\right)}\right)\right]} \tag{5.20}$$

By substituting secondary side current I_2, given in (5.20) into (5.18), we get

$$V_1 = I_1\left(\frac{1}{j\omega C_1}\right) + j\omega L_1 I_1 + \left(\frac{\omega^2 M^2}{j\omega L_2 + \left(\frac{R_L}{R_L j\omega C_2 + 1}\right)}\right) I_1 \tag{5.21}$$

It can be observed from (5.21), from the point of view of the first coil, the secondary side parallel compensated coil is seen as a transformed impedance or reflected impedance (Z_{r_SP}) of the secondary network as seen from the primary side. Therefore, Z_{r_SP} and Z_{t_SP} is given by (5.22) and (5.23).

$$Z_{r\_SP} = \frac{\omega^2 M^2}{\left[j\omega L_2 + \frac{R_L}{R_L j\omega C_2 + 1}\right]} = \frac{\omega^2 M^2}{{Z_2}^P} \tag{5.22}$$

$$Z_{t\_SP} = \frac{1}{j\omega C_1} + j\omega L_1 + \frac{\omega^2 M^2}{j\omega L_2 + \left(\frac{R_L}{j\omega C_2 R_L + 1}\right)} \tag{5.23}$$

The current observed from the source is given by (5.24)

$$I_{1\_SP} = \frac{V_1}{Z_{t\_SP}} \tag{5.24}$$

In order to obtain high power transfer capability, the operating frequency of the power supply should be equal to the secondary resonant frequency (ω_o) and the secondary side compensation capacitor C_2 is given by (5.25)

$$C_2 = \frac{1}{{\omega_o}^2 L_2} \tag{5.25}$$

When operating the CPT system at this frequency, the self inductance of the secondary winding is fully compensated by the primary compensation capacitor and therefore the impedance of the secondary as seen by the primary is purely resistive in nature. Therefore, on substituting (5.25) into (5.22) and (5.23), the secondary side impedance (${Z_2}^P$) and the reflected impedance (Z_{r_SP}) is given by (5.26) and (5.27).

$${Z_2}^P = \frac{{\omega_o}^2 {L_2}^2}{R_L - j\omega_o L_2} \tag{5.26}$$

$$Z_{r\_SP} = \frac{M^2 R_L}{{L_2}^2} - \frac{j\omega_o M^2}{L_2} \tag{5.27}$$

It can be observed from (5.27), if the secondary is parallel compensated it has a reactive component. This introduces a phase shift in the system. This phase shift ($\frac{-M^2}{L_2}$) should be compensated in the primary side of the system. For this reason, a large primary capacitance is usually used in parallel compensated CPT system. Therefore, in order to operate the SP compensated CPT system under resonance frequency and to obtain high efficiency, the compensated capacitors, C_1 and C_2 are given by (5.28).

$$C_1 = \frac{1}{{\omega_o}^2 \left(L_1 - \frac{M^2}{L_2}\right)} \quad ; \quad C_2 = \frac{1}{{\omega_o}^2 L_2} \tag{5.28}$$

The total impedance (Z_{t_SP}) at resonance is given by (5.29)

$$Z_{t\_SP} = \frac{M^2 R_L}{{L_2}^2} \tag{5.29}$$

On substituting (5.28) into (5.19), the relation between I_2 and I_1 can be obtained, where I_2 leads I_1 at some angle.

$$\frac{I_2}{I_1} = \frac{j\omega M}{\left(\frac{{\omega_o}^2 {L_2}^2}{R_L - j\omega_o L_2}\right)} \tag{5.30}$$

$$I_2 = G_2 I_1 = \frac{j\omega_o M \left(R_L - j\omega_o L_2\right)}{{\omega_o}^2 {L_2}^2} \tag{5.31}$$

Using (5.18) - (5.31), the input power (P_i), output power (P_o) and total efficiency of the system are calculated.

$$P_i = {I_1}^2 Z_{t\_SP} \tag{5.32}$$

$$P_o = I_2^2 R_L = G_2^2 I_1^2 R_L \tag{5.33}$$

Using these equations, efficiency for SP compensation is given by (5.34).

$$\eta_{SP} = \frac{{G_2}^2 {\omega_o}^2 {L_2}^2}{Z_{t\_SP}\left(R_L - j\omega_o L_2\right)} \tag{5.34}$$

5.2.5 Parallel-series (PS) compensation topology

The steady state equations for primary parallel and secondary series compensation can be written on phasor form as given by (5.35) and (5.36)

$$V_1 = I_{C1}\left(\frac{1}{j\omega C_1}\right) = I_{L1}j\omega L_1 - j\omega M I_2 \tag{5.35}$$

$$j\omega M I_{L1} = j\omega L_2 I_2 + I_2\left(\frac{1}{j\omega C_2}\right) + I_2 R_L \tag{5.36}$$

The secondary side current I_2 in PS compensation can be obtained from (5.37).

$$I_2 = \frac{j\omega M I_{L1}}{j\omega L_2 + \left(\frac{1}{j\omega C_2}\right) + R_L} \tag{5.37}$$

By substituting the secondary side current I_2, given in (5.37) into (5.35), we get

$$V_1 = j\omega L_1 I_{L1} + \frac{\omega^2 M^2}{j\omega L_2 + \left(\frac{1}{j\omega C_2}\right) + R_L} I_{L1} \tag{5.38}$$

As explained above, from the point of view of the first coil, the secondary coil is seen as a transformed impedance or reflected impedance (Z_{r_PS}) of the secondary network as seen from the primary side is given by (5.39).

$$Z_{r\_PS} = \frac{\omega^2 M^2}{\left[j\omega L_2 + \frac{1}{j\omega C_2} + R_L\right]} = \frac{\omega^2 M^2}{{Z_2}^s} \tag{5.39}$$

On substituting (5.37) in (5.35), the current through primary side inductor (I_{L1}) and capacitor (I_{C1}) is obtained.

$$I_{L1} = \frac{V_1}{j\omega L_1 + \frac{\omega^2 M^2}{{Z_2}^s}} \tag{5.40}$$

$$I_{C1} = \frac{V_1}{\frac{1}{j\omega C_1}} \tag{5.41}$$

From Figure 5.5, the total impedance (Z_{t_PS}) of the PS compensation is given by (5.42). The total

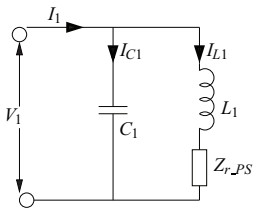

Figure 5.5: Parallel compensated primary.

current observed from the primary side is given by (5.43).

$$Z_{t\_PS} = \frac{1}{j\omega C_1 + \frac{1}{j\omega L_1 + Z_{r\_PS}}} \tag{5.42}$$

$$I_{1\_PS} = \frac{V_1}{Z_{t\_PS}} \tag{5.43}$$

To obtain high efficiency in PS compensated CPT system, the system should operate under resonance condition. The resonance capacitance for parallel and series compensated primary is same as the basic resonance condition as given by (5.44).

$$C_1 = \frac{1}{{\omega_o}^2 L_1} \tag{5.44}$$

On substituting (5.44) into (5.42), the total impedance at resonance condition is given by

$$Z_{t\_PS} = \frac{{Z_2}^S {L_1}^2}{M^2} - j\omega_o L_1 \tag{5.45}$$

It has been seen from (5.45) has some constraints on $({Z_2}^S)$ for the system to be in resonance. While for the system to be in parallel compensated, ${Z_2}^S$ has some resistive and reactive part, say

$${Z_2}^S = R_L + jX \tag{5.46}$$

The criteria for resonance is, the inductance due to parallel primary side should be compensated in the secondary side coil such that the primary side impedance is resistive in nature. This condition is achieved when the reactance is in the form given below:

$$X = \omega_o \frac{M^2}{L_1} \tag{5.47}$$

On substituting (5.46) in (5.42) and (Z_{t_PS}) can be obtained as given by (5.48)

$$Z_{t\_PS} = \frac{R_L {L_1}^2}{M^2} \tag{5.48}$$

Thus, when the primary side is parallel compensated a phase shift is introduced to the secondary side that brings the secondary side out of resonance. Therefore, the compensation capacitance in PS is defined as given below:

$$C_1 = \frac{1}{{\omega_o}^2 L_1}; \qquad C_2 = \frac{1}{{\omega_o}^2 \left(L_2 - \frac{M^2}{L_1}\right)} \tag{5.49}$$

Using these condition (5.49), the secondary side impedance (${Z_2}^S$) given in (5.39) can be given by (5.50).

$${Z_2}^S = j\omega_o \frac{M^2}{L_1} + R_L \tag{5.50}$$

The secondary current (I_2) can be given in (5.36) can be modified by substituting I_{L1} and ${Z_2}^S$ given in (5.50) and (5.40). Therefore, I_2 at resonance can be written as given by (5.51). The primary current (I_1) can be written as given by (5.52).

$$I_2 = \frac{M}{L_1 R_L} V_1 \tag{5.51}$$

$$I_1 = \frac{M^2}{R_L {L_1}^2} V_1 \tag{5.52}$$

Using (5.37) and (5.52), the input power (P_i), output power (P_o) and total efficiency of the system are calculated.

5.2.6 Parallel-parallel (PP) compensation topology

The steady state equations for primary and secondary parallel compensation can be written on phasor form as given by (5.53) and (5.54)

$$V_1 = I_{C1}\left(\frac{1}{j\omega C_1}\right) = I_{L1} j\omega L_1 - j\omega M I_2 \tag{5.53}$$

$$j\omega M I_{L1} = j\omega L_2 I_2 + I_2 \left(\frac{1}{\frac{1}{\left(\frac{1}{j\omega C2}\right)} + \frac{1}{R_L}}\right) \tag{5.54}$$

The secondary side current I_2 in PP compensation can be obtained from (5.55).

$$I_2 = \frac{j\omega M}{\left(j\omega L_2 + \frac{R_L}{R_L j\omega C_2 + 1}\right)} I_{L1} = \frac{j\omega M}{{Z_2}^p} I_{L1} \tag{5.55}$$

By substituting the secondary side current I_2 (given in (5.55)) into (5.53) we get:

$$V_1 = j\omega L_1 I_{L1} + \left(\frac{\omega^2 M^2}{j\omega L_2 + \frac{R_L}{R_L j\omega C_2 + 1}}\right) I_{L1} \tag{5.56}$$

As explained above, from the point of view of the first coil, the secondary coil is seen as a transformed impedance or reflected impedance (Z_{r_PP}) of the secondary network as seen from the primary side and is given by (5.57).

$$Z_{r\_PP} = \frac{\omega^2 M^2}{j\omega L_2 + \frac{R_L}{j\omega C_2 R_L + 1}} = \frac{\omega^2 M^2}{{Z_2}^p} \tag{5.57}$$

From (5.56), the current through primary side inductor (I_{L1}) and capacitor (I_{C1}) is obtained. The total impedance (Z_{t_PP}) of PP compensation is given by (5.60).

$$I_{L1} = \frac{V_1}{j\omega L_1 + \frac{\omega^2 M^2}{{Z_2}^p}} \tag{5.58}$$

$$I_{C1} = \frac{V_1}{\frac{1}{j\omega C_1}} \tag{5.59}$$

$$Z_{t\_PP} = \frac{1}{\frac{1}{j\omega L_1 + \frac{\omega^2 M^2}{{Z_2}^P}} + j\omega C_1} \tag{5.60}$$

The total current observed from the primary side is given by (5.61).

$$I_1 = \frac{V_1}{Z_{t\_PP}} \tag{5.61}$$

In case of parallel compensated primary and secondary, the system has reactive components, which introduces phase shifts on both sides of the system (as explained above). Hence for parallel compensated system, the compensation capacitors are defined as given by (5.62). This is the reason a large primary and secondary capacitor is usually added on both sides of CPT systems.

$$C_1 = \frac{1}{{\omega_o}^2\left(L_1 - \frac{M^2}{L_2}\right)} \quad ; \quad C_2 = \frac{1}{{\omega_o}^2\left(L_2 - \frac{M^2}{L_1}\right)} \tag{5.62}$$

On substituting (5.61), the secondary side impedance (${Z_2}^S$), reflected impedance (Z_{r_PP}) and total impedance (Z_{t_PP}) can be derived as given by (5.63)-(5.65).

$${Z_2}^p = \frac{{\omega_o}^2 L_2\left(L_2 - \frac{M^2}{L_1}\right) + j\omega_o \frac{M^2}{L_1} R_L}{R_L - j\omega_o\left(L_2 - \frac{M^2}{L_1}\right)} \tag{5.63}$$

$$Z_{r\_PP} = \frac{\omega^2 M^2\left(R_L - j\omega_o\left(L_2 - \frac{M^2}{L_1}\right)\right)}{{\omega_o}^2 L_2\left(L_2 - \frac{M^2}{L_1}\right) + j\omega_o \frac{M^2}{L_1} R_L} \tag{5.64}$$

$$Z_{t\_PP} = \frac{{\omega_o}^2 {L_1}^2 - {\omega_o}^2 L_1 \frac{M^2}{L_2} - j\omega_o L_1 Z_{r\_PP} + j\omega_o \frac{M^2}{L_2} Z_{r\_PP}}{j\omega_o \frac{M^2}{L_2} + Z_{r\_PP}} \tag{5.65}$$

The primary current and load current is given by (5.66) and (5.67).

$$I_1 = \frac{V_1}{Z_{t\_PP}} = \frac{j\omega_o \frac{M^2}{L_2} + Z_r}{{\omega_o}^2 {L_1}^2 - {\omega_o}^2 L_1 \frac{M^2}{L_2} - j\omega_o L_1 Z_r + j\omega_o \frac{M^2}{L_2} Z_r} V_1 \tag{5.66}$$

$$I_L = \frac{V_L}{R_L} = \frac{Z^p I_2}{R_L} = \frac{I_2}{(R_L j\omega C_2 + 1)} \tag{5.67}$$

On substituting the current I_2, the load current I_L can be derived as given below:

$$I_L = \frac{M}{j\omega_o \left(L_1 L_2 - M^2\right)} V \tag{5.68}$$

Using (5.57) - (5.68), the input power, output power and efficiency of parallel compensated system can be obtained. The level of compensation in the circuit is defined by the term quality factor. The quality factor is defined by the ratio of active power and reactive power. The primary quality factor (Q_1) and secondary quality factor (Q_2) is given by (5.69) and (5.70), where VAR1 and VAR2 are the primary and secondary side reactive power respectively.

$$Q_1 = \frac{VAR_1}{P} \tag{5.69}$$

$$Q_2 = \frac{VAR_2}{P} \tag{5.70}$$

In secondary side, large Q_2 increases the power transfer capability, the value of Q_2 varies from 2 to 10. Q_1 is defined based on the input current. The value of Q_1 changes based on various design methods and its value ranges from 2 to 50. The rate of Q_1 and Q_2 is very important. There are three cases $Q_1 >> Q_2$, $Q_1 \sim Q_2$ and $Q_1 << Q_2$. For achieving proper stability in CPT systems, Q_1 should be always greater than Q_2.

5.3 Description of experimental set-up

5.3.1 Design stages

The design of CPT system includes various stages. The block diagram of design stages is shown in Figure 5.6. A short description of the blocks include in the design procedure is detailed as follows:

- Firstly, the system specifications are decided, which includes power rating, input supply, control circuit operating range w.r.t power circuit. It also depends on shape of the coil, power range and applications.

- Next the inductive coils are designed. The coil design plays an important role in the development of CPT system. The power transfer capability and efficiency of CPT system directly depends upon the coil design. Shape and size of the coils are chosen depending upon the application. Litz wire coils are used in CPT system to avoid losses at high frequency.

- System level theoretical and analytical verification of its characteristics helps in visualizing the

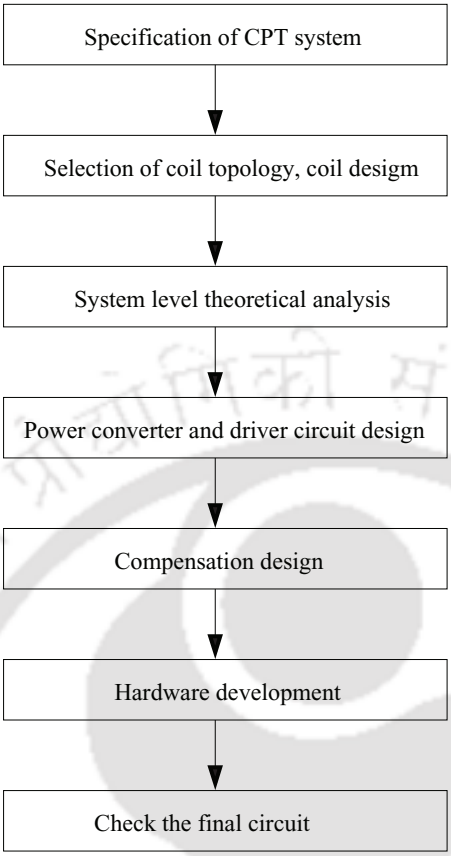

Figure 5.6: Block diagram of design procedure.

behavior of CPT system.

- Following to which, the power converter and driving circuit design can be done.
- The choice of primary and secondary compensation topology is also an important stage in the design of CPT system. By which, the load connected to the CPT system is seen as an ohmic load from the power supply side. The compensation topology determines the system behavior and sensitivity for variable load and air gap distance.
- Finally the development, building and testing of CPT system prototype is done.

5.3.2 Block diagram

The CPT system can be controlled with either fixed frequency control or variable frequency control. In the first case, the system is controlled to supply the load with fixed voltage and frequency. While

in the second case, the system is controlled to supply the load with variable voltage and frequency. In this work, PWM based variable frequency control has been used to control the power converter of the CPT system. The basic building blocks of CPT system is shown in Figure 5.7. The complete layout

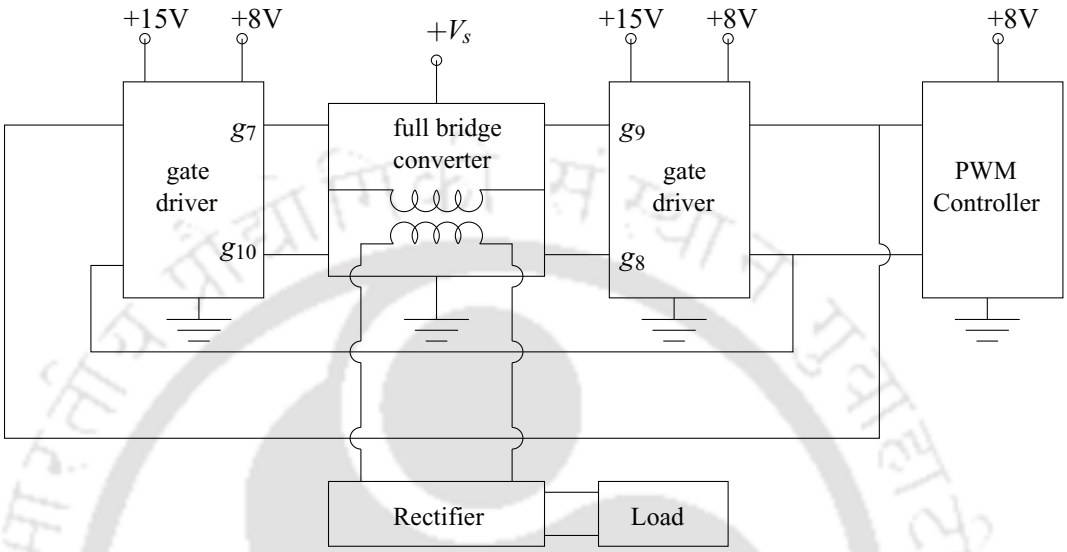

Figure 5.7: Basic building blocks of CPT system.

of CPT system consists of five blocks : full bridge converter, gate driver, PWM controller, rectifier module and load. As already explained, the primary and secondary side of the system is physically isolated and magnetically coupled to each other. The primary side of the coil is connected to a full bridge converter. The full bridge converter is controlled by a PWM based frequency control to control the power output of the CPT system. To increase the power output and to amplify the gate signal two gate driver circuits are used to control the high and low side switches. The secondary winding of the coil is connected to full bridge rectifier block and load.

5.3.3 Power circuit and coil description

The CPT system is built in the laboratory to validate the performance of four compensation topology. The primary and secondary windings of contactless coils forms a system of magnetically coupled inductor. The inductive coils are powered by a full bridge converter. The primary winding of inductive coil is connected through full bridge inverter (S_7-S_{10}), while secondary winding is connected through diode rectifier module (D_{11}-D_{14}) to the load. The primary side full bridge converter consists of MOSFET based inverter and converts rectified dc link voltage into alternating voltage. This

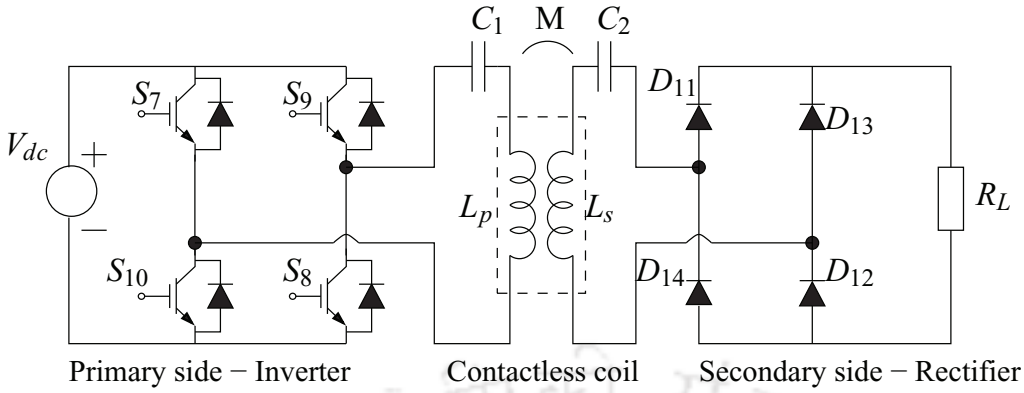

Figure 5.8: Power circuit.

alternating voltage supplied in the primary coil generates a magnetic field which induces a current in the secondary coil. The induced voltage in the secondary side of the coil is rectified using diode rectifier (D_{11}-D_{14}) shown in Figure 5.8 is connected to the load R_L (can be used to power a device or storage system). Load in the circuit is varied from 1.2Ω to 38Ω. Due to large leakage inductance of CPT system and to improve the power transfer capability, compensation capacitors (C_1, C_2) are used on both sides of the inductive coils (SS compensation is shown in Figure 5.8). The method of compensation are chosen based on the application of CPT system. Compensation capacitors C_1 and C_2 are chosen to be different based on the topology and its design equations are given in Section 5.2. Different ceramic capacitors ranging from 3.998μF to 8.454μF have been used as compensation capacitors in the CPT system. The compensation capacitors along with coil inductor acts as LC filter to remove the voltage and current ripples in the circuit. The full bridge converter switches in the primary side are controlled to control the power flow in the system. For this purpose, PWM based frequency controller is used with two gate driving circuits to drive high and low side MOSFETs. The frequency of the converter is controlled by a frequency controller which helps to adjust the instantaneous value of primary peak current and voltage and guarantees the zero phase difference at resonance condition. The power converter in the primary side is made of high power switching MOSFET IRF540 of 100V, 30A have been used to meet the desired voltage and current requirements for triggering the switches (S_7 - S_{10}) of the converter. The primary and secondary side of inductive coils are made of 10 turns of multi-strand AWG#25 copper wire. The secondary side diode rectifier is build of QRD0610T30 fast recovery diode module having reverse blocking voltage of 600V and average forward current of 50A.

The inductive coils are wounded on two same sized separate piece of wooden board placed in parallel using supporting staffs separated by an air gap. The coils are wound in spiral fashion to represent a closed square and rectangular coil to provide a complete current path. The arrangement is made such that the primary coil is fixed for all experiments and the secondary coil is varied over 2cm to 10cm vertical distance. Four wooden staffs are used and the arrangement of the set-up is made in such a way that the air-gap distance between the coil can be adjusted to observe its variation over large vertical distance (h) as shown in Figure 5.2. Hence, leakage inductance of the coil may also change in a wide range.

5.3.4 Control circuit description

The control circuit of CPT system has been designed to perform reliable and stable operation. Low cost, highly reliable PWM based controller has been used to control the power circuit of CPT system. The gate pulses (g_7- g_{10}) for the converter switches are provided from IR2110 driver circuit. Two gate drivers provides high and low side outputs (HO and LO), which is given as gate pulses. The IR2110 is supplied from SG3525 PWM controller. The outputs of PWM controller are HIN and LIN. The frequency of the controller has been designed to vary from 200Hz and 200kHz. The control circuit is made to adjust the switching frequency of the converter to operate at variable range of frequencies. Variable frequency controller have been used because the power supply of the inductive coils have to be regulated to keep the minimum difference of phase angle between primary voltage and current by changing its operating frequency at resonance. The control blocks of CPT system can be divided into two stages. The first stage is pulse width modulation (PWM) based control signal generation stage, which controls the frequency of the pulses of the converter. The second stage is the driver stage which obtains input from first stage circuit and amplifies the high and low side gate drive signal for switching on the MOSFET. The detailed block representation of control circuit is shown in Figure 5.9. In the first stage, SG3525 based PWM controller have been used to control the frequency of the converter. The frequency of the PWM controller is dependent on the value of timing capacitor (C_t) and resistor (R_t), which is externally connected to the circuit. To avoid short circuits in the legs of the converter dead time have been introduced using a potentiometer (R_d) in the circuit. The output frequency of the frequency controller (HIN and LIN) is determined using the in-built oscillator present in SG3525 controller, where the frequency of the system is controlled using timing resistor (R_t), timing capacitor (C_t) and damping resistor (R_d). Here, dead time is provided using R_d to avoid short circuits in the

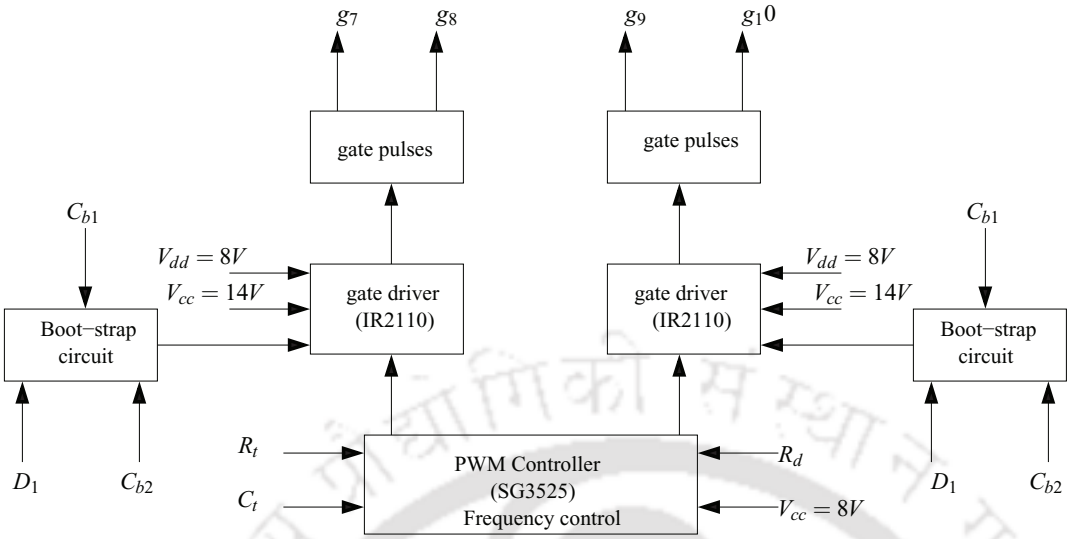

Figure 5.9: Controller blocks.

legs of the converter. The oscillator frequency is determined using the (5.71) presented below.

$$f_{osc} = \frac{1}{C_t\,(0.7R_t + 3R_d)} \tag{5.71}$$

The value of R_t, R_d and C_t are $10k\Omega$, $1k\Omega$ and $1\mu F$, which has been chosen to obtain wide variation of frequency. An input supply of 8V have been used for frequency controller. The reference voltage has been varied through potentiometer R_t to vary the duty cycle of the pulses. The output voltage of the frequency controller has a current rating of 350mA. To increase the output current and to avoid excessive power and heat dissipation of frequency controller, the high and low side gate signals are given to the second stage driver circuit. The driver circuit in the control system is made of two International Rectifier IR2110 integrated chip to drive high and low side switches of MOSFET. It features bootstrap operation and is tolerant to negative transient voltage. High and low side signals are given to upper and lower side switches of the converter. A logic supply (V_{dd}) of 8V and a supply of 14V has been used in the driver circuit. Two outputs: high side output (HO) and low side output (LO) are taken from the gate driver. The upper terminal in the primary side of the coil is connected to the terminal V_s of the gate driver. The detailed circuit diagram of laboratory sketch is give in Figure 5.10. In Figure 5.10, the diode along with the capacitor (10μF) form the bootstrap circuitry connected at the terminal V_b. In addition boot strap circuit is made of IN4001 diode (D_1), $0.001\mu F$

and $0.0001\mu F$ capacitor to amplify the signal, then the output gate signal (g_7, g_8, g_9, g_{10}) is supplied to high and low side switches of the voltage source converter.

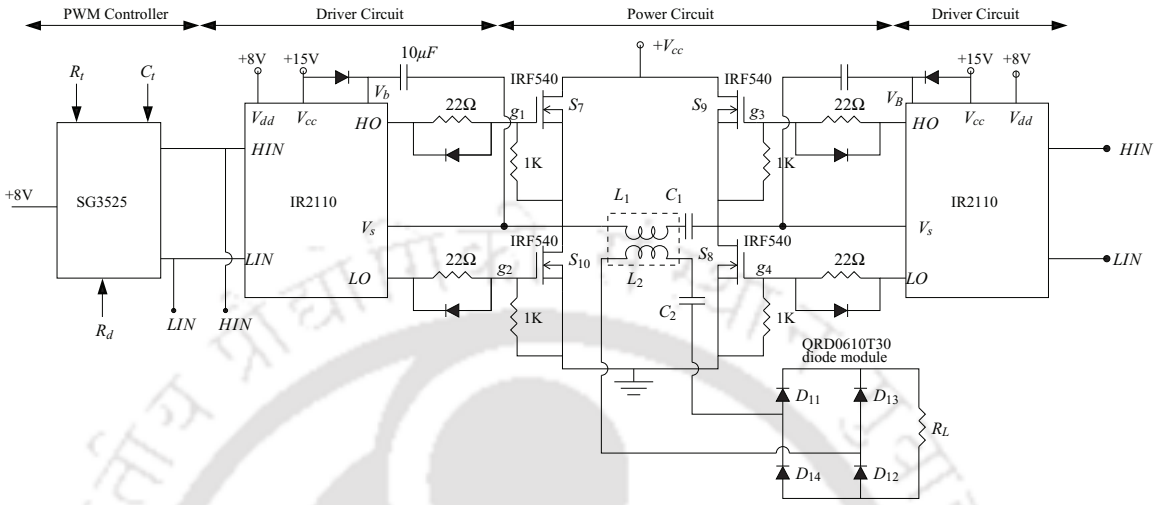

Figure 5.10: Power circuit connected with controller.

The CPT system is designed for a frequency of 15.432kHz. The circuit parameters of the inverter module are same as shown in Table 5.1. Figure 5.11 shows the view of the experimental prototype made in the laboratory.

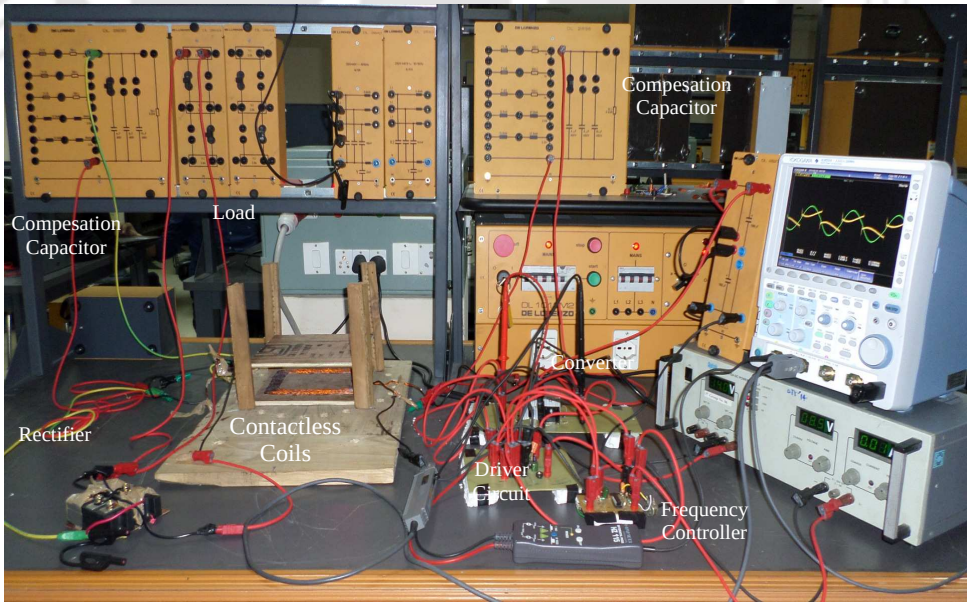

Figure 5.11: Experiential set-up.

Table 5.1: Specifications.

Specification	Term	SS	SP	PS	PP
N_1	Number of primary turn	10	10	10	10
N_2	Number of secondary turn	10	10	10	10
L_1	Primary side inductance	26.6μH	26.6μH	26.6μH	26.6μH
L_2	Secondary side inductance	24.6μH	24.6μH	24.6μH	24.6μH
C_1	primary compensation	3.998μF	7.8508μF	3.99866μF	7.8508μF
C_2	secondary compensation	4.3062μF	4.3062μF	8.454μF	8.454μF

5.4 Results and discussion

This section describes the performance characteristics of four compensation topology of CPT system obtained from experiments under various operating conditions. The frequency range of experimental circuit has been observed from 200Hz to 175kHz, over a wide load range between 1.2Ω to 36Ω. The investigation has been carried out for a maximum vertical distance of 10cm. The oscillograms of input voltage voltage (V_i), input current (I_i), output voltage (V_o), output currents (I_o) for four compensation topologies at distance D=2cm, R_L=1.2Ω are shown from Figure 5.12 - 5.15. Figure 5.12 depicts the voltage and current waveform at the input and output side of SS compensation connected with a load resistance $R_L = 1.2ohm$ at a distance D of 2cm. As it can be seen from the Figure 5.12, the input side voltage and current (V_i and I_i) are in zero phase angle at an optimum resonance frequency of 15.432kHz. However, there is a deviation in outputs in V_o and V_i due to practical losses in the system.

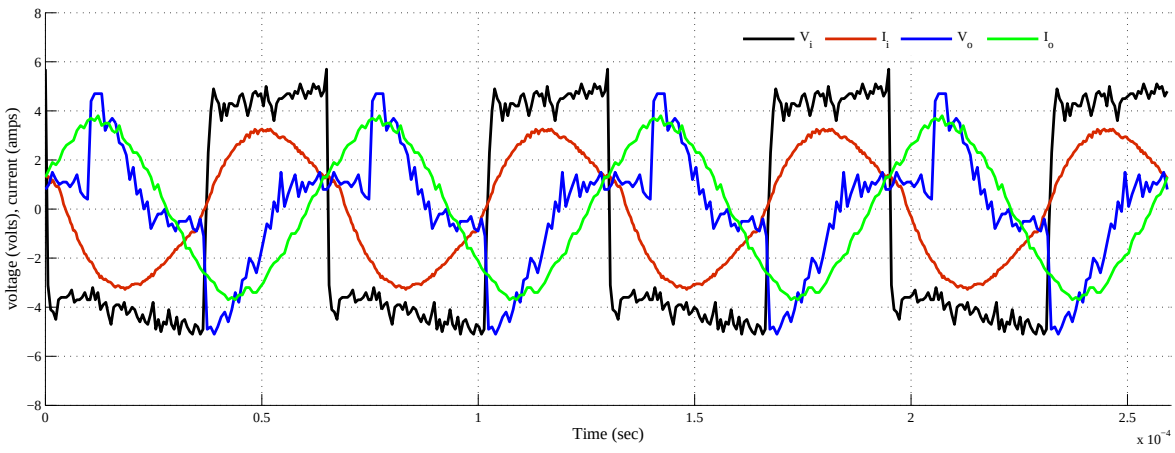

Figure 5.12: Voltage and current waveform at input and output side for SS compensation.

Figure 5.13 depicts the voltage and current waveform at the input and output side of SP compensation. The voltage and current waveform of the parallel compensation is almost sinusoidal due to parallel capacitor at the output side. However, it can be seen that the resonance frequency in the circuit is slightly shifted due to practical losses in the system.

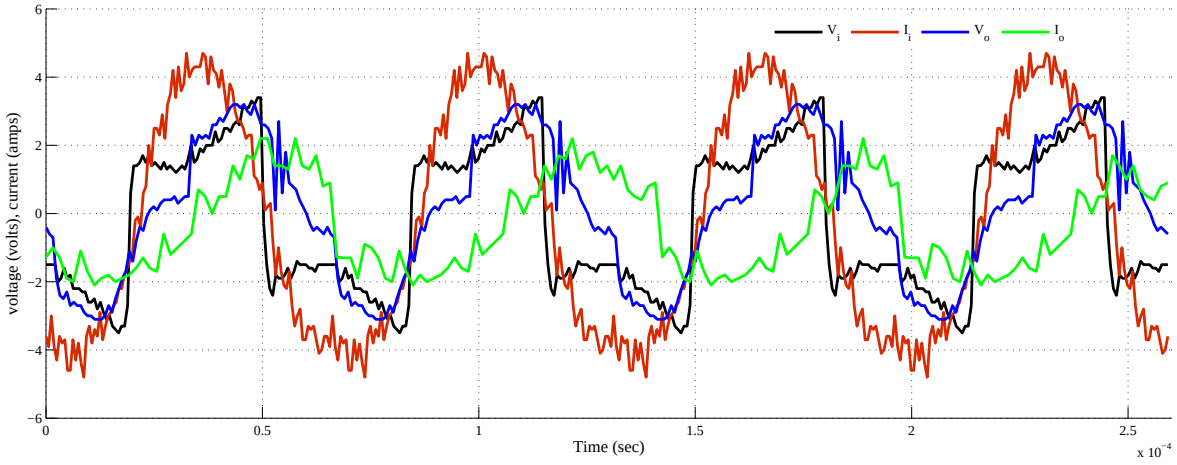

Figure 5.13: Voltage and current waveform at input and output side for SP compensation.

Figure 5.14 shows the voltage and current waveform at the input and output side of primary parallel and secondary series compensation. At resonance condition, the voltage and current has 90° phase shift at the input side. The output voltage and current has slight deviation in phase angle due to practical losses in the system. The waveforms are sinusoidal as the coil along with compensation capacitor acts as a filter in the circuit.

Figure 5.15 shows the comparison of measured voltage and current waveform at the input and output side of PP compensation. It has been observed that the input voltage is sinusoidal with less distortion. However, the outputs has more distortion at resonance condition. This shows that the output power of PP compensation need to be controlled at both sides of the controller, so that the circuit operates at resonance condition.

The oscillograms shown in Figure 5.16 and Figure 5.17 illustrates the capacitors' voltage, inductor voltage and current at the input and output side at resonance condition. When CPT system achieves resonance state, the magnitudes of voltage across capacitor and inductor should be same with 90° phase difference between them. However, it has been observed from Figure 5.16 their is a slight difference in magnitude due to some losses in the practical system. The magnitude of capacitor voltage is seen

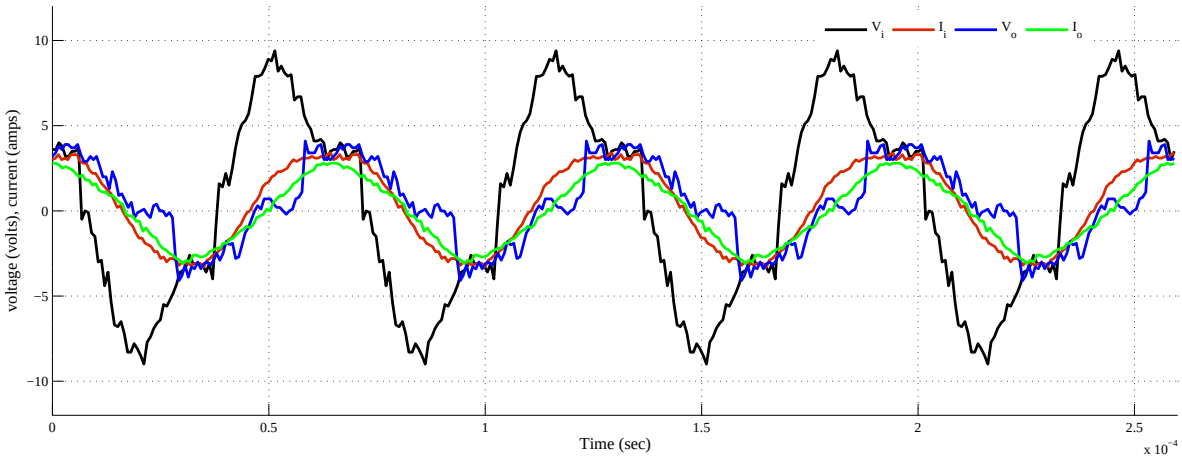

Figure 5.14: Voltage and current waveform at input and output side for PS compensation.

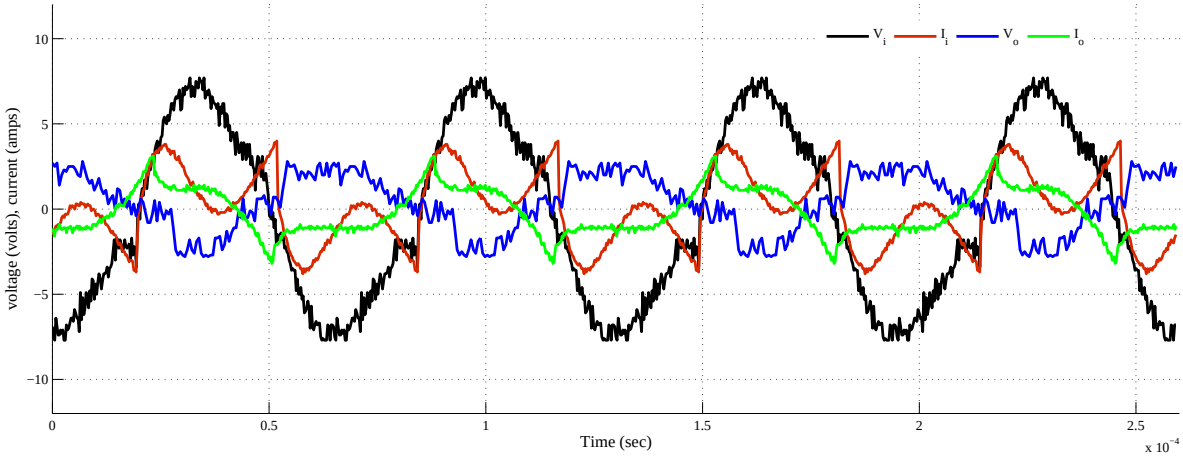

Figure 5.15: Voltage and current waveform at input and output side for PP compensation.

to be more than the inductor voltage due to this their is a phase angle difference in the current at the primary side.

The oscillograms of voltage of the capacitor and inductor and current at the secondary side of the system is shown in Figure 5.17. It has been noticed, the voltage and current magnitude got decreased at the secondary side but the phase angle difference is similar to the primary side of the system.

Further, the investigation has been carried out under three cases of variations: variation w.r.t frequency, distance and load.

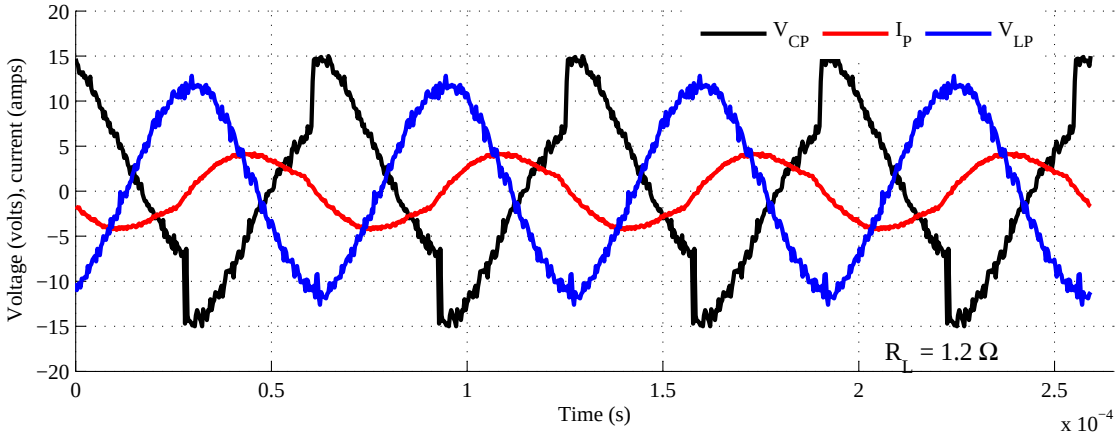

Figure 5.16: Voltage and current waveforms of capacitor and inductor at the primary side.

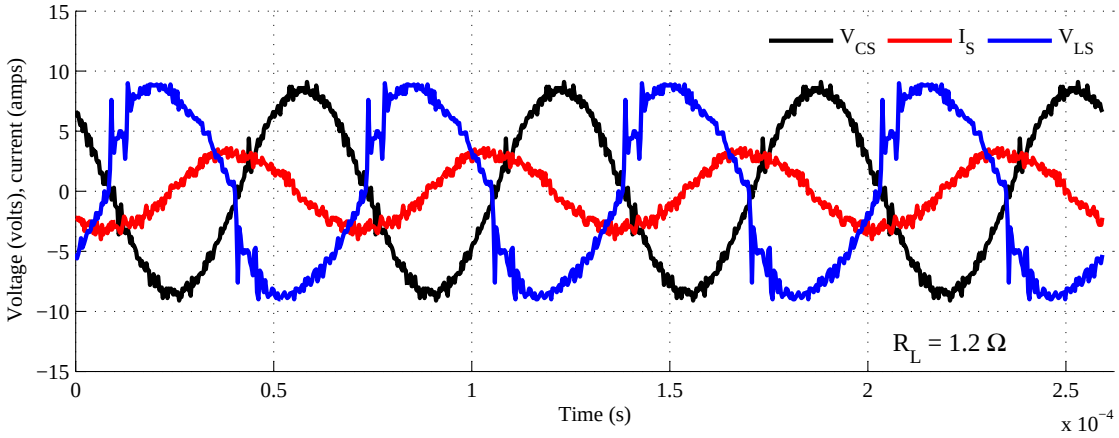

Figure 5.17: Voltage and current waveforms of capacitor and inductor at the secondary side.

case (i): Variation w.r.t frequency: In the first case of analysis, the behavior of CPT system has been studied for variation in frequency. Figure 5.18 and 5.19 shows the output power characteristics for the frequency range of 200Hz to 175kHz over different loads and distances. In Figure 5.18, the magnitude of output power is highest during resonance frequency and is lowest for lower distances and loads. This variation has been shown by fixing the supply voltage at a constant load of 1.2Ω resistance. It has also been noticed their is another bell shape found at 5kHz frequency, this is due to measurement error due to some practical variations in the system. While, in case of Figure 5.19, the distance has been fixed at 2cm. It can be observed from the plots, for the system under investigation the resonant frequency is slightly changed due to the switching losses of the semiconductor devices

used. Further, it has also been observed in Figure 5.19, as the distance is fixed at 2cm there is not much variation in the output power for initial load change, while for higher load resistances the power transferred has been decreased.

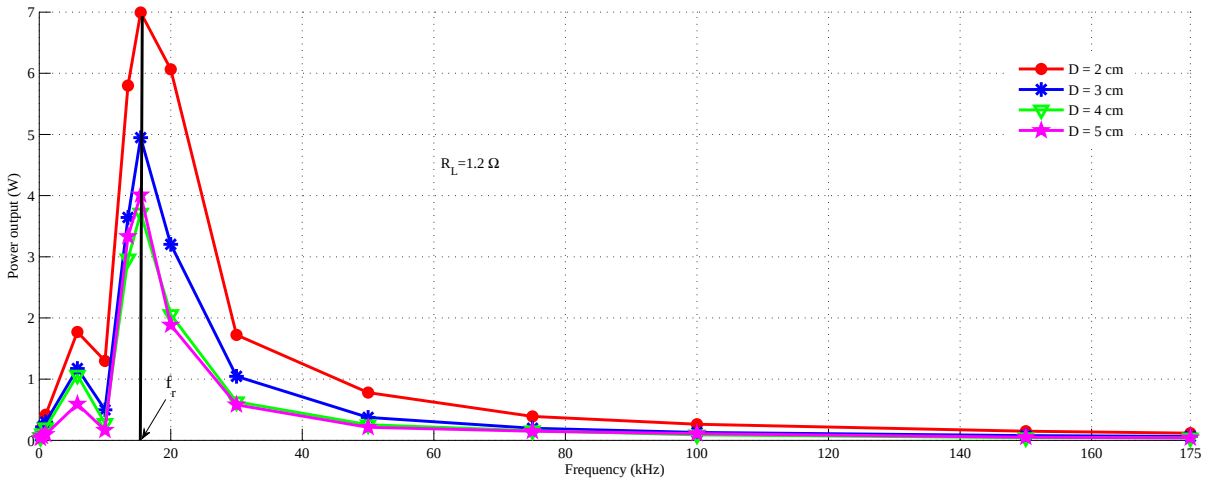

Figure 5.18: Output power as function of operating frequency for varying distance (SS).

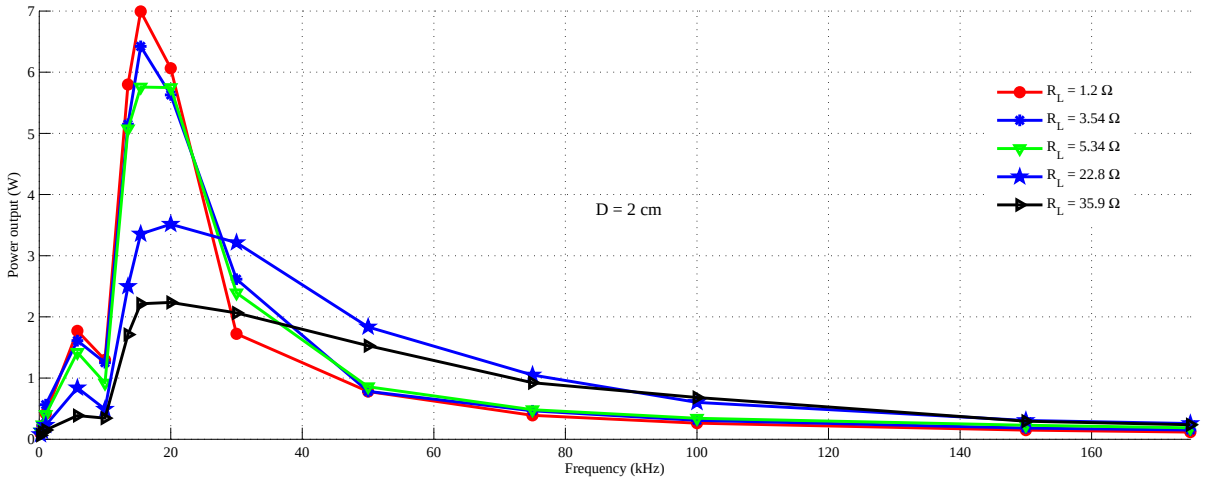

Figure 5.19: Output power as function of operating frequency for varying loads (SS).

Figure 5.20 show the efficiency curve for variable frequency for variable distance. The measured efficiency in this case (including the losses) is approximately 40%-70%. Figure 5.21 show the variation in coupling of the coil as a function of air gap distance for different loads. It has been observed the coupling of the coil decreases as the distance increases.

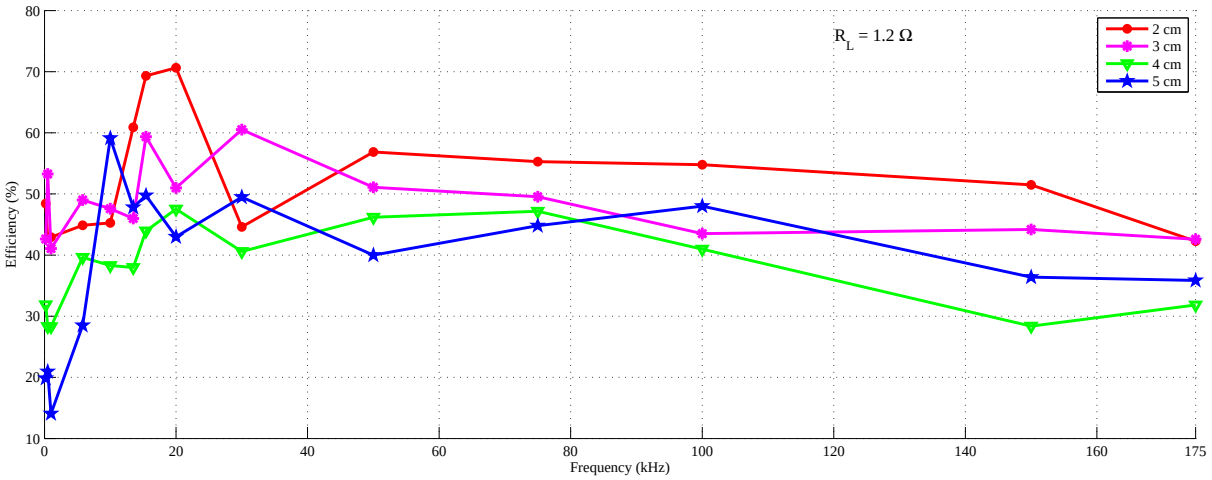

Figure 5.20: Efficiency versus operating frequency for varying distance (SS).

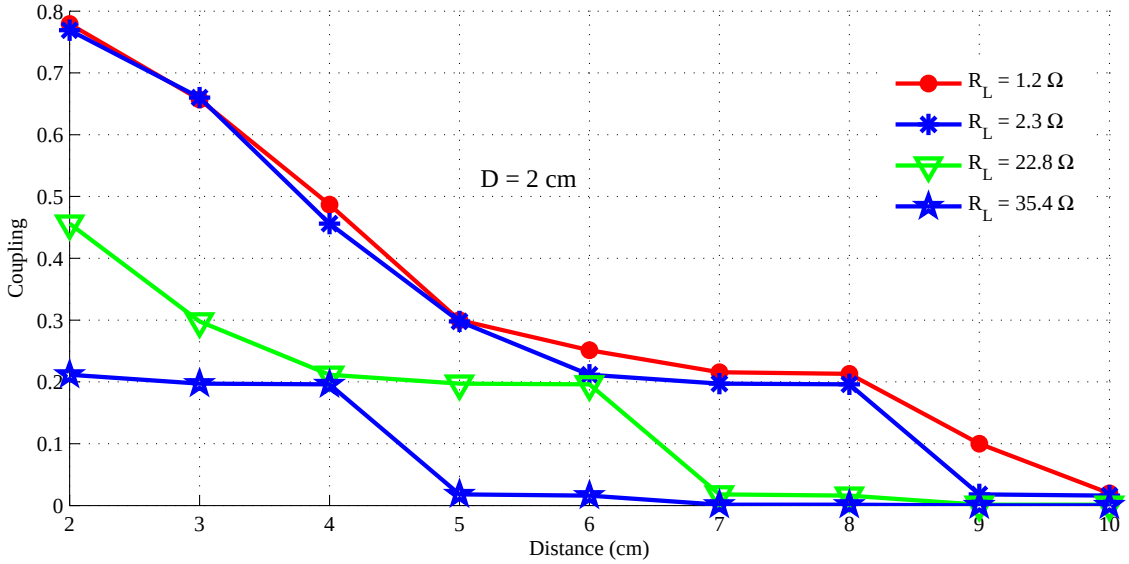

Figure 5.21: Coupling versus distance for varying loads (SS).

To compare the practical efficiency of four compensations for variation in operational frequency, efficiency versus frequency curve is plotted keeping the secondary coil at D=2cm and $R_L = 1.2\Omega$ as shown in Figure 5.22. This is the efficiency of contactless coil including its compensation capacitor. As expected, CPT system have achieved high efficiency at resonance condition and the efficiency has dropped when the system is out of resonance. It has also been noticed when compared to four

compensation topologies, SS and PS has maintained high efficiency than SP and PP compensation. The efficiency of SP and PP compensation is very less and has even reduced lesser than 10% at higher frequencies. This shows parallel capacitor in the secondary side of the coil is sensitive for variable frequency operation.

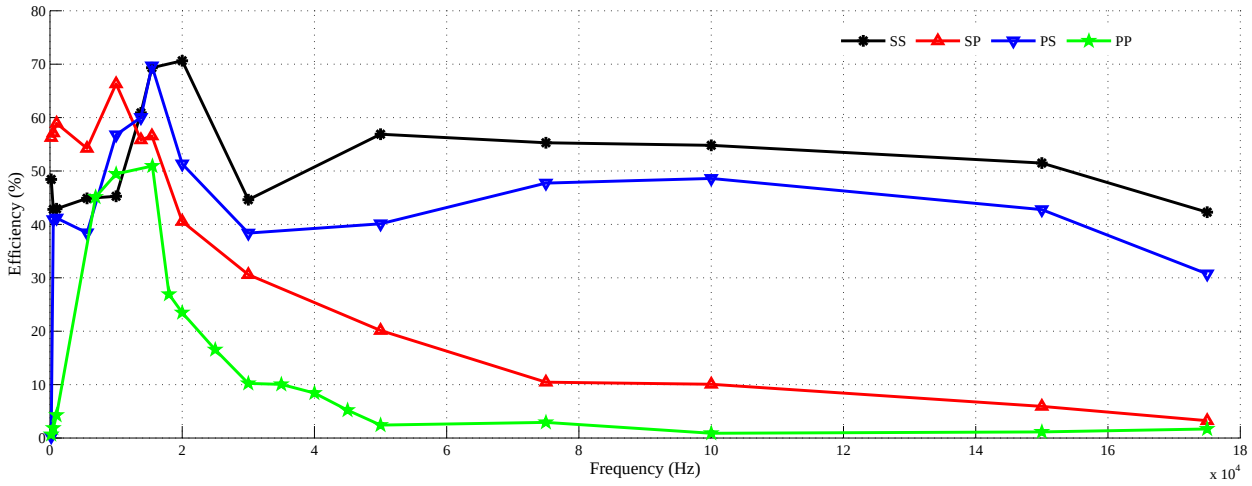

Figure 5.22: Efficiency versus frequency at d=2cm, $R_L = 1.2\Omega$.

Figure 5.23 shows the efficiency of inductive coupling system as a function of frequency for variation in load resistances. As it can be seen from the figure, the characteristics of efficiency over variable frequency has changed for increase in load. A sub efficient point is also found at the intermediate frequency of 10kHz. This is a non-resonant point.

case (ii): Variation w.r.t distance: In the second case of analysis, the behavior of CPT system has been studied for variation in distance. Figure 5.24 and 5.25 shows the characteristic plots of voltage and current variation w.r.t distance. It has been noticed, the input side current is low at lower distances and when the distance increases the current has been raised. This is because an opposite current is set in the secondary side circuit which brings an opposite flux to cancel the original field according to Faraday's Law of Induction. This effect is normal and is more at lower distance and has gradually decreased when the coil is moved away from the primary coil.

Figure 5.26 and 5.27 shows the variation power output and efficiency w.r.t distance for variable load. As explained above, for larger distances the power and voltage outputs seen in the secondary side has decreased irrespective of the load and frequency variations. The measured efficiency in this

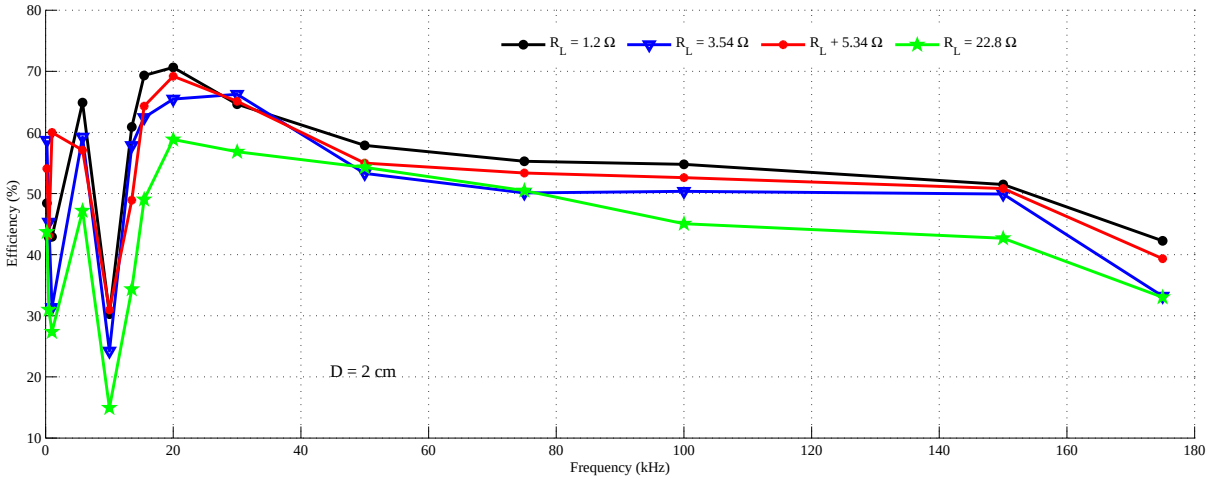

Figure 5.23: Efficiency versus frequency over variable load resistance (SS).

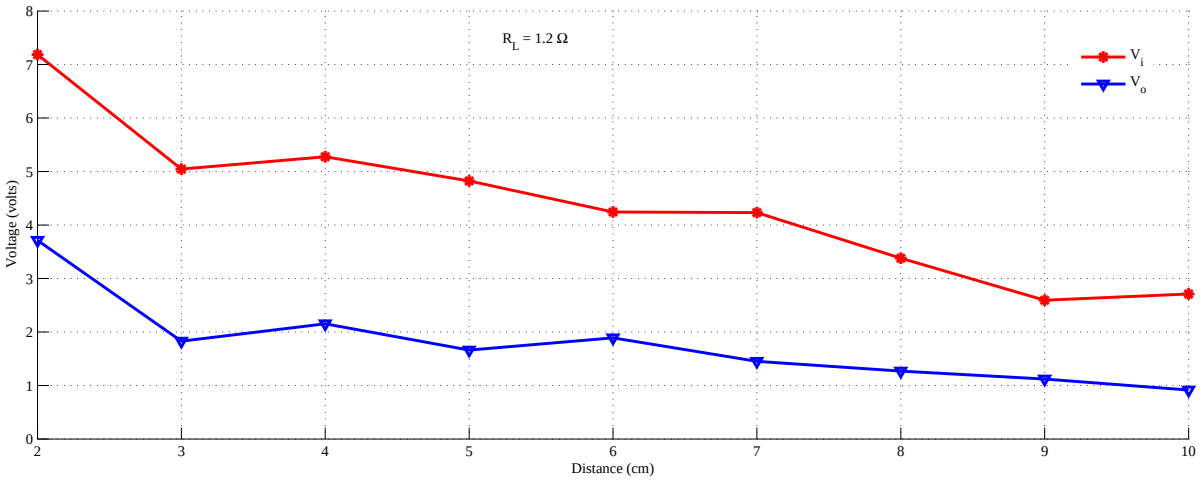

Figure 5.24: Comparison of input and output voltage (SS).

case (including the losses) is approximately 50% - 70% till 5cm distance and then it has dropped down for high loads.

Figure 5.28 shows the comparison of efficiency curve at variable distance. It has been noticed at distance 2cm, SS, SP and PS compensation has reached an efficiency of around 70%, however for PP compensation the efficiency is only 50%. The efficiency has dropped around 4% all four compensation for a distance of 10cm. This shows, as the distance between the coil increases the leakage flux of the

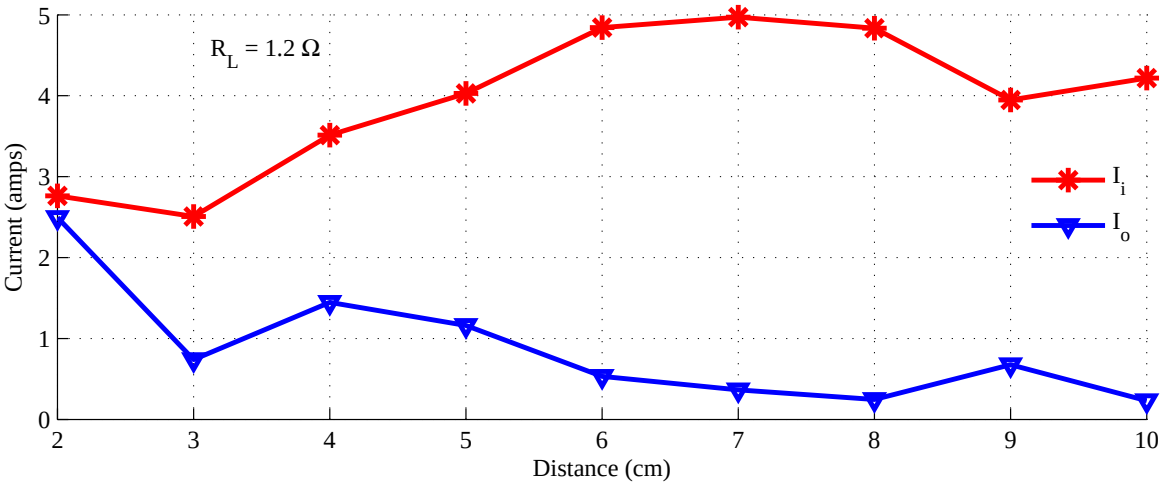

Figure 5.25: Comparison of input and output current (SS).

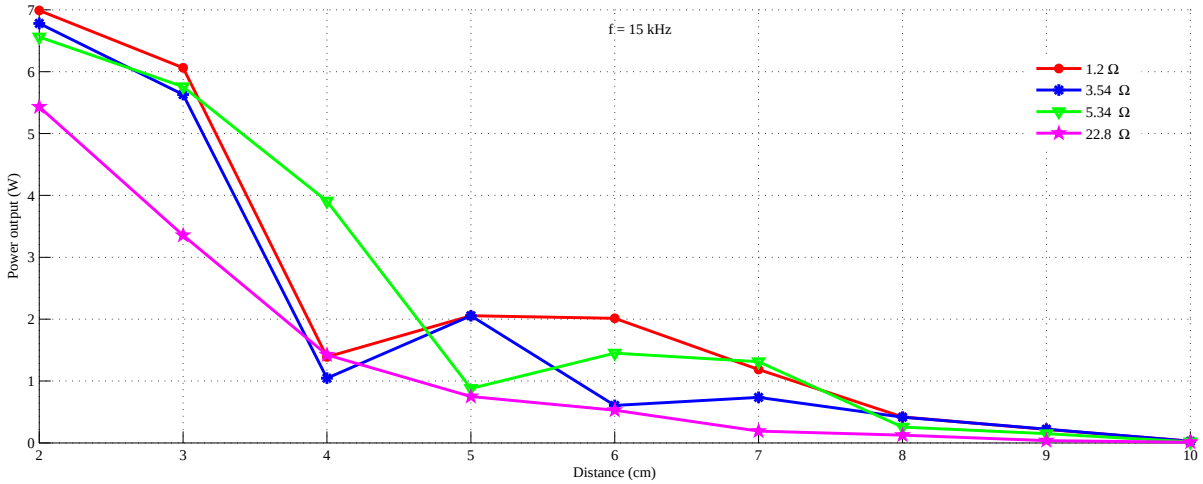

Figure 5.26: Output power versus distance for variable loads (SS).

circuit changes and the circuit deviates from the resonance condition.

Figure 5.29 shows the efficiency of CPT system as a function of distance for variable frequency range. It can be seen from Figure 5.29, the efficiency of the system is decreasing with distance irrespective of the variations in load resistance. While, the efficiency of the system beyond 6cm is found to be low in all cases of frequencies. This is because the efficiency of the system has been decreased over the distance because the system becomes more sensitive when magnetic coupling between the coil changes irrespective of the loads chosen.

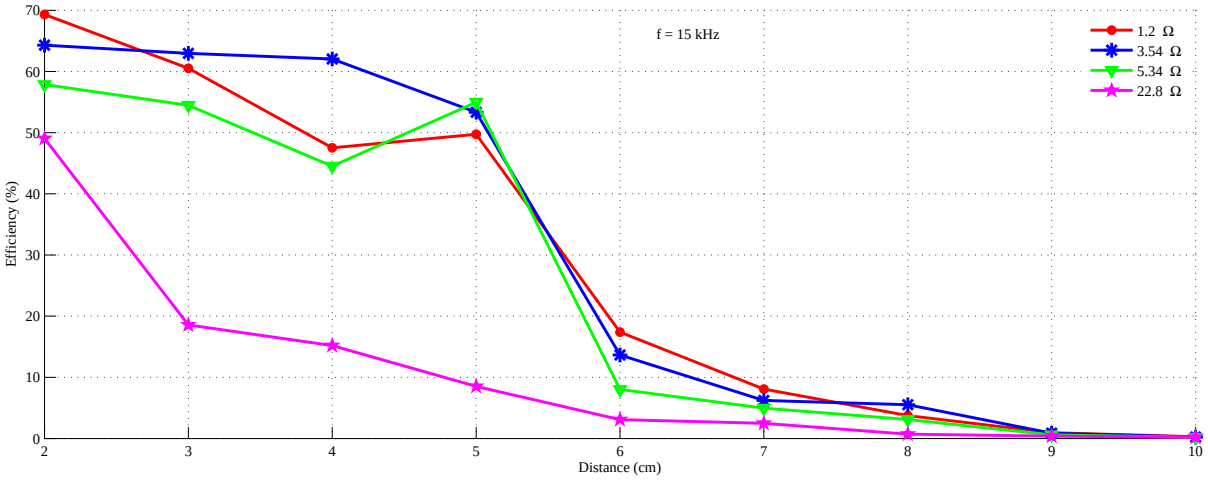

Figure 5.27: Efficiency versus distance for variable loads (SS).

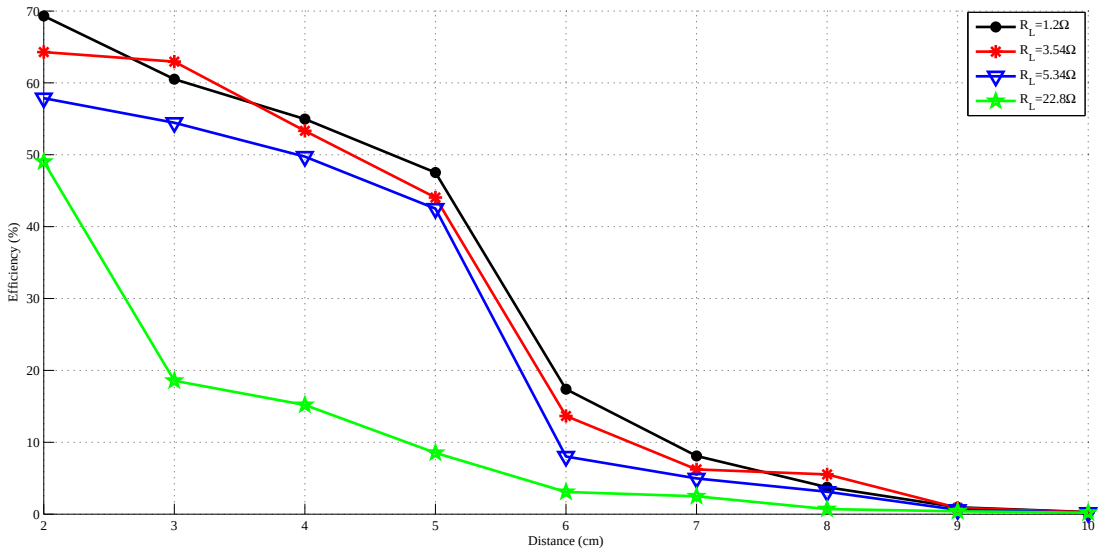

Figure 5.28: Efficiency versus distance at f=15.432kHz

Figure 5.30 shows the comparison of efficiency curve at variable distance for four compensation topologies. It has been noticed at distance 2cm, SS, SP and PS compensation has reached an efficiency of around 70%, however for PP compensation the efficiency is only 50%. The efficiency has dropped around 4% all four compensation for a distance of 10cm. This shows, as the distance between the coil increases the leakage flux of the circuit changes and the circuit deviates from the resonance condition.

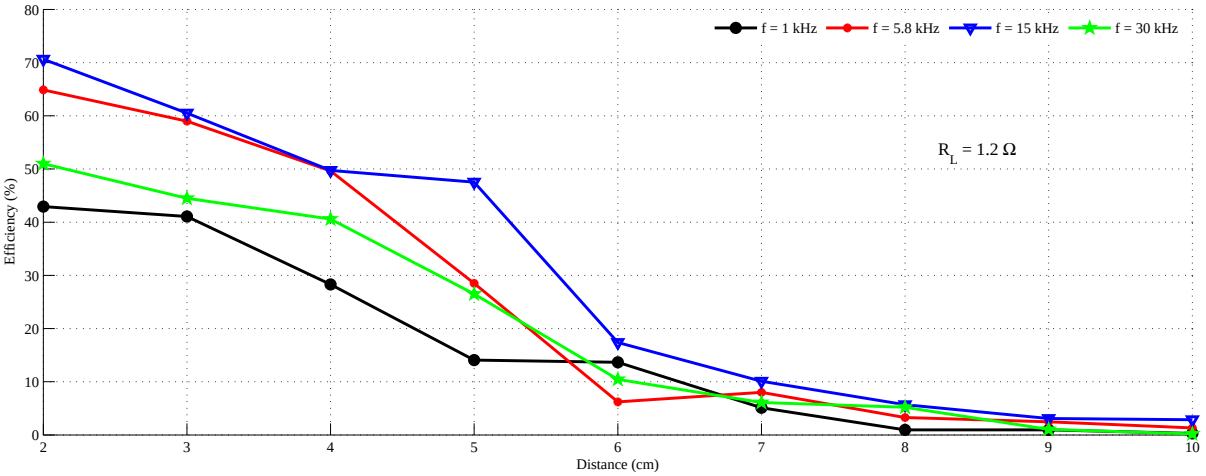

Figure 5.29: Efficiency versus distance over variable frequency range.

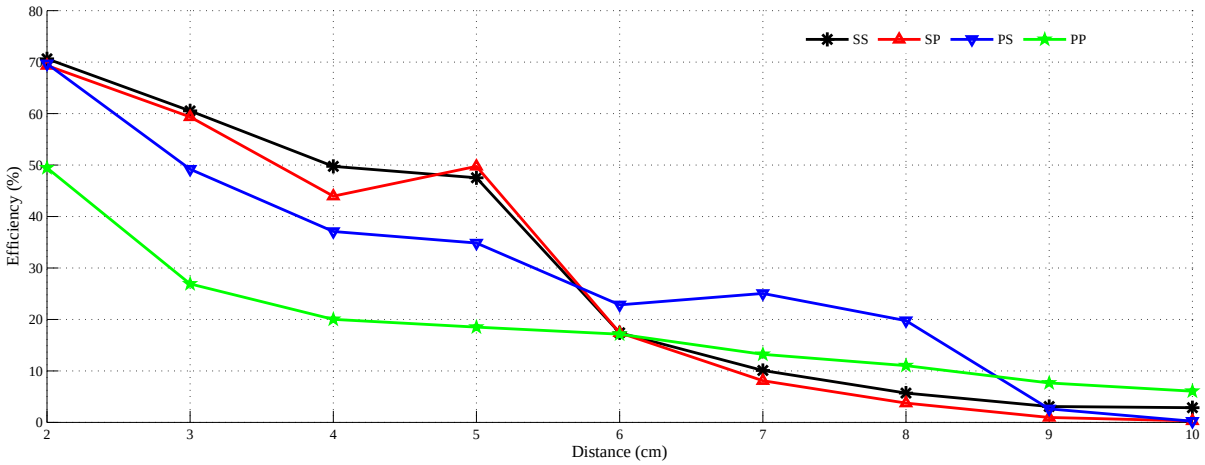

Figure 5.30: Efficiency versus distance at f=15.432kHz, $R_L = 1.2\Omega$.

It has also been observed from the curves, the system has highest efficiency in and around the resonance condition (15.432kHz) of the system. As the coefficient of coupling lowers, the efficiency of the system has decreased because the impedance of the circuit matches only at particular frequency. It can also be inferred from these figures, the circuit should always be controlled and operated in safe working area to achieve maximum efficiency of transmitted power.

case (iii): Variation w.r.t load: In the third case of analysis, the variation in load resistances with frequency and load resistance is given in Figure 5.31 and 5.32 show the power output and efficiency w.r.t load. It is important to note in Figure 5.31, the power output with variation in load has almost

linear change. In Figure 5.32 it has been observed, their is variation in efficiency due to frequency change.

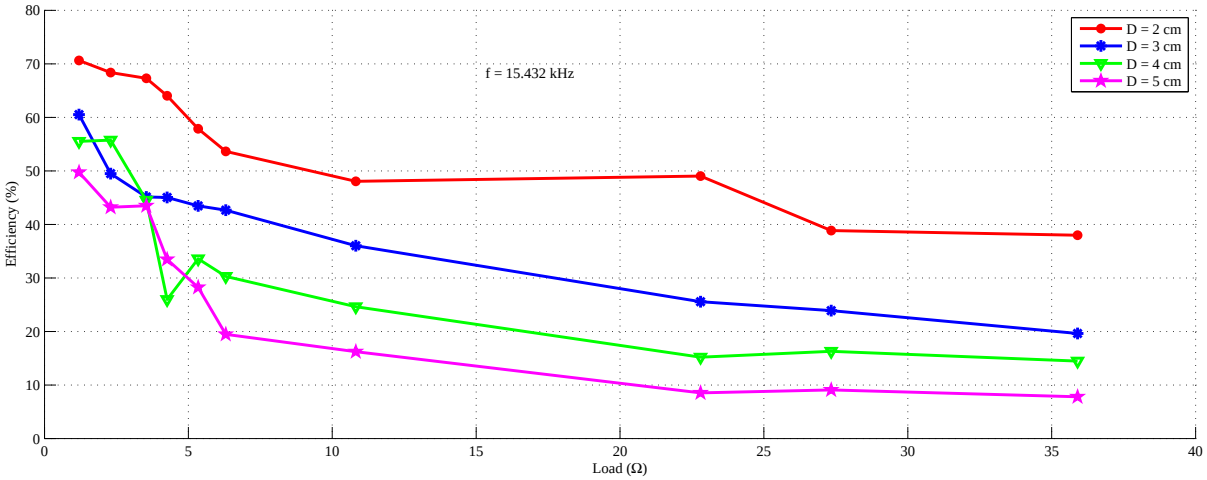

Figure 5.31: Efficiency as a function of load (SS) for variable distance.

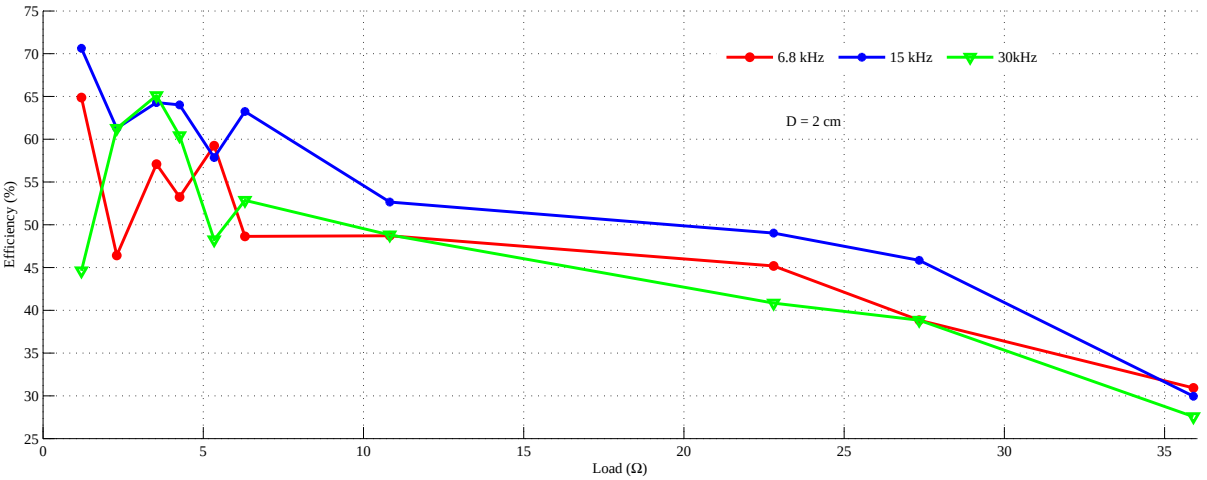

Figure 5.32: Efficiency as function of load (SS) for variable frequencies.

Figure 5.33 shows the efficiency of inductive coupling system as a function of load resistance for variable load resistances. It can be seen from Figure 5.33, the efficiency of the system is decreasing with distance irrespective of the variations in load resistance.

Figure 5.34 shows the comparison of efficiency curves for variable load resistance. The variation of efficiency with respect to load follows similar patten for all compensation except PP topology. At

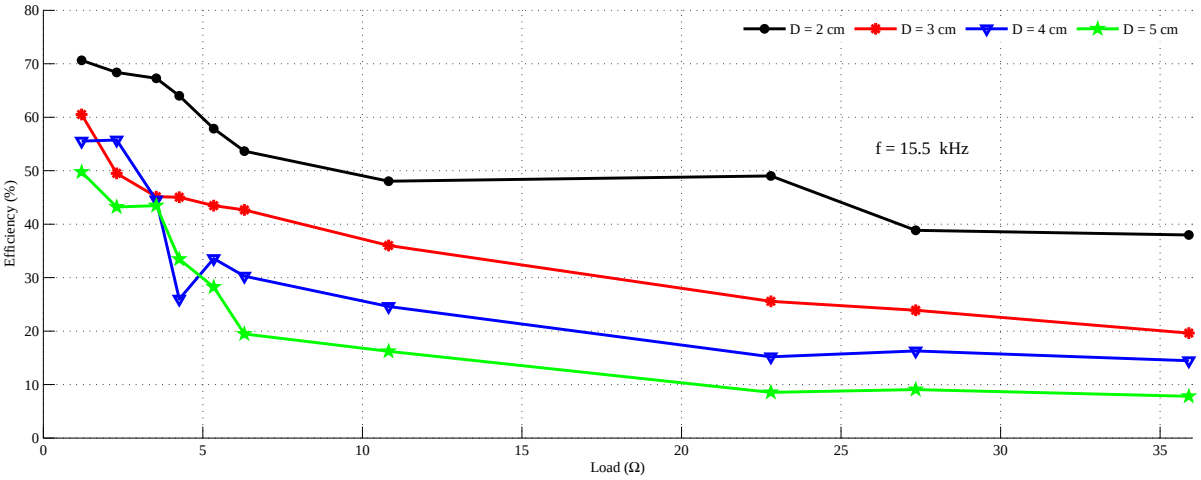

Figure 5.33: Efficiency versus load resistance over variable distance (SS).

lower load resistance values, efficiency is high and starts falling for higher resistances. The efficiency of SS compensation is around 40% at $R_L = 35.9\Omega$ and for SP and PS it is around 30% to 20% . While for PP compensation, efficiency has fallen below 10% at $R_L = 35.9\Omega$.

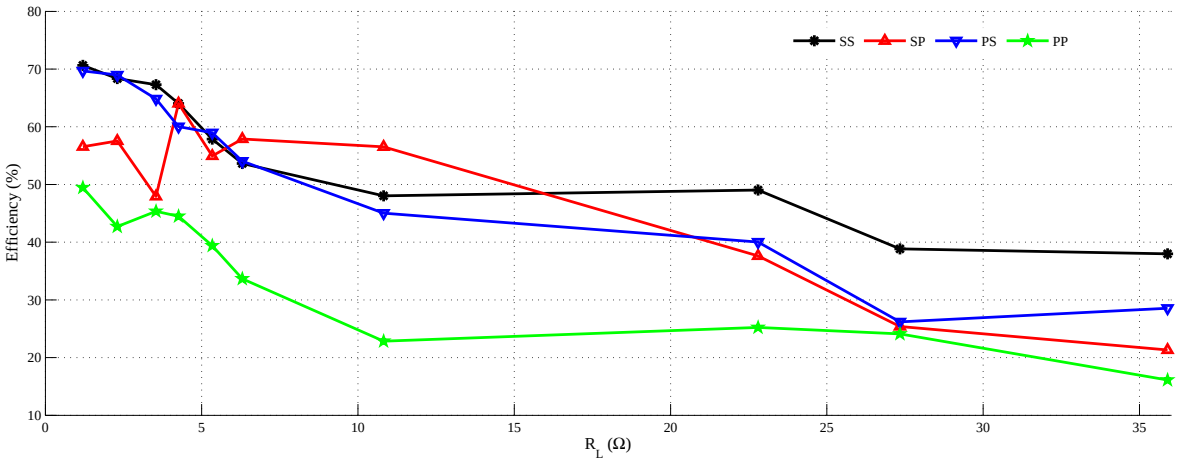

Figure 5.34: Efficiency versus load resistance at d=2cm, f=15.432kHz.

From the above plots, it has been concluded impedance matching circuits using compensation capacitor can be used as an effective method to enhance the power transfer efficiency in the CPT system. To transfer maximum efficiency in the CPT system, the circuit should be ideally operated in the resonance condition. Any deviation of frequency from the resonance condition would reduce

the power transfer efficiency. Depending on the variation in distance between the coils or variation in load, the optimum power transferred in the system may reduce. Further, this can be improved by an additional control strategy in the primary and secondary side converter. The rest of the graphs are shown in Appendix A.6.

Generally, the contactless system has losses due to leakage inductances as the primary and secondary coils are loosely coupled. The experimental results reported in this paper has achieved a maximum efficiency of 70% (excluding the losses), due to large leakage inductances as the coils are loosely coupled. In this case, a higher efficiency can also be obtained, however the experimental study reported in this paper no attempt was made to improve the efficiency of the system. Since the primary objective of the work is to observe the variations over different range of frequency, load and distances. The summary of four compensation topology is given in Table 5.2. It has been observed, SS and PS topology are not frequency sensitive. However, when compared to other topologies, the performance of SS topology is found to be better than other topologies.

Table 5.2: Summary of comparison of four compensation.

Type	output current / voltage	sensitiveness	size of compensation	application
SS	constant output voltage	for variation in distance	less value on both sides	intermediate dc bus voltage
SP	constant output current	for variation in frequency, load and distance	large primary	battery charging
PS	constant output voltage	for variation in load and distance	large secondary	dc bus voltage
PP	constant output current	for variation in frequency, load and distance	large value on both sides	battery charging

5.5 Conclusions

An investigation has been done with series-series (SS), series-parallel (SP), parallel-series (PS) and parallel-parallel (PP) compensation topologies in contactless power transfer (CPT) system. Equivalent circuit model have been used to explain the theory of CPT system and its various parameters are summarized. The implementation procedure and its hardware circuitry has been explained in detail. An experimental set-up is made in the laboratory to verify the theory of CPT system and has been tested with four compensation topology. The circuit has been tested for variable operating conditions such as load, distance and frequency. The efficiency plots of four compensation topologies

are compared. The analysis shows that the compensation with secondary series has good performance for variable frequency operation. The performance of SP and PS is comparable in case of for variable load and distances. However it has been noticed, PP compensation has very poor efficiency in all cases of analysis, when compared to other compensations.

6

Conclusions and Future Work

Contents

6.1 Concluding remarks 141
6.2 Suggestions for future work 144

6.1 Concluding remarks

The research reported in this thesis had addressed the investigation mainly on contact based and contactless EV charging systems. Theoretical modeling of charging system and its coordination in a CS, mutual inductance computation of contactless system and analysis of four compensation elements in contactless systems were addressed. The introduction chapter has presented the classifications of EV chargers, theory of contactless system along with CPT technology and has summarized the major challenges and goals identified in this thesis. Chapter II describes a contact based charging station and its coordination for voltage regulation in the distribution node. The next chapter in this thesis has investigated contactless system application on multiple charging system architecture in a CS connected with EV batteries with suitable controllers (Chapter III). In which, the performance of the charging system has been validated for grid to vehicle and vehicle to grid operations. An analytical approach is then presented to compute mutual inductance (MI) between two contactless coils placed in a flat planar surface (Chapter IV). Following to that, the performance of CPT system has been compared with different compensation elements and its results are reported (Chapter V). Thus, the chapters of this thesis has reported several new results required for the design and development of contact based and contactless charging of EVs. Briefly, the contents of the research contrasted to previous works are summarized as follows.

6.1.1 Introduction chapter

A brief introduction about the classification of EV chargers, theory of contactless system, EVs and CPT technology are presented in Chapter I. It has summarized the classification of EV chargers, the overview of CPT system, theory on mutual flux, mutual inductance computation, EVs and CPT technology, induction coupling system, need for bidirectional charging systems, vehicle to grid and grid to vehicle technology are presented. In addition, the major challenges and goals of this research, contribution of this thesis and thesis organization are described.

6.1.2 Modeling of Contact based Charging Station for Voltage Regulation

It has previously been observed, there has not been much technical analysis done in both active and reactive power control with component level contact based charging system model to regulate the distribution node voltage. To address this problem, Chapter I has described a contact based EV CS for voltage regulation in the distribution node. A CS is modeled with 35 charging systems which

enables EVs of different ratings to charge and discharge. The individual charging system has grid connected three-phase ac-dc converter and a series connected dc-dc converter with suitable controllers to exchange active and reactive power between the distribution node and the CS. Electric circuit based battery models have been used to represent the aggregated EV battery model. The constraints of EVs are considered by taking into account of vehicles battery characteristics such as state-of-charge (SOC), charge/discharge rate limits and charging/discharging requirements. In addition, to control and coordinate the sudden arrival and departure of EVs and to regulate the specified voltage limit (1 ± 0.13), the CS is externally controlled using a FLC and an aggregator. Here, FLC has been used in place of other traditional control methods; which often results in computational burden due to large number of trigonometric operations. However, the use of FLC does not require neither detailed knowledge of the system under control nor its precise descriptions in terms of mathematical model. Voltage profile evaluations have been done with different power exchange approaches such as active power, reactive power and combined active and reactive power to forsee the CS behavior. Simulation results shows consistent and accurate results with significant voltage improvement due to real time use of EVs through charging systems. The results show that the charging system and its controllers are found to be efficient in performance; since it provides better voltage control while managing the EVs batteries in the CS.

6.1.3 Theoretical Modeling of Contactless Charging Station

In Chapter III, the theoretical modeling of multiple parallel connected contactless charging system model is described. The developed model has multiple charging panel arrangement connected with an ac bus. The model proposed in this chapter details the basics of contactless system design, converters and controllers required for charging and discharging of EVs. Battery modules are connected to their respective charging points through high frequency coreless coils are described. In addition, the chapter has also investigated the bidirectional operation to facilitate forward and the reverse power flow. All the results obtained in Chapter III are very promising and such a method could be successfully applied for the future implementation of EV charging systems.

6.1.4 Computation of Mutual Inductance for Contactless System

In Chapter IV, an analytical approach for computing the mutual inductance for contactless system is proposed. Unlike transformer coils, the contactless coils are loosely coupled and the secondary of

the coil is connected with the load. The design of contactless system is very complex as the coils are usually misaligned due to variations in the system and worsen the coupling between the coils. The magnetic coupling between the primary and the secondary side depends on mutual inductance between the coils. Hence, mutual inductance is one of the crucial factors in the design of CPT system and will play a key role in determination of efficiency, power transfer, compensation capacitor etc. In order to compute mutual inductance between two coils including all lateral and angular misalignments, an analytical approach is proposed in this chapter. The method proposed is a straight forward approach based on Biot-Savart principle and their integral are computed numerically. The method works by approximating the area of secondary coil with small regions, encompassing the entire square and thereby considering the complete spiral square coils. To carry out this process, a sequence of program routine have been used. In addition, the prosed method is validated using Finite Element Analysis (FEA) and an experimental set-up is built in the laboratory. The commercial 3-D finite element tool ANSYS Maxwell 14.0.0 has been used for validating the analytical model. Finally, the analysis in this chapter compares the results of three mutual inductance calculations. The comparison of numerical values and graphical plots are shown to show the variations of mutual inductance values obtained from the three analysis. It has been observed from the results, larger the distance lowers the coupling between the coils and mutual inductance value has decreased. It has been concluded the analytical and FEA results show a very good agreement and experimental result has an error less than 10%.

6.1.5 Compensation Topologies for Contactless System

It has previously been observed from the literature, only theoretical and simulation studies have been conducted to analyze the suitable compensation topologies in CPT systems. However, the main characteristics of CPT system is the physical isolation between the source and the load as the secondary winding of the coil is movable and connected to the load. For such a loosely coupled system, a systematic analysis can cause significant errors. Overcoming this drawbacks, chapter V has presented an experimental prototype to analyze the four compensation topologies using a practical CPT system. The study has reported the behavior of CPT system under three different cases and its characteristics plots are generated for wide range of frequency, load and distance such that the real time situations of CPT system can be analyzed. Electric equivalent circuit models of different compensation topologies are developed to explain the mechanism of power transfer in the CPT system. A comparative analysis has been done to compare the efficiency of four compensation topologies with variations in frequency,

load and distance. Thus, the theory of CPT system using compensation topology is verified using an experimental set-up connected to a rectangular primary coil and secondary coil. With these results obtained from the experiments, the theory of CPT system can be well understood and it provides a foundation for future implementation of CPT system.

6.2 Suggestions for future work

The main focus of this thesis has been towards the investigation on contactless system especially for EV battery charging application. There are several ways in which the work in this thesis can be extended and further investigated. A series of points enumerated below describes the outline directions of research that could be pursued.

6.2.1 Future research on reducing the bulk semiconverters on either side of contactless system

One major drawback of contactless charging system compared to traditional charging system is the requirement of additional high frequency converters for powering the contactless coils. Therefore, an off-vehicle bidirectional contactless charging system requires additional high frequency converters on its either side to generate high frequency current in the primary track or coil. This extra semiconductor switches can be costly and bulky, which also increases the power losses, electromagnetic interference effect, switching stress and control complexity. However, the contactless system described in Chapter 2 rely on two-stage converter (ac-dc-ac, number of stages may increase for high power conversion). In order to reduce the size of the converter/number of stages in conversion, an alternate reduced switch converter topologies could be used to generate high frequency current in the primary coil. For example, direct ac-ac converter and resonant converters could be used for this purpose.

One such direct ac-ac converter is the matrix converter, since this converter has proposed it has gained more attention for its advantages. Its main advantages are adjustable input power factor, small volume and compact design and does not require large energy storage components. In recent years there are indirect ac-ac converter topologies such as sparse matric converter, very sparse matrix converter and ultra sparse matrix converter. These topologies have a reduced number of input switches but has same functionality as compared to the standard indirect matrix converter. This technology has obtained much attention in ac-ac power conversion field in recent years. As an alternate option, dc-ac resonant converter could be used. The switches in the resonant converter is operated based on

discrete energy injection control and free oscillation technology.

In addition, a comparative analysis using these converters such as direct ac-ac converter, ac-dc-dc (H-bridge), ac-dc-dc (resonant) converter could be done in order to prove its feasibility and practicability.

6.2.2 Future research on wide air gap distance and misalignments in the coils

Two major issues involved in contactless charging of EVs are wide air gap distance and misalignments. This is mainly due to different positioning of the vehicle, different air gap pressure in the tyres, uneven surface impacts and road conditions, passenger density inside the vehicle etc. The charging system model described in Chapter 2 and Chapter 3 has considered a constant coupling factor assuming a perfect alignment between the primary and secondary coils. If the defined coupling changes, it leads to an impracticable efficient transmission, unless some way of improving the coupling factor is found. Moreover, a perfect alignment is always required to transfer the required power between the primary and secondary coil. Any disposition of the coil naturally causes significant reduction of power transmitted to the secondary coil with decrease in efficiency. While, the research described in Chapter 4 and Chapter 5 has limited its analysis to study only the impacts of wide air gap distance and misalignments. However, it will be more interesting if the proposed system can be dealt with additional control strategy to improve the coupling factor for variations in the coils. Better control methods can be adopted in the system either in the primary side (duty cycle control, phase angle control, frequency control) or in the secondary side (dynamic tuning control or directional tuning control) or could be modelled using a coordinated control for both primary and secondary side of the coil. Therefore, the major concern in EV charging system is the voltage supplied to the load side must be maintained constant even if their is a change in the circuit parameters like batteries of different ratings, variations in magnetic coupling, drifting of primary operating frequency etc.

6.2.3 Future research on contactless coil arranged in a platform surface

The experimental prototype developed in this thesis has considered single primary and secondary coil. The performance of contactless system can be improved, if multiple coil structures are arranged in a platform surface.

6.2.4 Future research on bidirectional charging system

The experimental prototype reported in this thesis have considered a resistive load and has validated only for unidirectional operation. However, in order to verify contactless charging of EVs, more wider investigation having the combination of different converter configuration connected to a battery should be investigated to check its bidirectional power flow between the grid and the charging system. In addition, a hardware prototype of synchronization circuit could be developed and tested by interconnecting the charging system converter with a 2kW generator, which can represent a grid waveform.

6.2.5 Future research on stability studies

It will be an interesting and an useful research to analyze the stability of converters and controllers in the contactless charging system.

6.2.6 Future research to calculate power losses in contact based and contactless charging system

It will be an interesting and an useful research work, if a contact based and contactless charging system model is developed in the laboratory to compare its power losses and its efficiency.

6.2.7 Future research on active and reactive power exchange between the grid and the charging system

A component level bidirectional contactless charging station model could be developed and tested in the laboratory to analyze the four quadrant operation of the converter to transfer either active power or reactive power or both active and reactive power exchange on both the directions.

6.2.8 Overall future research

The investigation performed in this research has mostly employed fuzzy logic controller. It would be interesting to analyze the performance of the charging system with other control methods.

A

Supplementary Materials

Contents

A.1 Additional figures from Chapter 2 149
A.2 Fuzzification & defuzzification for master control of Chapter 2 150
A.3 Membership function and rule base of CC-FLC, M-FLC and PA-FLC of Chapter 2 152
A.4 Fuzzification and defuzzification process for power angle control of Chapter 3 154
A.5 Sample calculation for mutual inductance of Chapter 4 157
A.6 Remaining results of Chapter 5 157

भारतीय प्रौद्योगिकी संस्थान गुवाहाटी
Indian Institute of Technology Guwahati

A.1 Additional figures from Chapter 2

Figure A.1 shows the simplified distribution system of Guwahati city taken for this study.

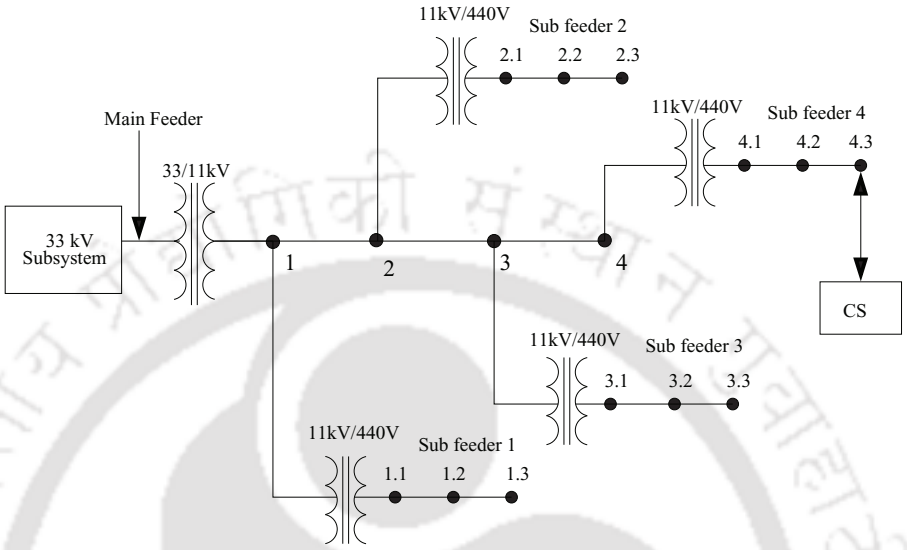

Figure A.1: Simplified distribution system under study.

Figure A.2 shows the daily load profile of the **DN 4.3** of the Guwahati distribution network. The load data is provided by the Assam State Electricity Board located in Guwahati city.

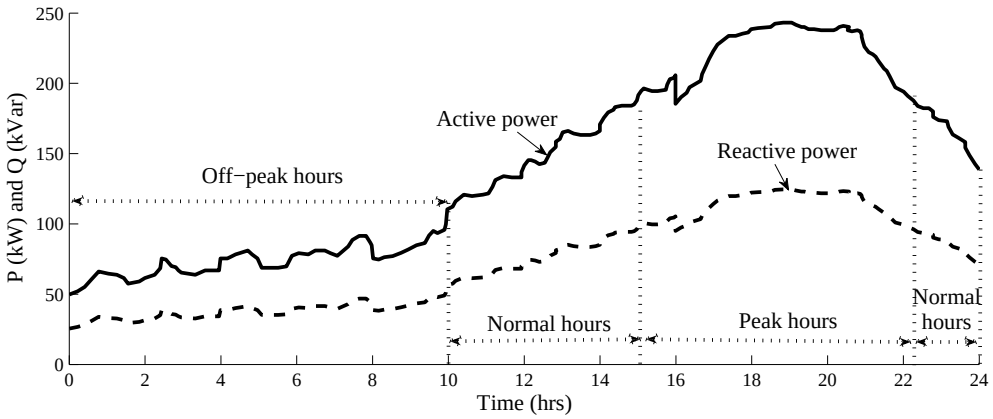

Figure A.2: Load profile of subfeeder 4.3 during one day.

A.2 Fuzzification & defuzzification for master control of Chapter 2

This part describes the fuzzification and defuzzification process of master control FLC in the charging station (CS) given in Chapter 2 for a practical example.

The controller inputs are node voltage (V_1) and total energy availabilities (E_t) of EVs in the CS. The range of V_1 is taken to be between 0.83 to 1.13 p.u. The range of E_t is taken to be between 0 (minimum available energy of the CS) and 1 (maximum available/capacity of the CS). The range of output power (S') has been taken between -1 (maximum power support given to the grid) and 1 (maximum power drawn from the grid). The controls logic is designed in terms of 49 fuzzy rules. These rules transform the input variables to an output based on the real time conditions of EVs and node voltage. Consider the inputs: V_1 as 0.97 p.u and E_t as 0.933302 p.u as shown in Figure A.3.

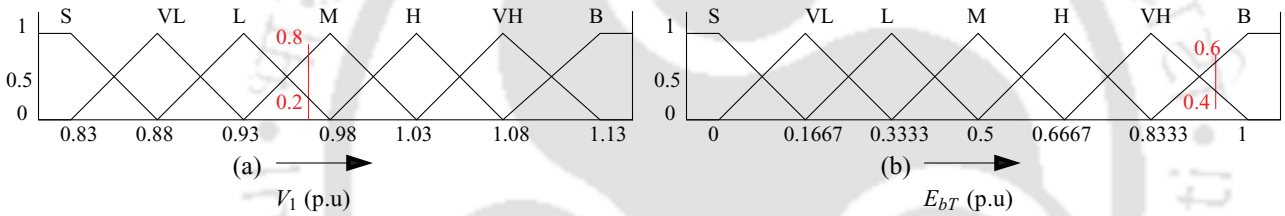

Figure A.3: Input and output membership functions.

It can be seen from Figure A.3, the value of V_1 and E_t belongs to two membership function. The corresponding four rules given by the membership functions are as follows:

- Rule 1 : If V_1 is Medium and E_t is Big, then S' is Z.
- Rule 2 : If V_1 is Medium and E_t is Very High, then S' is Z.
- Rule 3 : If V_1 is Low and E_t is Big, then S' is NL.
- Rule 4 : If V_1 is Low (L) and E_t is Very High, then S' is NVL.

These rules shows that the available energy of the EVs are high and the distribution network is in normal hours, therefore power can be either injected or drawn to the grid depending on the available energy of the CS and the requirement of the grid. The first step in this process is fuzzification. As discussed above, V_1 is a member of two membership functions representing M and L and has different

degree of membership function. E_t is also a member of two membership function. The fuzzy set of V_1 contributes 80% Medium and 20% Low and E_t contributes 60% Big and 40% Very High. The next step is the inference process, where each rule is checked for the degrees of membership for the participating inputs. Here, rule 1 says that if the fuzzy set of V_1 contributes 80% Medium and E_t is 60% Big, then S' is Z. Rule 2 says, V_1 is 80% Medium and E_t is 40% Very High, then S' is Z. Rule 3 says, V_1 is 20% Low and E_t is 60% Big, then S' is NL. Rule 4 says, V_1 is 20% Low and E_t is 40% Very High, then S' is NVL. In order to determine the degree of certainty of S', the minimum method is applied. That means the minimum of the degree of membership values of the inputs is going to be the values for the output. This is defined mathematically as:

$$\mu_0\left(S'\right) = \min\left(\mu_0\left(V_1\right), \mu_0\left(E_t\right)\right) \tag{A.1}$$

where $\mu_0\ (V_1)$, $\mu_0\ (E_t)$ and $\mu_0\ (S')$ are membership functions of node voltage, total energy and power respectively. Using (A.1), the values for the output can be found as given below.

- Rule1: $\min[\mu_S(V_1),\mu_{VH}(E_t)] = \min(0.8, 0.6) = 0.6$ is Z.
- Rule2: $\min[\mu_S(V_1),\mu_B(E_t)] = \min(0.8, 0.4) = 0.4$ is Z.
- Rule3: $\min[\mu_{VL}(V_1),\mu_{VH}(E_t)] = \min(0.2, 0.6) = 0.2$ is NL.
- Rule4: $\min[\mu_{VL}(V_1),\mu_B(E_t)] = \min(0.2, 0.4) = 0.2$ is NVL.

This implies for Rule 1, there is 60% certainty that the output will be Z. Rule 2 there is 40% certainty that the output will be a part of the Z. Rule 3 there is 20% certainty that the output will be a part of the NL. Rule 4 there is 20% certainty that the output will be a part of the NVL, which is seen from Figure A.4.

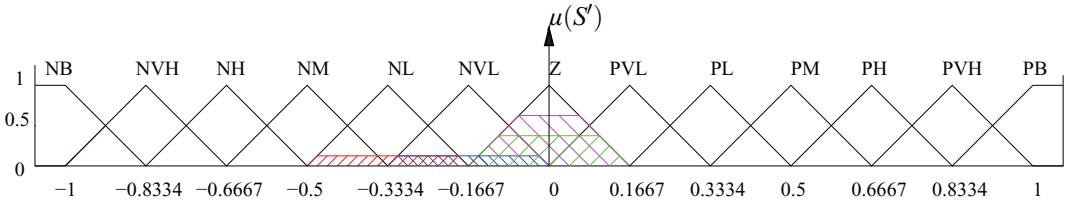

Figure A.4: Output membership function.

Once the certainty for each rule is determined, the consequent for each rule can be found. It is found by taking the membership function of the premise and multiplying the certainty to quantify the "then" operation to perform product function. This results in two half triangles and two rectangles at the bottom of Figure A.5.

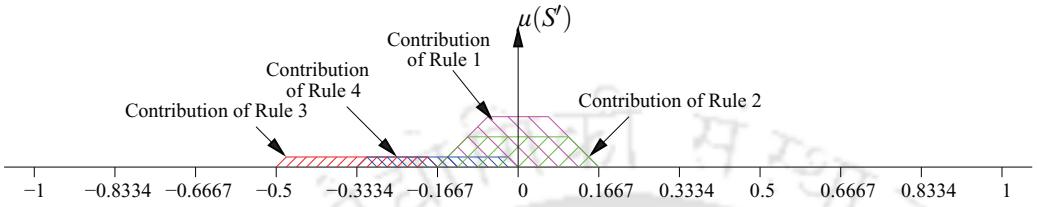

Figure A.5: Defuzzification process.

$$\mu\left(S'\right) = \frac{\begin{array}{c}(-0.5 \times 0) + (-0.467 \times 0.2) + (-0.133 \times 0.2) + (-0.067 \times 0.6) \\ + (0.067 \times 0.6) + (0.167 \times 0)\end{array}}{0 + 0.2 + 0.2 + 0.6 + 0.6 + 0} \tag{A.2}$$

Now based on (A.2), the crisp value of the output power can be calculated from the Figure A.5 as given in (A.2). The defuzzification is performed using the center of gravity method. In this case the output power is -0.075. This implies controller has directed the power to be flown to the DN from the CS. Negative power indicates that the CS will have to supply its energy to the DN to perform V2G operation.

A.3 Membership function and rule base of CC-FLC, M-FLC and PA-FLC of Chapter 2

The input and output fuzzy membership function of CC-FLC, PA-FLC shown and M-FLC is shown in Figure A.6 - A.7. The rule base used for CC-FLC, M-FLC and PA-FLC are shown in Table A.1 - A.2

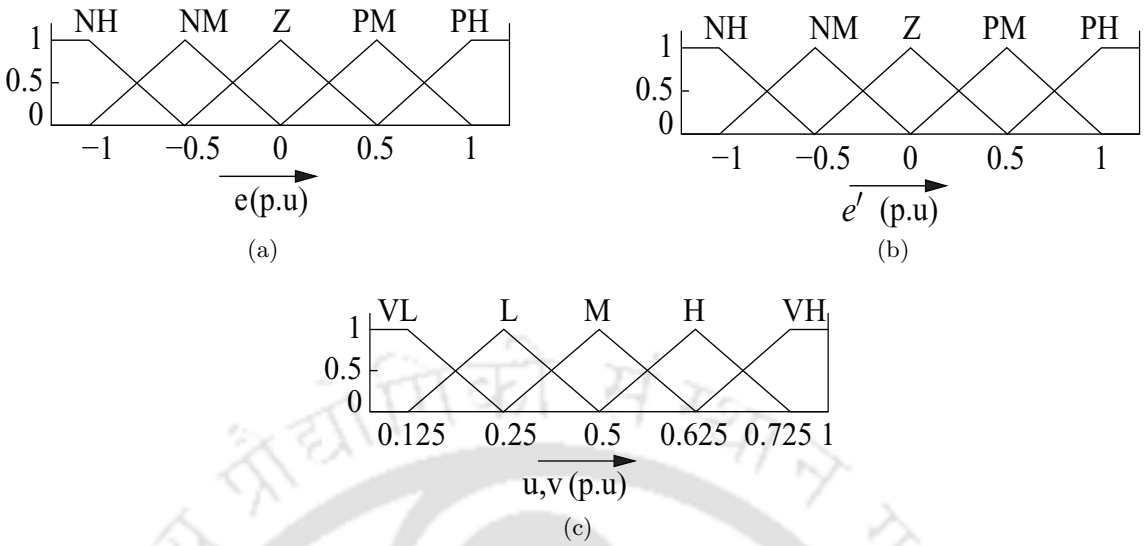

Figure A.6: Membership function of constant current constant voltage fuzzy control (CC-CV FLC) and magnitude fuzzy control (M-FLC) (a) input: error (e) (b) input: error rate (e') (c) output: reference signals (u and v).

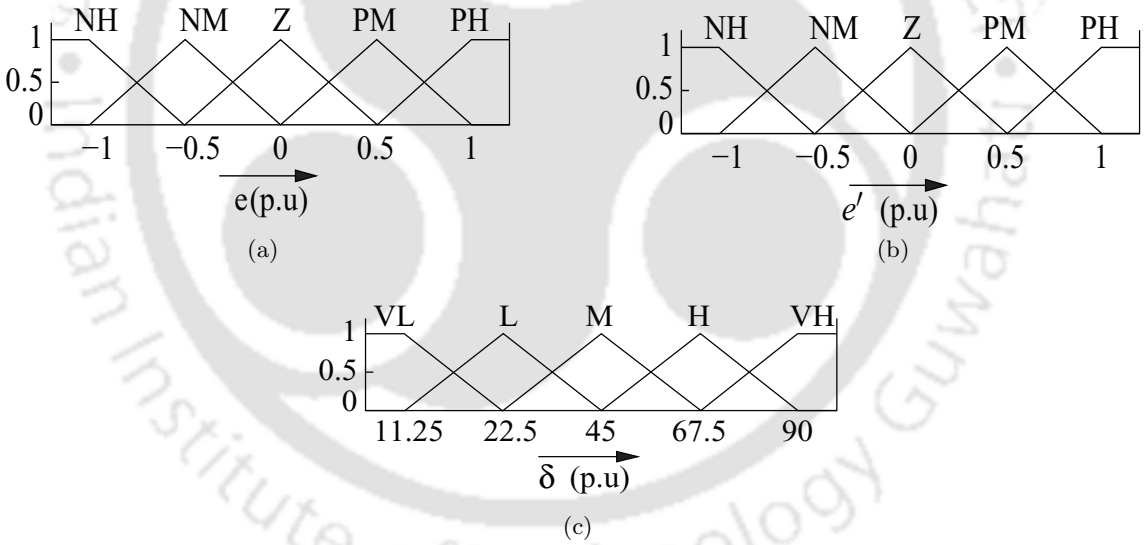

Figure A.7: Membership function of power angle fuzzy control (PA-FLC) (a) input: error (e) (b) input: error rate (e') (c) output: power angle (δ').

Table A.1: Rule base of CC-CV FLC and M-FLC

e, e'	NH	NM	Z	PM	PH
NH	VL	L	M	H	VH
NM	VL	L	M	H	VH
Z	VL	L	M	H	VH
PM	VL	L	M	H	VH
PH	VL	L	M	H	VH

Table A.2: Rule base of power angle FLC (PA-FLC)

e, e'	NH	NM	Z	PM	PH
NH	VL	L	M	H	VH
NM	VL	L	M	H	VH
Z	VL	L	M	H	VH
PM	VL	L	M	H	VH
PH	VL	L	M	H	VH

A.4 Fuzzification and defuzzification process for power angle control of Chapter 3

This part describes the fuzzification and defuzzification process of power angle control given in Chapter 3 for a practical example.

The controller inputs are error (E_r) and error rate (ΔE_r) obtained from reference power P_r and measured power (P_m). The range of E_r is taken to be between -1 to 1 p.u. The range of ΔE_r is taken to be between -1 to 1 p.u. The range of output power (δ) has been taken between 0 to 90°. The controls logic is designed in terms of 25 fuzzy rules. These rules transform the input variable to an output variable.

Consider the inputs: E_r as -0.7 p.u and ΔE_r as -0.1 p.u as shown in Figure A.8.

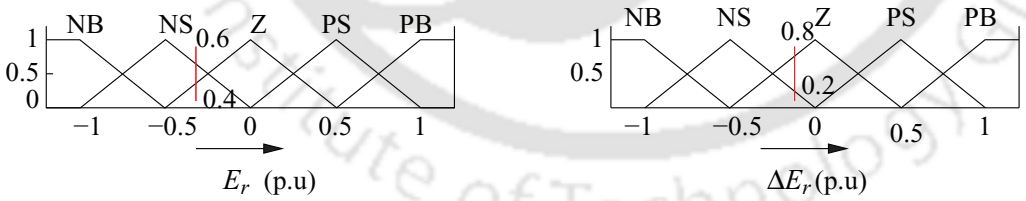

Figure A.8: Input membership function: E_r and ΔE_r.

It can be seen from Figure A.8, the value of E_r and ΔE_r belongs to two membership function. The corresponding four rules given by the membership functions are as follows:

- Rule 1 : If E_r is Negative Small (NS) and ΔE_r is Zero (Z) , then δ' is Medium (M).
- Rule 2 : If E_r is Negative Small (NS) and ΔE_r is Negative Small (NS), then δ' is Low (L).

- Rule 3 : If E_r is Zero (Z) and ΔE_r is Zero (Z), then δ' is Medium (M).
- Rule 4 : If E_r is Zero (Z) and ΔE_r is Negative Small (NS), then δ' is Low (L).

These rules shows that the power measured (P_m) from the charging system is more than the reference power (P_r), therefore the power has to be regulated to the level of P_r. The first step in this process is fuzzification. As discussed above, E_r is a member of two membership functions representing NS and Z and has different degree of membership function. ΔE_r is also a member of two membership function. The fuzzy set of E_r contributes 80% Z and 20% NS and ΔE_r contributes 80% Z and 20% NS. The next step is the inference process, where each rule is checked for the degrees of membership for the participating inputs. Here, rule 1 says that if the fuzzy set of E_r contributes 60% NS and ΔE_r is 80% Z, then δ' is M. Rule 2 says, E_r is 60% NS and ΔE_r is 20% NS, then δ' is L. Rule 3 says, E_r is 40% Z and ΔE_r is 80% Z, then δ' is M. Rule 4 says, E_r is 40% Z and ΔE_r is 20% NS, then δ' is L. In order to determine the degree of certainty of δ', the minimum method is applied. That means the minimum of the degree of membership values of the inputs is going to be the values for the output. This is defined mathematically as:

$$\mu_o(\delta') = \min\left(\mu_o(E_r),\, \mu_o(\Delta E_r)\right) \tag{A.3}$$

where $\mu_0\ (E_r)$, $\mu_0\ (\Delta E_r)$ and $\mu_0\ (\delta'\ )$ are membership functions of node voltage, total energy and power respectively. Using (A.3), the values for the output can be found as given below.

- Rule1: $\min[\mu_{NS}(E_r),\, \mu_Z(\Delta E_r)] = \min(0.6, 0.8) = 0.6$ is M.
- Rule2: $\min[\mu_{NS}(E_r),\, \mu_{NS}(\Delta E_r)] = \min(0.6, 0.2) = 0.2$ is L.
- Rule3: $\min[\mu_Z(E_r),\, \mu_Z(\Delta E_r)] = \min(0.4, 0.8) = 0.4$ is M.
- Rule4: $\min[\mu_Z(E_r),\, \mu_{NS}(\Delta E_r)] = \min(0.4, 0.2) = 0.2$ is L.

This implies for Rule 1, there is 60% certainty that the output will be M. Rule 2 there is 20% certainty that the output will be a part of the L. Rule 3 there is 40% certainty that the output will be a part of the M. Rule 4 there is 20% certainty that the output will be a part of the L, which is seen from Figure A.9.

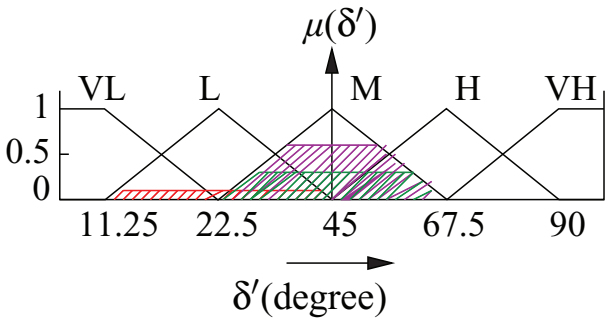

Figure A.9: Output membership function.

Once the certainty for each rule is determined, the consequent for each rule can be found. It is found by taking the membership function of the premise and multiplying the certainty to quantify the "then" operation to perform product function. This results in two half triangles and two rectangles at the bottom of Figure A.10.

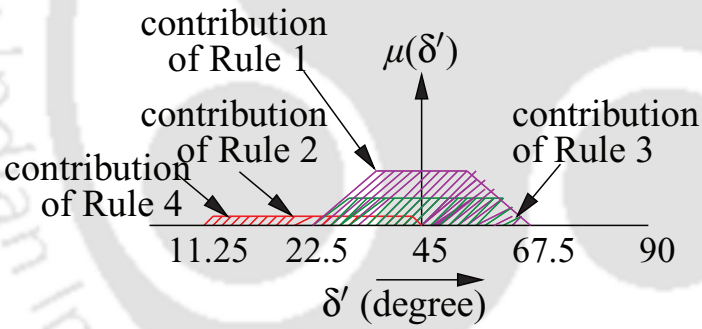

Figure A.10: Defuzzification process.

$$\mu\left(\delta'\right) = \frac{\begin{array}{c}(11.25 \times 0) + (12 \times 0.2) + (28.125 \times 0.4) \\ + (34 \times 0.6) + (56.25 \times 0.6) + (61.9 \times 0.4)\end{array}}{0 + 0.2 + 0.4 + 0.6 + 0.6 + 0.4} \tag{A.4}$$

Now based on (A.4), the crisp value of power angle can be calculated from the Figure A.10 as given in (A.4). The defuzzification is performed using the center of gravity method. In this case the delay angle is 42°.

A.5 Sample calculation for mutual inductance of Chapter 4

This part describes the computation procedure of MI computation described in Chapter 4. The following set of example considered details the calculation procedure. Consider two square coils of length (L) and width (W) of 18cm having a conductor diameter of 1.83mm. The number of turns for excitation (EC) and observation coils (OC) are 11 and 9 respectively. The current flow in EC is taken to be 10A. The following cases of variations are chosen for explanation of analytical model.

Case I: Perfect alignment - vertical variation: OC kept at a vertical height of 2cm with respect to EC.

Case II: Perfect alignment - planar variation: OC kept at a vertical height of 2.1cm and rotated with an angle of 10°.

Case III: Angular misalignment: The center to center distance between OC and EC is 12.8cm. OC is tilted to an angle of 10° with respect to EC.

The numerical values obtained in each step for multiple turns of OC are summarized in Table A.3 for the above considered cases. The flux linkage for each turn of OC is calculated using (4.8) and (4.9). From these results, the total flux linkage and mutual inductance is calculated using (4.10) and (4.1).

Table A.3: Results for sample calculation.

	SOC_{lt}						
φ_1	20.78	19.72	3.27	φ_6	20.03	18.87	2.83
φ_2	20.81	19.69	3.18	φ_7	19.60	18.49	2.74
φ_3	20.76	19.59	3.10	φ_8	19.09	18.04	2.64
φ_4	20.61	19.42	3.01	φ_9	18.49	17.52	2.55
φ_5	20.37	19.18	2.92				
λ_{12}	180.50	170.50	26.20				
M	18.05μH	17.05μH	2.62μH				

A.6 Remaining results of Chapter 5

This part has described the rest of the results from Chapter 5. Here the analysis explains to study the operation of the converter at three different modes of frequencies.

- Converter operation at resonance frequency ($f = f_o$)
- Converter operation above resonance frequency ($f > f_o$)

- Converter operation below resonance frequency ($f < f_o$)

Figure f-11 presents the experimental oscillograms of voltage and current at the primary and secondary side of the inductive system for converter operation at resonance frequency ($R_L = 1.2\Omega$ and $d = 2cm$). It has been seen, V_{in} and I_{in} has almost zero phase angle difference between them at $f = f_o$ and thereby the voltage and current are in phase. The circuit has only resistive nature due to which maximum current flow occurs in the system. As expected, highest power transfer occurs for operation at resonance frequency. Figure f-12 presents the experimental oscillograms of voltage and current

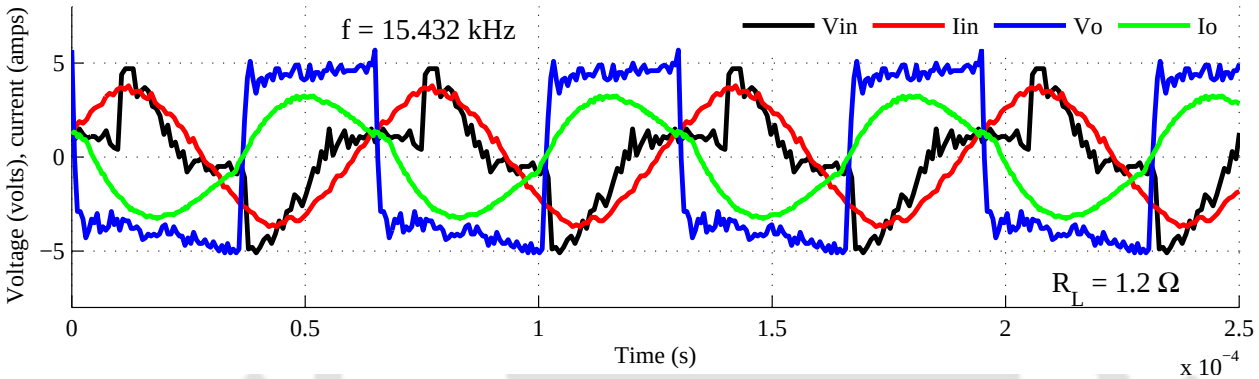

Figure f-11: Input and output voltage and current waveforms at $f = f_o$.

at the primary and secondary side of the inductive system for converter operation above resonance frequency ($R_L = 1.2\Omega$ and $d = 2cm$). In this case, V_{in} and I_{in} has phase angle difference between them. The current in the primary side is seen to be lagging the voltage while in secondary side, the current is leading the voltage. This shows for the primary side circuit, the inductive reactance is more and for the secondary side circuit capacitive reactance is more. It has also been noticed that the magnitudes of voltage and current is decreased which shows the frequency has been changed beyond the resonance point. Therefore, the power transfer in this case is less than the resonance condition.

Figure f-13 presents the experimental oscillograms of voltage and current at the primary and secondary side of the inductive system for converter operation below resonance frequency ($R_L = 1.2\Omega$ and $d = 2cm$). As the system is operated far below the resonance condition, the input current is not sinusoidal and seen to be oscillating. The current in the primary side is seen to be leading the voltage at low frequency while in secondary side, the current is lagging the voltage. This shows for the primary side circuit, the capacitive reactance is more and for the secondary side circuit inductive reactance is more. Due to large phase difference between the primary and secondary side, the voltage

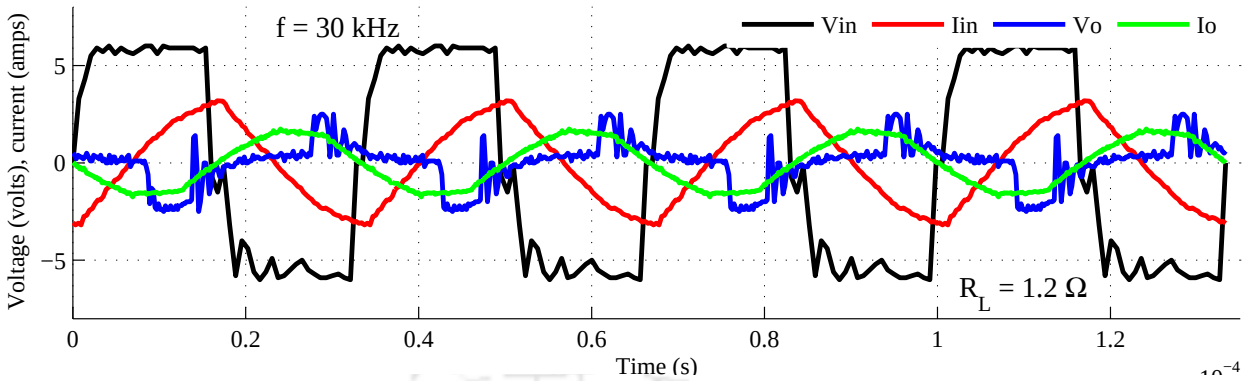

Figure f-12: Input and output voltage and current waveforms at $f > f_o$.

induced in the secondary side coil is less and the efficiency in this case is also got reduced.

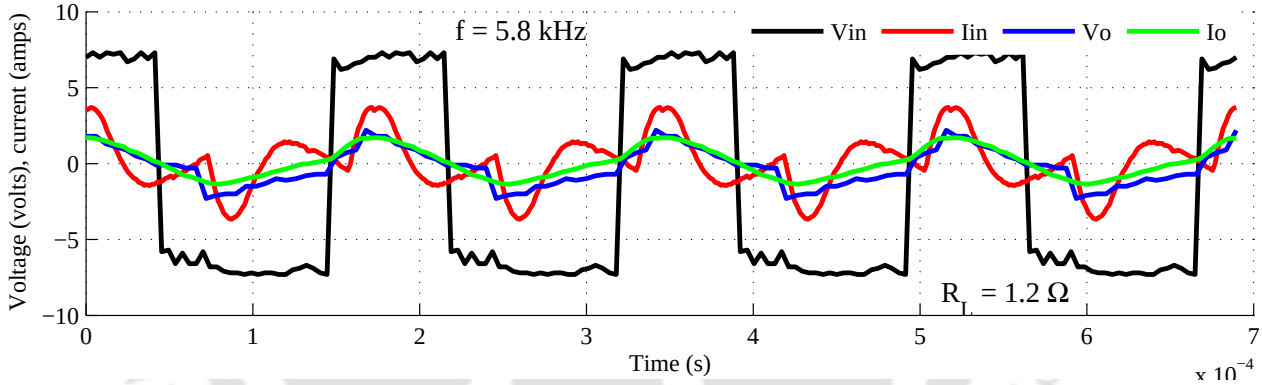

Figure f-13: Input and output voltage and current waveforms at $f < f_o$.

Figure f-14 shows the comparison of efficiency for four compensations at distance 4cm and $R_L = 1.2\Omega$. As explained, SS and PS topology has higher efficiency than SP and PP compensation. However, when compared at D=2cm the efficiency got reduced to 50% at distance 4cm and is further reduced for higher frequencies. This is because at higher distance causes leakage flux more than the main flux linkage due to larger air gap between the coils.

Figure f-15 shows the comparison of efficiency at 20kHz operating frequency for variable air gap distance of four compensation topology. The performance characteristics of efficiency curve is almost similar to the optimum resonance condition. This is because, the system has an operating range and it has higher efficiency in and around resonance condition. If the circuit goes far beyond the resonance point i.e. too higher or lower, the efficiency gradually falls. This necessitates the requirement of

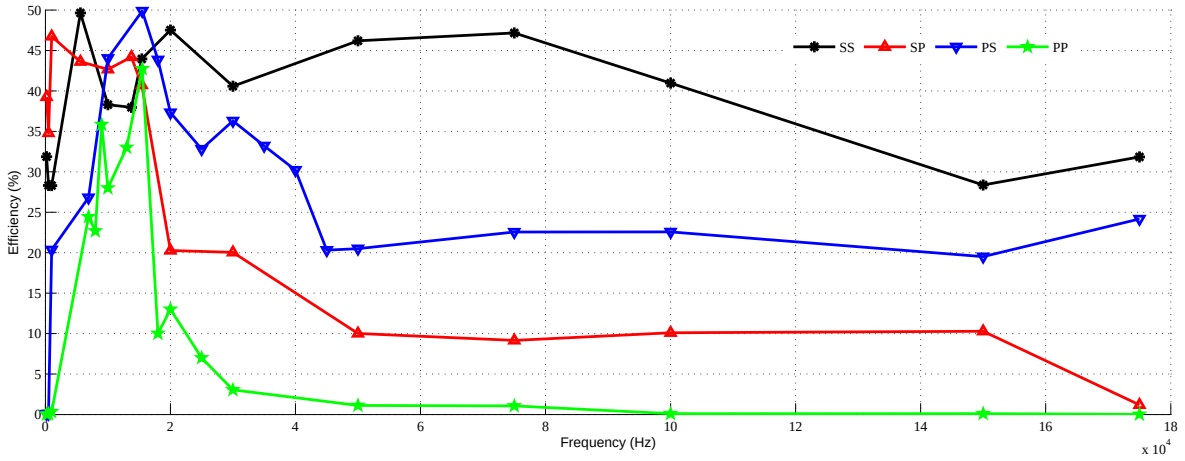

Figure f-14: Efficiency versus frequency at d=4cm, $R_L = 1.2\Omega$.

frequency control in the CPT system.

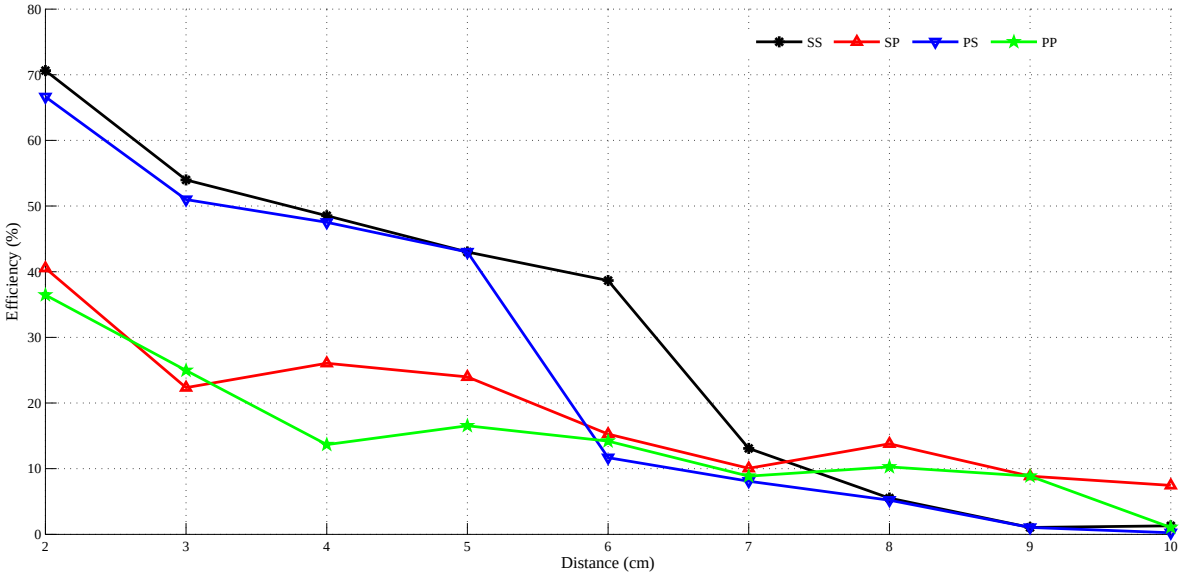

Figure f-15: Efficiency versus distance at f=20kHz, $R_L = 1.2\Omega$.

Figure f-16 shows the efficiency plot for variable load resistance at distance 4cm. As explained above, the efficiency of the system is less at higher distance due to large air gap. The leakage flux in the system is more than the main flux linked in the secondary. Furthermore, the impedance of the system changes due to which the efficiency of the system has changed.

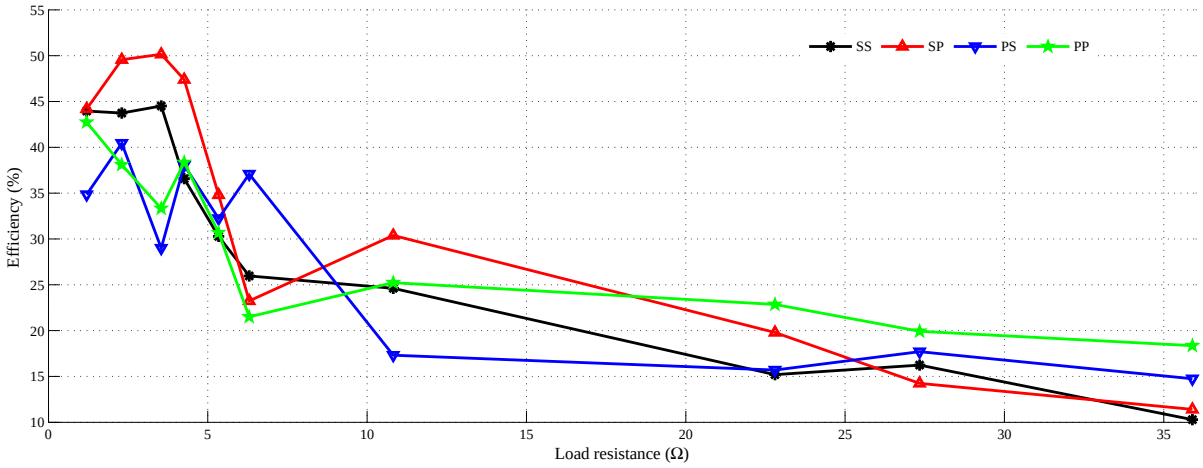

Figure f-16: Efficiency versus load resistance at d=4cm, f=15.432kHz.

Bibliography

[1] M. Kisacikoglu, B. Ozpineci, and L. Tolbert, "Ev/phev bidirectional charger assessment for v2g reactive power operation," *IEEE Transn. on Power Electron.*, vol. 28, no. 12, pp. 5717–5727, Dec 2013.

[2] M. Yilmaz and P. Krein, "Review of battery charger topologies, charging power levels, and infrastructure for plug-in electric and hybrid vehicles," *IEEE Transn. on Power Electron.*, vol. 28, no. 5, pp. 2151–2169, May 2013.

[3] D. Mayfield, "Siting electric vehicle charging stations," Sust. Transp. Strat., Clean Fuels Ohio, Apr. 2012.

[4] "Electric vehicle charging infrastructure deployment guidelines for the oregon i-5 metro areas of portland, salem, corvallis and eugene," Electric Transp. Eng. corp., Ecotality Company, Apr. 2010.

[5] "Residential electric vehicle (ev) charger guidelines," City of Riverside Building and Safety Division, ECOtality Company, Dec. 2012.

[6] D. Mayfield, "Selectric vehicle charging for persons with disabilities," Sust. Transp. Strat., Clean Fuels Ohio, Feb. 2012.

[7] "Long-range ev charging infrastructure plan for western oregon," City of Riverside Building and Safety Division, ECOtality Company, Aug. 2010.

[8] D. Mayfield, "Site design for electric vehicle charging stations," Sust. Transp. Strat., Clean Fuels Ohio, Jul. 2012.

[9] "Electric vehicle charging stations technical installation guide," Sust. Transp. Strat., Hydro-Quebec, Jan. 2012.

[10] G. Pistoia, *Electric and Hybrid Vehicles power sources, Models, sustainability, infrastructure and the market.* Elsev. Scien. and Tech. Rights, 2010.

[11] J. Larminie and J. Lowry, *Electric Vehicle Technology Explained.* John Wiley and Sons Ltd., 2003.

[12] M. Ehsani, Y. Gao, S. E.Gay, and A. Emadi, *Modern Electric, Hybrid Electric and Fuel Cell Vehicles, Fundamentals Theory and Design*, M. H. Rashid, Ed. CRC Press, 2005.

[13] Z. Liu, F. Wen, and G. Ledwich, "Optimal planning of electric-vehicle charging stations in distribution systems," *IEEE Trans. on Pow. Deliv.*, vol. 28, no. 1, pp. 102–110, 2013.

[14] J. L. Villa, J. Sallan, A. Llombart, and J. F. Sanz, "Design of a high frequency inductively coupled power transfer system for electric vehicle battery charge," *Appl. Ener.*, vol. 86, no. 3, pp. 355 – 363, 2009.

[15] M. F. M. Elias, K. M. Nor, N. Rahim, and A. K. Arof, "Lithium-ion battery charger for high energy application," *Nation. Pow. Eng. Conf.*, pp. 283–288, 2003.

[16] S. Bai and S. Lukic, "Unified active filter and energy storage system for an mw electric vehicle charging station," *IEEE Trans. on Pow. Electron.*, vol. 28, no. 12, pp. 5793–5803, Dec 2013.

[17] M. Etezadi-Amoli, K. Choma, and J. Stefani, "Rapid-charge electric-vehicle stations," *IEEE Trans. on Pow. Deliv.*, vol. 25, no. 3, pp. 1883–1887, 2010.

[18] S. Haghbin, S. Lundmark, M. Alakula, and O. Carlson, "Grid-connected integrated battery chargers in vehicle applications: Review and new solution," *IEEE Trans. on Ind. Electron.*, vol. 60, no. 2, pp. 459–473, 2013.

[19] X. Zhou, S. Lukic, S. Bhattacharya, and A. Huang, "Design and control of grid-connected converter in bi-directional battery charger for plug-in hybrid electric vehicle application," *IEEE Veh. Pow. and Propul. Conf. VPPC '09.*, pp. 1716–1721, 2009.

[20] K. Young, C. Wang, L. Wang, and K. Strunz, "Electric vehicle battery technologies," *Electric Veh. Integ. into Modern Pow. Net.*, pp. 15–56, 2013. [Online]. Available: http://dx.doi.org/10.1007/978-1-4614-0134-6_2.

[21] S. Chopra and P. Bauer, "Driving range extension of ev with on-road contactless power transfer x2014;a case study," *IEEE Trans. on Ind. Electron.*, vol. 60, no. 1, pp. 329–338, 2013.

[22] C.-S. Wang, G. Covic, and O. Stielau, "Power transfer capability and bifurcation phenomena of loosely coupled inductive power transfer systems," *IEEE Trans. on Ind. Electron.*, vol. 51, no. 1, pp. 148–157, 2004.

[23] C.-S. Wang, O. Stielau, and G. Covic, "Design considerations for a contactless electric vehicle battery charger," *IEEE Transn. on Ind. Electron.*, vol. 52, no. 5, pp. 1308–1314, Oct 2005.

[24] H. Bergner, K. Hempel, and G. Sargsjan, "Contactless detection of optical induced current in microelectronic devices by capacitive coupling," *Microelectron. Eng.*, vol. 2, no. 4, pp. 115 – 122, 1996.

[25] M. Koerdel, F. Alatas, A. Schick, S. Rupitsch, and R. Lerch, "Contactless inspection of planar electronic devices by capacitive coupling: Development of a model describing the sensor signal and its impact on signal post-processing," *Sensors and Actuators A: Physical*, vol. 172, no. 1, pp. 88 – 97, 2011.

[26] A. Hu, C. Liu, and H. L. Li, "A novel contactless battery charging system for soccer playing robot," *15th Intern. Conf. on Mech. and Mach. Vision in Practice*, pp. 646–650, 2008.

[27] M. Kline, I. Izyumin, B. Boser, and S. Sanders, "Capacitive power transfer for contactless charging," *Twenty-Sixth IEEE Ann. Appl. Pow. Electron. Conf. and Exposit. (APEC)*, pp. 1398–1404, 2011.

[28] C. Liu, A. Hu, and X. Dai, "A contactless power transfer system with capacitively coupled matrix pad," *IEEE Ener. Conv. Cong. and Exposit.(ECCE)*, pp. 3488–3494, 2011.

[29] W. P. Choi, W. C. Ho, X. Liu, and S. Hui, "Comparative study on power conversion methods for wireless battery charging platform," *14th Intern. Pow. Electron. and Mot. Cont. Conf. (EPE/PEMC)*, pp. S15–9–S15–16, 2010.

[30] E. Joy, A. Dalal, and P. Kumar, "The accurate computation of mutual inductance of two air core square coils with lateral and angular misalignments in a flat planar surface," *IEEE Trans. on Mag.*, pp. 1–9, Jan. 2014.

[31] J. Villa, J. Sallan, J. Sanz Osorio, and A. Llombart, "High-misalignment tolerant compensation topology for icpt systems," *IEEE Trans. on Ind. Electron.*, vol. 59, no. 2, pp. 945–951, Feb. 2012.

[32] S. Xun Liu ; Shatin ; Hui, "Simulation study and experimental verification of a universal contactless battery charging platform with localized charging features," *IEEE Trans. on Power Electron.*, vol. 22, no. 6, pp. 2202 – 2210, Nov. 2007.

[33] X. . H. S. Zhong, W.X. ; Kowloon; Liu, "A novel single-layer winding array and receiver coil structure for contactless battery charging systems with free-positioning and localized charging features," *IEEE Trans. on Ind. Electron.*, vol. 58, no. 9, pp. 4136 – 4144, Sept. 2011.

[34] C. Mecke, R.; Rathge, "High frequency resonant inverter for contactless energy transmission over large air gap," *IEEE 35th Ann. (Volume:3) Power Electron. Specia. Conf., PESC 04.*, vol. 58, no. 9, pp. 1737 – 1743, June. 2004.

[35] J. T. Boys, G. A. Covic, and A. W. Green, "Stability and control of inductively coupled power transfer systems," *Electric Power Applications, IEE Proceedings* -, vol. 147, no. 1, pp. 37–43, Jan. 2000.

[36] J. Sallan, J. Villa, A. Llombart, and J. Sanz, "Optimal design of icpt systems applied to electric vehicle battery charge," *IEEE Transn. on Ind. Electron.*, vol. 56, no. 6, pp. 2140–2149, June 2009.

[37] X. Liu and S. Hui, "Optimal design of a hybrid winding structure for planar contactless battery charging platform," *IEEE Trans. on Power Electron.*, vol. 23, no. 1, pp. 455–463, Jan 2008.

[38] M. Budhia, G. Covic, and J. Boys, "Magnetic design of a three-phase inductive power transfer system for roadway powered electric vehicles," pp. 1–6, Sept 2010.

[39] D. K. Cheng, *Field and Wave Electromagnetics*, 2nd ed., ser. The Addison-Wesley series in electrical engineering. Addison-Wesley, Jan. 1989. [Online]. Available: http://www.amazon.com/exec/obidos/redirect?tag=citeulike07-20\&path=ASIN/0201128195

[40] C. Zhou, K. Qian, M. Allan, and W. Zhou, "Modeling of the cost of ev battery wear due to v2g application in power systems," *IEEE Trans. on Ener. Conv.*, vol. 26, no. 4, pp. 1041–1050, 2011.

[41] C. Rathge and D. Kuschner, "High efficient inductive energy and data transmission system with special coil geometry," *13th Europ. Conf. on Pow. Electron. and Appln, EPE '09.*, pp. 1–8, Sept. 2009.

[42] J. Shin, S. Shin, Y. Kim, S. Ahn, S. Lee, G. Jung, S. Jeon, and D. Cho, "Design and implementation of shaped magnetic resonance based wireless power transfer system for roadway-powered moving electric vehicles," *IEEE Trans. on Ind. Electron.*, vol. PP, no. 99, pp. 1–1, March 2013.

[43] A. Kelley and W. Owens, "Connectorless power supply for an aircraft-passenger entertainment system," *IEEE Trans. on Pow. Electron.*, vol. 4, no. 3, pp. 348–354, Jul. 1989.

[44] J. Barnard, J. Ferreira, and J. Van Wyk, "Sliding transformers for linear contactless power delivery," *IEEE Trans. on Ind. Electron.*, vol. 44, no. 6, pp. 774–779, Dec. 1997.

[45] C.-G. Kim, D.-H. Seo, J.-S. You, J.-H. Park, and B. H. Cho, "Design of a contactless battery charger for cellular phone," *IEEE Trans. on Ind. Electron.*, vol. 48, no. 6, pp. 1238–1247, Dec. 2001.

[46] T. Bieler, M. Perrottet, V. Nguyen, and Y. Perriard, "Contactless power and information transmission," *IEEE Trans. on Ind. Appln.*, vol. 38, no. 5, pp. 1266–1272, Sept/Oct. 2002.

[47] Y. Jang and M. Jovanovic, "A contactless electrical energy transmission system for portable-telephone battery chargers," *IEEE Trans. on Ind. Electron.*, vol. 50, no. 3, pp. 520–527, June 2003.

[48] G. A. J. Elliott, G. Covic, D. Kacprzak, and J. Boys, "A new concept: Asymmetrical pick-ups for inductively coupled power transfer monorail systems," *IEEE Trans. on Magn.*, vol. 42, no. 10, pp. 3389–3391, Oct. 2006.

[49] J. Casanova, Z. N. Low, and J. Lin, "Design and optimization of a class-e amplifier for a loosely coupled planar wireless power system," *IEEE Trans. on Circ. and Sys. II: Express Briefs,*, vol. 56, no. 11, pp. 830–834, Nov. 2009.

[50] D. A. G. Pedder, A. Brown, and J. Skinner, "A contactless electrical energy transmission system," *IEEE Trans. on Ind. Electron.*, vol. 46, no. 1, pp. 23–30, Feb. 1999.

[51] U. Madawala and D. Thrimawithana, "A bidirectional inductive power interface for electric vehicles in v2g systems," *IEEE Trans. on Ind. Electron.*, vol. 58, no. 10, pp. 4789–4796, Oct 2011.

[52] M. Kisacikoglu, B. Ozpineci, and L. Tolbert, "Examination of a phev bidirectional charger system for v2g reactive power compensation," *IEEE Twenty-Fifth Ann. Appl. Pow. Electron. Conf. and Exposit. (APEC)*, pp. 458–465, 2010.

[53] C. Tang, X. Dai, Z. Wang, Y. Su, and Y. Sun, "A bidirectional contactless power transfer system with dual-side power flow control," pp. 1–6, Oct 2012.

[54] A. Swain, M. Neath, U. Madawala, and D. Thrimawithana, "A dynamic multivariable state-space model for bidirectional inductive power transfer systems," *IEEE Trans. on Pow. Electron.*, vol. 27, no. 11, pp. 4772–4780, 2012.

[55] C. Guille and G. Gross, "Design of a conceptual framework for the v2g implementation," *IEEE Ener. 2030 Conf.*, pp. 1–3, 2008.

[56] D. P. Ghosh, R. J. Thomas, and S. B. Wicker, "A privacy-aware design for the vehicle-to-grid framework," *46th Hawaii Inter. Conf. on Sys. Scien. (HICSS)*, pp. 2283–2291, 2013.

[57] Y. Ota, H. Taniguchi, T. Nakajima, K. Liyanage, J. Baba, and A. Yokoyama, "Autonomous distributed v2g (vehicle-to-grid) satisfying scheduled charging," *IEEE Trans. on Smart Grid*, vol. 3, no. 1, pp. 559–564, 2012.

[58] E. Sortomme and M. El-Sharkawi, "Optimal scheduling of vehicle-to-grid energy and ancillary services," *IEEE Trans. on Smart Grid*, vol. 3, no. 1, pp. 351–359, 2012.

[59] Z. Darabi and M. Ferdowsi, "Aggregated impact of plug-in hybrid electric vehicles on electricity demand profile," *IEEE Trans. on Sust. Ener.*, vol. 2, no. 4, pp. 501–508, 2011.

[60] J. Pillai and B. Bak-Jensen, "Integration of vehicle-to-grid in the western danish power system," *IEEE Trans. on Sust. Ener.*, vol. 2, no. 1, pp. 12–19, 2011.

[61] H. Guo, Y. Wu, F. Bao, H. Chen, and M. Ma, "Ubapv2g: A unique batch authentication protocol for vehicle-to-grid communications," *IEEE Trans. on Smart Grid*, vol. 2, no. 4, pp. 707–714, 2011.

[62] T. Mishima, K. Akamatsu, and M. Nakaoka, "A high frequency-link secondary-side phase-shifted full-range soft-switching pwm dc-dc converter with zcs active rectifier for ev battery chargers," *IEEE Transn. on Power Electron.*, vol. 28, no. 12, pp. 5758–5773, Dec 2013.

[63] C.-Y. Oh, D.-H. Kim, D.-G. Woo, W.-Y. Sung, Y.-S. Kim, and B.-K. Lee, "A high-efficient nonisolated single-stage on-board battery charger for electric vehicles," *IEEE Transn. on Power Electron.*, vol. 28, no. 12, pp. 5746–5757, Dec 2013.

[64] B. Gu, J.-S. Lai, N. Kees, and C. Zheng, "Hybrid-switching full-bridge dc dc converter with minimal voltage stress of bridge rectifier, reduced circulating losses, and filter requirement for electric vehicle battery chargers," *IEEE Transn. on Power Electron.*, vol. 28, no. 3, pp. 1132–1144, March 2013.

[65] S. Deilami, A. Masoum, P. Moses, and M. Masoum, "Real-time coordination of plug-in electric vehicle charging in smart grids to minimize power losses and improve voltage profile," *IEEE Trans. Smart Grid*, vol. 2, no. 3, pp. 456–467, Sept. 2011.

[66] A. Masoum, S. Deilami, P. Moses, M. Masoum, and A. Abu-siada, "Smart load management of plug-in electric vehicles in distribution and residential networks with charging stations for peak shaving and loss minimisation considering voltage regulation," *IET Generation, Transmission Distribution*, vol. 5, no. 8, pp. 877–888, August 2011.

[67] R. Crosier, S. Wang, and M. Jamshidi, "A 4800-v grid-connected electric vehicle charging station that provides stacom-apf functions with a bi-directional, multi-level, cascaded converter," pp. 1508–1515, Feb 2012.

[68] S. Babic and C. Akyel, "New formulas for mutual inductance and axial magnetic force between magnetically coupled coils: Thick circular coil of the rectangular cross-section-thin disk coil (pancake)," *IEEE Trans. on Magn.*, vol. 49, no. 2, pp. 860–868, Feb. 2013.

[69] T. Ho, B. Gomersall, and L. Ran, "Contactless charging for electric vehicles with a large air gap," *Proceed. of Europ. Conf. on Pow. Electron. and Appln(EPE 2011)*, pp. 1–10, 2011.

[70] J. Wang, S. Ho, W. Fu, and M. Sun, "Analytical design study of a novel witricity charger with lateral and angular misalignments for efficient wireless energy transmission," *IEEE Trans. Magn.*, vol. 47, no. 10, pp. 2616 –2619, Oct. 2011.

[71] C.-S. Wang, G. Covic, and O. Stielau, "General stability criterions for zero phase angle controlled loosely coupled inductive power transfer systems," *27th IEEE Ann. Conf. of Ind. Electron. Soc. (IECON)*, vol. 2, pp. 1049–1054 vol.2, 2001.

[72] M. Khan, I. Husain, and Y. Sozer, "Integrated electric motor drive and power electronics for bidirectional power flow between the electric vehicle and dc or ac grid," *IEEE Transn. on Power Electron.*, vol. 28, no. 12, pp. 5774–5783, Dec 2013.

[73] K. Clement-Nyns, E. Haesen, and J. Driesen, "The impact of charging plug-in hybrid electric vehicles on a residential distribution grid," *IEEE Trans. on Power Sys.*, vol. 25, no. 1, pp. 371–380, Feb. 2010.

[74] Z. Yang, S. Yu, W. Lou, and C. Liu, "Privacy-preserving communication and precise reward architecture for V2G networks in smart grid," *IEEE Trans. Smart Grid*, vol. 2, no. 4, pp. 697–706, Dec. 2011.

[75] N. Rotering and M. Ilic, "Optimal charge control of plug-in hybrid electric vehicles in deregulated electricity markets," *IEEE Trans. Power Syst.*, vol. 26, no. 3, pp. 1021–1029, Aug. 2011.

[76] S. Bifaretti, P. Zanchetta, A. Watson, L. Tarisciotti, and J. Clare, "Advanced power electronic conversion and control system for universal and flexible power management," *IEEE Transn. on Smart Grid*, vol. 2, no. 2, pp. 231–243, June 2011.

[77] G. Capizzi, F. Bonanno, and G. Tina, "Recurrent neural network-based modeling and simulation of lead-acid batteries charge discharge," *IEEE Trans. on Energ. Conv.*, vol. 26, no. 2, pp. 435–443, June 2011.

[78] V. Agarwal, K. Uthaichana, R. DeCarlo, and L. Tsoukalas, "Development and validation of a battery model useful for discharging and charging power control and lifetime estimation," *IEEE Trans. on Energ. Conv.*, vol. 25, no. 3, pp. 821–835, Sept 2010.

[79] K. Thirugnanam, J. Ezhil Reena, M. Singh, and P. Kumar, "Mathematical modeling of li-ion battery using genetic algorithm approach for v2g applications," *IEEE Trans. on Energ. Conversn.*, vol. 29, no. 2, pp. 332–343, June 2014.

[80] S. Han, S. Han, and K. Sezaki, "Development of an optimal vehicle-to-grid aggregator for frequency regulation," *IEEE Trans. on Smart Grid*, vol. 1, no. 1, pp. 65–72, June 2010.

[81] ——, "Estimation of achievable power capacity from plug-in electric vehicles for V2G frequency regulation: Case studies for market participation," *IEEE Trans. Smart Grid*, vol. 2, no. 4, pp. 632–641, Dec. 2011.

[82] H. Liu, Z. Hu, Y. Song, and J. Lin, "Decentralized vehicle-to-grid control for primary frequency regulation considering charging demands," *IEEE Trans. Power Syst.*, vol. 28, no. 3, pp. 3480–3489, Aug. 2013.

[83] J. Escudero-Garzas, A. Garcia-Armada, and G. Seco-Granados, "Fair design of plug-in electric vehicles aggregator for v2g regulation," *IEEE Trans. Veh. Technol.*, vol. 61, no. 8, pp. 3406–3419, Oct. 2012.

[84] C. Evangelista, F. Valenciaga, and P. Puleston, "Active and reactive power control for wind turbine based on a mimo 2-sliding mode algorithm with variable gains," *IEEE Trans. on Energ. Conv.*, vol. 28, no. 3, pp. 682–689, Sept 2013.

[85] S. M. A. Cruz, "An active reactive power method for the diagnosis of rotor faults in three-phase induction motors operating under time-varying load conditions," *IEEE Trans. on Energ. Conv.*, vol. 27, no. 1, pp. 71–84, March 2012.

[86] A. Moawwad, V. Khadkikar, and J. Kirtley, "A new P-Q-V droop control method for an interline photovoltaic (I-PV) power system," *IEEE Trans. on Power Deliv.*, vol. 28, no. 2, pp. 658–668, April 2013.

[87] M. Singh, P. Kumar, and I. Kar, "Implementation of vehicle to grid infrastructure using fuzzy logic controller," *IEEE Trans. on Smart Grid*, vol. 3, no. 1, pp. 565–577, March 2012.

[88] P. M. S. Carvalho, P. F. Correia, and L. Ferreira, "Distributed reactive power generation control for voltage rise mitigation in distribution networks," *IEEE Trans. on Power Sys.*, vol. 23, no. 2, pp. 766–772, May 2008.

[89] R. H. Liang and Y. S. Wang, "Fuzzy-based reactive power and voltage control in a distribution system," *IEEE Trans. on Power Deliv.*, vol. 22, no. 12, pp. 64–64, Dec 2002.

[90] M. Helmbrecht, C. Olaverri-Monreal, K. Bengler, R. Vilimek, and A. Keinath, "How electric vehicles affect driving behavioral patterns," *IEEE Intell. Transp. Sys Magaz.*, vol. 6, no. 3, pp. 22–32, Fall 2014.

[91] Z. Duan, B. Gutierrez, and L. Wang, "Forecasting plug-in electric vehicle sales and the diurnal recharging load curve," *IEEE Trans. on Smart Grid*, vol. 5, no. 1, pp. 527–535, Jan 2014.

[92] Y. Ma, T. Houghton, A. Cruden, and D. Infield, "Modeling the benefits of vehicle-to-grid technology to a power system," *IEEE Trans. on Power Systm.*, vol. 27, no. 2, pp. 1012–1020, May 2012.

[93] S. Han, S. Han, and K. Sezaki, "Estimation of achievable power capacity from plug-in electric vehicles for v2g frequency regulation: Case studies for market participation," *IEEE Trans. on Smart Grid*, vol. 2, no. 4, pp. 632–641, Dec 2011.

[94] T. Ezhil Reena Joy, K. Thirugnanam, and P. Kumar, "A novel reduced switch count bidirectional contactless charging system for evs and phevs applications," *IEEE Students Confer.on Enging.and Sys. (SCES)*, pp. 1–6, 2013.

[95] Y. He, B. Venkatesh, and L. Guan, "Optimal scheduling for charging and discharging of electric vehicles," *IEEE Trans. on Smart Grid*, vol. 3, no. 3, pp. 1095–1105, Sept 2012.

[96] D. Wu, D. Aliprantis, and L. Ying, "Load scheduling and dispatch for aggregators of plug-in electric vehicles," *IEEE Trans. on Smart Grid*, vol. 3, no. 1, pp. 368–376, March 2012.

[97] C.-Y. Oh, D.-H. Kim, D.-G. Woo, W.-Y. Sung, Y.-S. Kim, and B.-K. Lee, "A high-efficient nonisolated single-stage on-board battery charger for electric vehicles," *IEEE Transn. on Power Electron.*, vol. 28, no. 12, pp. 5746–5757, Dec 2013.

[98] R. Metidji, B. Metidji, and B. Mendil, "Design and implementation of a unity power factor fuzzy battery charger using an ultrasparse matrix rectifier," *IEEE Transn. on Power Electron.*, vol. 28, no. 5, pp. 2269–2276, May 2013.

[99] R. . S. W. Crosier, "Dq- frame modeling of an active power filter integrated with a grid connected multifunctional electric vehcile charging station," *IEEE Transn. on Power Electron.*, 2013.

[100] F.-J. Lin, M.-S. Huang, P.-Y. Yeh, H.-C. Tsai, and C.-H. Kuan, "Dsp-based probabilistic fuzzy neural network control for li-ion battery charger," *IEEE Transn. on Power Electron.*, vol. 27, no. 8, pp. 3782–3794, Aug 2012.

[101] J. Traube, F. Lu, D. Maksimovic, J. Mossoba, M. Kromer, P. Faill, S. Katz, B. Borowy, S. Nichols, and L. Casey, "Mitigation of solar irradiance intermittency in photovoltaic power systems with integrated electric-vehicle charging functionality," *IEEE Transn. on Power Electron.*, vol. 28, no. 6, pp. 3058–3067, June 2013.

[102] G. Carli and S. Williamson, "Technical considerations on power conversion for electric and plug-in hybrid electric vehicle battery charging in photovoltaic installations," *IEEE Transn. on Power Electron.*, vol. 28, no. 12, pp. 5784–5792, Dec 2013.

[103] K. Aditya and S. S. Williamson, "Design considerations for loosely coupled inductive power transfer (ipt) system for electric vehicle battery charging a comprehensive review," *IEEE Transptn. Electrific. Conf. and Expo (ITEC), 2014*, June 2014.

[104] J. Hayes, M. Egan, J. M. D. Murphy, S. Schulz, and J. Hall, "Wide-load-range resonant converter supplying the sae j-1773 electric vehicle inductive charging interface," *IEEE Transn. on Industry Appln.*, vol. 35, no. 4, pp. 884–895, Jul 1999.

[105] G. Covic, J. Boys, M. Kissin, and H. Lu, "A three-phase inductive power transfer system for roadway-powered vehicles," *IEEE Transn. on Ind. Electron.*, vol. 54, no. 6, pp. 3370–3378, Dec 2007.

[106] D. Thrimawithana and U. Madawala, "A three-phase bi-directional ipt system for contactless charging of electric vehicles," pp. 1957–1962, June 2011.

[107] D. Thrimawithana and U. Madawala, "A novel matrix converter based bi-directional ipt power interface for v2g applications," pp. 495–500, Dec 2010.

[108] S. Nakadachi, S. Mochizuki, S. Sakaino, Y. Kaneko, S. Abe, and T. Yasuda, "Bidirectional contactless power transfer system expandable from unidirectional system," pp. 3651–3657, Sept 2013.

[109] H. Li, A. Hu, G. Covic, and C. Tang, "A new primary power regulation method for contactless power transfer," pp. 1–5, Feb 2009.

[110] M. H. Rashid, *Power Electronics Circuits Devices and Applications*, second edition ed. Pearson Education, 2004.

[111] S. Babic, F. Sirois, C. Akyel, G. Lemarquand, V. Lemarquand, and R. Ravaud, "New formulas for mutual inductance and axial magnetic force between a thin wall solenoid and a thick circular coil of rectangular cross-section," *IEEE Trans. Magn.*, vol. 47, no. 8, pp. 2034 –2044, Aug. 2011.

[112] Y. Su, X. Liu, and S. Hui, "Mutual inductance calculation of movable planar coils on parallel surfaces," *IEEE Trans.Power Electron.*, vol. 24, no. 4, pp. 1115 –1123, April 2009.

[113] M. Soma, D. C. Galbraith, and R. L. White, "Radio-frequency coils in implantable devices: Misalignment analysis and design procedure," *IEEE Trans. Biomed. Eng.*, vol. BME-34, no. 4, pp. 276 –282, April 1987.

[114] S. Hui, H. Chung, and S. Tang, "Coreless pcb-based transformers for power mosfet/igbt gate drive circuits," *28th Ann. IEEE Power Electron. Spec. Conf., PESC97*, vol. 2, pp. 1171 –1176, Jun 1997.

[115] F. Grover, *Inductances calculations.* Dover Pulications, News York, 1964.

[116] T. Engel and D. Mueller, "High-speed and high-accuracy method of mutual-inductance calculations," *IEEE Trans. Plas. Scien.*, vol. 37, no. 5, pp. 683 –692, May 2009.

[117] S. Babic and C. Akyel, "Calculating mutual inductance between circular coils with inclined axes in air," *IEEE Trans.Magn.*, vol. 44, no. 7, pp. 1743 –1750, July 2008.

[118] T. H. Fawzi and P. E. Burke, "The accurate computation of self and mutual inductances of circular coils," *IEEE Trans. Power Apparatus and Systm.*, vol. PAS-97, no. 2, pp. 464 –468, March 1978.

[119] T. Engel and S. Rohe, "A comparison of single-layer coaxial coil mutual inductance calculations using finite-element and tabulated methods," *IEEE Tran. Magnetics.*, vol. 42, no. 9, pp. 2159 –2163, Sept. 2006.

[120] D. Zhang and C. S. Koh, "An efficient semianalytic computation method of magnetic field for a circular coil with rectangular cross section," *IEEE Trans. Magn.*, vol. 48, no. 1, pp. 62 –68, Jan. 2012.

[121] J. Conway, "Noncoaxial inductance calculations without the vector potential for axisymmetric coils and planar coils," *IEEE Trans.Magn.*, vol. 44, no. 4, pp. 453 –462, Apr. 2008.

[122] S. Babic and C. Akyel, "Improvement in calculation of the self- and mutual inductance of thin-wall solenoids and disk coils," *IEEE Trans. Magn.*, vol. 36, no. 4, pp. 1970 – 1975, July 2000.

[123] S. Babic, C. Akyel, and S. Salon, "New procedures for calculating the mutual inductance of the system: filamentary circular coil-massive circular solenoid," *IEEE Trans.Magn.*, vol. 39, no. 3, pp. 1131 – 1134, May 2003.

[124] S. Babic, S. Salon, and C. Akyel, "The mutual inductance of two thin coaxial disk coils in air," *IEEE Trans. Magn.*, vol. 40, no. 2, pp. 822 – 825, March 2004.

[125] J. Conway, "Inductance calculations for circular coils of rectangular cross section and parallel axes using bessel and struve functions," *IEEE Trans.Magn.*, vol. 46, no. 1, pp. 75 –81, Jan. 2010.

[126] J.T. Conway,, "Exact solutions for the mutual inductance of circular coils and elliptic coils," *IEEE Trans.Magn.*, vol. 48, no. 1, pp. 81 –94, Jan. 2012.

[127] L. Forbes, S. Crozier, and D. Doddrell, "Rapid computation of static fields produced by thick circular solenoids," *IEEE Trans. Magn.*, vol. 33, no. 5, pp. 4405 –4410, Sept. 1997.

[128] R. Ravaud, G. Lemarquand, S. Babic, V. Lemarquand, and C. Akyel, "Cylindrical magnets and coils: Fields, forces, and inductances," *IEEE Trans. Magn.*, vol. 46, no. 9, pp. 3585 –3590, Sept. 2010.

[129] J. de Boeij, E. Lomonova, and A. Vandenput, "Contactless energy transfer to a moving load part i: Topology synthesis and fem simulation," *IEEE Intern. Symp. on Ind. Electron.*, vol. 2, pp. 739 –744, July 2006.

[130] J. L. Villa, J. Salln, A. Llombart, and J. F. Sanz, "Design of a high frequency inductively coupled power transfer system for electric vehicle battery charge," *Applied Energy*, Jun.

[131] K. O'Brien, G. Scheible, and H. Gueldner, "Design of large air-gap transformers for wireless power supplies," *34th Ann. Power Electron. Spec. Conf.*, vol. 4, pp. 1557 – 1562, June 2003.

[132] X. Liu and S. Hui, "Optimal design of a hybrid winding structure for planar contactless battery charging platform," *IEEE Trans. on Power Electron.*, vol. 5, no. 1, pp. 455–463, Jan. 2006.

[133] E. Joy, B. Kushwaha, G. Rituraj, and P. Kumar, "Impact of circuit parameters in contactless power transfer system," *IEEE International Conf. on Power Electron., Drives and Energ. Systems Conf.*, 2014.

[134] G. Rituraj, E. Joy, B. Kushwaha, and P. Kumar, "Analysis and comparison of series-series and series - parallel topology for contactless power transfer systems," *IEEE TENCON Conf.*, 2014.

[135] E. Joy, B. Kushwaha, G. Rituraj, and P. Kumar, "Analysis and comparison of four compensation topologies in contactless power transfer systems," 11^{th} *IEEE India Conf (INDICON).*, 2014.

[136] B. Kushwaha, G. Rituraj, E. Joy, and P. Kumar, "Modeling and analysis of inductively coupled power transfer systems," 11^{th} *IEEE India Conf (INDICON).*, 2014.

[137] M. Ryu, H. Cha, Y. Park, and J. Back, "Analysis of the contactless power transfer system using modelling and analysis of the contactless transformer," *31st IEEE Ann. Conf. of Ind. Electron. Societ. (IECON)*, pp. 7 pp.–, 2005.

[138] U. Madawala, M. Neath, and D. Thrimawithana, "A power frequency controller for bidirectional inductive power transfer systems," *IEEE Trans. on Ind. Electron.*, vol. 60, no. 1, pp. 310–317, Jan. 2013.

[139] U. Madawala and D. Thrimawithana, "A single controller for inductive power transfer systems," *35th IEEE Ann. Conf. of Indn. Electron.(IECON)*, pp. 109–113, 2009.

[140] H. Li, A. Hu, and G. Covic, "Current fluctuation analysis of a quantum ac-ac resonant converter for contactless power transfer," pp. 1838–1843, 2010.

[141] A. Abdolkhani and A. Hu, "A novel detached magnetic coupling structure for contactless power transfer," in *37th IEEE Ann. Conf. on Ind. Electron. Soc. (IECON)*, 2011, pp. 1103–1108.

[142] W. . J. N. . B. C. . T. A. Lim, "Low-profile contactless battery charger using planar printed circuit board windings as energy transfer device," *IEEE 33rd Ann. (Volume:2) Power Electron. Speci. Conf., pesc 02.*, vol. 2, no. 9, pp. 579 – 584, Sept. 2002.

[143] G. Chwei-Sen Wang ; Stielau, O.H. ; Covic, "Load models and their application in the design of loosely coupled inductive power transfer systems," *Intern. Conf. on Power Sys. Tech. PowerCon 2000.*, vol. 2, no. 1, pp. 1053 – 1058, Sept. 2000.

[144] M. Borage, S. Tiwari, and S. Kotaiah, "Lcl-t resonant converter with clamp diodes: A novel constant-current power supply with inherent constant-voltage limit," *IEEE Trans. on Ind. Electron.*, vol. 54, no. 2, pp. 741–746, April 2007.

[145] H. Abe, H. Sakamoto, and K. Harada, "A noncontact charger using a resonant converter with parallel capacitor of the secondary coil," *IEEE Transn. on Ind. Appln.*, vol. 36, no. 2, pp. 444–451, 2000.